THE UNIVERSITY OF
WARWICK

University of Warwick institutional repository: http://go.warwick.ac.uk/wrap

A Thesis Submitted for the Degree of PhD at the University of Warwick

http://go.warwick.ac.uk/wrap/51660

This thesis is made available online and is protected by original copyright.

Please scroll down to view the document itself.

Please refer to the repository record for this item for information to help you to cite it. Our policy information is available from the repository home page.

THE UNIVERSITY OF
WARWICK

AUTHOR: **Andrew Stephen Tatton** DEGREE: **Ph.D.**

TITLE: **Development of Solid-State NMR techniques for the characterisation of pharmaceutical compounds**

DATE OF DEPOSIT: .....

I agree that this thesis shall be available in accordance with the regulations governing the University of Warwick theses.

I agree that the summary of this thesis may be submitted for publication.

I **agree** that the thesis may be photocopied (single copies for study purposes only).

Theses with no restriction on photocopying will also be made available to the British Library for microfilming. The British Library may supply copies to individuals or libraries. subject to a statement from them that the copy is supplied for non-publishing purposes. All copies supplied by the British Library will carry the following statement:

> "Attention is drawn to the fact that the copyright of this thesis rests with its author. This copy of the thesis has been supplied on the condition that anyone who consults it is understood to recognise that its copyright rests with its author and that no quotation from the thesis and no information derived from it may be published without the author's written consent."

AUTHOR'S SIGNATURE: .....

USER'S DECLARATION

1. I undertake not to quote or make use of any information from this thesis without making acknowledgement to the author.
2. I further undertake to allow no-one else to use this thesis while it is in my care.

DATE SIGNATURE ADDRESS

.....

.....

.....

.....

.....

www.warwick.ac.uk

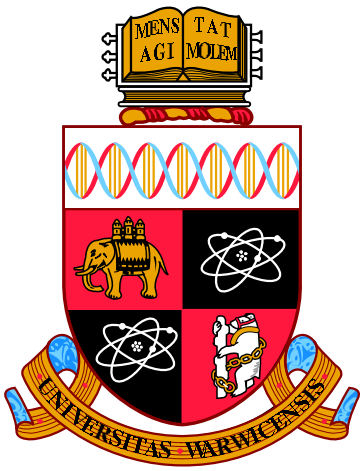

Development of Solid-State NMR techniques for the characterisation of pharmaceutical compounds

by

Andrew Stephen Tatton

Thesis

Submitted to the University of Warwick

for the degree of

Doctor of Philosophy

Department of Physics

September 2012

THE UNIVERSITY OF WARWICK

CONTENTS

LIST OF TABLES

LIST OF FIGURES

ACKNOWLEDGMENTS

Firstly, I wish to thank my supervisor, Professor Steven Brown, for all his help, support and encouragement over the past few years, including giving me the opportunity to work on interesting projects, allowing me to travel to a variety of destinations in the name of science and for always being willing to read through my work. I would also like to thank everybody at GSK for their help, particularly Tran Pham for taking a real interest in my work and for helping me see how solid-state NMR fits into the pharmaceutical industry, also thanks to Fred Vogt, Simon Watson and Andy Edwards for their help at various stages throughout my project and time at GSK. I would also like to thank all members of the Warwick group, particularly Dinu Iuga for his help with the ^{14}N-^{1}H experiments, and Jon Bradley for all his help and discussions throughout the thesis, particularly with the computational work. Also, I would like to thank Paul Hodgkinson for all his help in the homonuclear decoupling project. Financial support from EPSRC and GSK is gratefully acknowledged.

Outside of NMR, I would like to thank all the friends I have met at Warwick over all the last 8 years, as well as those from outside of Warwick, and back home. Finally, I would like to give a special thanks to all my family for their constant love and support throughout the years.

DECLARATIONS

All work performed in this thesis is original research carried out by this author, unless otherwise stated, in the Department of Physics at the University of Warwick, under the supervision of Professor Steven P. Brown between October 2008 and June 2012. An exception is experimental results in chapter 5, which were carried out by the author in the structural characterisation group at GlaxoSmithKline, Stevenage, UK, in the periods June 2010 to July 2010 and May 2011 to June 2011.

Some of the results presented have been published. Specifically, results from chapter 4:

A. S. Tatton, I. Frantsuzov, S. P. Brown and P. Hodgkinson. Unexpected effects of third-order cross-terms in heteronuclear spin systems under simultaneous radio-frequency irradiation and magic-angle spinning NMR. *J. Chem. Phys.*, 136:084503, 2012. [1]

Results in chapter 5 and chapter 7:

A. S. Tatton, T. N. Pham, F. G. Vogt, D. Iuga, A. J. Edwards and S. P. Brown. Probing intermolecular interactions and nitrogen protonation in pharmaceuticals by novel ^{15}N-edited and 2D ^{14}N^{1}H solid-state NMR. *CrystEngComm*, 14:2654-2659, 2012. [2]

Results in chapter 6:

A. L. Webber, S. Masiero, S. Pieraccini, J. C. Burley, A. S. Tatton, D. Iuga, T. N. Pham, G. P. Spada, and S. P. Brown. Identifying Guanosine Self Assembly at Natural Isotopic Abundance by High-Resolution ^{1}H and ^{13}C Solid-State NMR Spectroscopy. *J. Am. Chem. Soc.*, 133:19777-19795, 2011. [3]

This thesis has not been submitted for a degree at another university.

ABSTRACT

Structural characterisation in the solid state is an important step in understanding the physical and chemical properties of a material. In pharmaceuticals, an active pharmaceutical ingredient (API) may be medicinally favourable, but have undesirable physical properties, such as poor solubility, that potentially limit further development. Solid delivery forms, such as pharmaceutical salts, cocrystals and solid amorphous dispersions, potentially offer improvements in physical properties, whilst maintaining favourable medicinal characteristics. Solid-state NMR is an extremely sensitive probe of the local atomic environment and intermolecular interactions, for example hydrogen bonding, and is therefore well suited to studies of pharmaceuticals.

Solid-state NMR techniques applied to solid delivery forms are presented as an alternative to more established structural characterisation methods. The effect of homonuclear decoupling upon heteronuclear couplings is investigated using a combination of experimental and density-matrix simulation results acquired from a ^{13}C-^{1}H spin-echo pulse sequence, modulated by scalar couplings. It is found that third-order cross terms under MAS and homonuclear decoupling contribute to strong dephasing effects in the NMR signal. Density-matrix simulations allow access to parameters currently unattainable in experiment, and demonstrate that higher homonuclear decoupling *rf* nutation frequencies reduce the magnitude of third-order cross terms. ^{15}N-^{1}H spin-echo experiments were applied to pharmaceutically relevant samples to differentiate between the number of directly attached protons. Using this method, proton transfer in an acid-base reaction is proven in pharmaceutical salts.

The indirect detection of ^{14}N lineshapes via protons obtained using 2D ^{14}N-^{1}H HMQC experiments is presented, where coherence transfer is achieved via heteronuclear through-space dipolar couplings. The importance of fast MAS frequencies is demonstrated, and it is found that increasing the recoupling duration reveals longer range NH proximities. The 2D ^{14}N-^{1}H HMQC method is used to demonstrate the presence of specific hydrogen bonding interactions, and thus aid in identifying molecular association in a cocrystal and an amorphous dispersion. In addition, hydrogen bonding motifs were identified by observing the changes in the ^{14}N quadrupolar parameters between individual molecular components relative to the respective solid delivery form. First-principles calculations of NMR chemical shifts and quadrupolar parameters using the GIPAW method were combined with ^{14}N-^{1}H experimental results to assist with spectral assignment and the identification of the hydrogen bonding interactions.

ABBREVIATIONS

API	Active Pharmaceutical Ingredient
BABA	BAck-to-BAck
CP	Cross Polarisation
CRAMPS	Combined Rotation And Multiple Pulse Spectroscopy
CSA	Chemical Shift Anisotropy
DFT	Density Functional Theory
DSC	Differential Scanning Calorimetry
DQ	Double-Quantum
DUMBO	Decoupling Using Mind Boggling Optimisation
EFG	Electric Field Gradient
FID	Free Induction Decay
FSLG	Frequency-Switched Lee-Goldburg
FT	Fourier Transform
FWHMH	Full Width at Half Maximum Height
GIPAW	Gauge-Including Projector Augmented Waves
HETCOR	Heteronuclear Correlation
HMQC	Heteronuclear Multiple Quantum Coherence
INEPT	Insensitive Nuclei Enhanced by Polarisation Transfer
MAS	Magic Angle Spinning
NMR	Nuclear Magnetic Resonance
PAS	Principal Axis System
PMLG	Phase-Modulated Lee Goldburg
ppm	Parts Per Million
RDS	Residual Dipolar Splittings

REPT-HSQC	Recoupled Polarisation Transfer Heteronuclear Single-Quantum Correlation
rf	Radio-Frequency
SCXRD	Single Crystal X-ray Diffraction
SDG	Solvent Drop Grinding
S/N	Signal-to-Noise
SPINAL	Small Phase INcremental ALternation
SQ	Single-Quantum
TPPI	Time Proportional Phase Increment
TPPM	Two Pulse Phase Modulated
WHH	WaHuHa

CHAPTER

ONE

INTRODUCTION

1.1 Solid-State NMR development

Since the independent observations of the magnetic resonance phenomena by Purcell [4] and Bloch, [5] nuclear magnetic resonance (NMR) has rapidly progressed to become a key characterisation tool in chemistry laboratories throughout the world. NMR is a site-specific tool which is sensitive to subtle changes in chemical environments. Characterisation in the solid state is often more appropriate than liquid state analysis. For example, details concerning molecular packing configurations, such as hydrogen bonding and polymorphism are specific to the solid phase. In solution, molecular tumbling usually occurs on a faster timescale to that of the NMR interactions, which averages out broadening effects, resulting in narrow lineshapes and the simple extraction of chemical shift parameters. Consequently, the majority of NMR experiments are usually performed in the solution state. In the solid state, molecular tumbling does not usually occur, therefore anisotropic effects with an orientational dependence are not averaged by motional effects, leading to broad, featureless lineshapes that hinder extraction of chemical shift information. Solid-state NMR lineshapes are not lacking in information, rather the overload of structural information hinders analysis, contrasting to the solution state where analysis is simplified by narrow lineshapes.

A significant breakthrough in solid-state NMR was the independent invention of magic angle spinning (MAS) in the 1950's by Andrew [6,7] and Lowe. [8] The majority of anisotropic NMR interactions have a spatial dependence described by $3\cos^2\theta - 1$,

whose root is $\arctan\sqrt{2} \approx 54.7°$, known as the magic angle. If samples in the solid state are rotated at the magic angle relative to the external magnetic field, B_0, then a majority of anisotropic interactions average out over a complete rotor period, as if subject to molecular tumbling in the solution state. Improvements in probe technology has seen the introduction of ever smaller rotor diameters: currently the smallest diameter conventional probe commercially available is 1.0 mm, capable of achieving spinning frequencies approaching 80 kHz. [9] MAS is able to resolve sufficiently narrow lines for lower-γ nuclei, such as ^{13}C and ^{15}N, where the dominant interaction is the chemical shift anisotropy, however MAS does not completely average strong, non-commuting homonuclear (^{1}H-^{1}H, ^{19}F-^{19}F) dipolar couplings. This is problematic when analysing organic materials consisting of dense proton environments, as the homonuclear dipolar coupling is dependent upon the square of the gyromagnetic ratio and the internuclear distance between the coupled nuclei to the inverse cubed power. ^{1}H has the highest gyromagnetic ratio of NMR active nuclei (except for ^{3}H) and in organic materials close range proton-proton proximities are typically short (approximately 2-3 Å), therefore applying MAS alone does not sufficiently average strong dipolar couplings, which are tens of kHz in magnitude, and therefore severely hinder resolution in organic materials, such as pharmaceuticals. In order to average strong, non-commuting homonuclear dipolar couplings, homonuclear dipolar decoupling sequences have been developed, which involve the application of carefully choreographed radio-frequency (rf) nutation frequency to a sample.

The first demonstration of using rf irradiation to average homonuclear dipolar couplings and consequently obtain narrower lineshapes was the Lee-Goldburg technique, applied to CaF_2 to obtain narrow ^{19}F lineshapes. [10] This consists of off-resonance continuous rf irradiation, which rotates the spin-component of the magnetisation at an effective field aligned at the magic-angle relative to B_0. Further decoupling sequences were introduced, such as WaHuHa (WHH), [11, 12] which is composed of a series of on-resonance rf pulses of differing phase and evolution periods. The first decoupling schemes were designed for use in static cases. Whilst adequately averaging homonuclear dipolar couplings, other anisotropic interactions, such as the chemical shift anisotropy (CSA), are not averaged by such decoupling pulse sequences. In isolation, both MAS and homonuclear decoupling sequences can improve spectral quality,

however the combination of both methods, known as Combined Rotation and Multiple Pulse Sequences (CRAMPS) [13–15] can potentially result in significant improvements in spectral resolution.

Frequency Switched Lee-Goldburg (FSLG) [16, 17] and Phase Modulated Lee-Goldburg (PMLG) [18] are improvements of the Lee-Goldburg sequence, [10] and are examples of homonuclear decoupling sequences applicable in the CRAMPS approach. FSLG applies a series of off-resonance, effective 2π pulses with alternating, opposite signed frequencies. The Decoupling Using Mind Boggling Optimisation (DUMBO) [19, 20] family of decoupling sequences, including an experimentally optimised version, e-DUMBO-1_{22}, [21] involve the application of constant amplitude *rf* irradiation with rapid switching of the phase, and are also commonly applied CRAMPS methods. Both FSLG and eDUMBO-1_{22} are applied extensively throughout this thesis, and are explained in greater detail in chapter 3. The successful use of ever more complicating decoupling schemes owes much to the advent of more sophisticated hardware capable of delivering consistent, rapid phase shifts and high *rf* nutation frequencies.

CRAMPS is an important experimental consideration in a heteronuclear spin-echo experiment, which has been presented previously as a method for identifying different CH_n groups. [22, 23] Spin-echo sequences are of great importance in a range of magnetic resonance applications and were first proposed by Hahn in 1950, [24] and further developed by Carr and Purcell in 1954. [25] By refocusing the evolution due to inhomogeneous broadening, coherence lifetimes, as described by T_2' dephasing times, are extended, consequently reducing the corresponding (spin-echo) linewidths. A typical $^1J_{\text{13C-1H}}$ coupling is approximately 100 Hz, whereas the heteronuclear dipolar coupling between a chemically bonded CH pair is approximately 20 kHz. Therefore, averaging of strong heteronuclear and homonuclear dipolar couplings, in addition to refocusing of inhomogeneous broadening effects, is usually necessary to achieve sufficient resolution to observe a CH or NH J splitting. Different through-bond multiplicities yield specific splitting patterns, that can be resolved provided that the acquisition of narrow spin-echo lineshapes is achieved; in this way, the presence of through-bond coupling(s) can be proved.

The implementation of spin-echo pulse sequence elements modulated by through-bond couplings [26] has been demonstrated in numerous solid-state NMR experiments.

Two-dimensional heteronuclear correlation experiments, such as *J*-HMQC, [27], *J*-HSQC, [28] refocused INADEQUATE, [29–31] and the refocused INEPT sequence, [32, 33] all employ a spin-echo during the pulse sequence, and exploit magnetisation transfer via through-bond couplings. 2D experiments consist of two evolution periods, therefore allowing for interactions that are not directly observable in an NMR experiment to be indirectly probed. In addition to 2D experiments where coherence transfer occurs by isotropic J couplings, correlation via anisotropic couplings, such as the dipolar coupling, are an important tool in solid-state NMR.

Whilst anisotropic interactions hinder spectral resolution, they also contain valuable structural information, therefore the total removal of all anisotropic interactions is not always desirable. For example, the dipolar interaction, which is inversely dependent on the cube of the distance between coupled nuclei is a valuable source of information on internuclear distances. Therefore, re-introducing the dipolar coupling, which is removed by MAS, in a controlled manner is a powerful method for identifying intramolecular and intermolecular proximities. Recoupling of heteronuclear or homonuclear dipolar couplings is possible using different recoupling schemes. Heteronuclear dipolar recoupling schemes include rotary resonance recoupling (R^3), [34] and Rotational-Echo Double Resonance (REDOR), [35] whereas schemes such as Dipolar Recovery at the Magic Angle (DRAMA), [36] POST-C7, [37] and R-based sequences [38] are used to recouple homonuclear dipolar couplings.

The dipolar coupling interaction is directly utilised in the cross polarisation (CP) experiment. The sensitivity of a lower-γ nucleus, such as ^{13}C and ^{15}N, is enhanced by coherence transfer from an abundant nucleus, typically protons, through the dipolar couplings by achieving the Hartmann-Hahn matching condition. [39] Additionally, as ^{1}H nuclei typically have shorter T_1 times relative to ^{13}C or ^{15}N, CP can reduce the experimental time compared to direct acquisition. Initially, CP experiments were acquired under static conditions, [40,41] however CP is typically now applied under MAS conditions. [42] ^{13}C CPMAS is considered as a workhorse solid-state NMR experiment of organic materials, e.g., for pharmaceutical applications, [43] owing to its relatively simple set-up, acceptable experimental times and the rich information content available.

Insight into internuclear proximities can be gained from two-dimensional correlation experiments which exploit the dipolar coupling interaction. These include

2D experiments which utilise cross-polarisation, such as ^{13}C-^{1}H HETCOR experiments. [44–46] Alternatively, the dipolar coupling can be reintroduced for indirect observation using recoupling schemes; for example ^{1}H double-quantum correlation experiments. [47] Heteronuclear Multiple-Quantum Coherence (HMQC) experiments have been demonstrated utilising either through-bond couplings, [27, 48, 49] or via the recoupling of heteronuclear dipolar couplings. [50] HMQC experiments can be used to achieve correlation between two spin-$\frac{1}{2}$ nuclei, such as ^{13}C-^{1}H, or correlation between a spin-$\frac{1}{2}$ nucleus and a quadrupolar nucleus, such as ^{14}N. [51]

Computational techniques are a very useful complement to experimental data. The development of Hamiltonian propagator governed density-matrix simulation programs such as Simpson [52] or SPINEVOLUTION [53] are advantageous as they allow the user to investigate the viability of new experiments or complement existing experimental results. Furthermore, they allow access to experimental conditions not currently possible due to hardware limitations, and removal of specific interactions that are not of direct interest can aid understanding.

First-principles calculations utilising DFT (density functional theory) has rapidly progressed in solid-state NMR. The CASTEP platform [54] uses planewave pseudopotentials [55] to reconstruct the electron density throughout a material. Crystalline materials are particularly suited to CASTEP calculations, as they exploit periodicity in the crystal lattice. DFT calculations are ideally suited to optimising light-element positions determined by single crystal diffraction. GIPAW (gauge included projector augmented waves) [56–59] calculations using the CASTEP platform yield isotropic chemical shifts and EFG (electric field gradient) parameters to assist in the assignment of experimental data. GIPAW calculations of NMR parameters in a diverse range of systems has been demonstrated, [3, 60–63] including application to pharmaceutical molecules. [64–67]

1.2 Characterisation of pharmaceutical solids

Solid-state NMR is an increasingly applied methodology in pharmaceutical analysis. [43, 68–70] Demonstrated applications include identifying different polymorphic forms, [71, 72] characterising anhydrate as opposed to hydrate forms, [73, 74], establishing

the relative amorphous and crystalline content of pharmaceuticals, [75, 76] studies of dynamics within a pharmaceutical molecule, [77] and analysis of drug products. [78, 79]

1.2.1 Pharmaceutical formulations

Pharmaceutically interesting compounds with medicinally favourable properties will not always have desirable physical properties such as bio-availability, solubility and chemical stability. Numerous solid delivery forms are utilised to improve physical properties of an active pharmaceutical ingredient (API), [80] including but not limited to pharmaceutical salts, [81] cocrystals, [82–85] and solid amorphous dispersions. [86, 87] It is important, for both patent and regulatory reasons, that suitable screening of pharmaceutical solid forms are available, as small changes in molecular structure can have a significant impact upon the performance of a drug.

The most prominent multi-component delivery forms in the pharmaceutical industry are pharmaceutical salts. However, these are reliant upon the API being sufficiently ionisable. Despite the high proportion of pharmaceutical salts, the accessible design space of salt formations is considered to be restrictive owing to the relatively low number of non-toxic pharmaceutical acid or base formers available.

Cocrystals have recently received attention as an alternative to pharmaceutical salts. A cocrystal is typically, although not universally, defined as two or more neutral components in the solid phase, which are typically bound by covalent interactions, such as hydrogen bonding. [88] An amorphous solid-dispersion with a hydrophilic polymeric carrier maintains the advantageous solubility properties associated with the amorphous state, whilst also improving the thermodynamical stability relative to a free amorphous phase, which is thermodynamically unstable relative to the crystalline phase. Typically, intermolecular bonding between individual cocrystal constituents and between an amorphous API and corresponding hydrophilic carrier is via hydrogen bonding. Solid-state NMR has been shown to be an ideal characterisation tool for cocrystals [89–91] and amorphous dispersions. [92]

Cocrystal discovery utilises the solvent drop grinding synthesis route, discovery in this manner does not always allow for straightforward growth of a single crystal necessary for characterisation using single crystal X-ray diffraction (SCXRD). To date, full acceptance of cocrystal delivery forms has been limited by a lack of definitive charac-

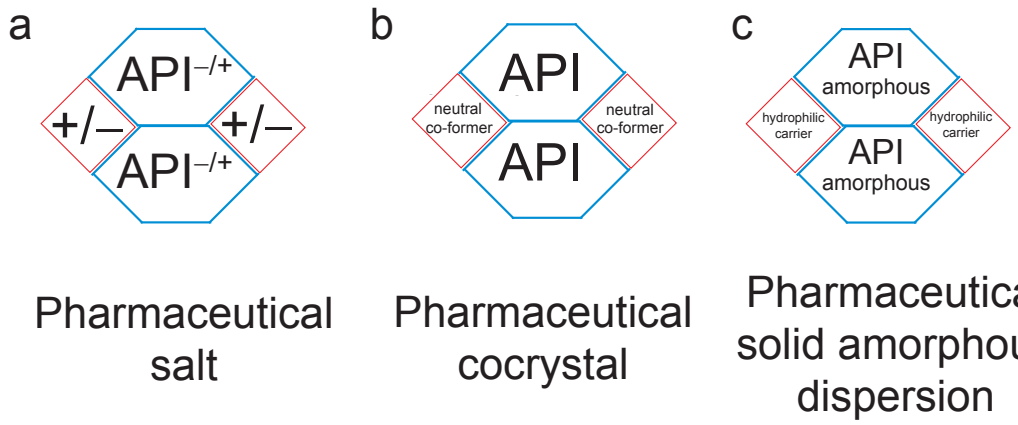

Figure 1.1: Schematics representation of (a) pharmaceutical salt, (b) pharmaceutical cocrystal and (c) amorphous solid dispersion. This figure is based around Fig. 1 in ref. [84].

terisation techniques. For amorphous materials, traditional structural characterisation methods, such as single crystal X-ray diffraction (SCXRD), are not suitable due to a lack of long-range order. Solid-state NMR is applicable to materials that are non-crystalline. Differential scanning calorimetry (DSC) techniques are currently the most prominent screening technique for solid amorphous dispersions, however interpretation of more complex systems has been shown to be challenging, particularly if glass transition temperature values (T_g) of separate components are similar (within 10°C). [93] Solid-state NMR is applicable to more complex systems, and furthermore, is able to accurately pinpoint the positions of lighter elements, such as ^{1}H, which are often not easily determined using diffraction techniques. Schematic representations of various solid delivery forms which are of interest in the pharmaceutical industry are shown in Fig. 1.1.

1.2.2 Hydrogen bonding

A hydrogen bond is a non-covalent interaction between a proton donor X-H, and an electronegative proton acceptor Y, commonly the Y nucleus is nitrogen, oxygen or fluorine. Hydrogen bonds are of particular interest as the interaction is strong enough to hold together molecules. By defining a hydrogen bond as X-H...Y, where X is directly bonded to the proton and Y is more electronegative than H, the strongest hydrogen bonding occurs when XY is at the shortest separation, as X-H and H...Y distances approach equivalence. [94] Hydrogen bonding interactions can be contained within a

molecule or as an intermolecular interaction.

Solid-state NMR has been demonstrated as a powerful probe of hydrogen bonding configurations. [95] The ^{1}H isotropic chemical shift is most deshielded (highest ppm) when the hydrogen bonding is strongest. [15, 96, 97] Additionally, changes in hydrogen bonding geometry can be identified from changes in extracted quadrupolar parameters, this has been demonstrated for numerous quadrupolar nuclei, including ^{14}N, ^{35}Cl and ^{17}O. [60, 98, 99] Recently, it has been shown that GIPAW calculations can assist in identifying and quantifying specific hydrogen bonding interactions. This is achieved through comparison of calculated ^{1}H chemical shifts of a full crystal structure relative to an isolated molecule. The isotropic proton chemical shift of the isolated molecule is found to be less deshielded relative to the full crystal, dependent upon the strength of the hydrogen bond interaction. [67, 100–102]

1.2.3 Nitrogen solid-state NMR methods

Nitrogen is present in a majority of pharmaceuticals compounds, and often is directly involved in acid-base interactions or hydrogen bonding interactions. Both naturally occurring nitrogen isotopes are NMR active, each possessing different challenges, and providing different information content. ^{14}N has a natural abundance of 99.6% compared to 0.37% ^{15}N abundance. ^{14}N has a lower gyro-magnetic ratio and is spin-1 compared to spin-$\frac{1}{2}$ for ^{15}N. Nuclei with spin greater than spin-$\frac{1}{2}$ possess a quadrupolar interaction arising from interaction between the nuclear quadrupole moment and the electric field gradients at the nucleus. This interaction can be of the order of MHz and results in broad lineshapes that are only partially averaged by MAS, as explained in more detail in section 2.4.5. However, the quadrupolar coupling, whilst hindering spectral resolution, yields electric field gradient (EFG) parameters which are inaccessible from spin-$\frac{1}{2}$ ^{15}N NMR.

^{15}N is a spin-$\frac{1}{2}$ nucleus and is therefore not complicated by the presence of the quadrupolar interaction. As is shown in this thesis, the identification of different XH_n functional groups (where X = ^{13}C or ^{15}N) can be achieved by establishing the number of through-bond coupling(s) using spectral editing methods. J-based spectral editing methods, referred to herein as $^{1}J_{15N\text{-}1H}$ editing for ^{15}N analysis, achieved using a heteronuclear spin-echo pulse sequence can be employed to establish the number

of directly attached protons to a spin-$\frac{1}{2}$ nucleus. [22] An inspection of signal changes over a range of τ values allows for the identification of different proton moieties as the magnetisation evolves according to the number of covalent bonds. As discussed, the most common multi-component delivery method of an API are pharmaceutical salts, which are composed of an ionised acid-base pair. Nitrogen sites often act as a proton acceptor during an acid-base reaction, therefore establishing the presence of proton transfer via the presence of a through-bond N-H coupling is a potentially powerful method for establishing whether a salt has formed.

Studies of ^{14}N have been limited relative to ^{15}N studies owing to unfavourable spin-1 properties, despite its much higher natural abundance. Indirect detection of ^{14}N via ^{1}H offers improvement in signal relative to direct ^{14}N detection. This is achieved herein using 2D ^{14}N-^{1}H HMQC experiments, [51] where if the correlation mechanism is dipolar coupling then qualitative information regarding intra and intermolecular proximities can be extracted. Probing the state of protonation in nitrogen functional groups and identifying hydrogen bonding configurations is a valuable tool during pharmaceutical development.

1.3 Thesis Outline

This thesis details the development and application of solid-state NMR for pharmaceutical characterisation. Solid-state NMR is shown to be a well suited technique for probing pharmaceutical salts, cocrystals and amorphous solid-dispersions. Additionally, windowless homonuclear dipolar decoupling sequences are investigated using a combination of experimental and density-matrix simulation results, particularly within the context of heteronuclear experiments.

Chapter 2 outlines the relevant theory concerning solid-state NMR. The underlying quantum mechanics is presented and Hamiltonian descriptions of key NMR interactions detailed. Experimental principles that are used within the thesis are introduced in chapter 3. Explanations of phase cycling, NMR lineshapes and 2D experiments of general relevance to solid-state NMR are detailed, in addition to more specialised techniques such as homonuclear decoupling and particular pulse sequences used in this thesis. Furthermore, computational methods, namely density-matrix simulations and

DFT GIPAW calculations are introduced.

Chapter 4 concerns the effect of homonuclear decoupling upon CH heteronuclear couplings, which was established using a combination of experiment and density-matrix simulations. It is well documented that homonuclear decoupling schemes scale isotropic interactions, including J couplings, however the important effect upon heteronuclear dipolar couplings was not previously realised. Experimental heteronuclear spin-echo modulation curves are presented for L-alanine, acquired using eDUMBO-1_{22} homonuclear decoupling during τ periods, for a range of cycle times and rf irradiation frequencies. Further understanding of the effect of homonuclear decoupling upon heteronuclear dipolar couplings is achieved using simulation results. The capability to include specific interactions of interest allows the relevance of separate interactions to be established. Although simulations were initially performed for a single CH spin pair, the number of spins was increased in order to gauge the effect of introducing additional close range protons. Using simulations, it was possible to record modulation curves for single crystals, and investigate the effect of rf nutation frequencies and corresponding decoupling cycle times currently not achievable experimentally.

^{15}N spectral editing experiments applied to pharmaceutical molecules are demonstrated in chapter 5. As nitrogen sites can be protonated in a pharmaceutical salt, proving protonation is an important regulatory and patent concern. Spectral editing techniques which utilise through-bond couplings were applied to tenoxicam Form III and pazopanib, both of which are in the form of pharmaceutical salts. Furthermore, the $^{1}J_{15N\text{-}1H}$ technique was applied to cimetidine, a pharmaceutical molecule. Calculated ^{15}N isotropic chemical shifts, obtained using the GIPAW method, were used to assist in the ^{15}N spectral assignment.

Chapter 6 begins with an investigation of the effect of changing the MAS frequency for ^{14}N-^{1}H HMQC experiments of the dipeptide β-AspAla. Furthermore, comparison between β-AspAla spectra acquired using correlation transfer via through-bond or through-space couplings is presented. For spectra acquired using correlation transfer via through-space couplings, the effect of different recoupling durations upon coherence transfer for various NH proximities was investigated experimentally, and complemented using simulation to establish semi-quantitative information regarding NH dipolar proximities. The experimental application of the 2D ^{14}N-^{1}H HMQC technique to a guano-

sine derivative is presented in order to establish that the sequence is applicable to systems beyond model set up materials. GIPAW calculations using CASTEP assist in the assignment of isotropic chemical shifts and by calculating ^{14}N EFG parameters.

Chapter 7 demonstrates application of the ^{14}N-^{1}H HMQC experiment to pharmaceutically relevant materials. Firstly, application to cimetidine is demonstrated, in conjunction with GIPAW calculation. The viability of 2D ^{14}N-^{1}H HMQC experiments as a possible cocrystal and amorphous dispersion screening technique is then presented. The example cocrystal investigated is nicotinamide palmitic-acid, whereas a solid amorphous dispersion of an API (acetaminophen) and a hydrophilic carrier (PVP) was selected. Of particular interest is the potential to probe intermolecular hydrogen bonding interactions, which indicate molecular association. Cocrystal results are aided by GIPAW calculation of isotropic chemical shifts and electric field gradient (EFG) parameters for the individual molecular components and the cocrystal form.

CHAPTER

TWO

NMR THEORY

When a nuclear spin is subject to a static external magnetic field, interactions between the magnetic moment and the external field lift the degeneracy of the energy levels. The energy of transitions between these levels are specific to each nuclear species, and the strength of the external field. If the sole insight from NMR was distinguishing between different nuclear species, then the appeal of NMR as a spectroscopic tool would be limited. However, subtle shifts to the energy of a transition provide valuable insight into the surrounding environment of the nucleus. Within this chapter, the spin angular momentum operators for a single spin are introduced, followed by the density operator formalism, which is a more suitable description for an ensemble of spins. External and internal NMR interactions are discussed, and individual Hamiltonians for each interaction are presented. The theory contained within this chapter is based upon that presented in refs. [103–105].

2.1 Spin Angular Momentum

Spin angular momentum is an intrinsic property of a nucleus, whose magnitude is quantised in discrete terms of $\hbar$, where $\hbar$ is equal to Planck's constant. A possible $2I + 1$ energy levels exist, where I is the total spin angular momentum quantum number. In the absence of a magnetic field the energy levels are degenerate, however application of a static, external magnetic field, B_0, lifts the degeneracy of the energy levels. This is due to an interaction between the magnetic moment and B_0. The splitting between the energy levels is known as the Zeeman interaction energy, the Hamiltonian of which

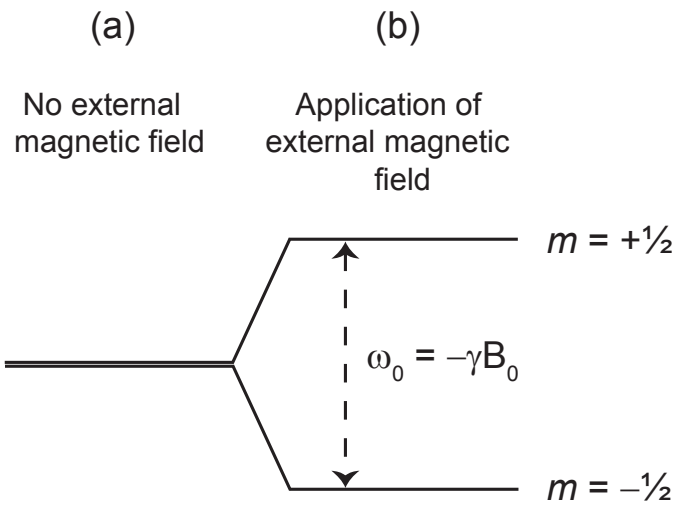

Figure 2.1: Representation of energy levels for an isolated spin-$\frac{1}{2}$ nucleus when (a) not subject to an external magnetic field, and (b) subject to an external magnetic field, therefore the degeneracy of the energy levels is lifted.

is given by:

$$\hat{H} = -\hat{\boldsymbol{\mu}} \cdot \boldsymbol{B_0} \tag{2.1}$$

The magnetic moment, $\hat{\boldsymbol{\mu}}$ is defined as:

$$\hat{\boldsymbol{\mu}} = \gamma \hat{\boldsymbol{I}} \tag{2.2}$$

where γ is the gyromagnetic ratio. For a case where the spin angular momentum is aligned along the direction of the external magnetic field, and convention dictates that this is taken along the z-axis, referred to as the longitudinal direction, the Zeeman energy Hamiltonian can be written as:

$$\begin{aligned} \hat{H} &= -\gamma \hat{I}_z B_0 \\ &= \omega_0 \hat{I}_z \end{aligned} \tag{2.3}$$

where ω_0 is the Larmor frequency,

$$\omega_0 = -\gamma B_0 \tag{2.4}$$

corresponding to the splitting between energy states. The splitting is proportional

to the gyro-magnetic ratio, γ, which is a constant for each nuclear species, and the strength of the external magnetic field, B_0. NMR yields information content owing to this splitting in energy levels, which is quantised and is sensitive to subtle changes in the local environment of a nucleus, which perturb the Zeeman splitting energy by small, but measurable quantities. Nuclei which have $I = 0$ (e.g., ^{12}C) have no energy splitting when subject to an external magnetic field, and are therefore not observable in an NMR experiment.

A wavefunction completely describes all spatial and spin properties of a system in quantum mechanical terms, and is denoted herein as $|\,\psi\rangle$. When an operator, $\hat{A}$, which represents a desired physical quantity, acts upon a system it yields a value detailing that physical property. Repeated experiments will yield an average value, known as the expectation value, which describe the result of a specific operator acting upon a defined system, given as:

$$\left\langle \hat{A} \right\rangle = \langle \psi |\, \hat{A}\, | \psi \rangle \tag{2.5}$$

A general operator, $\hat{A}$, can be expressed as a matrix, where the element A_{rs} is given as $\langle r\,|\,\hat{A}\,|\,s\rangle$:

$$\boldsymbol{A} = \begin{pmatrix} A_{\phi_1\phi_1} & A_{\phi_1\phi_2} \\ A_{\phi_2\phi_1} & A_{\phi_2\phi_2} \end{pmatrix} = \begin{pmatrix} \langle \phi_1\,|\,\hat{A}\,|\,\phi_1\rangle & \langle \phi_1\,|\,\hat{A}\,|\,\phi_2\rangle \\ \langle \phi_2\,|\,\hat{A}\,|\,\phi_1\rangle & \langle \phi_2\,|\,\hat{A}\,|\,\phi_2\rangle \end{pmatrix} \tag{2.6}$$

Observables relating to the nuclear spin can be extracted through application of the spin-angular momentum operator. The total magnitude of the spin-angular momentum squared, is given as:

$$\hat{I}^2 = \hat{I}_x^2 + \hat{I}_y^2 + \hat{I}_z^2 \tag{2.7}$$

The x, y, and z-components of spin-angular momentum, are expressed in matrix form as:

$$\hat{I}_x = \begin{pmatrix} 0 & \frac{1}{2} \\ \frac{1}{2} & 0 \end{pmatrix}, \qquad \hat{I}_y = i \begin{pmatrix} 0 & -\frac{1}{2} \\ \frac{1}{2} & 0 \end{pmatrix}, \qquad \hat{I}_z = \begin{pmatrix} \frac{1}{2} & 0 \\ 0 & -\frac{1}{2} \end{pmatrix} \tag{2.8}$$

Using the above matrix notations results in the following commutator relations:

$$\left[\hat{I}^2, \hat{I}_z\right] = 0 \tag{2.9}$$

$$\left[\hat{I}_x, \hat{I}_y\right] = i\hat{I}_z \tag{2.10}$$

As only a single component of the spin angular momentum commutes with the total spin angular momentum, this implies that only a single component of the spin angular momentum is observable at any single point in time, which by convention is the z-component. As discussed, the z-component is defined as being aligned parallel to the external field and is referred to as the longitudinal direction, whereas the x-y plane is defined as the transverse plane. The individual components of spin angular momentum do not commute with each other, therefore individual components of spin angular momentum are not observable at the same point in time. The operators $\hat{I}^2$ and $\hat{I}_z$, acting upon $|\psi\rangle$, yield the following eigenvalues:

$$\hat{I}^2 |\psi\rangle = \hbar I(I+1) |\psi\rangle \tag{2.11}$$

$$\hat{I}_z |\psi\rangle = \hbar m |\psi\rangle \tag{2.12}$$

where m is the z-component of the spin-angular momentum, and can take values of $-I$, $-I+1$ ... $I-1$, $+I$. Therefore, for a spin-$\frac{1}{2}$ nucleus there are two possible values of m, namely $+\frac{1}{2}$ and $-\frac{1}{2}$, as seen in Fig. 2.1. These eigenstates are defined as spin-up (α) and spin-down (β) respectively. Therefore, the operator $\hat{I}_z$, acting upon eigenstates $|\alpha\rangle$ and $|\beta\rangle$, yield the following eigenvalues:

$$\hat{I}_z |\alpha\rangle = +\frac{1}{2} |\alpha\rangle \tag{2.13}$$

$$\hat{I}_z |\beta\rangle = -\frac{1}{2} |\beta\rangle \tag{2.14}$$

As indicated by the x and y-components of the spin angular momentum not commuting with each other, $\hat{I}_x$ and $\hat{I}_y$ operators acting upon spin eigenstates $|\alpha\rangle$ and $|\beta\rangle$ results

in conversion to the other eigenstate:

$$\hat{I}_x \left|\alpha\right\rangle = \frac{1}{2} \left|\beta\right\rangle \tag{2.15}$$

$$\hat{I}_x \left|\beta\right\rangle = \frac{1}{2} \left|\alpha\right\rangle \tag{2.16}$$

$$\hat{I}_y \left|\alpha\right\rangle = \frac{1}{2} i \left|\beta\right\rangle \tag{2.17}$$

$$\hat{I}_y \left|\beta\right\rangle = -\frac{1}{2} i \left|\alpha\right\rangle \tag{2.18}$$

An isolated spin-$\frac{1}{2}$ nucleus is not required to exist purely in one eigenstate, rather it can be considered as a superposition of α and β states, written as:

$$\left|\psi\right\rangle = c_\alpha \left|\alpha\right\rangle + c_\beta \left|\beta\right\rangle \tag{2.19}$$

The expectation value of an operator, $\langle \hat{A} \rangle$ (recall equations 2.5 and 2.6), acting upon a spin-$\frac{1}{2}$ nucleus, can expressed as a matrix multiplication:

$$\begin{aligned} \langle \hat{A} \rangle &= \begin{pmatrix} c_\alpha^* & c_\beta^* \end{pmatrix} \begin{pmatrix} A_{\alpha\alpha} & A_{\alpha\beta} \\ A_{\beta\alpha} & A_{\beta\beta} \end{pmatrix} \begin{pmatrix} c_\alpha \\ c_\beta \end{pmatrix} \\ &= c_\alpha^* c_\alpha A_{\alpha\alpha} + c_\alpha^* c_\beta A_{\alpha\beta} + c_\beta^* c_\alpha A_{\beta\alpha} + c_\beta^* c_\beta A_{\beta\beta} \end{aligned} \tag{2.20}$$

The probability of residing in either state depends on c_α or c_β , where $|c_\alpha|^2 + |c_\beta|^2 = 1$. Note, that $\left|\psi\right\rangle$ and $\left\langle\psi\right|$ denote column and row vectors, respectively. Therefore, using equation 2.20, the operator $\hat{I}_z$, acting upon a spin-$\frac{1}{2}$ nucleus, yields the expectation value:

$$\begin{aligned} \left\langle \hat{I}_z \right\rangle =& \left\langle\psi\right| \hat{I}_z \left|\psi\right\rangle \\ =& \frac{1}{2}(c_\alpha c_\alpha^* - c_\beta c_\beta^*) \\ =& \frac{1}{2} \left|c_\alpha\right|^2 - \frac{1}{2} \left|c_\beta\right|^2 \end{aligned} \tag{2.21}$$

Therefore, the implication of equation 2.21 is that the longitudinal component of spin angular momentum is dependent upon direct-products ($c_\alpha^* c_\alpha$, $c_\beta^* c_\beta$) of the coefficients for either state, which corresponds to the on-diagonal matrix elements in equation 2.20. The expectation values of the transverse components of the spin-angular momentum

are cross-products ($c^*_\alpha c_\beta$, $c^*_\beta c_\alpha$) between the coefficients which describe either state, given as:

$$\langle \hat{I}_x \rangle = \frac{1}{2}(c_\alpha c^*_\beta + c_\beta c^*_\alpha) \tag{2.22}$$

$$\langle \hat{I}_y \rangle = \frac{1}{2} i(c_\alpha c^*_\beta - c_\beta c^*_\alpha) \tag{2.23}$$

2.2 The Density Operator

Although the above description is suitable for an isolated spin $\frac{1}{2}$ nucleus, to describe the NMR experiment for an ensemble of spins, where numerous spins are present, is necessary. A more complete manner of writing the scalar constants, c_i, in equation 2.6 is required. This is achieved by expressing an ensemble of spins as a density operator, which is defined as:

$$\hat{\rho} = \overline{|\psi\rangle\langle\psi|} \tag{2.24}$$

Here, $\hat{\rho}$ signifies the density operator. It is important to note that the overbar signifies an average over an ensemble of states. However, the overbar notation will be dropped from further expressions for convenience. The density operator is a more complete manner of describing a system of many spins. As for the isolated spin-$\frac{1}{2}$ nucleus, an expectation value can be calculated by applying an operator to a system. The density operator expressed for an ensemble of isolated spin-$\frac{1}{2}$ nuclei, in matrix form (the so-called density matrix) is expressed as:

$$|\psi\rangle\langle\psi| = \begin{pmatrix} c_\alpha \\ c_\beta \end{pmatrix} \begin{pmatrix} c^*_\alpha & c^*_\beta \end{pmatrix} = \begin{pmatrix} c_\alpha c^*_\alpha & c_\alpha c^*_\beta \\ c_\beta c^*_\alpha & c_\beta c^*_\beta \end{pmatrix} \tag{2.25}$$

The product of the density operator and an operator acting upon a system is:

$$\begin{aligned} \boldsymbol{\rho A} &= \begin{pmatrix} c_\alpha c^*_\alpha & c_\alpha c^*_\beta \\ c_\beta c^*_\alpha & c_\beta c^*_\beta \end{pmatrix} \begin{pmatrix} A_{\alpha\alpha} & A_{\alpha\beta} \\ A_{\beta\alpha} & A_{\beta\beta} \end{pmatrix} \\ &= \begin{pmatrix} c_\alpha c^*_\alpha A_{\alpha\alpha} + c_\alpha c^*_\beta A_{\beta\alpha} & c_\alpha c^*_\alpha A_{\alpha\beta} + c_\alpha c^*_\beta A_{\beta\beta} \\ c_\beta c^*_\alpha A_{\alpha\alpha} + c_\beta c^*_\beta A_{\beta\alpha} & c_\beta c^*_\alpha A_{\alpha\beta} + c_\beta c^*_\beta A_{\beta\beta} \end{pmatrix} \end{aligned} \tag{2.26}$$

Inspection of the matrix reveals that the on-diagonal elements correspond to the expectation value in equation 2.20. Therefore, the expectation value is determined as the trace of the matrix.

$$\langle \hat{A} \rangle = \mathrm{Tr}(\boldsymbol{\rho A}) \tag{2.27}$$

Expressing the coefficients in equation 2.19 as a product of a real coefficient, a_α or a_β, and a phase constant, ϕ_α or ϕ_β, allows better understanding of the significance of the on and off-diagonal elements of the density matrix.

$$|\psi\rangle = a_\alpha e^{i\phi_\alpha} |\alpha\rangle + a_\beta e^{i\phi_\beta} |\beta\rangle \tag{2.28}$$

Substitution of equation 2.28 into equation 2.24, yields a density operator to describe a system of isolated spins as:

$$\rho = \begin{pmatrix} {a_\alpha}^2 & a_\alpha a_\beta e^{i(\phi_\alpha - \phi_\beta)} \\ a_\alpha a_\beta e^{i(\phi_\beta - \phi_\alpha)} & {a_\beta}^2 \end{pmatrix} \tag{2.29}$$

If all spins reside in subtly different states, taken over an entire system, the values of $e^{i(\phi_\alpha - \phi_\beta)}$ will destructively interfere and average to zero, leaving on-diagonal terms only in equation 2.29. This is referred to as a population state. Note, that the retention of on-diagonal terms only is analogous to longitudinal spin angular momentum.

Now consider an ensemble of spins that reside in the same state, therefore, averaged over the whole system, the value of $e^{i(\phi_\alpha - \phi_\beta)}$ is non zero. Consequently, the off-diagonal terms in equation 2.29 are retained. This is referred to as a phase coherence between states. Importantly, only coherence states are observable in an NMR experiment, therefore the spin system must be manipulated from the population state at thermal equilibrium into an observable phase coherence (in reality, only single quantum coherences are directly observable in an NMR experiment, though other types of coherence can be indirectly observed in multi-dimensional experiments). The presence of off-diagonal components is akin to the transverse components of spin angular momentum, indicating that observation of a coherence requires magnetisation to be in the transverse plane.

2.2.1 The time dependence of the density operator

An NMR experiment consists of a combination of *rf* pulses and free evolution, therefore the density operator must be considered as a time dependent function. Differentiating the density operator with respect to time gives:

$$\begin{aligned}\frac{\mathrm{d}\hat{\rho}(t)}{\mathrm{d}t} &= \frac{\mathrm{d}}{\mathrm{d}t}(|\psi\rangle\langle\psi|) \\ &= \left(\frac{\mathrm{d}}{\mathrm{d}t}|\psi\rangle\right)\langle\psi| + |\psi\rangle\left(\frac{\mathrm{d}}{\mathrm{d}t}\langle\psi|\right)\end{aligned} \tag{2.30}$$

The time dependent Schrödinger equations for $|\psi\rangle$ and $\langle\psi|$ are:

$$\frac{\mathrm{d}}{\mathrm{d}t}|\psi\rangle = -i\hat{H}|\psi\rangle \tag{2.31}$$

$$\frac{\mathrm{d}}{\mathrm{d}t}\langle\psi| = i\langle\psi|\hat{H} \tag{2.32}$$

Therefore, substitution of the above expressions into equation 2.30 gives:

$$\frac{d}{dt}\hat{\rho}(t) = -i\left[\hat{H}, \hat{\rho}(t)\right] \tag{2.33}$$

This is known as the Liouville von-Neumann equation, the solution of which is:

$$\hat{\rho}(t) = \hat{U}(t)\hat{\rho}(0)\hat{U}(t)^{-1} \tag{2.34}$$

The propagator is defined as $\hat{U}$(t), and describes the Hamiltonian acting between t=0 and t=t. If the Hamiltonian does not change over this period then the propagator is:

$$\hat{U}(t) = e^{-i\hat{H}t} \tag{2.35}$$

Equations 2.34 and 2.35 imply that in order to calculate the time dependent density operator, then the initial state of the system must be known, in addition to the Hamiltonian(s) present during time period t=0 and t=t. However, different Hamiltonian interactions may be present at different points during an NMR experiment, therefore it is necessary to express the propagator as a series of Hamiltonians, written as:

$$\hat{U}(t) = e^{-i\hat{H}_n t_n}...e^{-i\hat{H}_2 t_2}e^{-i\hat{H}_1 t_1} \tag{2.36}$$

Note, that the Hamiltonian interactions are taken in chronological order. Individual Hamiltonian descriptions for relevant interactions are detailed in sections 2.3 and 2.4.

2.2.2 Hamiltonians

A total Hamiltonian operator can be constructed to describe all relevant interactions which evolve during an NMR experiment. In the context of an NMR experiment, Hamiltonians can be classed as either an external or internal interaction. The total Hamiltonian is then considered as a sum of all relevant Hamiltonian interactions:

$$\hat{H} = \hat{H}_Z + \hat{H}_{rf} + \hat{H}_\sigma + \hat{H}_D + \hat{H}_Q + \hat{H}_J \tag{2.37}$$

Here, $\hat{H}_Z$ and $\hat{H}_{rf}$ are external interactions representing the Zeeman interaction and *rf* pulses, respectively, and $\hat{H}_\sigma + \hat{H}_D + \hat{H}_Q + \hat{H}_J$ are internal spin interactions, signifying the chemical shielding, dipolar coupling, quadrupolar interaction and J coupling respectively. A Hamiltonian to describe an operator $\hat{A}$ is expressed in Cartesian coordinates as:

$$\begin{aligned} \hat{H}_A &= \hat{I}\tilde{A}\hat{S} \\ &= \begin{pmatrix} \hat{I}_x & \hat{I}_y & \hat{I}_z \end{pmatrix} \begin{pmatrix} A_{xx} & A_{xy} & A_{xz} \\ A_{yx} & A_{yy} & A_{yz} \\ A_{zx} & A_{zy} & A_{zz} \end{pmatrix} \begin{pmatrix} \hat{S}_x \\ \hat{S}_y \\ \hat{S}_z \end{pmatrix} \end{aligned} \tag{2.38}$$

$\hat{I}$ represents a spin operator I, $\tilde{A}$ describes the interaction and $\hat{S}$ can be a further interacting spin operator or an external variable.

2.3 External Interactions

Within this section, external interactions between the nuclear spin system and external variables, namely the external magnetic field, B_0, and *rf* pulses are introduced.

2.3.1 Thermal Equilibrium State

In a static, homogeneous magnetic field, the Hamiltonian describing the interaction between the external magnetic field and nuclear spin, $\hat{I}$, is given as:

$$\hat{H}_Z = -\gamma \hat{I}_z B_0 = \omega_0 \hat{I}_z \tag{2.39}$$

Therefore, the density operator can be written, using statistical physics, as:

$$\rho = \frac{e^{-\beta\hbar\omega_0 I_z}}{Tr\left[e^{-\beta\hbar\omega_0 I_z}\right]} \tag{2.40}$$

where, $\beta = \frac{1}{k_\beta T}$ and k_β is Boltzmann's constant. In the high temperature (T) approximation, which in reality is any temperature a few fractions of a Kelvin above absolute zero, it follows that $\beta \ll 1$. Furthermore, $e^{-n} \approx (1 - n)$. Therefore, equation 2.40 can be written as:

$$\rho \approx \frac{1 - \beta\hbar\omega_0 I_z}{Tr\left[e^{-\beta\hbar\omega_0 I_z}\right]} \tag{2.41}$$

Using the relationship, Tr[A] + Tr[B] = Tr[A+B], and that $Tr[1] = 2^N$, then equation 2.41 can be written as:

$$\rho_{eq} = const. - \frac{\beta\hbar\omega_0}{2^N} I_z \tag{2.42}$$

$$\rho_{eq} \propto I_z \tag{2.43}$$

This demonstrates that at thermal equilibrium the density operator is aligned along the z-axis. It is assumed that an NMR experiment always begins at thermal equilibrium, corresponding to magnetisation aligned along the z-direction in a population state. Only coherence states are measurable in an NMR experiment, therefore creation of coherence states between spins is required to observe an NMR signal.

2.3.2 Application of an *rf* pulse

As demonstrated, at thermal equilibrium the magnetisation resides in a population state aligned along I_z, and only a coherence state (transverse magnetisation) is observable in an NMR experiment. Coherence states are excited by applying a much weaker magnetic

field, B_1, whose oscillation frequency, ω_{rf} is close to ω_0, and is consequently capable of manipulating the magnetisation. ω_{rf} is applied in the radiofrequency range of the EM spectrum. The oscillating magnetic field, in this case aligned along x-direction, is written as:

$$\begin{aligned} B_1(t) &= 2B_1(cos[\omega_{rf}t + \phi])\mathbf{i} \\ &= B_1[\exp(+i\omega_{rf}t) + \exp(-i\omega_{rf}t)]\mathbf{i} \qquad \text{if} \qquad \phi = 0 \end{aligned} \tag{2.44}$$

where $\pm\omega_{rf}$ are counter rotating frequencies of the oscillating pulse, ϕ is the phase of the pulse and $\mathbf{i}$ is a unit vector aligned along the x-direction. The application of an on or close to on resonance *rf* pulse tilts the magnetisation away from the z-axis, and results in the bulk magnetisation precessing about the z-axis. Since only $+\omega_{rf}$ is sufficiently close to ω_0 for the pulse to have an effect upon the magnetisation, the effect of the $-\omega_{rf}$ term upon the magnetisation can be safely ignored. The Hamiltonian for an *rf* pulse is therefore simplified as:

$$\hat{H}_{rf} = \hat{I}.\tilde{Z}.\hat{B}_1 = -\gamma B_1[\hat{I}_x \cos(\omega_{rf}t + \phi) + \hat{I}_y \sin(\omega_{rf}t + \phi)] \tag{2.45}$$

By convention, the NMR frame is considered as the x-y axis precessing about the z-axis at a frequency of $+\omega_{rf}$, known as the rotating frame. Therefore, the *rf* Hamiltonian can be treated as time independent. In the rotating frame, the radiofrequency field appears static, and a pulse is simply seen as the application of a static magnetic field of magnitude B_1. Consequently, equation 2.45 can be expressed as:

$$\begin{aligned} \hat{H}_{rf}^{rot} &= -\gamma B_1[\hat{I}_x \cos(\phi) + \hat{I}_y \sin(\phi)] \\ &= \omega_1 \hat{I}_x \qquad \text{if} \qquad \phi = 0 \end{aligned} \tag{2.46}$$

where ω_1 is referred to as the nutation frequency of the *rf* pulse. As demonstrated in equation 2.46, when the phase of the *rf* pulse is zero the pulse is applied along the x-axis. In order to change the axis along which a pulse is applied, then the phase of the pulse must be changed. The time dependent density operator for an *rf* pulse applied

along the x-axis, is given as:

$$\hat{\rho}(t) = e^{-i\omega_1 t\hat{I}_x}\rho(0)e^{i\omega_1 t\hat{I}_x} \tag{2.47}$$

If the initial state of the system, which is assumed to consist of spin-$\frac{1}{2}$ nuclei only, is a population state, i.e., $\rho(0) = \hat{I}_z$, then expansion of equation 2.47 into matrix forms gives: [103]

$$\hat{\rho}(t) = \frac{1}{2}\begin{pmatrix} \cos(\omega_1 t) & i\sin(\omega_1 t) \\ -i\sin(\omega_1 t) & \cos(\omega_1 t) \end{pmatrix} \tag{2.48}$$

The expectation values of $\hat{I}_x$, $\hat{I}_y$ and $\hat{I}_z$ are calculated by taking the trace of the product of equation 2.48, and the relevant spin operator. The expectation values are therefore calculated as:

$$\left\langle \hat{I}_x \right\rangle = Tr\left[\rho I_x\right] = 0 \tag{2.49}$$

$$\left\langle \hat{I}_y \right\rangle = Tr\left[\rho I_y\right] = -\frac{1}{2}\sin(\omega_1 t) \tag{2.50}$$

$$\left\langle \hat{I}_z \right\rangle = Tr\left[\rho I_z\right] = \frac{1}{2}\cos(\omega_1 t) \tag{2.51}$$

The application of an *rf* pulse, aligned along the x-direction, rotates the magnetisation about the x-axis by a flip angle, defined as β, relative to the initial magnetisation state. The flip angle is determined by the strength of ω_1, and the time for which the pulse is applied, and is given as:

$$\beta = \omega_1 t_p \tag{2.52}$$

A vector representation of the application of a 90° pulse applied about x is shown in Fig. 2.2. It is evident, that if magnetisation is at thermal equilibrium, a flip angle of $\pi/2$ will create a pure coherence state, whereas a flip-angle of π will invert the population state.

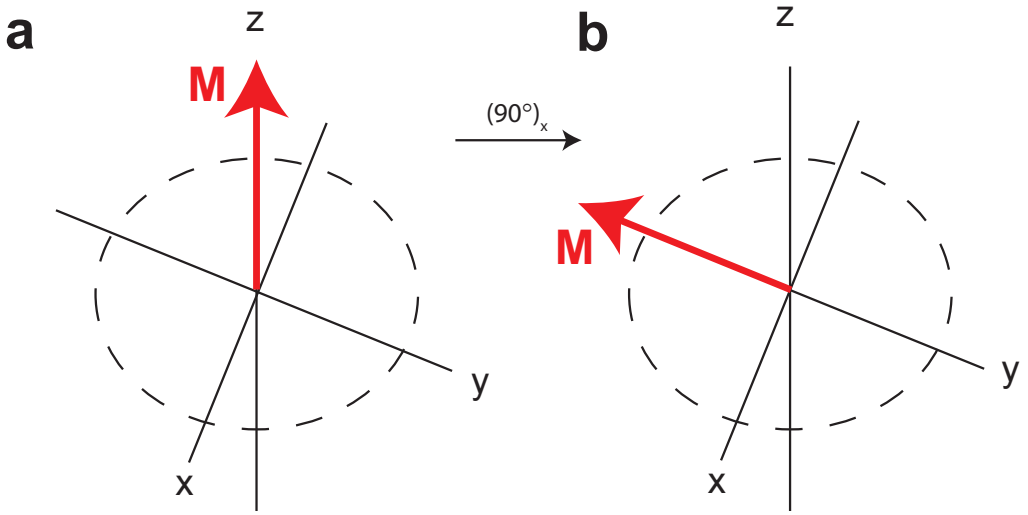

Figure 2.2: (a) Vector model of magnetisation residing in a population state, aligned parallel to the z-axis in the rotating frame. (b) After application of a 90° pulse about x the magnetisation resides in the x-y plane.

2.3.3 Evolution under an offset

Once a coherence state is created, and the *rf* pulse is switched off, then the magnetisation evolves in the transverse plane under a resonance offset. The resonance offset, Ω, emerges from considering the magnetisation in the rotating frame. It is defined as the difference between the Larmor frequency of a nucleus and the *rf* nutation frequency, i.e., $\Omega = \omega_0 - \omega_{rf}$. Switching to a rotating frame corresponds to the experimental mixing down of the NMR signal with a wave oscillating at ω_{rf}. In this way, the oscillating frequencies of the NMR signals are now of the order of kHz, rather than MHz, and are more manageable. The Hamiltonian which describes evolution under a resonance offset is defined as:

$$\hat{H} = \Omega \hat{I}_z \tag{2.53}$$

Therefore, it follows that the time dependent density operator, for initial transverse magnetisation $\hat{I}_x$, under a resonance offset is:

$$\hat{\rho}(t) = \frac{1}{2} \begin{pmatrix} 0 & e^{-i\Omega t} \\ e^{i\Omega t} & 0 \end{pmatrix} \tag{2.54}$$

An NMR signal is calculated by taking the trace of the product of ρ(t) and a raising operator, $\hat{I}_+$ ($\equiv \hat{I}_-^\dagger$), given as:

$$\hat{I}_+ = \hat{I}_x + i\hat{I}_y = \begin{pmatrix} 0 & 1 \\ 0 & 0 \end{pmatrix} \tag{2.55}$$

The raising operator describes quadrature detection, where both the real and imaginary component of the free induction decay (FID), corresponding to detection of two components perpendicular to each other, are recorded. Quadrature detection is explained in more detail in section 3.1.1. A detected NMR signal, under a resonance offset, is therefore given by:

$$\begin{aligned} s(t) &= \mathrm{Tr}[\hat{I}_+\hat{\rho}] \\ &= \mathrm{Tr}\left(\begin{pmatrix} 0 & 1 \\ 0 & 0 \end{pmatrix}\begin{pmatrix} 0 & e^{-i\Omega t} \\ e^{i\Omega t} & 0 \end{pmatrix}\right) \\ &= \frac{1}{2}\left(\cos(\Omega t) + i\sin(\Omega t)\right) \end{aligned} \tag{2.56}$$

The physical manifestation of equation 2.56 is that the transverse magnetisation, recorded as both a real and imaginary component (90° phase difference between the two signals), rotates in the transverse plane, inducing a current in a coil, which corresponds to the NMR signal.

2.3.4 Product Operators

Product operators are an alternative formalism to density operator theory. Although not suitable for explaining an ensemble of spins with numerous strong couplings present, they are adept at cases where weak couplings only are present. The changes in the bulk magnetisation, due to application of a pulse about the y-axis, of flip angle β, in product operator formalism, is: [103]

$$I_x \xrightarrow{\beta_y} I_x\cos\beta - I_z\sin\beta \tag{2.57}$$

Additionally, evolution under a resonance offset can also be described using the product operator formalism:

$$I_x \xrightarrow{\Omega t} I_x \cos \Omega t + I_y \sin \Omega t \tag{2.58}$$

Product operators are also able to describe evolution between weakly J coupled spins, where spins I and S can be the same, or different, nuclear species. The J coupling is an internal interaction between chemically bonded nuclei, and is described in more detail in section 2.4.6. If magnetisation is considered to initially reside upon $\hat{I}_x$, then evolution under a J coupling is, according to the product operator formalism:

$$I_x \xrightarrow{\pi J_{IS} t} I_x \cos \pi J_{IS} t + 2 I_y S_z \sin \pi J_{IS} t \tag{2.59}$$

The second term on the right hand side of equation 2.59 is a two-spin operator, created from the product of two single-spin operators, thus showing how the product operator formalism is able to describe the time evolution of a coupled system. If the magnetisation is initially upon the I spin, then magnetisation will evolve in time into a coupled state involving the S spin. Product operators are a useful tool to describe pulse sequences that involve magnetisation transfer via a J coupling. For weak interactions, evolution under a J coupling and resonance offset can be treated sequentially using product operators, despite the evolution under the distinct interactions occurring simultaneously.

2.4 Internal Interactions

The external interactions introduced in section 2.3 describe the interactions between the nuclear spin system and external variables. Internal interactions describe nuclear spin interactions within a nuclear spin system. The most convenient Hamiltonian expression for an internal interaction is its principal axis system (PAS), in which the interaction matrix is the Hamiltonian expression introduced in equation 2.38 is diagonalised. However, the principal axis system of different internal interactions do not

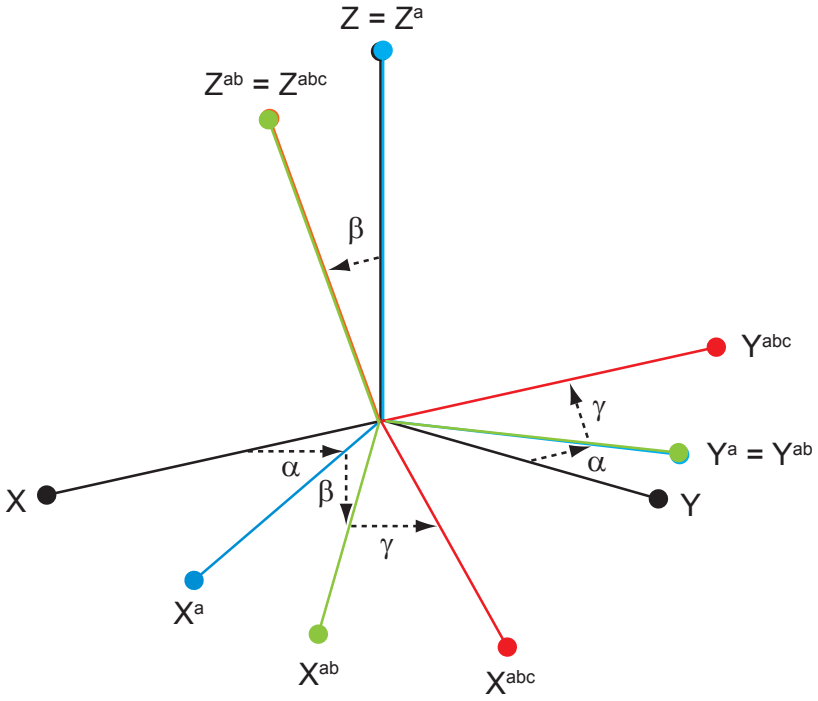

Figure 2.3: Euler angles defined in Cartesian coordinates

typically coincide. As an example, the dipolar coupling lies along the internuclear vector between the nuclei, however the chemical shielding frame of reference is determined by the surrounding electronic environment.

Owing to the dominance of the Zeeman interaction, which is aligned parallel to B_0, it is necessary to rotate all remaining interactions to this frame of reference, referred to herein as the Laboratory frame. Rotations are characterised by three angular rotations in the Cartesian coordinate system, defined as α, β and γ, and are known as the Euler angles. Initial rotation takes place under α, which rotates the coordinate system from (X,Y,Z) about Z to (X^a,Y^a,Z^a), followed by rotation under the angle β about Y^a, creating a new coordinate system, (X^{ab},Y^{ab},Z^{ab}), and finally rotation under γ about Z^{ab} occurs, which rotates the axes to (X^{abc},Y^{abc},Z^{abc}). The change in Cartesian coordinates when rotated by the Euler angles are shown in Fig. 2.3. In order to simplify the mathematical description of a rotation, Hamiltonians are best expressed in spherical tensor form, which are specified as:

$$\hat{H} = \sum_{j=0}^{2} \sum_{m=-j}^{+j} (-1)^m A_{jm} \hat{T}_{j-m} \tag{2.60}$$

where $\hat{T}_{j-m}$ is a tensor which describes the spin component, and A_{jm} is a tensor describing the spatial component. j and m describe the rank of the tensor and the order of the tensor, respectively, and can take values of $j = 0$, 1, 2 and $m = -j$, $-j + 1$,..., $j - 1$, j. When an interaction resides in the PAS then the tensor describing the interaction in equation 2.38 is diagonalised, i.e., only A_{xx}, A_{yy}, and A_{zz} terms are non-zero.

When spherical tensor forms are expressed as Cartesian coordinates, then only following terms listed below contain diagonal elements, hence for an interaction in the PAS, equation 2.60 can be written as:

$$\hat{H}_{\Lambda}^{P} = A_{00}^{P}\hat{T}_{00} + A_{20}^{P}\hat{T}_{20} + A_{2+2}^{P}\hat{T}_{2-2} + A_{2-2}^{P}\hat{T}_{2+2} \tag{2.61}$$

When applying a rotation transformation from the PAS to laboratory frame, only the above spatial terms need be considered. The rank of a spherical tensor is invariant under rotation, this is why the descriptions of rotations is simplified using spherical tensor expressions, as opposed to Cartesian coordinates. The rotation transformation produces a sum of tensors of the same rank, but of different order:

$$R(A_{jm}) = \sum_{m'=-j}^{+j} D_{m'm}^{j}(\alpha, \beta, \gamma) A_{jm'} \tag{2.62}$$

The rotation matrix, D_{kl}^{j}, is defined as

$$D_{kl}^{j}(\alpha, \beta, \gamma) = \exp(-ik\alpha)\, d_{kl}^{j}(\beta)\, \exp(-il\gamma) \tag{2.63}$$

where the elements d_{kl}^{j} are reduced Wigner rotation matrices:

$$d_{kl}^{j}(\beta) = \left\langle jk \left| \exp(-i\beta \hat{J}_y) \right| jl \right\rangle \tag{2.64}$$

Therefore, a specific rotation transformation under Euler Angles, taken from the PAS to the laboratory frame, is expressed as:

$$\hat{A}_{jm'}^{\mathrm{L}} = \sum_{m=-j}^{+j} D_{mm'}^{j}(\alpha_{PL}, \beta_{PL}, \gamma_{PL}) A_{jm}^{\mathrm{P}} \tag{2.65}$$

where the Euler Angles α_{PL}, β_{PL}, and γ_{PL} describe the relative orientations between the PAS and the laboratory frame.

2.4.1 Rotating Frame and the Secular Approximation

The Zeeman interaction is typically much larger than all remaining interactions, therefore all other interactions can be considered as a first-order perturbation to the Zeeman Hamiltonian. This is expressed as:

$$\hat{H}_{TOTAL} = \hat{H}_0 + \hat{H}_1 \tag{2.66}$$

where $\hat{H}_0$ is equal to the Zeeman Hamiltonian, and $\hat{H}_1$ is a first-order perturbation to the Zeeman interaction composed of all remaining interactions. Only interactions which commute with the Zeeman interaction are considered as a first-order perturbation. For this to be true then the interaction must be an eigenfunction of the Zeeman interaction, which can be written as:

$$\left[\hat{I}_z, \hat{T}_{jm}\right] = m\hat{T}_{jm} \tag{2.67}$$

It is evident that the left-hand side of equation 2.67 only commutes when $m = 0$, the consequence of which is that in the laboratory frame, i.e., defined by the Zeeman interaction, only spherical tensor terms with $m = 0$ need be considered providing that a first-order approximation is valid. Considering all further interactions to the Zeeman interaction as a first-order perturbation is referred to as the secular approximation. For this to be true, the applied B_0 must be a sufficiently high-field so that the Zeeman interaction is the dominant interaction.

2.4.2 Dipolar Coupling

Nuclei in close proximity exert a mutual magnetic field upon each other - this coupling, mediated through-space, is known as the dipolar coupling. As the dipolar coupling is a through-space interaction, the strength of the interaction is directly dependent upon internuclear distances. Reverting to the quantum mechanical description, for a simple case of coupling between two spin-$\frac{1}{2}$ nuclei, labelled I and S, there exists four possible Zeeman transition states, as shown shown in Fig. 2.4a. The transition between

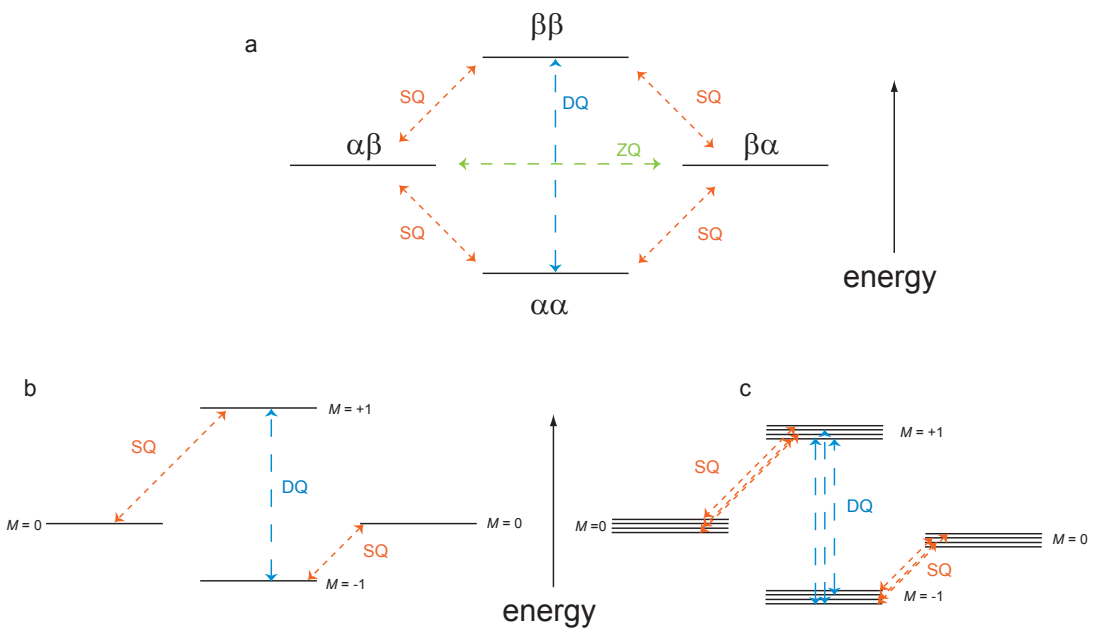

Figure 2.4: (a) Energy level diagram for two-coupled spin-$\frac{1}{2}$ nuclei. (b) Possible spin-spin transitions between two dipolar coupled heteronuclear spin-$\frac{1}{2}$ nuclei. Note the first-order perturbation to the Zeeman energy transitions. (c) Energy level transitions for a pair of dipolar coupled homonuclear spin-$\frac{1}{2}$ nuclei. Note, the energy levels are no longer Zeeman product eigenstates, rather a linear combination, therefore for many spins many different energy transitions exist.

degenerate energy levels $|\alpha\beta\rangle$ and $|\beta\alpha\rangle$ corresponds to a zero-quantum coherence. The transition between $|\alpha\alpha\rangle$ and $|\beta\beta\rangle$ corresponds to a double-quantum coherence. Double-quantum coherence cannot be created in an isolated spin-$\frac{1}{2}$ nucleus, only coupling to a second spin-$\frac{1}{2}$ nucleus allows for the creation of a double-quantum coherence. Note, that Fig. 2.4a only shows the possible coherence levels due to Zeeman transition states, no perturbations from internal interactions are specified. The dipolar Hamiltonian, in Cartesian coordinates, is,

$$\hat{H}_D = 2\sum_{i<j} \hat{I}_i \tilde{D} \hat{S}_j \tag{2.68}$$

where the mutual spins are represented by $\hat{I}_i$ and $\hat{S}_j$. If $\hat{I}_i$ and $\hat{S}_j$ are the same nuclear species then this is called a homonuclear dipolar coupling, whereas a dipolar coupling between unlike nuclear species is referred to as a heteronuclear dipolar coupling.

The PAS of the dipolar Hamiltonian is aligned along the internuclear vector, therefore as the Zeeman interaction is the dominant interaction, it is necessary to rotate from the dipolar PAS to the laboratory frame. For the dipolar coupling, in the PAS, only A_{20}^P is non-zero, therefore the Hamiltonian is written as:

$$\hat{H}_D^P = A_{20}^P \hat{T}_{20} \tag{2.69}$$

A_{20}^P is expressed as:

$$A_{20}^P = \sqrt{6} b_{IS} \tag{2.70}$$

where b_{IS} is the dipolar coupling constant (in radians), given as:

$$b_{IS} = -\frac{\mu_0 \gamma_I \gamma_S \hbar}{4\pi r_{IS}^3} \tag{2.71}$$

Owing to the secular approximation, only $m = 0$ terms in the laboratory frame need to be considered. Applying the relevant rotation matrix and the corresponding reduced Wigner rotation matrices gives:

$$\begin{aligned} A_{20}^L &= A_{20}^P D_{00}^2 \\ &= \sqrt{6} b_{IS} \left\{ \exp(-i\alpha_{PL}.0) d_{00}^2(\beta_{PL}) \exp(-i\gamma_{PL}.0) \right\} \\ &= \sqrt{6} b_{IS} \frac{1}{2} (3cos^2\beta_{PL} - 1) \end{aligned} \tag{2.72}$$

The corresponding spin term, $\hat{T}_{20}$, is defined as:

$$\hat{T}_{20} = \frac{1}{\sqrt{6}} \left(\hat{I}_z \hat{S}_z - \frac{1}{2} \left(\hat{I}_x \hat{S}_x + \hat{I}_y \hat{S}_y \right) \right) \tag{2.73}$$

Assuming that the dipolar coupling is between two spin-$\frac{1}{2}$ nuclei, then in matrix form this is expressed as:

$$\hat{T}_{20} = \frac{1}{2\sqrt{6}} \begin{pmatrix} 1 & 0 & 0 & 0 \\ 0 & -1 & -1 & 0 \\ 1 & -1 & -1 & 0 \\ 0 & 0 & 0 & 1 \end{pmatrix} \tag{2.74}$$

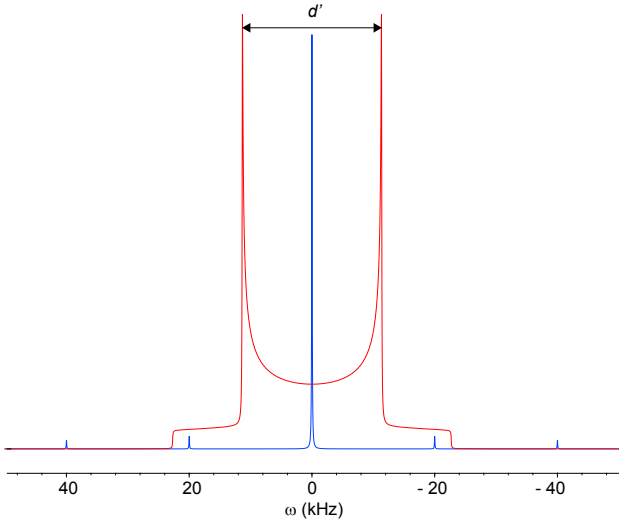

Figure 2.5: Simulated NMR lineshape for a heteronuclear dipolar coupling between two spin-$\frac{1}{2}$ nuclei. The splitting, labelled *d'*, is defined as $b_{IS}[3\cos^2\beta_{PL} - 1]$. The red line corresponds to acquisition under static conditions, consequently a Pake powder pattern is observed, whereas the blue line corresponds to acquisition using an MAS frequency of 20 kHz. Spinning sidebands are observed at integer ratios of the MAS frequency (see section 2.4.4).

Therefore, for a static experiment the Hamiltonian for the dipolar coupling in the laboratory frame can be written as:

$$\hat{H}_D = -b_{IS}\left(3\cos^2\beta_{PL} - 1\right)\left(2\hat{I}_z\hat{S}_z - \left(\hat{I}_x\hat{S}_x + \hat{I}_y\hat{S}_y\right)\right) \tag{2.75}$$

For a heteronuclear dipolar coupling, only the on-diagonal elements in equation 2.74 are present, i.e., only the $\hat{I}_z\hat{S}_z$ term. Therefore, the spin eigenstates are the Zeeman product states, given as $\alpha\alpha$, $\alpha\beta$, $\beta\alpha$ and $\beta\beta$. This acts as a first-order energy shift to the Zeeman interaction, with possible Zeeman product states shown in Fig. 2.4b. A typical lineshape obtained for a heteronuclear dipolar coupling under static conditions is seen in Fig. 2.5, which is known as a Pake doublet. Additionally, a lineshape acquired under MAS, which is discussed in section 2.4.4, is shown, with spinning sidebands appearing at multiples of the spinning frequency ($\nu_r = 20$ kHz). The splitting between the two horns is equal to *d'*, which is defined in the figure caption. Each horn reflects two separate crystallite orientations, which are perpendicular to the external magnetic field, B_0. The broadening effect due to a heteronuclear dipolar coupling is orientationally dependent.

For a homonuclear dipolar coupling, additional complications arise due to the additional $(\hat{I}_x\hat{S}_x + \hat{I}_y\hat{S}_y)$ term in equation 2.73. This is reflected in the presence of

non-diagonal terms in equation 2.74. This term can be expressed as a combination of lowering and raising operators, given as $(\hat{I}_-\hat{S}_+ + \hat{I}_+\hat{S}_-)$, and is commonly known as the flip-flop term. Note that the spin eigenstates are no longer Zeeman products, but now consist of linear combinations of degenerate Zeeman levels. Therefore, in a many nuclei system, a variety of degenerate eigenstates exist, which contribute different transition frequencies, and consequently the Hamiltonians no longer commute at different time points. Crucially, this anisotropic broadening effect is not fully removable under MAS alone.

2.4.3 Chemical Shielding

When subject to an external magnetic field, electrons will orbit a nucleus, therefore inducing a secondary magnetic field. Consequently, different electron configurations shield the nucleus from B_0, resulting in subtle, but measurable differences in precession frequencies for different electron environments for the same nuclear species. It is the chemical shielding that produces a range of observed resonances depending upon electron configurations. The chemical shielding tensor, $\hat{\sigma}$, is not recorded in an NMR experiment, instead a resonance frequency is observed, and an NMR spectrum is typically presented as corresponding chemical shift values, defined by δ. The chemical shift is expressed in parts per million (ppm), and is quoted relative to a reference frequency, ω_{ref}, where ω is the observed resonance frequency.

$$\delta = \frac{\omega - \omega_{ref}}{\omega_{ref}} \times 10^6 \tag{2.76}$$

Use of this notation, notably the factor of 10^6, converts the Hertz scale to a parts per million (ppm) scale, allowing for direct comparison between resonances observed at different magnetic field strengths. The chemical shift value given above allows for discrimination between different functional groups of the same nuclear species. The Hamiltonian for the chemical shift in Cartesian coordinates is given by:

$$\hat{H}_\sigma = \gamma \hat{I} \hat{\sigma} \hat{B}_0 \tag{2.77}$$

The second-rank chemical shielding tensor is:

$$\hat{\sigma} = \begin{pmatrix} \sigma_{xx} & \frac{1}{2}(\sigma_{xy} + \sigma_{yx}) & \frac{1}{2}(\sigma_{xz} + \sigma_{zx}) \\ \frac{1}{2}(\sigma_{xy} + \sigma_{yx}) & \sigma_{yy} & \frac{1}{2}(\sigma_{yz} + \sigma_{zy}) \\ \frac{1}{2}(\sigma_{xz} + \sigma_{zx}) & \frac{1}{2}(\sigma_{yz} + \sigma_{zy}) & \sigma_{zz} \end{pmatrix} \tag{2.78}$$

In the principal-axis system of the chemical shielding interaction, the second-rank tensor in equation 2.78 is diagonalised, i.e., all off-diagonal terms are non-zero. In spherical tensor form, the collection of non-zero terms leaves the following Hamiltonian in the principal-axis system:

$$\hat{H}_{\sigma}^{P} = A_{00}^{P}\hat{T}_{00}^{P} + A_{20}^{P}\hat{T}_{20}^{P} + A_{2\pm2}^{P}\hat{T}_{2\mp2}^{P} \tag{2.79}$$

To describe the effect of the chemical shielding on the NMR spectrum, the spatial terms need to be rotated into the laboratory frame. The A_{00}^{P} term is an isotropic term and is invariant under rotation. Rotation of the relevant spatial terms to the laboratory frame, using the secular approximation, is given as:

$$\begin{aligned} A_{20}^{L} &= \sum_{m=-2}^{2} A_{2m}^{P}\, d_{m0}^{2}(\beta_{PL}) \exp(-im\alpha_{PL}) \\ &= A_{20}^{P}\, d_{00}^{2}(\beta_{PL}) + A_{22}^{P}\, d_{20}^{2}(\beta_{PL}) \exp(-2i\alpha_{PL}) + A_{2-2}^{P}\, d_{-20}^{2}(\beta_{PL}) \exp(2i\alpha_{PL}) \\ &= A_{20}^{P}\, \frac{1}{2}(3\cos^{2}\beta_{PL} - 1) + A_{2\pm2}^{P} \sqrt{\frac{3}{2}} \sin^{2}\beta_{PL} \cos 2\alpha_{PL} \end{aligned} \tag{2.80}$$

where,

$$A_{00}^{P} = \gamma \sqrt{\frac{1}{3}} \left(\sigma_{xx}^{P} + \sigma_{yy}^{P} + \sigma_{zz}^{P}\right) \tag{2.81}$$

$$A_{20}^{P} = \gamma \sqrt{\frac{1}{6}} \left(2\sigma_{zz}^{P} - \sigma_{xx}^{P} - \sigma_{yy}^{P}\right) \tag{2.82}$$

$$A_{2\pm2}^{P} = \gamma \frac{1}{2} \left(\sigma_{xx}^{P} - \sigma_{yy}^{P}\right) \tag{2.83}$$

Therefore, inclusion of relevant spin components, and isotropic terms, gives $\hat{H}_{\sigma}^{L}$ as:

$$\hat{H}_{\sigma}^{L} = -\omega_0 \sigma_{iso} - \frac{1}{2}\omega_0 \sigma_{aniso}(3\cos^{2}\beta_{PL} - 1 + \eta \sin^{2}\beta_{PL} \cos 2\alpha_{PL}) \tag{2.84}$$

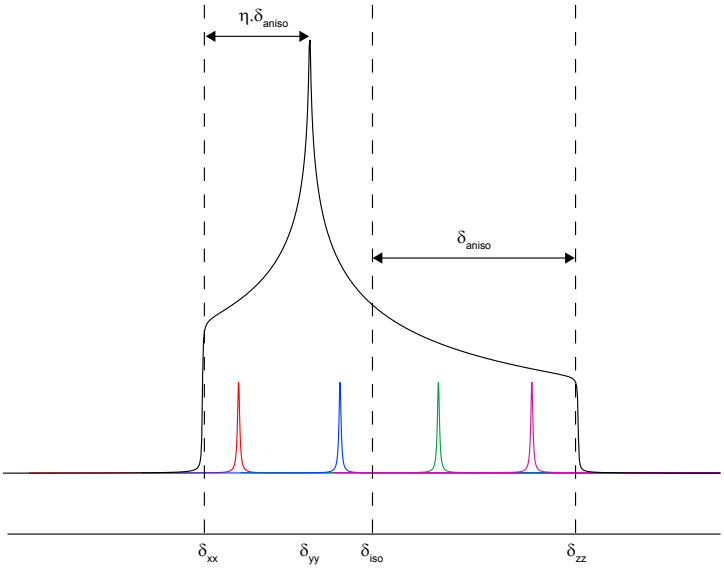

Figure 2.6: Simulated powder pattern showing a CSA lineshape, where $\eta = 0.5$. A selection of individual crystalline components are shown within the lineshape. δ_{iso} is labelled at the centre of gravity of the spectrum, whereas δ_{aniso} corresponds to the difference between the outlying component in the PAS and δ_{iso}, as labelled.

where σ_{iso} is the isotropic chemical shielding, σ_{aniso} is the anisotropic chemical shielding and η is the asymmetry parameter. However, as discussed, it is not the shielding tensor, but rather the chemical shift tensor that describes the appearance of an NMR spectrum. Conversion of the shielding tensor to a chemical shift tensor is as follows:

$$\delta_{\alpha\beta} = \frac{\sigma_{\alpha\beta}(\text{ref}) - \sigma_{\alpha\beta}}{1 - \sigma_{\alpha\beta}(\text{ref})} \tag{2.85}$$

Therefore, the observed values of δ_{iso} and δ_{aniso}, in addition to η, are written as:

$$\delta_{iso} = \frac{1}{3}(\delta^P_{xx} + \delta^P_{yy} + \delta^P_{zz}) \tag{2.86}$$

$$\delta_{aniso} = \delta^P_{zz} - \delta_{iso} \tag{2.87}$$

$$\eta = \frac{\delta^P_{xx} - \delta^P_{yy}}{\delta_{aniso}} \tag{2.88}$$

Using the Haeberlen convention, [106] the relative magnitudes of the three principal components of the chemical shielding are given as:

$$|\delta^P_{zz} - \delta_{iso}| \geq |\delta^P_{xx} - \delta_{iso}| \geq |\delta^P_{yy} - \delta_{iso}| \tag{2.89}$$

The isotropic chemical shift is an average of the principal components of the chemical

shift tensor (or the trace of the tensor in equation 2.78). However, under static conditions overlapping lineshapes are often too broad to extract δ_{iso}. For a single crystallite, a peak centered at the chemical shift for that particular orientation is observed. However, in a powder sample all molecular orientations are present, therefore a continuous range of chemical shift values are observed, which will overlap with each other, giving rise to a broad lineshape. An example lineshape obtained under static conditions, due to a CSA interaction for a spin-$\frac{1}{2}$ nucleus is shown in Fig. 2.6. The principal components detailed in equation 2.86 are all observed in Fig. 2.6. The centre of gravity of the lineshape is taken as the isotropic chemical shift value, whereas δ_{aniso} reflects the maximum span between the centre of gravity of the spectrum, i.e., the isotropic chemical shift, and the largest principal-axis component.

2.4.4 Internal Interactions under Magic Angle Spinning

Magic-angle spinning is a widely applied technique in NMR, which is capable of averaging many anisotropic interactions present in solid-state NMR. Experimentally, MAS is the physical rotation of a powder sample at an angle (the so-called magic angle) relative to B_0. The mathematical description of MAS requires the introduction of an additional, intermediate rotation between the PAS and the laboratory frame. The rotations required, specified using Euler angles, are $\mathbf{R}(\alpha_{PR},\ \beta_{PR},\ \gamma_{PR})$, followed by $\mathbf{R}(\alpha_{RL},\ \beta_{RL},\ \gamma_{RL})$. The subscript PR describes rotation from the PAS to the rotor frame, while the subscript RL signifies a subsequent rotation from the rotor frame to the laboratory frame. A schematic representation of MAS is presented in Fig. 2.7 that indicates a first rotation from the PAS to the rotor frame, and second, from the rotor frame to the laboratory frame. α_{RL} is subtended by the rotation of the rotor, whose spinning frequency is ω_r. γ_{PR} is defined as the phase of the rotor. Isotropic terms are invariant under rotation, therefore only anisotropic terms are considered. Rotation of the A_{20}^{P} term, which is non-zero for the chemical shielding and dipolar Hamiltonian, expressed in the laboratory frame, after two successive frame rotations (PAS to rotor frame, followed by rotor frame to laboratory), is, using the secular approximation:

$$A_{20}^{L} = A_{20}^{P} \sum_{m'=-2}^{2} D_{0m'}^{2}(\alpha_{PR}, \beta_{PR}, \gamma_{PR}) d_{m'0}^{2}(\beta_{RL}) e^{im'\omega_r t} \tag{2.90}$$

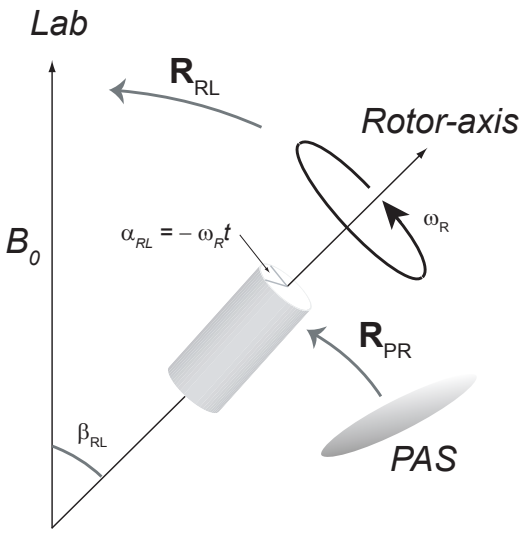

Figure 2.7: Illustration of a rotor aligned at β_{RL} relative to the B_0. The rotation is time dependent, demonstrated herein by the angle subtended, α_{RL}, as a product of the spinning frequency and time period. Furthermore, an additional rotation from the PAS of a general NMR interaction is shown, according to $\mathbf{R}(\alpha_{PR}, \beta_{PR}, \gamma_{PR})$.

Therefore, it follows that, over a complete rotor period, terms with non-zero m' will average to zero over a complete rotation.

$$\int_0^{\tau_R} e^{im'\omega_r t} \mathrm{d}t = 0 \qquad \text{if} \qquad m' \neq 0 \tag{2.91}$$

Providing acquisition is over a complete rotor-period, then application of rotation matrices, as per previous examples, means that equation 2.90 can be written as:

$$\left\langle A_{20}^L \right\rangle_{\tau_r} = A_{20}^P \left[\frac{1}{4} (3\cos^2 \beta_{PR} - 1)(3\cos^2 \beta_{RL} - 1) \right] \tag{2.92}$$

It is evident that if β_{RL} is set to 54.7°, then equation 2.92 will average to zero. Experimentally, acquisition over a complete rotor-period is called rotor-synchronisation. Data points are acquired at points equal to $n\tau_r$ only. If acquisition is not acquired at an integer of the rotation period, then the interaction must be considered over all

relevant spatial components, written as:

$$A_{20}^{L} = A_{20}^{P} \left[\begin{array}{l} D_{00}^{2}(\Omega_{PR}) D_{00}^{2}(\Omega_{RL}) + \\ D_{01}^{2}(\Omega_{PR}) D_{10}^{2}(\Omega_{RL}) + D_{0-1}^{2}(\Omega_{PR}) D_{-10}^{2}(\Omega_{RL}) + \\ D_{02}^{2}(\Omega_{PR}) D_{20}^{2}(\Omega_{RL}) + D_{0-2}^{2}(\Omega_{PR}) D_{-20}^{2}(\Omega_{RL}) \end{array} \right] \tag{2.93}$$

Defining rotation matrices in terms of reduced Wigner matrices, as per equation 2.64, allows equation 2.93 to be simplified:

$$A_{20}^{L} = A_{20}^{P} \left[\begin{array}{l} d_{00}^{2}(\beta_{PR}) d_{00}^{2}(\beta_{RL}) + \\ d_{01}^{2}(\beta_{PR}) d_{10}^{2}(\beta_{RL}) 2\cos(\gamma_{PR} + \omega_r t) + \\ d_{02}^{2}(\beta_{PR}) d_{20}^{2}(\beta_{RL}) 2\cos(2\gamma_{PR} + 2\omega_r t) \end{array} \right] \tag{2.94}$$

Expanding the reduced Wigner matrices, equation 2.94 becomes:

$$A_{20}^{L} = A_{20}^{P} \left[\begin{array}{l} \frac{1}{4}(3\cos^2\beta_{PR} - 1)(3\cos^2\beta_{RL} - 1) - \\ \frac{3}{4}\sin 2\beta_{PR} \sin 2\beta_{RL} \cos(\gamma_{PR} + \omega_r t) + \\ \frac{3}{4}\sin^2\beta_{PR} \sin^2\beta_{RL} \cos(2\gamma_{PR} + 2\omega_r t) \end{array} \right] \tag{2.95}$$

If β_{PR} is set to 54.7 °, then the first term will cancel to zero. The second and third terms in equation 2.95 explain the appearance of spinning sideband patterns, as seen in the simulated dipolar sideband pattern in Fig. 2.5. Experimentally, spinning sidebands are found at increments of the spinning frequency, and occur when the dwell time is not equal to an integer ratio of the rotation period.

2.4.5 Quadrupolar Interaction

Nuclei with nuclear spin greater than $\frac{1}{2}$ possess an electric quadrupolar moment, which interacts with the electric field gradient traversing a nucleus. Quadrupolar moments arise from the charge distribution within a nucleus. The resultant interaction is known as the quadrupolar interaction, which perturbs the Zeeman transition energy levels. The quadrupolar Hamiltonian, in Cartesian coordinates, is written as:

$$\hat{H}_Q = \frac{eQ}{2I(2I-1)\hbar} \hat{I}.\hat{V}.\hat{I} \tag{2.96}$$

The interaction can be described by a (3x3) tensor, $\tilde{V}$, which describes the Cartesian components of the electric field gradient:

$$\tilde{V} = \begin{pmatrix} V_{xx} & V_{xy} & V_{xz} \\ V_{yx} & V_{yy} & V_{yz} \\ V_{zx} & V_{zy} & V_{zz} \end{pmatrix} \tag{2.97}$$

The components of $\tilde{V}$, in the PAS are described by the parameters C_Q and η_Q:

$$C_Q = \frac{e^2qQ}{h} = \frac{eQV_{zz}}{h} \tag{2.98}$$

$$\eta_Q = \frac{V_{xx} - V_{yy}}{V_{zz}} \tag{2.99}$$

$$\text{where}, |V_{xx}| \leq |V_{yy}| \leq |V_{zz}|$$

C_Q describes the strength of the quadrupolar moment, which is the product of the electric field gradient at the nucleus, and is measured in units of Hz. e is the electric charge, q is the electric field gradient at the nucleus, $V_{zz} = eq$, Q is the isotope-specific nuclear quadrupolar moment and h is Planck's constant. A low C_Q value indicates that a site is spherically symmetric, whereas larger C_Q values indicates that a large electric field gradient traverses the nucleus. The asymmetry parameter, η_Q, details the relative strength of the electric field gradient in three orthogonal directions. When $\eta_Q = 0$, the electric field gradient is axially symmetric, whereas if $\eta_Q \approx 1$ the charge distribution is highly asymmetric.

Despite the typically large magnitude of the quadrupolar interaction relative to other internal interaction discussed (of the order MHz), for quadrupolar nuclei considered in this work the Zeeman interaction remains the dominant interaction, therefore rotation of the Hamiltonian from the PAS to the laboratory frame is required. Rotating the Hamiltonian to the laboratory frame is most easily achieved by expressing the Hamiltonian in spherical tensor form, and applying relevant rotation matrices. The quadrupolar Hamiltonian in the principal-axis system is:

$$\hat{H}_Q^P = \frac{2\pi}{2I(2I-1)} \left(A_{20}^P \hat{T}_{20} - A_{22}^P \hat{T}_{2-2} - A_{2-2}^P \hat{T}_{22} \right) \tag{2.100}$$

where the spatial terms in the principal-axis system are defined as:

$$\begin{aligned} A_{20}^{P} =& \sqrt{\frac{3}{2}} C_Q \\ A_{22}^{P} = A_{2-2}^{P} =& \frac{1}{2} \eta_Q C_Q \end{aligned} \tag{2.101}$$

The full Hamiltonian in the laboratory frame, in spherical tensor form is given as:

$$\hat{H}_Q^L = \frac{2\pi}{2I(2I-1)} \left(A_{20}^L \hat{T}_{20} - A_{21}^L \hat{T}_{2-1} - A_{2-1}^L \hat{T}_{21} + A_{22}^L \hat{T}_{2-2} + A_{2-2}^L \hat{T}_{22} \right) \tag{2.102}$$

If a first-order perturbation is considered, then the secular approximation can be assumed, therefore only the A_{20}^L spatial term need be considered. Constructing A_{20}^L in terms of PAS components gives:

$$A_{20}^L = A_{20}^P D_{00}^2 + A_{22}^P D_{20}^2 + A_{2-2}^P D_{-20}^2 \tag{2.103}$$

Once again, relevant rotation matrices are used in the same manner as for the chemical shift and the dipolar coupling, therefore the spatial component of the Hamiltonian described in the laboratory frame to a first-order perturbation, can be expressed as:

$$A_{20}^L = \sqrt{\frac{3}{2}} \frac{C_Q}{2I(2I-1)} \frac{1}{2} \left[(3\cos^2 \beta_{PL} - 1) + \eta_Q \sin^2 \beta_{PL} \cos 2\alpha_{PL} \right] \tag{2.104}$$

Consequently, it follows that the first-order quadrupolar Hamiltonian can be written as:

$$\hat{H}_Q^L = \sqrt{\frac{3}{2}} \frac{C_Q}{2I(2I-1)} \frac{1}{2} \left[(3\cos^2 \beta_{PL} - 1) + \eta_Q \sin^2 \beta_{PL} \cos 2\alpha_{PL} \right] \hat{T}_{20} \tag{2.105}$$

The first-order perturbation to the Zeeman energy levels is given as:

$$E_m^{(1)} = \left\langle m \left| \hat{H}^1 \right| m \right\rangle \tag{2.106}$$

Therefore, substitution of the quadrupolar Hamiltonian, yields a first-order energy

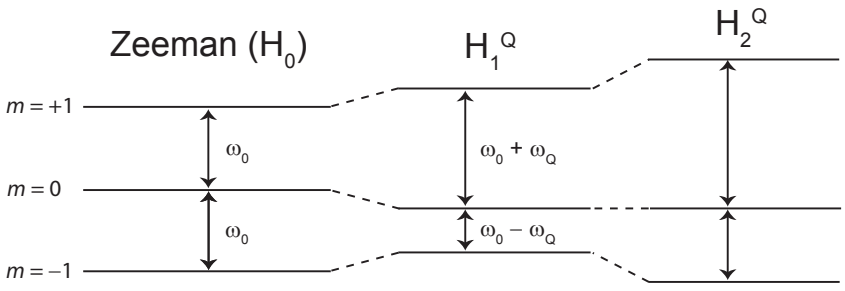

Figure 2.8: Perturbation to the Zeeman energy levels for a spin-1 nucleus when considering the first-order and second-order perturbation due to the quadrupolar interaction. Note, that the first-order perturbation does not effect the total transition energy splitting between $m = +1$ and $m = -1$ states. The second-order perturbation does alter the energy splitting between $m = +1$ and $m = -1$ levels. The perturbations to energy levels shown are exaggerated in order to suitably demonstrate the effect upon the energy levels.

perturbation to the Zeeman transition energy, m, of magnitude:

$$E_m^{(1)} = \sqrt{\frac{3}{2}} \frac{C_Q}{2I(2I-1)} \frac{1}{2} (3m^2 - I(I+1)) \left[(3\cos^2 \beta_{PL} - 1) + \eta_Q \sin^2 \beta_{PL} \cos 2\alpha_{PL} \right] \tag{2.107}$$

In this thesis, only the spin-1 quadrupolar nucleus ^{14}N is considered, where there are three possible energy levels ($m = 0, \pm 1$), and consequently two energy transitions are possible. When considered as a first-order perturbation to the Zeeman Hamiltonian, the total energy transition between $m = +1$ and $m = -1$ states is unchanged relative to the total Zeeman splitting. However, the transition energy between $m = +1 \rightarrow 0$ and $m = 0 \rightarrow -1$ levels is different. Fig. 2.8 presents the perturbation to the energy levels due to a first-order perturbation by the quadrupolar interaction.

The quadrupolar coupling is often sufficiently large (order of MHz) so that it must be considered as a second-order perturbation to the Zeeman interaction. The second-order perturbation to the Zeeman energy is given by:

$$E_m^{(2)} = \sum_{m \neq n} \frac{\left\langle n \left| \hat{H}^1 \right| m \right\rangle \left\langle m \left| \hat{H}^1 \right| n \right\rangle}{E_n^{(0)} - E_m^{(0)}} \tag{2.108}$$

In order to calculate the quadrupolar Hamiltonian to the second order, where the secular

approximation is no longer valid, all $A^L_{2-m,..,m}$ terms must be considered. These are calculated in the same manner as was shown for A^L_{20} in equation 2.105. Calculation of the second-order perturbation is achieved by multiplication of spatial terms, A^2_{2m}, the products of which are found using Clebsch-Gordan coefficients. The product of A^2_{2m}. A^2_{2m}, yields zero-rank, second-rank and fourth-rank Wigner rotation matrices. Therefore, it follows that the second-order energy perturbation defined by the spin quantum number, m, is given as: [105]

$$E^{(2)}_m = -\left(\frac{C_Q}{4I(2I-1)}\right)^2 \frac{2}{\omega_0} m \begin{bmatrix} [I(I+1) - 3m^2]D^{0(Q)}_{00} \\ +[8I(I+1) - 12m^2 - 3]D^{2(Q)}_{20} \\ +[18I(I+1) - 34m^2 - 5]D^{4(Q)}_{40} \end{bmatrix} \tag{2.109}$$

where:

$$\begin{aligned} D^{0(Q)}_{00} &= -\frac{1}{5}(3+\eta_Q^2) \\ D^{2(Q)}_{20} &= \frac{1}{28}\begin{bmatrix} (\eta_Q^2 - 3)(3\cos^2\beta_{PL} - 1) + 6\eta_Q \sin^2\beta_{PL} cos\alpha_{PL} \end{bmatrix} \\ D^{4(Q)}_{40} &= \frac{1}{8}\begin{bmatrix} \frac{1}{140}(18+\eta_Q^2)(35\cos^4\beta_{PL} - 30\cos^2\beta_{PL} + 3) \\ +\frac{3}{7}\eta_Q \sin^2\beta_{PL}(7\cos^2\beta_{PL} - 1)\cos 2\alpha_{RL} \\ +\frac{1}{4}\eta_Q^2 \sin^4\beta_{PL}\cos 4\alpha_{PL} \end{bmatrix} \end{aligned} \tag{2.110}$$

For a spin-1 nucleus, the transition between $m = +1 \rightarrow m = -1$ energy levels does not change if only a first-order quadrupolar interaction is considered. However, as seen from substitution of the relevant spin quantum numbers into equation 2.109, if a second-order quadrupolar interaction is considered, the $m = +1 \rightarrow m = -1$ transition is now perturbed relative to a first-order quadrupolar interaction, in addition to perturbations of the separate transitions between $m = +1 \rightarrow m = 0$ and $m = 0 \rightarrow m = -1$. The changes in the energy level splittings are presented in Fig. 2.8. The magnitude of the second-order energy perturbation is inversely proportional to ω_0, therefore at higher magnetic field strengths the contribution from the quadrupolar interaction is reduced.

The zero-rank term is isotropic, with no orientational dependence. Therefore, the isotropic dimension in an NMR spectrum of a quadrupolar nucleus contains a further isotropic shift, in addition to the isotropic chemical shift, which is determined by the magnitude of the quadrupolar parameters. This is known as the isotropic quadrupo-

lar induced shift, δ_{QIS}, and in the ppm scale for a $m \rightarrow m-1$ transition is defined as: [107]

$$\delta_{QIS} = -\left(\frac{3}{40}\right)\left(\frac{P_Q}{\nu_0}\right)^2 \frac{[I(I+1) - 9m(m-1) - 3]}{[I^2(2I-1)^2]} \times 10^6 \tag{2.111}$$

which when $I = 1$ and $m = 0$ or $m = +1$, is simplified as:

$$\delta_{QIS} = \left(\frac{3}{40}\right)\left(\frac{P_Q}{\nu_0}\right)^2 \times 10^6, \tag{2.112}$$

where P_Q is the quadrupolar product, given as:

$$P_Q = C_Q\sqrt{1 + \frac{\eta_Q^2}{3}} \tag{2.113}$$

Evidently, for lower C_Q values, the second-order contribution need not be considered and any additional isotropic contribution, relative to the isotropic chemical shift, can be considered negligible. The second-rank term in equation 2.109 has an orientational dependence. Therefore, as discussed in the context of the dipolar coupling and the chemical shielding interactions, the second-rank contribution from the second-order term is averaged under MAS.

Finally, note the presence of a fourth-rank rotation matrix. This is also orientationally dependent, however, it is not possible to average both second-rank and fourth-rank terms under rotation at any single angle. Thus, a residual quadrupolar broadening remains under MAS conditions.

2.4.6 *J* coupling

A J coupling interaction exists between covalently bonded nuclei and is mediated through sharing of electrons. The J coupling consists of an isotropic and anisotropic component. The anisotropic component has the same angular dependency as the dipolar coupling, however in the context of the nuclei used in this work the magnitude of the anisotropic component can be considered sufficiently small that it can be disregarded. The isotropic component is also relatively small compared to other internal interactions, ~ 100 Hz for a one-bond CH or NH J coupling. In the solution state, where the lines are sufficiently narrow, different splitting patterns are seen depending upon the number

of chemical bonds to a nucleus. In the solid state, lineshapes are usually too broad to resolve a splitting pattern. However, the J coupling can be utilised to indirectly identify chemically bonded nuclei during correlation experiments based on spin-echoes as magnetisation is transferred across covalent bonds, thus assisting in determining the presence of through-bond couplings and chemical connectivities within a molecule.

The J coupling Hamiltonian, in Cartesian coordinates, is:

$$\hat{H}_J = \sum_{i<j} \hat{I}_i . \widetilde{J} . \hat{S}_j \tag{2.114}$$

where $\widetilde{J}$ is the J coupling tensor, and $\hat{I}_i$ and $\hat{S}_j$ are the through-bond coupled spins. Isotropic J coupling interactions have no orientation dependency and are invariant under MAS. Therefore, no rotation of the spatial component is required in order to calculate the Hamiltonian in the laboratory frame.

CHAPTER

THREE

SOLID-STATE NMR EXPERIMENTAL PROCEDURES

In this chapter, experimental and computational solid-state NMR methodologies applied within this thesis are introduced. Firstly, one-dimensional and two-dimensional NMR experiments and lineshapes are considered, and two-dimensional phase and amplitude modulated experiments are compared. The principles of phase cycling are introduced, which are required to select specific coherences. Solid-state NMR methods to improve sensitivity and resolution are discussed, namely cross-polarisation and heteronuclear and homonuclear decoupling schemes. Relevant pulse sequences are presented, namely spin-echo and HMQC experiments. Finally, computational methods which complement experimental procedures are discussed. These include DFT-based techniques used to calculate NMR parameters, or optimise diffraction structures for accurate internuclear distance measurements. Additionally, density matrix simulation methods, primarily employed within this thesis to investigate homonuclear decoupling sequences, are introduced.

3.1 1D and 2D lineshapes

3.1.1 1D lineshapes

As demonstrated in section 2.3, when an NMR active nucleus is placed in an external magnetic field and irradiated with an on-resonance radiofrequency pulse, then a measurable, time oscillating signal is produced. In an NMR experiment, the time oscillating signal is in the form of an induced current, which is detected in a coil aligned

perpendicular to the external magnetic field. If all internal interactions are assumed to be absent, and evolution under a resonance offset only is considered, as shown in equation 2.56, then the time oscillating signal is given as:

$$s(t) = (\cos(\Omega t) + i\sin(\Omega t)) \tag{3.1}$$

The above terms describe the real and imaginary components of the complex time-domain signal. Recording both the real and imaginary components of the signal is referred to as quadrature detection, which is necessary to identify the sign of the offset frequency, Ω.

It is also necessary to include an additional exponential term to detail transverse relaxation effects, which describe the loss of coherence between spins. This is characterised by the parameter T_2, which is typically on the order of milliseconds for organic materials discussed within this thesis. The transverse relaxation time is discussed in more detail in section 3.3.2. Accounting for transverse relaxation, the complex time-domain signal under a resonance offset is given as:

$$\begin{aligned} s(t) &= \exp(i\Omega t)\exp(-t/T_2) && t \geq 0 \\ s(t) &= 0 && t < 0 \end{aligned} \tag{3.2}$$

The signal described in equation 3.2 is referred to as the Free Induction Decay (FID). The time taken for magnetisation to return to thermal equilibrium is described by the spin-lattice or longitudinal relaxation time, and characterised by T_1. For materials studied in this thesis, T_1 values range from seconds to minutes. In an NMR experiment, it is necessary to include a sufficient time delay between the recording of each FID to allow for recovery of the longitudinal magnetisation. If the delay chosen is too long then this is an inefficient application of an NMR experiment, as the additional time is better served recording additional FIDs, which improves the signal to noise ratio (proportional to $\sqrt{n}$, where n is the number of added FIDs). If the time delay between FIDs is too short, then the full magnetisation will not reside at thermal equilibrium at the start of each measurement.

The time oscillating signal is not easily interpreted, a more informative representation is found from observation of resonant peaks in a frequency-domain spectrum.

This is achieved through a Fourier transform of the time dependent signal,

$$S(\omega) = \int_{-\infty}^{+\infty} s(t) \exp(-i\omega t) dt$$
$$S(\omega) = A(\omega)^{+} - iD(\omega)^{+} \tag{3.3}$$

where the real-part of the signal is described by $A(\omega)^{+}$, and the imaginary-part by $D(\omega)^{+}$, fully expanded as:

$$A(\omega)^{+} = \frac{1/T_2}{(1/T_2)^2 + (\omega - \Omega)^2} \tag{3.4}$$
$$D(\omega)^{+} = \frac{\omega - \Omega}{(1/T_2)^2 + (\omega - \Omega)^2} \tag{3.5}$$

Figure 3.1 shows the real and imaginary components of the NMR spectrum centred at Ω. Note that the absorptive lineshape is at a maximum at the resonance offset, Ω, contrastingly the dispersive lineshape is at zero intensity at the resonance offset, Ω. The absorptive lineshape is also narrower relative to the dispersive lineshape, and is therefore more favourable for observation of a resonant frequency. It is often necessary to apply a phase adjustment to an NMR lineshape, so that the real part of the spectrum is purely absorptive, and the imaginary part is purely dispersive, referred to as phasing of a spectrum. For an absorptive spectrum, the linewidth, in units of Hertz, is given by $(1/\pi T_2)$, referred to as the full width at half maximum height (FWHMH).

The detection of both the real and imaginary signal is achieved by physically obtaining two orthogonal signals, which can be described using the density operator formalism as taking the trace of the $\hat{I}_{-}^{\dagger} \equiv \hat{I}_{+}$ operator applied to the spin system (see equation 2.56). If only a single spin operator (i.e., $\hat{I}_x$ or $\hat{I}_y$) is applied there would be no sign-discrimination, which manifests itself as a mirror image in the spectral window at frequencies of $+\Omega$ and $-\Omega$. Detection of both real and imaginary components is achieved through the application of the $\hat{I}_{+} = \hat{I}_x + i\hat{I}_y$ spin operator.

3.1.2 2D lineshapes

Whereas for a 1D experiment, only a single evolution time is considered, a 2D experiment is described by two evolution periods. Higher dimension NMR experiments are possible, however for the purpose of this thesis only 1D and 2D experiments are

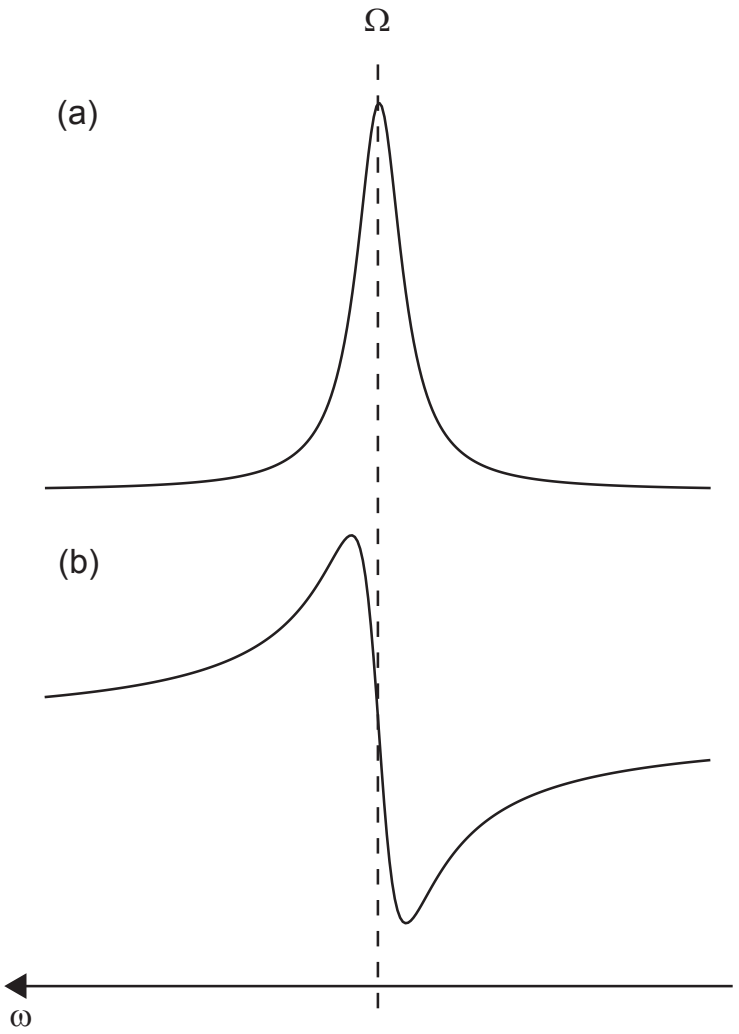

Figure 3.1: Simulated 1D NMR lineshapes showing (a) absorptive and (b) dispersive lineshapes for an isolated spin-$\frac{1}{2}$ nucleus under a resonance offset only.

recorded. The advantage of a 2D experiment is the capability to probe different spin interactions during a single experiment. In a 2D experiment, the direct acquisition time is defined as t_2, which is analogous to the 1D acquisition time period. A second evolution time is included in a 2D experiment, defined as t_1, with increment Δt_1. Recording a series of FIDs, as a function of t_1, yields a 2D dataset. The frequency in the direct dimension is denoted by ω_2, with an axis labelled F_2, whereas the indirect dimension is labelled F_1, with resonances at frequency ω_1.

A simple 2D experiment is shown in Fig. 3.2a, which consists of four separate stages. Firstly, a preparation pulse is required to excite spin coherences for detection during t_1. Following the preparation stage, evolution during the incremented time t_1 occurs. It is then necessary to convert the spin coherence into an observable form, i.e.,

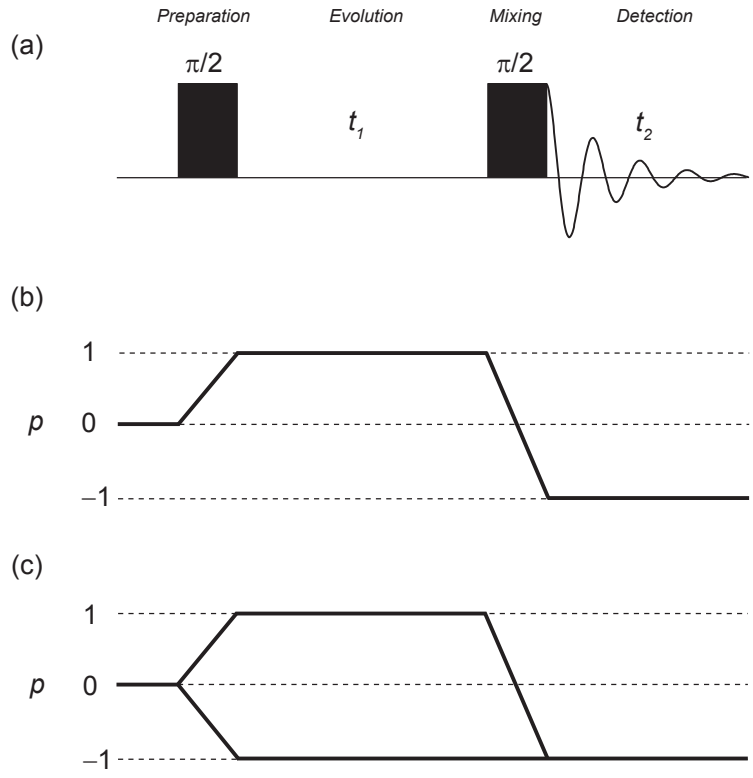

Figure 3.2: (a) A simple two-dimensional pulse sequence, showing the four stages of a 2D experiment: preparation, evolution, mixing and detection. The two time evolution periods are labelled t_2 and t_1. (b) Coherence pathway for a phase-modulated experiment. (c) Coherence pathway for an amplitude modulated pathway. Phase and amplitude modulated pathways are selected by appropriate phase cycling.

in-phase single-quantum coherence - this is referred to as the mixing stage. Finally, the NMR signal is detected during t_2 as an in-phase single-quantum coherence.

In an NMR experiment, changes in coherence at different stages can be visualised by means of coherence pathways. The selection of a specific coherence is achieved through phase cycling, which will be discussed in section 3.1.4. In addition to a simple 2D pulse sequence shown in Fig. 3.2a, two possible coherence pathways are presented. Fig. 3.2b shows a phase modulated experiment with respect to t_1. Note, that only p=+1 is present during t_1, whereas, in Fig. 3.2c both positive and negative coherence pathways evolve during t_1, known as an amplitude modulated experiment. The general form of a 2D signal with respect to both t_1 and t_2, assuming evolution under a resonance offset only, can be written as:

$$s(t_1, t_2) = \exp\left(-ip\Omega t_1\right) \exp(-t_1/T_2^{(1)}) \exp(i\Omega t_2) \exp(-t_2/T_2^{(2)}) \tag{3.6}$$

where p are the coherence order(s) selected in t_1.

When an experiment is phase modulated with respect to t_1, the real and imaginary components evolve as a function of the phase during t_1. If the phase modulated case in Fig. 3.2b is considered, then only a coherence of $p = +1$ is present during t_1, therefore the 2D signal can be written as:

$$s(t_1, t_2) = \exp(-i\Omega t_1) \exp(-t_1/T_2^{(1)}) \exp(i\Omega t_2) \exp(-t_2/T_2^{(2)}) \tag{3.7}$$

Fourier Transform with respect to t_2, performed in the same manner as in equation 3.3, yields:

$$s(t_1, \omega_2) = \exp(-i\Omega t_1) \exp(-t_1/T_2^{(1)})(A_2^+ - iD_2^+) \tag{3.8}$$

Subsequent Fourier Transform with respect to t_1 of equation 3.8 results in a 2D lineshape in the frequency domain:

$$\begin{aligned} s(\omega_1, \omega_2) &= (A_1^- - iD_1^-)(A_2^+ - iD_2^+) \\ &= (A_1^- A_2^+ - D_1^- D_2^+) - i(A_1^- D_2^+ + D_1^- A_2^+) \end{aligned} \tag{3.9}$$

Inspection of equation 3.9 reveals that all the components in F_1 have the same sign precession frequency ($A_1{}^-$, $D_1{}^-$), indicating that there is sign discrimination in the F_1 dimension. However, both the real and imaginary parts of the signal are a mixture of absorptive and dispersive components, which results in a phase-twisted lineshape, which is undesirable as this results in significantly broader lineshapes that reduce the resolution of distinct lineshapes.

A phase twisted spectrum can be avoided by using an amplitude modulated experiment, where both positive and negative coherence orders are present during t_1, as shown in Fig. 3.2c. During an amplitude modulated experiment, the real and imaginary components evolve as a function of the signal intensity during t_1. Furthermore, a hyper-complex Fourier transform is applied to the signal, which requires the separation of the real and imaginary components prior to Fourier Transform in t_1. An amplitude

modulated 2D dataset, for the selected coherence pathways in Fig. 3.2c, is written as:

$$\begin{aligned} s(t_1, t_2) &= [\exp(-i\Omega t_1) + \exp(+i\Omega t_1)] \exp(-t_1/T_2^{(1)}) \exp(i\Omega t_2) \exp(-t_2/T_2^{(2)}) \\ &= 2\cos(\Omega t_1) \exp(-t_1/T_2^{(1)}) \exp(i\Omega t_2) \exp(-t_2/T_2^{(2)}) \end{aligned} \tag{3.10}$$

Then, performing the Fourier transform with respect to t_2 yields:

$$\begin{aligned} s(t_1, \omega_2) &= 2\cos(\Omega t_1) \exp(-t_1/T_2^{(1)})(A_2^+ - iD_2^+) \\ &= [\exp(-i\Omega t_1) + \exp(i\Omega t_1)] \exp(-t_1/T_2^{(1)})(A_2^+ - iD_2^+) \end{aligned} \tag{3.11}$$

Fourier transform, with respect to t_1, of the real and imaginary components in equation 3.11 are then performed separately:

$$\begin{aligned} s(t_1, \omega_2)^{\mathrm{Re}} &= [\exp(-i\Omega t_1) + \exp(i\Omega t_1)] \exp(-t_1/T_2^{(1)}) A_2^+ \\ s(\omega_1, \omega_2)^{\mathrm{Re}} &= (A_1^- + A_1^+)A_2^+ - i(D_1^- + D_1^+)A_2^+ \end{aligned} \tag{3.12}$$

$$\begin{aligned} s(t_1, \omega_2)^{\mathrm{Im}} &= [\exp(-i\Omega t_1) + \exp(i\Omega t_1)] \exp(-t_1/T_2^{(1)}) D_2^+ \\ s(\omega_1, \omega_2)^{\mathrm{Im}} &= (A_1^+ + A_1^-)D_2^+ - i(D_1^+ + D_1^-)D_2^+ \end{aligned} \tag{3.13}$$

The real part of the spectrum in equation 3.12 is purely absorptive in F_1 ($A_1{}^- + A_1{}^+$), i.e., phase twisted lineshapes are avoided. However, note that there is no sign-discrimination. This is evident from the real component containing both negative and positive precession offset frequencies in F_1. Therefore, in a 2D spectrum, mirrored peaks at offset frequencies of $\pm\Omega_1$ are observed. For amplitude modulated 2D experiments, sign-discrimination in F_1 is achieved by recording the NMR signal using a 2D sign-discrimination method.

3.1.3 States acquisition

One of the most common 2D sign-discrimination acquisition modes is the States method. [108] Implementing the States method requires that FIDs are recorded twice for each t_1 value. The second FID is acquired with the phase of the preparation pulse increased by $\pi/(2\,|p|)$, where $|p|$ is the coherence order that evolves during t_1. This has the effect of recording two signals that are 90° out of phase with respect to the evolution that

takes place during t_1:

$$\begin{aligned} s_{\cos}(t_1, t_2) &= [\exp(-i\Omega t_1) + \exp(+i\Omega t_1)] \exp(-t_1/T_2^{(1)}) \exp(+i\Omega t_2) \exp(-t_2/T_2^{(2)}) \\ &= 2\cos(\Omega t_1) \exp(-t_1/T_2^{(1)}) \exp(+i\Omega t_2) \exp(-t_2/T_2^{(2)}) \end{aligned} \tag{3.14}$$

$$\begin{aligned} s_{\sin}(t_1, t_2) &= i\,[\exp(-i\Omega t_1) - \exp(+i\Omega t_1)] \exp(-t_1/T_2^{(1)}) \exp(+i\Omega t_2) \exp(-t_2/T_2^{(2)}) \\ &= 2\sin(\Omega t_1) \exp(-t_1/T_2^{(1)}) \exp(+i\Omega t_2) \exp(-t_2/T_2^{(2)}) \end{aligned} \tag{3.15}$$

Fourier transform of both the cosine and sine components with respect to t_2 gives:

$$s_{\cos}(t_1, \omega_2) = 2\cos(\Omega t_1) \exp(-t_1/T_2^{(1)})(A_2^+ - iD_2^+) \tag{3.16}$$

$$s_{\sin}(t_1, \omega_1) = 2\sin(\Omega t_1) \exp(-t_1/T_2^{(1)})(A_2^+ - iD_2^+) \tag{3.17}$$

Taking an appropriate combination of the real parts of both the cos and sin components, the expression becomes:

$$\begin{aligned} s(t_1, \omega_2) &= \mathrm{Re}(s_{\cos}(t_1, \omega_2)) + i\mathrm{Re}(s_{\sin}(t_1, \omega_2)) \\ &= 2\exp(\Omega t_1) \exp(t_1/T_2^{(1)}) A_2^+ \end{aligned} \tag{3.18}$$

Fourier transforming with respect to t_1 yields:

$$s(\omega_1, \omega_2) = 2(A_1^+ - iD_1^+)A_2^+ \tag{3.19}$$

Therefore, the real component of the lineshape is purely absorptive with sign discrimination in F_1, as required.

3.1.4 Phase Cycling

When a suitable *rf* pulse is applied to a nuclear spin, coherences of different orders between spins can be excited (as described in section 2.3.2). However, an *rf* pulse does not create a specific coherence, rather a range of the possible coherence states, depending upon the possible eigenstates, can exist. Selection of specific coherences is used to filter different interactions, which have a dependency upon specific spin coherences. For

example, a dipolar coupling between two spin-$\frac{1}{2}$ nuclei can generate a double-quantum coherence, as shown in Fig. 2.4, whereas an isolated spin-$\frac{1}{2}$ nucleus cannot support a double-quantum coherence. Selection of a required coherence is achieved by phase cycling of *rf* pulses. Phase cycling is applied by repetition of a pulse sequence N times, where the phase of designated *rf* pulses, and the receiver phase are changed according to the Golden rules of phase cycling for each FID. Addition over all FIDs results in only desired coherence pathways remaining, unwanted coherences destructively interfere with each other. The 'Golden Rules' of phase cycling are: [103]

- **1**: If the phase of a pulse (or group of pulses) is shifted by $\Delta\phi$, then a coherence change, defined as Δp, experiences a phase shift of $-\Delta\phi.\Delta p$ as detected by the receiver.

- **2**: If a phase cycle step of 360°/N is used, then in addition to the desired coherence change of Δp, additional changes in coherence of $\Delta p \pm n$N, will also be selected, where n = 1, 2, 3, ... All remaining pathways are blocked.

It is important to note that it is changes in coherence order that are selected by phase cycling. The initial and final coherence of an NMR experiment are fixed. As discussed in section 2.3.1, the initial state of the nuclear magnetisation in thermal equilibrium is aligned parallel to the direction of the external magnetic field, in a population state. As shown, a population state corresponds to no coherence between spins, i.e., $p = 0$. As all NMR experiments are considered to begin at thermal equilibrium, the coherence, p, is zero at the beginning of an NMR experiment. Additionally, only an in-phase single-quantum coherence is directly observable in an NMR experiment, all other coherences are not directly observable, regardless of their presence. Consequently, as the initial and final coherences are fixed, it is not necessary to phase cycle for all *rf* pulses, only (s − 1) phase cycling steps are required, where s is the number of events. It is imperative that the number of FIDs recorded is equal to an integer multiple of N, as unwanted coherences only cancel over the complete phase cycle.

A possible phase cycle for selection of $\Delta p = +1$ is shown in Table 3.1. According to Golden rule **2**, if a 4-step phase cycle is excited, then changes in coherence of Δp = +1, +5, +9, etc and Δp = −3, −7, −11, etc will also be selected. Excitement of higher order coherence levels is significantly less efficient than excitement of lower order

Table 3.1: Selection of $\Delta p = +1$ coherence order change by phase cycling.

Step	ϕ_A	$-\Delta\phi_A$	ϕ_R	Difference
1	0	0	0	0
2	90	−90 (270)	270	0
3	180	−180 (180)	180	0
4	270	−270 (90)	90	0

Table 3.2: Full phase cycle for the DQ experiment shown in Fig. 3.3. Pulses A and C are each cycled through four steps to select coherence changes of $\Delta p = \pm 2$ and $\Delta p = -1$, respectively.

Step	ϕ_A	$-\Delta\phi_A \Delta p = -2\phi_A$	ϕ_C	$-\Delta\phi_C \Delta p = \phi_C$	$\phi_R = -2\phi_A + \phi_C$
1	0	0	0	0	0
2	90	180	0	0	180
3	180	0	0	0	0
4	270	180	0	0	180
5	0	0	90	90	90
6	90	180	90	90	270
7	180	0	90	90	90
8	270	180	90	90	270
9	0	0	180	180	180
10	90	180	180	180	0
11	180	0	180	180	180
12	270	180	180	180	0
13	0	0	270	270	270
14	90	180	270	270	90
15	180	0	270	270	270
16	270	180	270	270	90

coherence levels, therefore the contribution of higher order coherence levels can usually be considered negligible.

Many pulse sequences require multiple changes in coherence, for these cases a nested phase cycle is required. When constructing a nested phase cycle the phases of the individual pulses are chosen according to the Golden Rules of phase cycling, however the overall receiver phase is calculated as the sum of all the individual receiver phases specified for each change in coherence, which are defined according to Golden Rule **1**. An example full phase cycle of a 2D double quantum correlation experiment, [47] is shown in Table 3.2, with a corresponding pulse sequence and coherence pathway presented in Fig. 3.3. A 4-step phase cycle is applied to pulse A to excite a double-quantum coherence. Selection of $\Delta p = +2$ using a 4-step phase cycle, will also select a change in coherence of $\Delta p = -2$ according to Golden Rule **2**. Therefore, the evolution

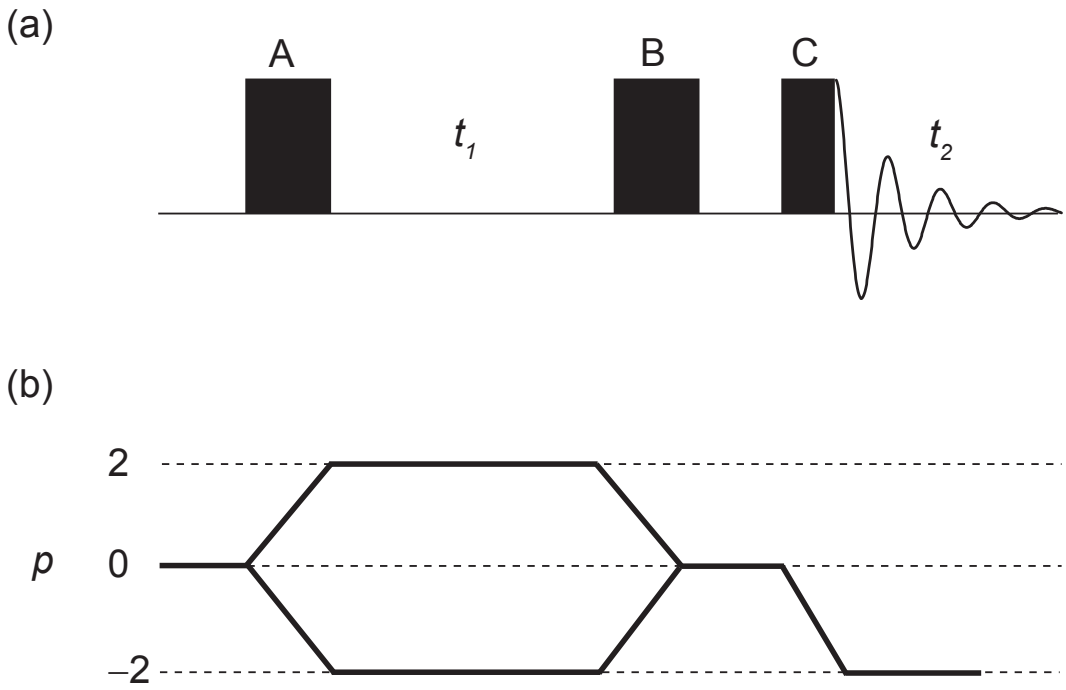

Figure 3.3: (a) Pulse sequence for a two-dimensional Double Quantum homonuclear correlation experiment. The preparation pulse, labelled A, is phase cycled to select double quantum coherence. The final mixing pulse, labelled C, is phase cycled to convert longitudinal magnetisation into an observable in-phase single quantum coherence ($\Delta p = -1$) (b) Corresponding coherence pathways, where coherences are selected using the phase cycle in Table 3.2.

in t_1 is amplitude modulated, as positive and negative coherence pathways are selected. Coherences equal to $\pm 2 + 4n$, where $n = \pm 1, \pm 2, \pm 3$, etc. are also selected, however the contribution from these coherences is safely ignored. All remaining coherences destructively interfere over a complete phase cycle. It is only necessary to phase cycle two of the pulses, as the initial and final coherence orders are known. Here, the final pulse, labelled C, also employs a 4-step phase cycle, however the desired change in coherence is $\Delta p = -1$. Therefore, $\Delta p = +3, +7$ ... and $\Delta p = -5, -9$ ... are also selected, however their contribution before t_2 can be considered negligible.

The receiver phase is simply the sum of the individual receiver phases for pulse A and pulse C, according to Golden rule **1** of phase cycling. Changes in the receiver phase are taken between 0° and 360°. A 90° phase shift is achieved by multiplication by factor i (i.e., swap the real and imaginary parts of the real signal), whereas a 180° phase shift is achieved by multiplication by -1. In order to complete the full phase-cycle presented

in Table 3.2, it is necessary to record an integer multiple of 16 FIDs. The total number of FIDs recorded in an NMR experiment is referred to as the number of co-added transients. In reality, the "pulses" that excite and reconvert double quantum coherence, labelled as A and B, respectively, in Fig. 3.3, are a dipolar recoupling scheme, such as Back to Back (BABA). [109] This consists of a block of pulses, however, for the purpose of phase cycling they are treated as a single pulse block.

3.2 Experimental Techniques

3.2.1 Heteronuclear Decoupling

In organic materials, which typically contain dense proton environments, heteronuclear decoupling is often applied to an abundant spin species, (e.g., ^{1}H), when acquiring an NMR signal of a dilute nucleus, (e.g., ^{13}C, ^{15}N). Heteronuclear dipolar decoupling is usually applied in addition to MAS to assist in averaging heteronuclear dipolar couplings, consequently reducing NMR linewidths of a dilute heteronucleus. [110]

Heteronuclear decoupling is typically applied via continuous, high *rf* nutation frequency irradiation to an abundant spin species. To be effective, the magnitude of the *rf* nutation frequency is typically required to be at least three times larger than the highest magnitude X-H dipolar coupling. [105] A directly bonded ^{13}C-^{1}H dipolar coupling is approximately 23 kHz, therefore an *rf* nutation frequency of 100 kHz satisfies this condition. The effect of constant *rf* irradiation at a nutation frequency of ν_1, is to excite continuous transitions between $|\alpha\rangle$ and $|\beta\rangle$ states in a ^{1}H nucleus at a frequency of ν_1. Providing the *rf* nutation frequency is sufficiently high, then the timescale of the transitions between $|\alpha\rangle$ and $|\beta\rangle$ states is fast relative to the heteronuclear dipolar coupling, and this rapid transition between states contributes towards averaging of the heteronuclear dipolar coupling.

In practice, decoupling sequences consisting of *rf* pulse blocks, with phase switching between individual *rf* pulses, such as Two Pulse Phase Modulated (TPPM) [111] or SPINAL-64 (small phase incremental alternation with 64 steps), [112,113] offer better performance. SPINAL-64 heteronuclear decoupling is used within this thesis; the decoupling scheme is presented in Fig. 3.4, and the corresponding phase parameters used are detailed in the figure caption.

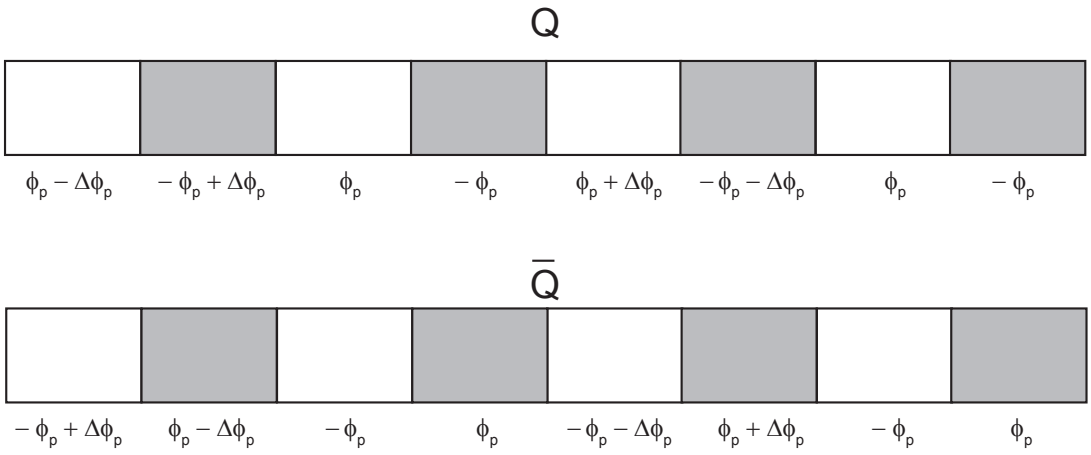

Figure 3.4: Schematic representation of the SPINAL-64 heteronuclear decoupling sequence. Each pulse is slightly shorter than a π pulse, which is determined from the strength of the *rf* nutation frequency. For all results presented in this work $\phi_p = 15°$ and $\Delta\phi_p = 5°$, and blocks Q and $\overline{\text{Q}}$ are arranged as: Q$\overline{\text{Q}}\overline{\text{Q}}Q\overline{\text{Q}}QQ\overline{\text{Q}}$, which constitutes a total of 64 steps.

3.2.2 Homonuclear Decoupling

As discussed in section 2.4.2, homonuclear dipolar couplings are not completely averaged under MAS alone. This is problematic in organic materials, where dense proton networks contribute strong homonuclear ^{1}H-^{1}H dipolar couplings, which broaden the NMR lineshapes. Increasing the spinning frequency does accomplish significant averaging of the homonuclear dipolar coupling, however this is reliant on the use of small diameter rotors. Within this thesis, Frequency Switched Lee-Goldburg (FSLG) and Decoupling Using Mind Boggling Optimisation (DUMBO) homonuclear decoupling sequences are applied, both of which are described below.

3.2.3 FSLG

While homonuclear dipolar decoupling, that is based upon the rotation of the nuclear spins by *rf* irradiation, was originally proposed in the absence of MAS, modern applications are typically employed in conjunction with fast MAS. As discussed in chapter 1, the combination of homonuclear decoupling and MAS is referred to as CRAMPS. FSLG is an example of a homonuclear decoupling scheme which averages homonuclear dipolar coupling through application of off-resonance irradiation.

When applying a pulse of arbitrary phase, ϕ, aligned along the x-axis, it has a magnitude of ω_1. The z-component of the pulse is of magnitude Ω. If the pulse

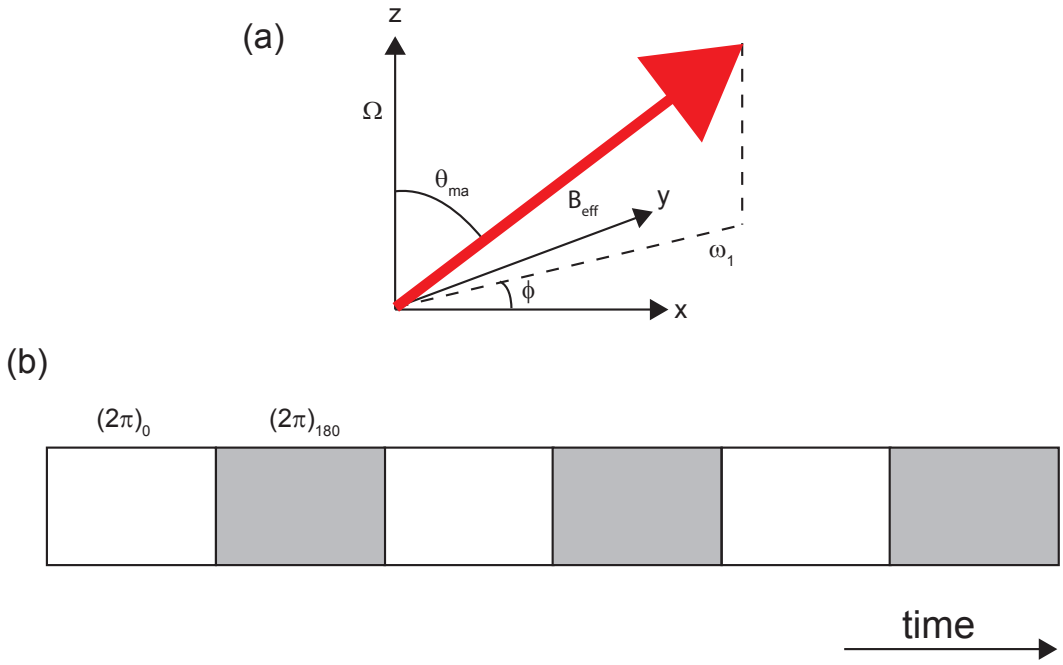

Figure 3.5: (a) Schematic representation of the Lee-Goldburg condition. (b) Pulse sequence for Frequency Switched Lee-Goldburg (FSLG) homonuclear decoupling. Each pulse is applied off-resonance, by an offset of $\pm\,\omega_1/\sqrt{2}$ (alternating between pulses), so that the effective field is aligned at the magic angle relative to B_0.

is applied on-resonance, then the magnitude of z-component of the pulse is zero, and the magnetisation will rotate about the axis of the applied pulse (see section 2.3.2). However, if the pulse is applied off-resonance then the pulse will rotate at a subtended angle which is dependent upon the relative magnitude of the x and z components of the *rf* pulse. If the pulse is applied such that $\omega_1/\Omega = \sqrt{2}$, then in the rotating frame the bulk magnetisation is aligned at the magic-angle relative to the external field. This condition is known as the Lee-Goldburg condition, [10] which is visualised in Fig. 3.5a.

Frequency Switched Lee-Goldburg (FSLG) is an improvement on the Lee-Goldburg sequence, [16, 17] and is an example of an off-resonance homonuclear decoupling sequence. Pulses are applied with opposite phase and frequency, and are of duration 2π in the effective field, which is at the magic angle relative to B_0, therefore ensuring complete rotation of the nuclear spin. An FSLG decoupling scheme is presented in Fig. 3.5b.

3.2.4 DUMBO

The DUMBO family of sequences consists of rapid phase switching of discrete pulses, applied on resonance at a constant nutation frequency. [19] Within this thesis, phase switching in the DUMBO sequence occurs at intervals of 100 ns, therefore it is imperative that the experimental equipment is capable of delivering consistent, rapid switching of phase values to ensure consistency of results. The DUMBO family of sequences were adapted from the BLEW-12 decoupling sequence, [114] which consists of twelve $\pi/2$ pulses applied simultaneously, each with a phase switch of 90° relative to the previous discrete pulse. The motivation behind the proposing of the DUMBO approach was to combat experimental imperfections arising from the use of discrete $\pi/2$ pulses, by applying a more continuous modulation of the phase of the *rf* field.

The original sequence, named DUMBO-1 was computationally optimised under static conditions for a coupled two-spin ^{1}H system. Later, the sequence was optimised experimentally during a ^{1}H MAS experiment, at an MAS frequency of 22 kHz. This is referred to as eDUMBO-1_{22} decoupling, [21] and it is this version of the DUMBO family which is implemented within this thesis. The Hamiltonian describing the *rf* nutation is given as:

$$\hat{H}_{rf} = \omega_1(t)[\cos\phi(t)\hat{I}_x + \sin\phi(t)\hat{I}_y] \tag{3.20}$$

where the phase values are a periodic time dependent function determined by a Fourier series:

$$\phi(t) = \sum_{n=1}^{6}[a_n\cos(2n\omega_c t) + b_n\sin(2n\omega_c t)] \qquad 0 \leq t \leq \tau_c/2$$

$$\phi(t) = \pi + \phi(\tau_c - t) \qquad \tau_c/2 \leq t \leq \tau_c \tag{3.21}$$

where τ_c is the length of one complete cycle, and $\omega_c = 2\pi/\tau_c$. An example of the phase values used in an eDUMBO-1_{22} scheme consisting of 320 points is presented in Fig. 3.6a. The length of one complete cycle is defined as being equal to a 6π pulse, according to the *rf* nutation frequency ω_c. Note, the phase values are a reflection about the centre of one basic cycle, with an addition of π to all phase values in the range $\tau_c/2$ $\leq t \leq \tau c$. Calculated phase values without the addition of π to the reflected points

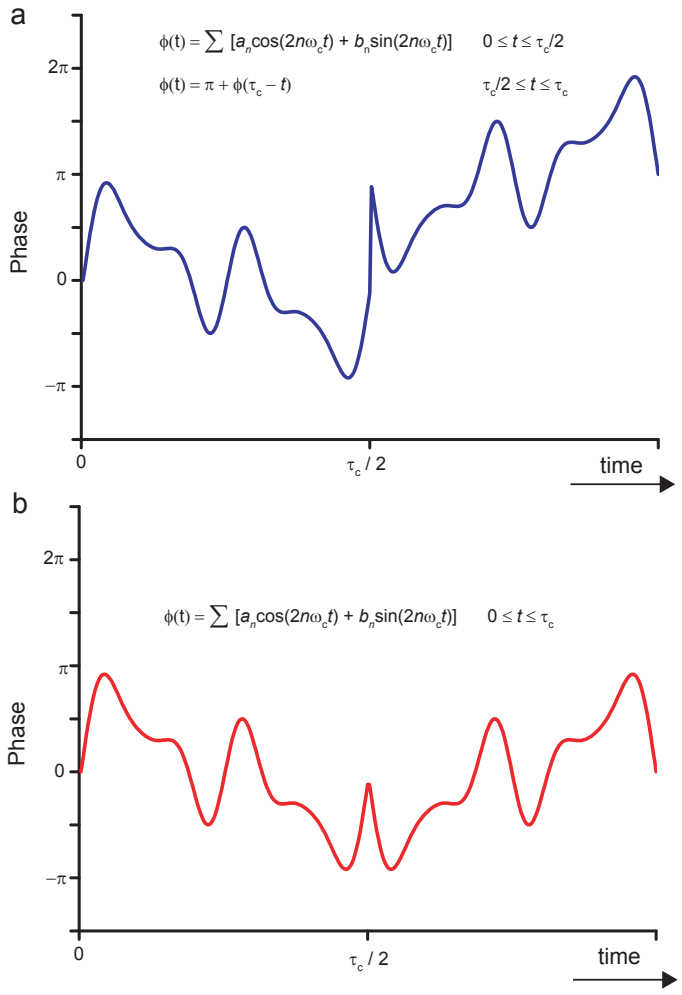

Figure 3.6: (a) Schematic of one complete cycle of an eDUMBO-1_{22} homonuclear decoupling sequence. The sequence shown contains 320 points. The sequence is symmetric about the centre point according to equation 3.21, with the addition of π to the second half of the cycle. The length of one complete cycle is a 6π pulse, calculated from the *rf* nutation frequency, ω_c. (b) Schematic of eDUMBO-1_{22} sequence without the addition of π to all reflected points after $\tau_c/2$.

after $\tau_c/2$ is presented in Fig. 3.6b.

3.2.5 Homonuclear decoupling considerations

Homonuclear decoupling can be applied in a windowed or windowless form. Windowed homonuclear decoupling is necessary to enable the application of homonuclear decoupling during ^{1}H acquisition. At designated points between decoupling cycles, a point in the NMR signal is acquired. Windowless decoupling, where the decoupling scheme is applied continuously, is often applied in 2D experiments, where averaging of ^{1}H-^{1}H dipolar couplings is required during t_1. Initial developments of Lee-Goldburg

decoupling sequences were applicable as a windowless sequence only, however later developments, such as windowed Phase Modulated Lee Goldburg (w-PMLG), [115] allow for windowed acquisition. Within this thesis only windowless homonuclear decoupling is utilised.

A further complication of homonuclear decoupling is the scaling of ^{1}H chemical shifts and heteronuclear J couplings due to the precession of the magnetisation in a frame tilted away from the transverse plane. If the magnetisation evolves in a plane aligned along $\langle 111 \rangle$, then an ideal scaling factor, defined as λ, of $1/\sqrt{3}$ (≈ 0.57) results. If perfect decoupling is not achieved, then the scaling factor will deviate from 0.57. The scaling factor is applicable to all ^{1}H interactions which are not averaged to zero during the NMR experiment. Proton chemical shift values are scaled accordingly, therefore if performing ^{1}H NMR using homonuclear decoupling schemes, the chemical shift axis must be scaled accordingly. Of greater interest within this thesis is the scaling of heteronuclear XH through-bond couplings. As the J coupling is a weak interaction, a larger effective J coupling is favourable to improve resolution of a splitting pattern. However, if the scaling factor is too large then this indicates that the effective field is not aligned at the magic angle relative to B_0, and therefore homonuclear dipolar couplings are not averaged to zero. Scaling factors can be measured by comparing ^{1}H chemical shifts, acquired with and without homonuclear decoupling, for a pair of ^{1}H resonances of known ^{1}H chemical shifts (e.g., 2 well resolved resonances in a fast MAS spectrum).

3.3 Pulse sequences

3.3.1 Cross Polarisation

Cross-polarisation is used to enhance magnetisation in dilute, lower-γ nuclei, such as ^{15}N or ^{13}C, by transferring polarisation via heteronuclear dipolar couplings from an abundant nucleus, such as ^{1}H. A full CPMAS pulse sequence, utilising a ramped polarisation transfer step (which is discussed below), is presented in Fig. 3.7. Note the application of heteronuclear dipolar decoupling, introduced in section 3.2.1, during t_2. ^{13}C is only 1.1% isotopically abundant, ^{12}C has a far greater natural abundance, however due to possessing $I = 0$ it is not observable in an NMR experiment. It is possible

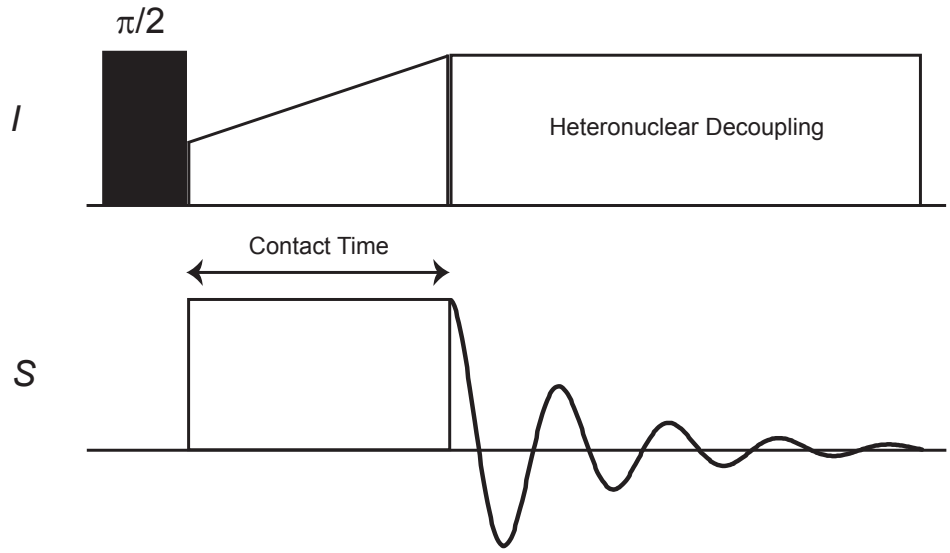

Figure 3.7: Ramped cross-polarisation pulse sequence used to transfer magnetisation from an abundant nucleus (e.g., ^{1}H) to a dilute nucleus (e.g., ^{13}C or ^{15}N) by ensuring that the Hartmann-Hahn condition is met. In this pulse sequence a ramped polarisation step is applied to ^{1}H spins to reduce sensitivity to misset of the Hartmann-Hahn matching condition. Signal is acquired for the dilute nucleus, and heteronuclear dipolar decoupling is applied to the ^{1}H channel during acquisition, which is detailed in section 3.2.1.

to isotopically enrich the proportion of ^{13}C atoms, however this is both time consuming and expensive. In the case of nitrogen, ^{14}N is the most isotopically abundant nucelus (99.6%). ^{14}N is an NMR active nucleus, however it is a spin-1 quadrupolar nucleus, and as discussed in section 2.4.5, this introduces complications arising from the presence of the quadrupolar interaction. Therefore, it often simpler to observe the spin-$\frac{1}{2}$ ^{15}N nucleus, however this is limited by a low natural isotopic abundance (0.37%).

Furthermore, lower-γ nuclei such as ^{13}C and ^{15}N, typically have longer spin-lattice relaxation times, described by T_1, than a high-γ nucleus such as ^{1}H. This is owing to a lack of strong homonuclear dipolar couplings between dilute nuclei considered in this thesis, namely ^{13}C and ^{15}N. Strong homonuclear dipolar couplings enable transitions back to the population state at a faster rate than weaker heteronuclear dipolar couplings.

Efficient cross-polarisation occurs when the Hartmann-Hahn matching condition is satisfied. [39] For a static sample, Hartmann-Hahn matching between the abundant nucleus (^{1}H for the purpose of this work) and X (^{13}C or ^{15}N within this thesis), is given

by:

$$\gamma_I B_{1I} = \gamma_S B_{1S} \tag{3.22}$$

As CP is mediated through heteronuclear dipolar couplings, then close proximity nuclei typically have the quickest magnetisation transfer rate. Longer range couplings typically require a longer contact time to achieve optimal signal transfer. For an isolated XH pair, magnetisation transfer will oscillate between the coupled pair. However, as is the case for most organic materials, strong ^{1}H homonuclear networks exist, which act to further distribute magnetisation through the system, consequently enhancing polarisation transfer. When optimising a contact time, it is important to recognise that ^{1}H magnetisation excited in the transverse plane will relax back to a population state, even under the so-called "spin-lock"pulse. Therefore, relaxation back to thermal equilibrium effects the polarisation transfer, if a contact time is too long then magnetisation is not sustained and polarisation transfer is inhibited.

Dynamics within a molecule can also effect polarisation transfer mechanisms. For instance, motional effects in a methyl group average dipolar couplings, which consequently effects the optimal contact time. For an organic material, a ^{13}C-^{1}H cross-polarisation experiment typically requires contact times ranging from 0.5 ms to 5 ms, depending upon the exact nature of the system and the resonances of interest. In addition to intrinsic motion within a molecule, dynamics from MAS also effect heteronuclear dipolar couplings. Therefore, under non-static conditions, the Hartmann-Hahn condition introduced in equation 3.22 requires an additional term to account for MAS, given as:

$$\gamma_I B_{1I} = \gamma_S B_{1S} + n\omega_r \tag{3.23}$$

where $n = 1$, 2, and ω_r is the MAS frequency. As CP is mediated through heteronuclear dipolar couplings, the introduction of MAS averages heteronuclear dipolar couplings, reducing the efficiency of polarisation transfer. A common methodology to improve polarisation transfer in a CP experiment under MAS conditions is to apply a ramped polarisation transfer step to the ^{1}H channel. [116] A suitably calibrated ramped polarisation transfer step can increase intensity, and reduces the sensitivity to a misset in

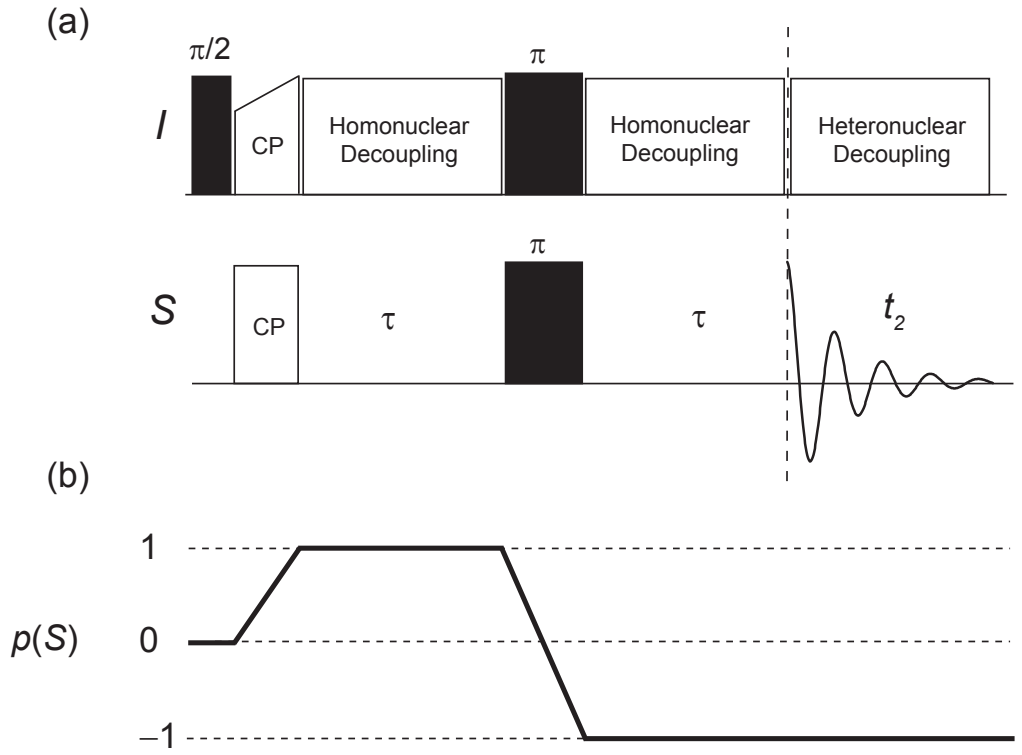

Figure 3.8: Pulse sequence for a heteronuclear spin-echo experiment, and corresponding coherence pathway for the S spin. Note, a CP ramp is often applied to transfer magnetisation to the S spin. Furthermore, in order to adequately resolve a heteronuclear J splitting, it is necessary to apply efficient homonuclear decoupling during τ periods. Heteronuclear decoupling is also applied during t_2 acquisition.

the Hartmann-Hahn matching condition. An adiabatic shaped ramp has been demonstrated as a more efficient ramp shape for strongly coupled spins in a sparse proton environment, where polarisation is not easily transferred throughout the system. [117] Furthermore, adiabatic transfer has been shown to be more effective than a ramped step when studying ^{15}N nuclei with long-range proton proximities. [118]

3.3.2 Spin-echo

A spin-echo experiment implements a τ-π-τ sequence to refocus evolution under a resonance offset, thus removing inhomogeneous effects due to e.g., chemical shift disorder. A heteronuclear spin-echo pulse sequence, and corresponding coherence pathway, are presented in Fig. 3.8. The true transverse relaxation time is defined as T_2, however in reality this parameter is not measured in a solid-state NMR experiment due to the presence of experimental imperfections, spin interactions and differences in precession frequencies throughout a sample, all of which contribute towards the loss, or dephas-

ing, of transverse magnetisation. The apparent linewidth in an NMR experiment is described by the inverse of $T_2{}^*$, which includes all additional broadening contributions. The spin-echo dephasing time measured during a spin-echo experiment is defined as $T_2{}'$. [29] In the solid state, this is usually much shorter than T_2 as it retains broadening effects from spin interactions and contributions from imperfect decoupling, however it is important to note that $T_2{}^*$ is always less than $T_2{}'$. As NMR linewidths are inversely proportional to T_2, it follows that an increase in the transverse dephasing time due to refocusing of inhomogeneous effects reduces NMR linewidths. This is advantageous when identifying small couplings, such as a J coupling interaction, which are typically not observed unless inhomogeneous broadening effects are refocused.

For a heteronuclear spin-echo, the in-phase magnetisation on the S spin as a function of τ is given as: [22, 103]

$$S(\tau) = S(0)\cos^n(2\pi J_{IS}\tau)\exp -2\tau/T_2^{'} \tag{3.24}$$

$S(0)$ is the intensity of the FID at $\tau = 0$ ms and n is the number of directly attached nuclei. The $\cos(2\pi J_{IS}\tau)$ term in equation 3.24 evolves to the power n, therefore heteronuclear spin-echo modulation curves can be used to identify different XH_n groups, where X is a spin-$\frac{1}{2}$ nucleus. In Fig. 3.9, spin-echo modulation for different CH_n groups is modelled according to equation 3.24. The dephasing term in equation 3.24 incorporates relaxation effects due to transverse dephasing, described by $T_2{}'$. Note, that the evolution under inhomogeneous chemical shifts are refocused due to application of inversion pulse on the I and S spins. The application of an inversion pulse to both channels retains evolution under a heteronuclear scalar coupling, J_{IS}. Application of a pulse to the S spin only would refocus the heteronuclear scalar coupling, in addition to inhomogeneous chemical shifts. It is necessary that strong interactions, such as dipolar couplings and the chemical shift anisotropy, are sufficiently averaged during τ periods. This is assumed to be achieved using a combination of MAS (heteronuclear dipolar coupling and CSA) and dipolar decoupling sequences (homonuclear dipolar coupling), as explained in section 2.4.4 and section 3.2.2, respectively. However, as will be detailed in chapter 4, this assumption is challenged by unexpected dephasing under heteronuclear dipolar couplings in a heteronuclear spin-echo pulse sequence when homonuclear

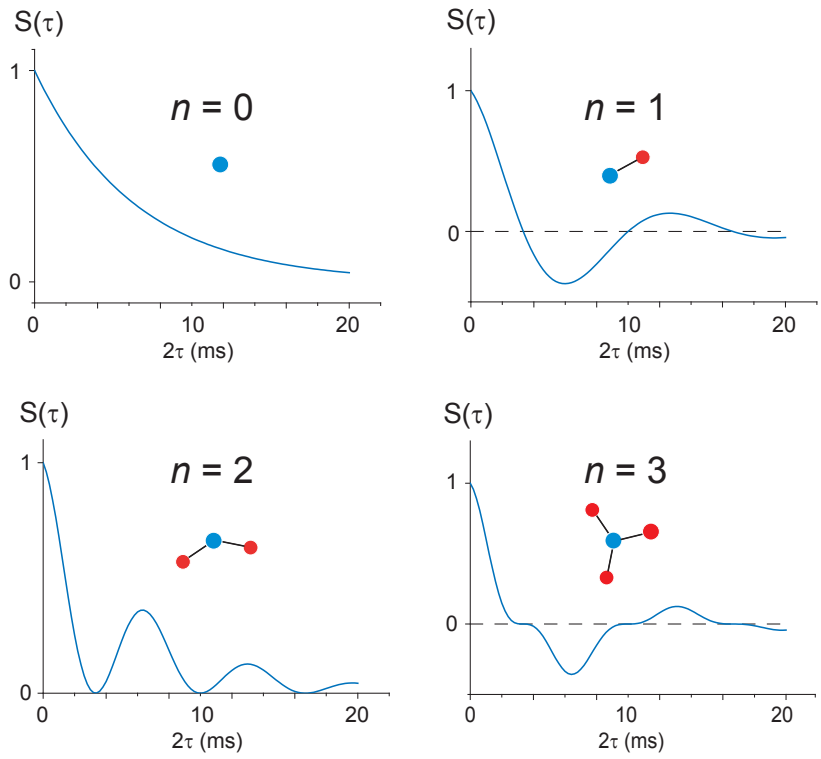

Figure 3.9: Calculated heteronuclear spin echo modulation curves calculated using a J_{IS} = 150 Hz and T_2' = 6.3 ms, where signal evolves according to $\cos^n(2\pi J_{IS}\tau).\exp(-2\tau/T_2')$, where n is specified for each modulation curve.

decoupling is employed during the τ periods.

As is evident in equation 3.24 and Fig. 3.9, an odd-number of heteronuclear direct covalent bonds (i.e. n = 1, 3) results in an inversion of the modulation. Alternatively, if n = 0 or 2 then the modulation will not invert after any time period. It is possible to calculate the effective coupling from the crossing points in a spin-echo modulation curve. As magnetisation evolves according to a $\cos(2\pi J_{IS}\tau)^n$ term, then the first zero intensity point in a modulation curve occurs when the condition ($2\pi J_{IS}\tau$ = $\pi/2$) is satisfied. This corresponds to an effective coupling equal to $1/(4\tau)$, where τ is the first zero crossing point of the spin-echo signal. The effective coupling takes into account scaling of isotropic interactions owing to application of homonuclear decoupling, as described in section 3.2.2. Note, that the above definition only applies if the evolution period before and after the π pulse is equal to a total duration of length 2τ (the spin-echo can alternatively be described as $\tau/2$ - π - $\tau/2$).

3.3.3 HMQC

Heteronuclear Multiple Quantum Coherence (HMQC) experiments establish correlation between two different nuclear species, e.g., ^{14}N-^{1}H. Direct detection occurs on the higher-γ nucleus, therefore the sensitivity is enhanced relative to direct detection of the lower-γ nucleus. The nuclear magnetic moment is proportional to γ (equation 2.2), therefore higher γ values result in a large macroscopic magnetic moment, hence a stronger NMR signal. Secondly, as presented in equation 2.4, the Larmor frequency is proportional to γ, therefore as the induced current in the NMR coil is dependent upon the Larmor frequency, the strength of the NMR signal is enhanced by higher γ values. Additionally, at thermal equilibrium the Boltzmann distribution is proportional to ω_0, and hence γ, consequently a larger Boltzmann distribution enhances the NMR signal in a HMQC experiment.

An example pulse sequence, and corresponding coherence pathway are presented in Fig. 3.10. As an indicator of the gain in sensitivity possible using the HMQC experiment, the gyromagnetic ratio of ^{1}H relative to ^{13}C is approximately a factor four, whilst the ratio $\gamma(^{1}\mathrm{H})$ relative to $\gamma(^{14}\mathrm{N})$ is approximately fourteen. Therefore, the inherent sensitivity is significantly higher if observing via ^{1}H, opposed to lower γ nuclei, such as ^{14}N. After creation of transverse magnetisation on the I spin, magnetisation is transferred from the I spin to the S spin. Magnetisation transfer from the I spin to the S spin is enabled by means of multiple heteronuclear interactions. Examples of magnetisation transfer via heteronuclear J coupling or residual dipolar splittings (RDS) have been demonstrated elsewhere, herein the majority of spectra presented achieve magnetisation transfer via ^{14}N-^{1}H heteronuclear dipolar couplings.

As shown in section 2.4.4, heteronuclear dipolar couplings are averaged by MAS, therefore heteronuclear dipolar correlation experiments require the reintroduction of the heteronuclear dipolar coupling in a controlled manner. Rotary-resonance recoupling (R^3) [34] was selected to recouple heteronuclear dipolar couplings for all experiments presented herein. Single or double-quantum coherence orders are excited and reconverted on the S spin through application of the pulses labelled τ_p in Fig. 3.10. SQ or DQ coherence is selected by implementing a 2-step phase cycle ($\Delta p = \pm 1$) or a 4-step phase cycle ($\Delta p = \pm 2$) to either τ_p pulse.

The HMQC experiment is best understood by applying the product operator

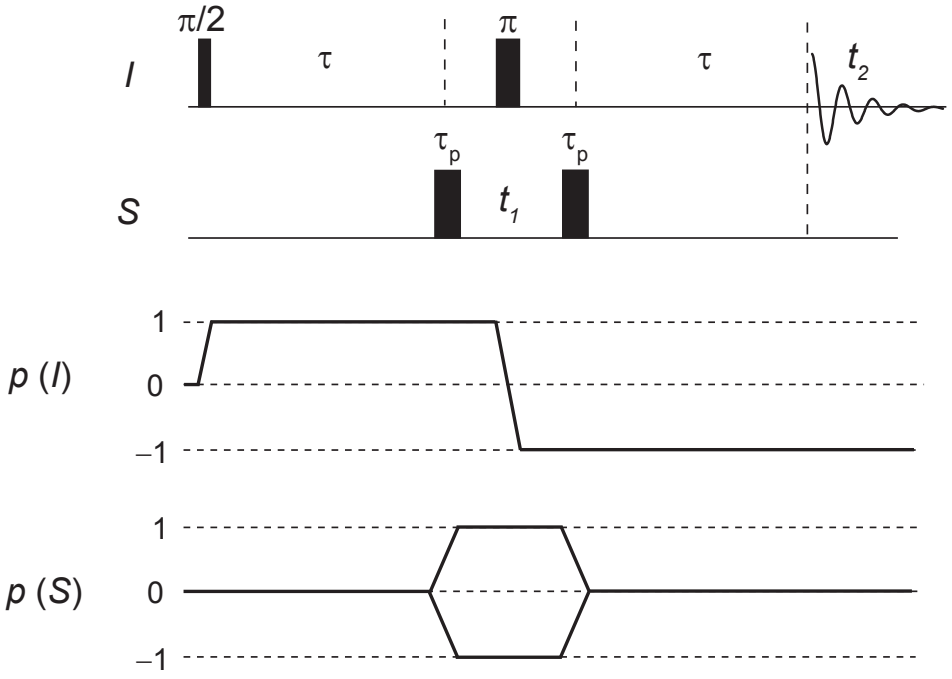

Figure 3.10: Pulse sequence for a HMQC experiment. Note that the heteronuclear MQ coherence can be created via through-bond or through-space couplings. In Fig. 6.1, a specific pulse sequence employing rotary resonance recoupling (R^3) [34] to recouple heteronuclear dipolar couplings is presented. The π pulse applied to the I spin refocuses resonance offset differences. The τ_p pulse on the S spins excites coherence for observation during t_1.

formalism introduced in section 2.3.4. Here, the calculation is presented for the case of a heteronuclear J coupling, but the same principles apply if the heteronuclear multiple quantum coherence is created via a dipolar coupling. Evolution under Ω_I is not included as this is refocused by the application of a refocusing $(\pi_x)_I$ pulse. Assuming that the experiment begins at thermal equilibrium, the application of the initial 90° pulse to the I spin, and the subsequent evolution period yields:

$$\begin{aligned} I_z &\xrightarrow{(90^\circ_x)_I} \xrightarrow{\pi J_{IS}\tau} \\ &- I_y \cos \pi J_{IS}\tau + 2I_x S_z \sin \pi J_{IS}\tau \end{aligned} \tag{3.25}$$

If the excitation duration, labelled τ, is set to equal to $1/2J_{IS}$ then the anti-phase term in equation 3.25 is maximised. Therefore, following the application of a 90° pulse about

x to the S spin, the magnetisation is given as:

$$\begin{aligned} &= 2I_xS_z \\ \xrightarrow{(90^\circ_x)_S} &-2I_xS_y \end{aligned} \tag{3.26}$$

The term in equation 3.26 represents a heteronuclear multiple quantum coherence that will evolve during t_1 under the S spin chemical shift. The effect of the inversion pulse on the I spin is not explicitly included here, but as discussed above its role is to refocus evolution under Ω_I. In the following, to show the reconversion back to spin I magnetisation, consider the case where $t_1 = 0$ ms. Therefore, following the second 90° pulse on the S spin, the heteronuclear multiple quantum coherence order is converted into a single-quantum coherence on the I spin:

$$\xrightarrow{(90^\circ_x)_S} -2I_xS_z \tag{3.27}$$

The term in equation 3.27 evolves under J_{IS} during the second τ period. The reconversion τ period is set equal to the excitation τ period (which is equal to $1/2J_{IS}$ for this specific case). Therefore, after considering the evolution of the magnetisation under J_{IS}, the magnetisation at $t_2 = 0$ ms is given by:

$$\begin{aligned} \xrightarrow{\pi J_{IS}\tau} &- I_y \sin \pi J_{IS}\tau - 2I_xS_z \cos \pi J_{IS}\tau \\ &- I_y \end{aligned} \tag{3.28}$$

Hence, the magnetisation is an observable state on the I spin, which is detected during t_2.

3.4 Computational Techniques

3.4.1 GIPAW calculations

Using Density Functional Theory (DFT), it is possible to calculate NMR shielding tensor and electric field gradient parameters to complement experimental results. The approach employed in this thesis applies a planewave basis set using pseudopotentials, [119] which exploits periodicity in a crystalline material to describe the electron

wavefunction. The approach of pseudo-potentials assumes that the core electrons do not significantly affect the physical and chemical properties. Assuming that the core electrons are passive reduces the complexity of the calculation, and therefore the time requirements of a calculation. However, for accurate calculations the effect of core electrons must be considered. The Gauge Including Projector Augmented Wavefunction (GIPAW) approach reconstructs the electron wavefunction of the core electrons so that a full electron model is considered. [56, 57]

Calculations presented within this thesis consist of two distinct stages. Initially, X-ray or neutron diffraction studies are obtained from the Cambridge Structural Database (CSD), [120] however, the position of light elements (e.g., ^{1}H) is usually only approximated by diffraction studies. For NMR calculations of organic materials it is necessary to geometry optimise the positions of light elements, which is achieved using the DFT CASTEP code. [54, 121] It may also be necessary to optimise the position of heavier elements, such as ^{13}C; the level of geometry optimisation is explicitly stated for each calculation presented. In a geometry optimisation calculation the unit cell parameters are fixed, but the atomic positions are allowed to relax to their lowest energy state. Where internuclear proximities are stated in this thesis, they are extracted from the geometry optimised positions.

Once geometry optimisation is complete, GIPAW calculation of NMR shielding tensor and electric field gradient parameters is performed using the CASTEP code. The direct output of calculations include the absolute chemical shielding tensor, defined as $\sigma(r)$, which as shown in section 2.4.3, can be expressed as an isotropic shielding value according to:

$$\sigma_{iso}(r) = \frac{1}{3}\mathrm{Tr}[\sigma(r)] \tag{3.29}$$

To compare with experimentally observed shifts, the following expression is used:

$$\delta_{iso} = -[\sigma_{iso}(r) - \sigma_{ref}] \tag{3.30}$$

For all values of the shielding reference, σ_{ref}, used within this thesis, the value is calculated from the average of experimental values of δ_{iso}, and calculated values of $\sigma_{iso}(r)$. Values of σ_{ref} should approximately agree when calculated for different mate-

rials, although low ppm values are typically overestimated, whereas high ppm values are underestimated. [58, 102] The electric field gradient parameters outputted from a GIPAW calculation are directly comparable to experiment.

3.4.2 Density Matrix Simulations

The density matrix, introduced in section 2.2, is able to describe an ensemble of coupled spins. The Liouville-von Neumann equation, constructed using propagators dependent upon the interaction Hamiltonians presented, describes the solution to the time evolution of the density matrix. Numerous simulation packages exist which exploit the Liouville-von Neumann equation to simulate an NMR experiment. [52, 53, 122] All simulations presented herein were generated using the SPINEVOLUTION simulation package. [53]

The computational time required for a simulation increases by 2^N, where N is the number of nuclei in the simulated spin system. Simulations are not presented beyond 8-spins for this thesis, however they have been demonstrated for larger spin-systems elsewhere. [123–125] The flexibility of simulations relative to experiment allows the user to simplify the spin-system or the pulse sequence in order to reduce computational time. For instance, it is possible to record a pseudo 2D experiment, providing that direct observation of only a single-spin is required, as magnetisation in a multi-spin simulation can be specified so that only a single spin is observed. Therefore, the first point in t_2 only needs to be simulated, which corresponds to the integrated peak area in the Fourier-transformed frequency domain for the single resonance, at each t_1 increment. This corresponds to a slice of a 2D experiment, centred on a specific resonance frequency at ω_2.

Simulations can be used to assist in understanding experimental effects. As all interactions present can be specified by the user, it is possible to identify the evolution under different interactions during an experiment. As an example, in a multi-spin system it is possible to specify the couplings present between individual spins, systematically removing the different interactions. Furthermore, simulations allow the user to specify parameters that are not yet achievable experimentally, such as high *rf* nutation frequencies and ultra-fast MAS frequencies. Experimental imperfections arising from discrete pulses can be removed in simulations, through application of ideal pulses,

where the required rotation of the magnetisation is achieved, but the time applied for an *rf* pulse is effectively zero duration.

CHAPTER

FOUR

CHARACTERISTICS OF HOMONUCLEAR DECOUPLING DURING A HETERONUCLEAR SPIN-ECHO

4.1 Introduction

This chapter, partially based around recently published results, [1] concerns the behaviour of heteronuclear couplings when subject to proton homonuclear decoupling. Organic materials, such as pharmaceuticals, typically contain dense proton networks, where non-commuting ^{1}H-^{1}H dipolar couplings are not averaged by MAS alone. As discussed in section 3.2.2, numerous homonuclear decoupling *rf* pulse sequences have been developed with the aim of removing the effect of strong homonuclear ^{1}H-^{1}H dipolar couplings. Early decoupling sequences were performed on static samples, whereas later decoupling sequence were developed to be compatible with MAS. Simultaneous application of MAS and homonuclear decoupling is known as CRAMPS. Initially, CRAMPS techniques were limited to slower spinning frequencies (i.e., $\nu_r \leq 5$ kHz), known as the quasi-static regime, for which the decoupling cycle times are short relative to the MAS rotation period. However, it has now been demonstrated that homonuclear decoupling sequences can work outside of the quasi-static regime, provided that synchronisation conditions between the rotor period and decoupling cycle times are avoided. Schemes such as FSLG, [16, 17], PMLG, [18, 115] and DUMBO sequences [19] are compatible with fast MAS. Numerous demonstrations of CRAMPS for moderate to high spinning frequencies have been presented. [20, 126–133]

Many 2D heteronuclear correlation experiments, such as *J*-INEPT [32] and ^{13}C-

^{1}H HETCOR, [45] have been been demonstrated on pharmaceutical systems. [65–67, 74, 79, 134] Successful implementation of these experiments is reliant upon efficient ^{1}H homonuclear decoupling. Identification of the number of proton(s) attached to a heteronucleus can be achieved using a heteronuclear spin-echo experiment. [22] As shown in section 3.3.2, the evolution of a J coupling during free precession is dependent upon a cosine term to the power n, where n is the number of covalently bonded protons to a heteronucleus. Therefore, a heteronuclear spin-echo sequence with efficient proton homonuclear decoupling, as presented in Fig. 4.1, is able to discriminate between different CH_n functional groups.

In this chapter, the effectiveness of windowless homonuclear decoupling sequences are examined both experimentally and by simulation results. Experimental spin-echoes were recorded for L-alanine in order to establish the behaviour of eDUMBO-1_{22} during τ periods, particularly establishing the effects of changing the rf nutation frequency for different decoupling cycle times, and how performance differed when compared to heteronuclear decoupling schemes. Comparison of experiment to simulation is considered, including observation of scaling factors for single crystallite orientations. Furthermore, the effect of homonuclear decoupling on CH_3 groups are also considered, and similarities and differences to effects observed for a CH group noted. Simulations were recorded using SPINEVOLUTION. [53]

4.2 Experimental Observations

4.2.1 Experimental Details

L-alanine was purchased from Sigma Aldrich and used with no further purification. Confirmation of the zwitterionic form of L-alanine comes from a single-crystal diffraction study (CSD refcode:LALNIN23), [135] together with the ^{1}H isotropic chemical shift values from solid-state NMR. All experiments were performed at room temperature unless otherwise stated. Experiments were performed on a Bruker Avance II+ spectrometer at a ^{1}H Larmor frequency of 599.4 MHz. A Bruker 2.5 mm MAS double resonance probe was used for all experiments. A MAS frequency of 20.833 kHz was used for a 32 μs eDUMBO-1_{22} cycle time and a MAS frequency of 25 kHz for a 24 μs eDUMBO-1_{22} cycle time. Different MAS frequencies are required in order to avoid

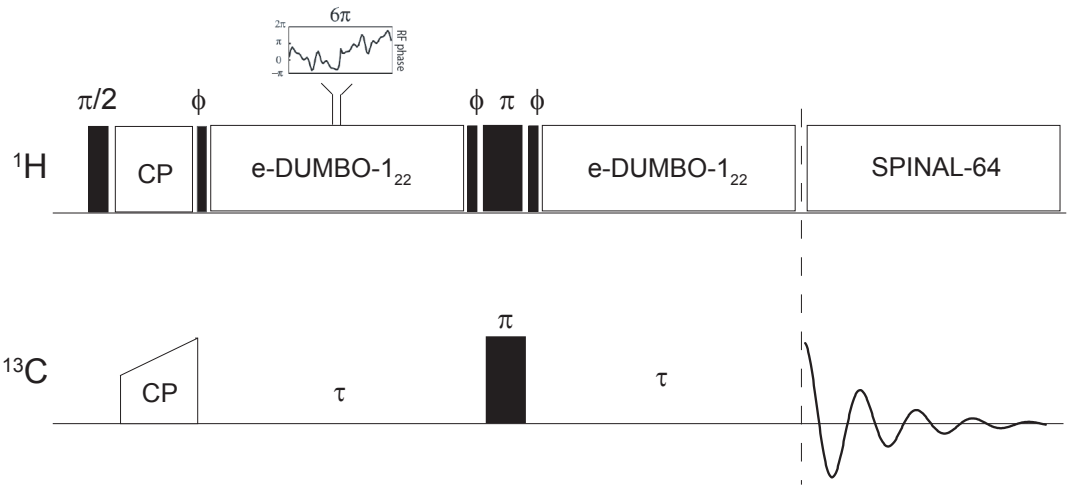

Figure 4.1: ^{13}C-^{1}H heteronuclear spin-echo pulse sequence that can be used for $^{1}J_{13C\text{-}1H}$ spectral editing.

synchronisation conditions between decoupling cycle time and rotor period, which are discussed herein. ^{1}H 90° and 180° pulses were of duration 2.5 μs and 5 μs, respectively, while the 180° pulse duration was 8 μs for ^{13}C. ^{13}C magnetisation was created using a cross-polarisation (CP) ramp of magnitude 80% to 100% on the ^{1}H channel with a contact time of 1 ms. A total of 128 transients were co-added using a recycle delay of 3 seconds. The spin-echo duration, 2τ, was incremented by 0.96 ms. A nested 8-step phase cycle was used to achieve coherence order changes of $\Delta p = \pm 1$ on the initial ^{1}H pulse (2 steps) and $\Delta p = \pm 2$ (4 steps) for the ^{13}C 180° pulse.

Heteronuclear spin-echo sequences employed SPINAL-64 [112] heteronuclear decoupling during t_2 for a duration of 20 ms, where individual pulse lengths were 4.4 μs, and a ^{1}H nutation frequency equal to 100 kHz was used. For homonuclear decoupling during τ, windowless eDUMBO-1$_{22}$ was applied at various ^{1}H nutation frequencies, specific details can be found within individual figure captions. eDUMBO-1$_{22}$ cycles of length 32 μs consisted of 320 separate events, each of length 100 ns, whereas 24 μs eDUMBO-1$_{22}$ cycle consisted of 240 events, each of 100 ns length. Pre-pulses of length 1.4 μs were applied with a nutation frequency of 100 kHz where necessary. For homonuclear spin-echo experiments, SPINAL-64 was applied during t_1 and t_2 (duration 20 ms). The ^{1}H nutation frequency was 100 kHz and each individual pulse length was 4.6 μs. Peak integrations for the CH and CH_3 groups in L-alanine were taken over chemical shift ranges of 56.8 - 44.8 ppm and 26.8 - 14.8 ppm for homonuclear spin-echo

experiments and 54.4 - 48.4 ppm and 23.4 - 17.4 ppm for heteronuclear spin-echo experiments, respectively, after applying 100 Hz of apodisation. Experimental spin-echo modulation curves were fitted using MATLAB with the following fitting functions:

$$A\cos(2\pi J\tau)\exp(-2\tau/T_2^{'}) \qquad \text{CH(eDUMBO-1}_{22}\text{)} \qquad (4.1)$$

$$A\cos^3(2\pi J\tau)\exp(-2\tau/T_2^{'}) \qquad \text{CH}_3\text{(eDUMBO-1}_{22}\text{)} \qquad (4.2)$$

$$A\exp(-2\tau/T_2^{'}) \qquad \text{CH/CH}_3\text{(SPINAL-64)} \qquad (4.3)$$

4.2.2 Results and Discussion

Figure 4.2 shows $^1J_{13C\text{-}1H}$ spectral editing spectra recorded using the heteronuclear spin-echo pulse sequence in Fig. 4.1, obtained at a range of different 2τ increments. The spectra shown were obtained with eDUMBO-1_{22} homonuclear decoupling during τ periods, with one complete cycle length of 32 μs. The CH and CH_3 resonances in L-alanine invert after a suitable 2τ increment, owing to the odd number of attached protons. Furthermore, as the carbonyl site has no direct proton attached, modulation is dependent upon an exponential decay only, described by T_2'.

As discussed in section 3.2.2, the application of homonuclear decoupling scales isotropic interactions, namely the ^{1}H chemical shifts and $^1J_{13C\text{-}1H}$ couplings, and is therefore an important experimental consideration. A ^{13}C spectrum of L-alanine in solution state was obtained to measure the unscaled, heteronuclear CH J coupling of the CH and CH_3 sites. This allows comparison between scaled and non-scaled couplings in the solid state. Specifically, the non-scaled (solution) J coupling for CH and CH_3 in L-alanine were measured as 145.0 $\pm$ 0.1 Hz and 129.7 $\pm$ 0.1 Hz, respectively, as seen in Fig. 4.3. The CH doublet pattern confirms a single through-bond CH coupling, whereas the CH_3 bonding configuration exhibits a quartet lineshape. Furthermore, weaker ^{13}C-^{1}H covalent bonding between the CH carbon site and the CH_3 protons results in a quartet pattern in each CH doublet component, and weak couplings between the CH_3 carbon and the CH proton results in a doublet pattern in each of the CH_3 quartet components. The relative J coupling values are consistent with the later zero-crossing point of the CH_3 resonance relative to the CH resonance; a smaller magnitude J coupling corresponds to a later zero crossing point of signal in τ.

Figure 4.4 presents ^{13}C-^{1}H heteronuclear spin-echo curves as a function of 2τ for

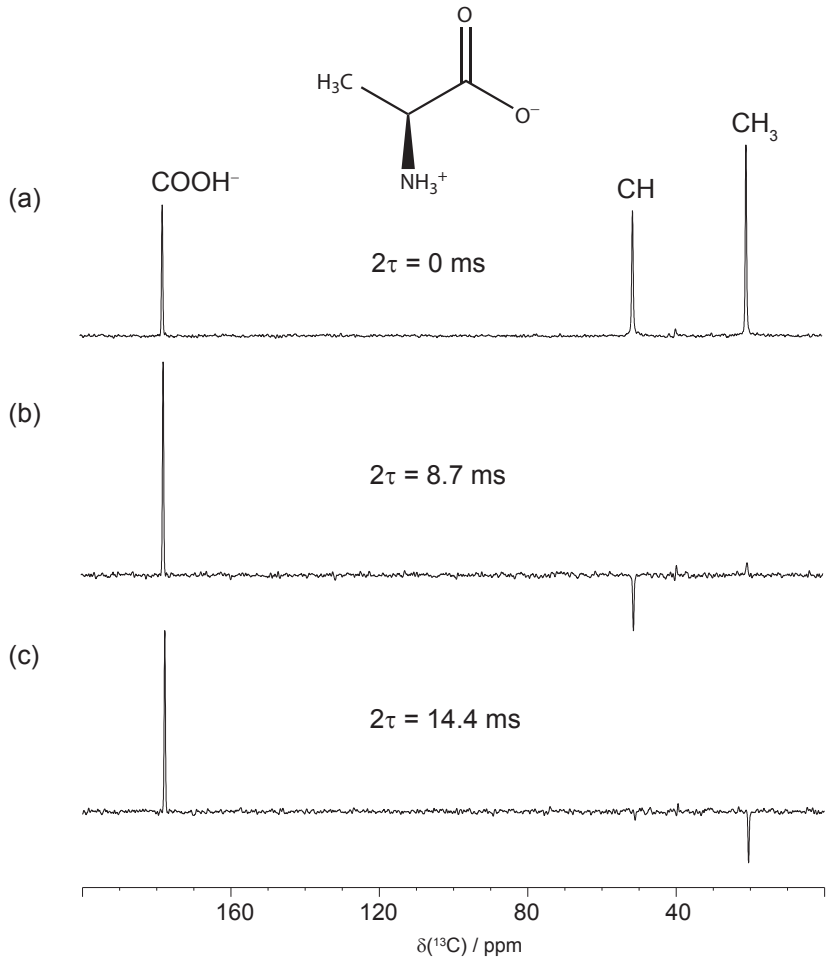

Figure 4.2: (a-c) $^{1}J_{13C\text{-}1H}$ (600 MHz, 20.833 kHz MAS) spectral editing 1-D spectra recorded using the heteronuclear spin-echo pulse sequence in Fig. 4.1, obtained at 2τ = 0 ms, 2τ = 8.7 ms and 2τ = 14.4 ms. Inversion of the CH and CH_3 sites demonstrate modulation according to the number of attached protons. eDUMBO-1_{22} was applied during τ periods, at an *rf* nutation frequency of 120 kHz, where one complete cycle time was of duration 32 μs. The τ_r/τ_c ratio was 3/2 for all spectra shown.

the CH and CH_3 resonances in L-alanine. eDUMBO-1_{22} homonuclear decoupling was applied during τ periods, using cycle times of duration (a, b) 32 μs and (c, d) 24 μs. The spin-echo curves were recorded using a range of homonuclear decoupling *rf* nutation frequencies. Each FID was recorded at a 2τ duration of 0.96 ms. Each point in a curve represents the integrated peak area. Table 4.1 and Table 4.2 show extracted T_2' and J coupling values from each curve in Fig. 4.4, fitted using MATLAB to equations 4.1 and 4.2.

The definition of best homonuclear decoupling in the context of this work is defined as the parameters that yield the longest T_2' dephasing time, and consequently improve spectral resolution of a J-splitting. For a heteronuclear CH spin-echo curve

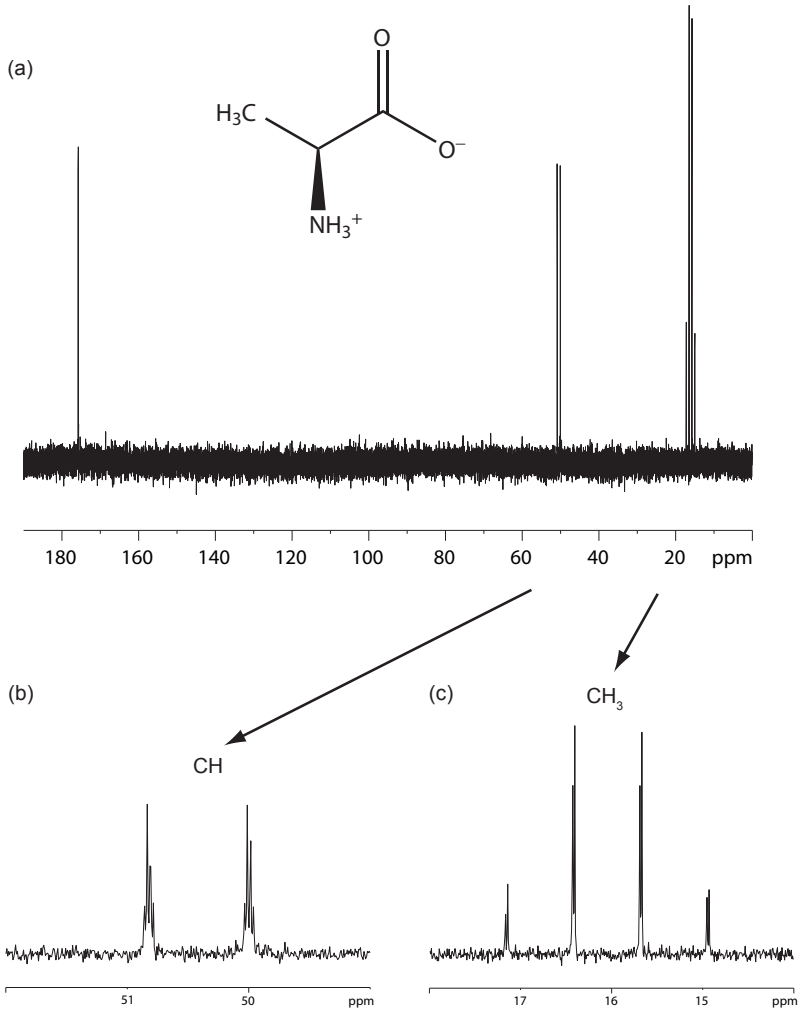

Figure 4.3: (a) ^{13}C one-pulse solution-state NMR spectrum of L-alanine obtained at a ^{1}H Larmor frequency of 700 MHz. L-alanine was dissolved into D_2O and acquisition was recorded over 128 co-added transients for a recycle delay of 2 seconds. (b-c) Zoomed in regions of the aliphatic and methyl resonances revealing detailed splitting patterns.

modulated by a J coupling, a longer T_2' dephasing time will typically result in a greater negative inversion of the spin-echo curve, relative to a curve with a shorter T_2' dephasing time. Therefore, inspection of Table 4.1 and Fig. 4.4 shows that for a 32 μs cycle time optimal performance is observed for a nutation frequency of 120 - 130 kHz, according to the definition of best homonuclear decoupling described above. Also of note is that the zero crossing point increases for higher *rf* nutation frequencies, corresponding to a decrease in the scaling factor of through-bond couplings. Changes in zero crossing points are dependent upon changes in the effective coupling, therefore it follows that an increase in nutation frequency results in a decrease in the effective

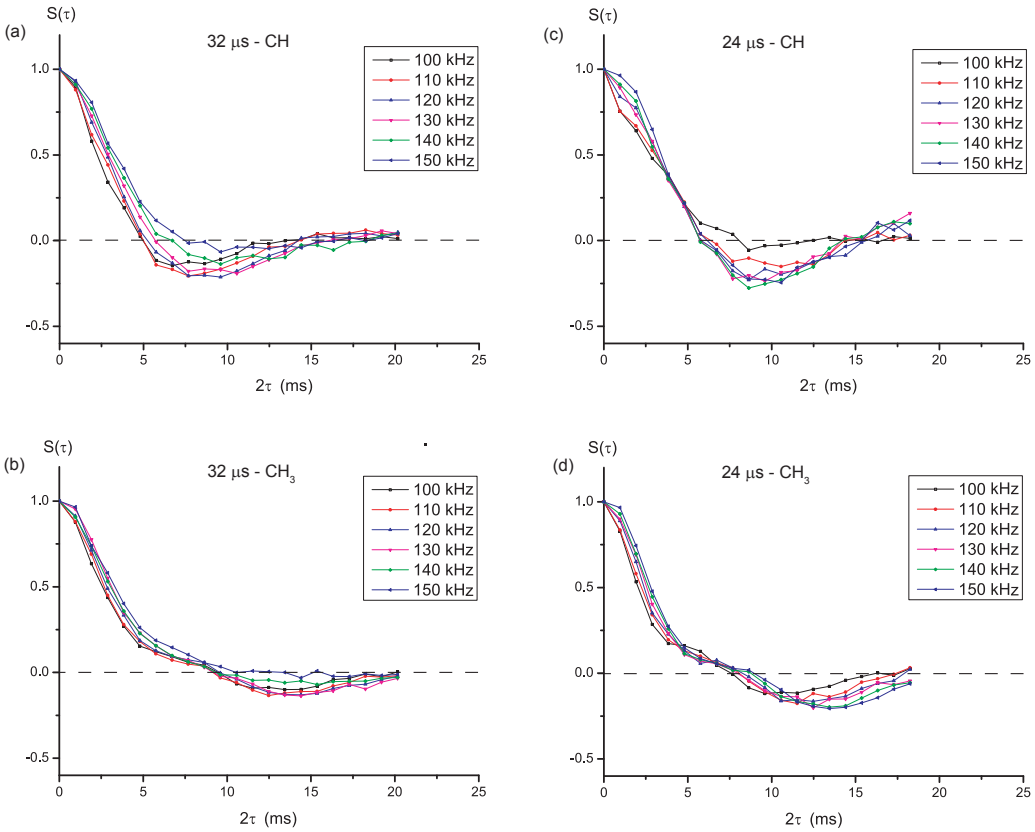

Figure 4.4: ^{13}C-^{1}H spin-echo curves of CH and CH_3 resonances in L-alanine, obtained at a ^{1}H Larmor frequency of 600 MHz and a MAS frequency of (a, b) 20.833 kHz and (c, d) 25 kHz. Each point was acquired using eDUMBO-1_{22} homonuclear decoupling during τ, with *rf* nutation frequencies ranging from 100 kHz to 150 kHz, with one complete cycle of length (a-b) 32 μs and (c-d) 24 μs, during τ periods. The τ_r/τ_c ratio was (a, b) 3/2 and (c, d) 5/3.

coupling for both CH and CH_3 resonances.

When an eDUMBO-1_{22} cycle time of 24 μs is used during the τ periods (Fig. 4.4c, d), optimal performance occurs at higher *rf* nutation frequencies of 140 - 150 kHz relative to that observed for a 32 μs eDUMBO-1_{22} cycle time. Furthermore, as seen from calculated dephasing times in Table 4.2, T_2' times are longer for a 24 μs eDUMBO-1_{22} cycle time relative to a 32 μs cycle time. Changes in dephasing times and effective couplings are not as dispersed when varying *rf* nutation frequencies in a 24 μs eDUMBO-1_{22} cycle time relative to a 32 μs cycle time. It is of note that an exception to the above statement is when lower *rf* nutation frequencies (100 kHz) are applied. Here it is assumed that the homonuclear decoupling is not effective, as a cycle time of 24 μs is too short for lower *rf* nutation frequencies (100 kHz). As detailed in section

Table 4.1: Effective ^{13}C-^{1}H couplings and T_2' times obtained from fitting the experimental data for L-alanine in Fig. 4.4 for a 32 μs eDUMBO-1$_{22}$ cycle.

Nutation frequency / kHz	Site	Effective coupling / Hz	T_2' / ms
100	CH	102 ± 2	4.5 ± 0.2
110	CH	101 ± 2	5.6 ± 0.2
120	CH	95 ± 2	6.0 ± 0.2
130	CH	87 ± 1	6.1 ± 0.2
140	CH	75 ± 2	5.6 ± 0.2
150	CH	62 ± 2	5.0 ± 0.2
100	CH_3	60 ± 2	6.6 ± 0.5
110	CH_3	62 ± 2	7.4 ± 0.5
120	CH_3	58 ± 2	8.0 ± 0.5
130	CH_3	55 ± 1	8.3 ± 0.5
140	CH_3	46 ± 2	7.4 ± 0.7
150	CH_3	39 ± 3	6.9 ± 0.9

Table 4.2: Effective ^{13}C-^{1}H couplings and T_2' times obtained from fitting the experimental data for L-alanine in Fig. 4.4 for a 24 μs eDUMBO-1$_{22}$ cycle.

Nutation frequency / kHz	Site	Effective coupling / Hz	T_2' / ms
100	CH	56 ± 3	4.3 ± 0.2
110	CH	78 ± 2	5.8 ± 0.2
120	CH	85 ± 1	6.7 ± 0.2
130	CH	90 ± 1	6.6 ± 0.2
140	CH	90 ± 1	7.0 ± 0.3
150	CH	85 ± 1	6.7 ± 0.2
100	CH_3	77 ± 3	5.8 ± 0.5
110	CH_3	75 ± 2	7.1 ± 0.5
120	CH_3	72 ± 2	7.6 ± 0.5
130	CH_3	70 ± 1	8.0 ± 0.5
140	CH_3	68 ± 1	8.7 ± 0.5
150	CH_3	66 ± 1	9.2 ± 0.5

3.2.4, DUMBO is an evolution of the BLEW-12 decoupling scheme, [114] which consists of phase switching over a cycle time equal to a 6π pulse length, calculated from *rf* nutation frequency. A 32 and 24 μs decoupling cycle time correspond to ideal *rf* nutation frequencies of 94 and 125 kHz, respectively, therefore the optimal decoupling performance in the context of this work does not correspond to a 6π pulse length.

Despite the indication that better performance occurs at higher *rf* nutation frequencies, providing a suitable choice of cycle time is implemented, the two cases are not directly comparable as they were recorded with different MAS frequencies, which may influence the dephasing time. In order to satisfy necessary rotor-synchronisation

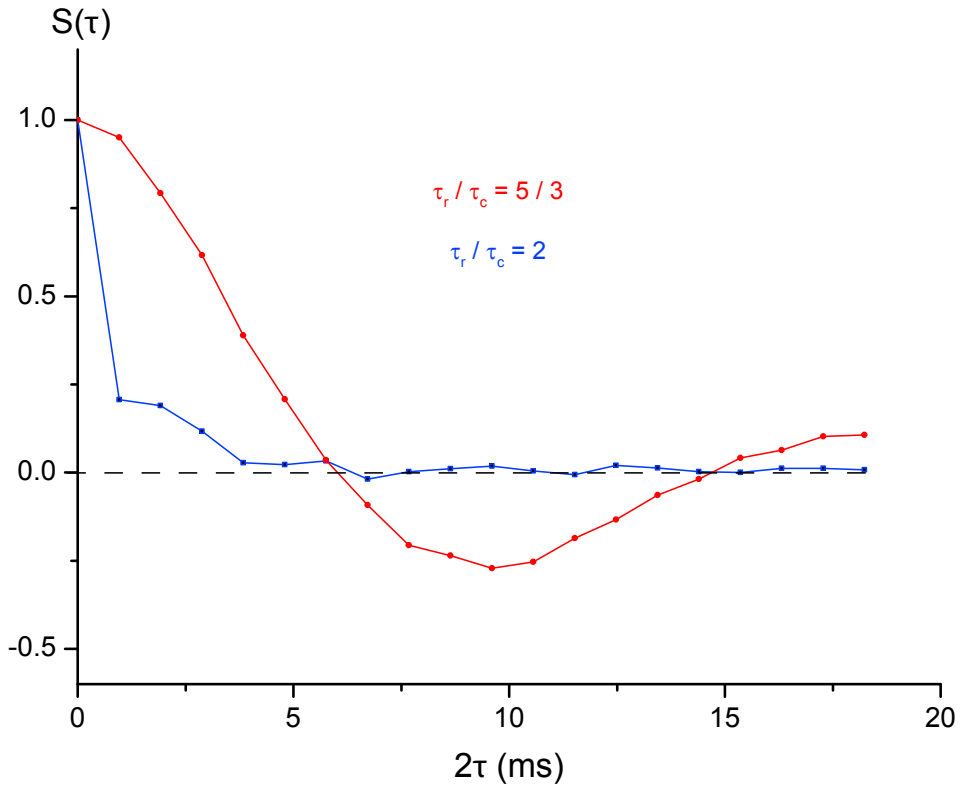

Figure 4.5: $^{1}J_{13C\text{-}1H}$ spin-echo curves obtained for the CH group in L-alanine at a ^{1}H Larmor frequency of 600 MHz. eDUMBO-1_{22} was applied during τ periods with one complete cycle time of 24 μs. Spinning frequencies of 25 kHz (red line) and 20.833 kHz (blue line) were used to demonstrate the effect of integer and non-integer ratios between the rotor period and decoupling cycle time.

conditions between a rotor-period and decoupling cycle time, different spinning frequencies were required for different length decoupling cycle times. For an MAS frequency of 20.833 kHz and a eDUMBO-1_{22} cycle time of 24 μs, the ratio between τ_r and τ_c is an integer. Destructive interference at small integer ratios of τ_r/τ_c have been demonstrated elsewhere for numerous homonuclear decoupling sequences, including PMLG, [136] WHH-4, [137] DUMBO-1, [20] and FSLG. [138] Confirmation is presented in Fig. 4.5, where CH_α modulation curves acquired using a $\tau_r/\tau_c = 2$ ratio (τ_r = 48 μs, τ_c = 24 μs) result in a significant deterioration in spectral quality relative to modulation curves recorded under $\tau_r/\tau_c = 5/3$ conditions (τ_r = 40 μs, τ_c = 24 μs).

Additional complications arise from a requirement that the total τ increment must be rotor-synchronised with respect to the time for one rotation period, as inhomogeneous interactions are only refocused over complete rotor-periods. The consequences of not applying correct τ increments with respect to rotation periods are discussed in chapter 5 for an NH modulation curve.

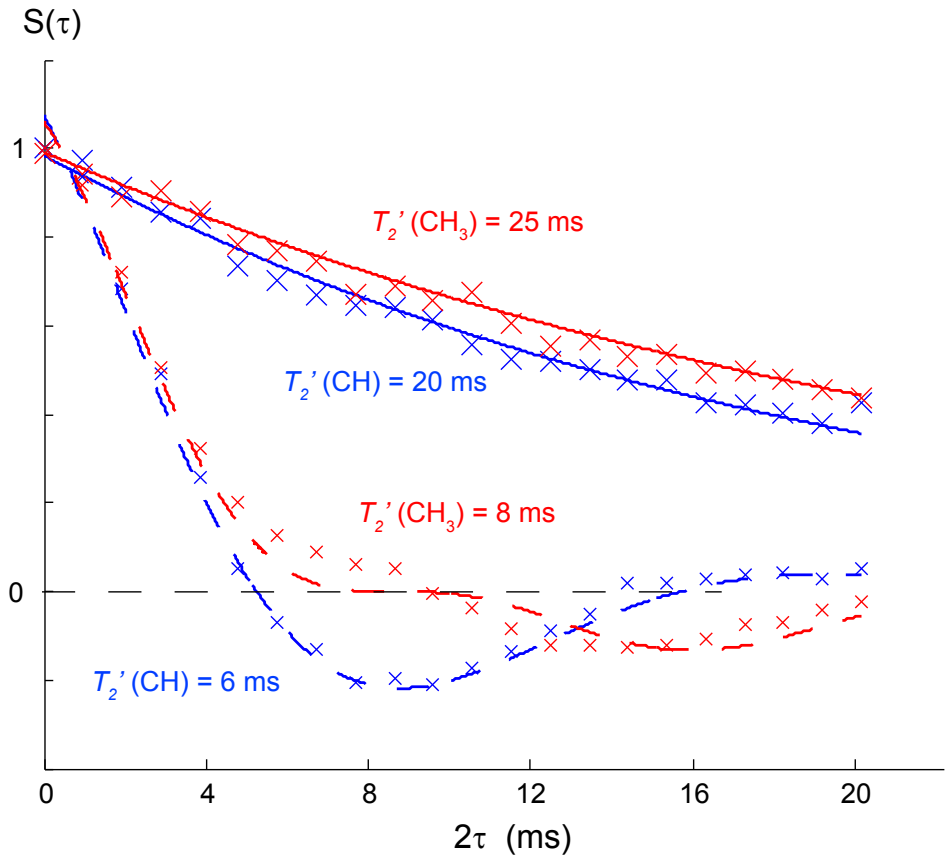

Figure 4.6: ^{13}C spin-echo curves for the CH and CH_3 carbons in L-alanine obtained at a ^{1}H Larmor frequency of 600 MHz. Each increment was recorded using eDUMBO-1_{22} (dashed line, heteronuclear spin-echo curve) and SPINAL-64 (solid line, homonuclear spin-echo curve) during rotor synchronised τ periods. An MAS frequency of 20.833 kHz was used for all curves shown. The signal integral at each τ increment is taken. Where homonuclear decoupling is applied, the τ_r/τ_c ratio was 3/2.

In Fig. 4.6, spin-echo curves are presented for the CH and CH_3 groups in L-alanine for ^{13}C-^{1}H heteronuclear (dashed line) and ^{13}C homonuclear (solid lines) spin-echo experiments. All curves are fitted (using MATLAB) to an exponential decay with decay constant T_2'. Heteronuclear spin-echo curves include an additional fitting term describing cosine modulation (see equations 4.1 and 4.2), with fitting parameter J. The homonuclear spin-echo experiment fitting term is found in equation 4.3. The fitting parameters to the modulation curves in Fig. 4.6 are presented in Table 4.3. For the heteronuclear spin-echo data (dashed lines), reasonable fits to the fitting equation are observed: it is clear that the introduction of homonuclear decoupling significantly shortens coherence lifetimes relative to ^{13}C homonuclear spin-echoes. When heteronuclear decoupling, in this case SPINAL-64, is applied during τ periods, the calculated T_2' times are approximately three times longer than the corresponding heteronuclear

Table 4.3: ^{13}C fitting parameters for spin-echo curves

Site	T_2' / ms	J scaled / Hz	J (soln.) / Hz
CH (SPINAL-64)	20 ± 2	-	-
CH_3 (SPINAL-64)	25 ± 2	-	-
CH (eDUMBO-1_{22})	6.0 ± 0.2	95 ± 2	145.0 ± 0.1
CH_3 (eDUMBO-1_{22})	8.0 ± 0.5	58 ± 2	129.7 ± 0.1

curves employing homonuclear decoupling. It will be shown that the introduction of homonuclear decoupling results in non-zero scaling of the heteronuclear dipolar couplings, resulting in additional dephasing which inhibits resolution and therefore limits the accuracy of J coupling calculations. The contribution from the interaction between heteronuclear dipolar couplings and homonuclear decoupling must be taken into consideration when analysing dephasing in a heteronuclear spin echo experiment.

In order to isolate interactions of interest, and access higher *rf* nutation frequencies not readily available experimentally, simulations proved to be a valuable tool for gaining a more complete understanding of the experimentally observed effects.

4.3 Simulated Results

4.3.1 Simulation Details

SPINEVOLUTION was used for all simulations presented. SPINEVOLUTION performs all simulations assuming a temperature of 0 K. All simulations are effective 1D simulations recorded as a function of t_1, where each point in the simulation is recorded at $t_2 = 0$ ms. A two-spin system consisted of a C-H pair separated by 1.1 Å (corresponding to a heteronuclear dipolar coupling of 23 kHz) and a through-bond coupling of 150 Hz. For a two spin system, the offset for the CH_α proton was equal to 2.9 kHz relative to the ^{1}H transmitter. The effects of homonuclear decoupling were also investigated for a CH_7 system, constructed using a L-alanine crystal file (CSD refcode:LALNIN23), [135] geometry optimised using a DFT-Based quantum code (GAUSSIAN03). The geometry optimised CH_α bond length was 1.095 Angstrom. The additional ^{1}H coordinates were extracted from the CH_3 and NH_3^+ proton positions. The ^{1}H nuclei of CH_3 were assumed to be in fast exchange, although including the motional averaging within a CH_3 group (also for NH_3^+ protons) only modified overall dephasing rates and did not significantly

affect the results observed. The ^{1}H isotropic chemical shifts were chosen to approximately match those found experimentally, with the offset of the $^{1}H_{\alpha}$ resonance at +2.1 kHz relative to the ^{1}H transmitter frequency (corresponding to 3.5 ppm at a ^{1}H Larmor frequency of 600 MHz). The CH_3 system was built around the ^{1}H positions extracted from the same geometry optimised system used to construct the CH_7 spin system, and CH_3 proton offsets were set to +0.6 kHz. The heteronuclear through-bond couplings were equal to 150 Hz. Additionally, only the heteronuclear dipolar couplings were present. Powder averaging was performed using 100 α and β powder angle pairs using the REPULSION averaging scheme and a total of 16 γ-angles. [139] The magnitude of the ^{13}C signal at the end of the τ-π-τ spin-echo period was calculated. For simulations of FSLG, ^{1}H nutation frequencies of 102.06 kHz or 220.45 kHz were employed, and the spin-echo modulation curve recorded over 128 points using a 2τ increment of 800 μs, using a spinning frequency of 10 kHz. FSLG *rf* nutation frequencies were selected so as to achieve rotor-synchronisation, which significantly decreases calculation times. Simulations employing eDUMBO-1_{22} consisted of cycle times of 32 μs , 24 μs and 16 μs, and each phase change occurred at intervals of 100 ns. The corresponding ^{1}H nutation frequencies are stated within each figure caption. The 32 μs and 16 μs eDUMBO-1_{22} cycle times coincided with MAS frequencies of 20.833 kHz, unless otherwise stated, with a 2τ increment of 192 μs (3 and 6 cycles), whereas the 24 μs eDUMBO-1_{22} cycle time coincided with a spinning frequency of 25 kHz in order to avoid integer ratios between the cycle time and rotation period and a 2τ increment of 240 μs (5 cycles). All simulations presented were processed using GSim software. [140] A representative input file can be found in the Appendix A.1.

4.3.2 Two-spin simulations

Two-spin CH simulations were initially performed without homonuclear decoupling. This was to establish the behaviour under a J coupling only, for comparison to later simulations, where homonuclear decoupling is applied. Fig. 4.7 show simulated spin-echo curves for a CH spin pair with a heteronuclear dipolar coupling and a heteronuclear through-bond coupling of 150 Hz. When MAS is included the heteronuclear dipolar coupling is averaged over complete rotor periods, and cosine modulation under a J coupling only occurs. An absence of MAS results in rapid dephasing of signal. If the

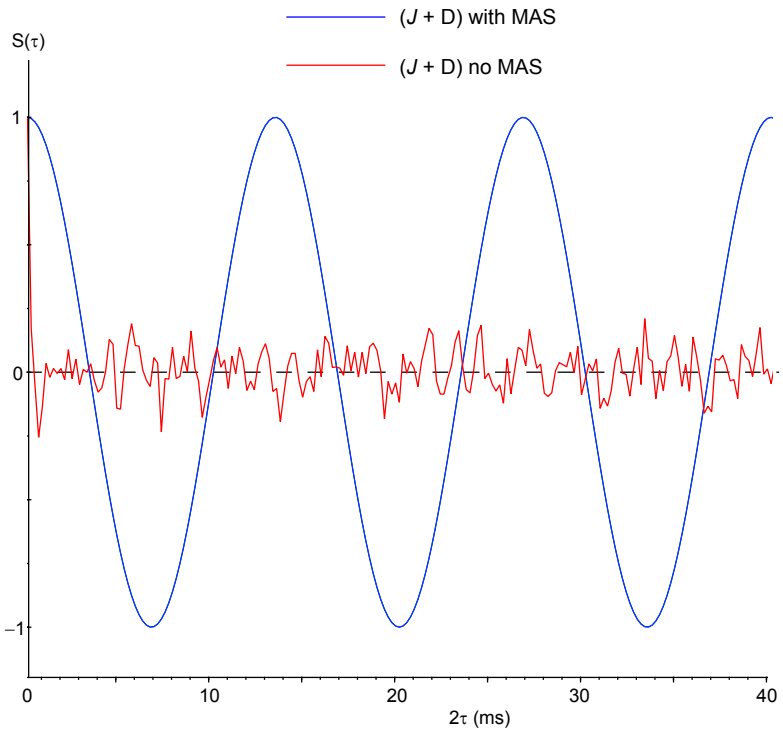

Figure 4.7: ^{13}C-^{1}H spin-echo simulations recorded at a ^{1}H Larmor frequency of 600 MHz for a CH spin pair with a J coupling equal to 150 Hz. Spin-echo curves were recorded with a heteronuclear dipolar coupling, and comparison made between modulation curves acquired with an MAS frequency of 20 kHz (blue line) and under static conditions (red line).

heteronuclear dipolar coupling is removed and a through-bond coupling only is present, a spin-echo curve would evolve under the through-bond coupling only and would exactly replicate cosine modulation under a J coupling and heteronuclear dipolar coupling under MAS (dashed line in Fig. 4.7). All further simulations include MAS.

Figures 4.8a, b show the effects of introducing homonuclear decoupling during τ upon a CH cosine modulation curve. Separate simulations, applying FSLG and eDUMBO-1_{22}, were performed in order to ensure that effects were not specific to individual homonuclear decoupling schemes. In order to identify the effect of homonuclear decoupling, evolution under a J coupling only is also shown. Introducing homonuclear dipolar decoupling in the absence of a heteronuclear dipolar coupling interaction does not lead to any dephasing of the modulation curve. However, scaling of the isotropic J coupling due to homonuclear decoupling results in a slower oscillation period relative to the case of an absence of homonuclear decoupling, as a later zero crossing point corresponds to a smaller effective coupling. Introduction of a heteronuclear dipolar

coupling when applying homonuclear decoupling results in significant damping of the modulation, that is in addition to the scaling of the isotropic J coupling. Fig. 4.8c, d show the effect that the scaling (blue line) and damping (green line) have upon the corresponding spectra. As the CH spin pair has a single through-bond J coupling, a doublet pattern is observed with a splitting equal to the effective coupling. ^{13}C isotropic chemical shifts are refocused by spin-echo sequences, therefore all spectra are centred at 0 Hz. An increase in damping of a FID is reflected by increased spectral deterioration, seen here as a reduction in the resolution of the doublet pattern.

Until recently, it was assumed that the heteronuclear dipolar coupling had little effect upon ^{1}H homonuclear decoupling applied under MAS, however in conjunction with Fig. 4.6 and simulations presented here it is evident that this is not the case. Significant dephasing was observed in modulation curves recorded with FSLG or eDUMBO-1_{22} homonuclear decoupling applied during τ periods.

4.3.3 Third-order effects

Recently, it has been demonstrated that the unexpected dephasing effects presented in sections 4.2.2 and 4.3.2 have their origin in third-order cross-terms which arise from large heteronuclear dipolar couplings being subject to homonuclear decoupling. [1] The derivation of equations 4.4 - 4.7 was performed by Dr. Paul Hodgkinson of Durham University, the full derivations of which can be found in a recently published article. [1] The analysis shown is for FSLG homonuclear decoupling, however, as demonstrated herein similar observations were noted experimentally and by simulation for eDUMBO-1_{22}.

Consideration of an I-S spin system, where I is the irradiated nucleus and S is the observed nucleus, yield different order terms which contribute to the splitting term for a heteronucleus coupled to irradiated protons, i.e., the S spin,

$$\Delta^1 = |J_{IS}\cos\theta| \tag{4.4}$$

$$\Delta^2 = \frac{\sin^2\theta}{\omega_{\text{eff}}}\left((4\omega_I^{(2)}\omega_D^{(2)} - \omega_I^{(1)}\omega_D^{(1)}) + \Omega J_{IS}\right) \tag{4.5}$$

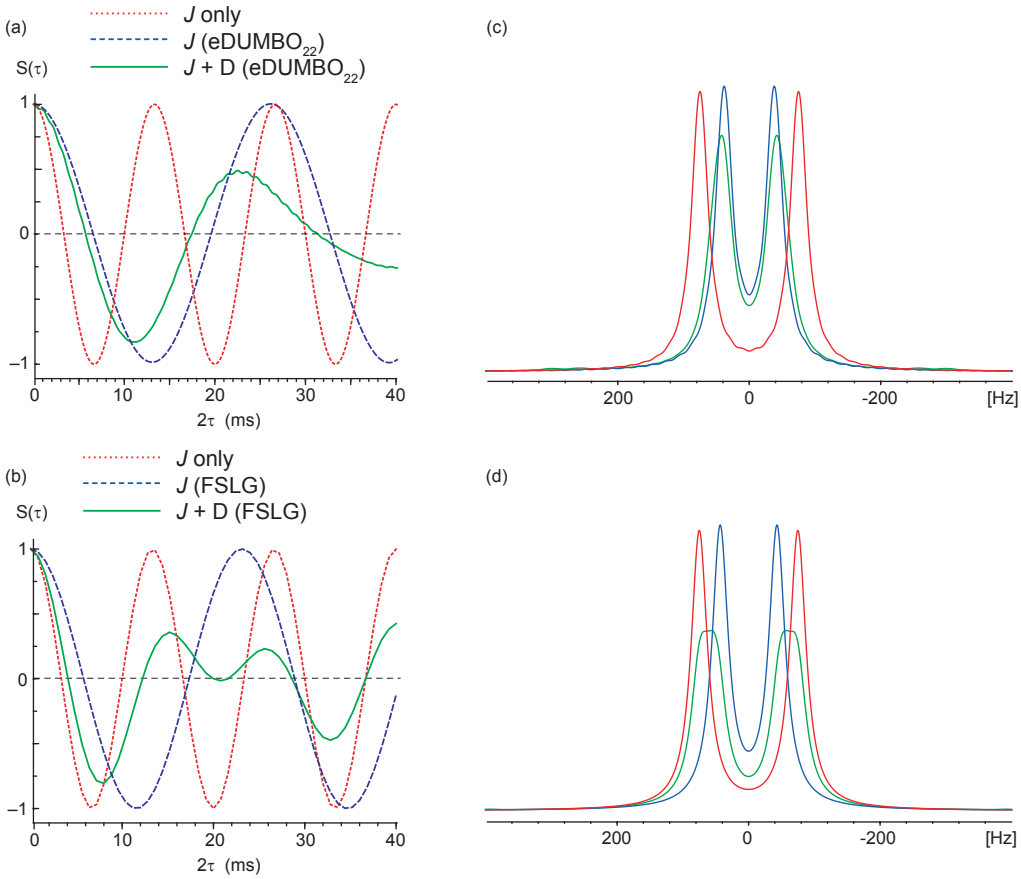

Figure 4.8: ^{13}C ^{1}H spin-echo curves and corresponding spectra for 2 spin simulations of a CH pair with a J coupling of 150 Hz, demonstrating the effect that homonuclear decoupling has upon evolution under heteronuclear couplings, obtained at a simulated ^{1}H Larmor frequency of 600 MHz. (a) is for eDUMBO-1_{22} at an *rf* of 150 kHz over a cycle time of 32 μs during τ periods ($\tau_r/\tau_c = 3/2$), whereas (b) shows behaviour recorded applying FSLG at 102.06 kHz during τ ($\tau_r/\tau_c = 25/4$). Evolution under a J coupling only without the application of homonuclear decoupling (red line) is included for reference. The blue line demonstrates the effect of homonuclear decoupling when the heteronuclear dipolar coupling is not present, and the J coupling is scaled by homonuclear decoupling, indicated by a change in the zero-crossing point. The green line shows the effect of introducing a heteronuclear dipolar coupling when applying homonuclear decoupling, leading to dephasing of the spin-echo curve and deterioration in spectral resolution. (c-d) show the corresponding Fourier transformed spectra obtained from the simulated FIDs in (a) and (b).

$$\Delta^3 = \frac{6\sin^2\theta \cos\theta}{\omega_{\text{eff}}^2} \omega_D^{(2)}(\omega_D^{(1)})^2 \tag{4.6}$$

where $\Delta^{1,\,2,\,3}$ represent the first, second, and third-order contributions to the splitting term on the S spin. J_{IS} is the heteronuclear J coupling interaction in units of Hertz, ω_D is the heteronuclear dipolar coupling and ω_I is the chemical shift of the irradiated nucleus relative to the irradiation offset frequency. The terms $\omega_\Lambda^{(n)}$, where Λ is the interaction of interest (e.g., dipolar coupling, chemical shift) and n is an integer, signifying the order n coefficient, corresponding to the specified tensor describing the interaction Λ. Further information regarding $\omega_\Lambda^{(n)}$ terms can be found in Appendix A of ref. [141]. Note, that $\omega_D^{(0)} = 0$, and that $\omega_I^{(0)}$ is equal to Ω, where Ω is the isotropic spin frequency of the irradiated nucleus relative to the applied *rf* frequency, as introduced in section 2.3.3. θ is the tilt axis angle, which describes the angle at which the spin-component of the magnetisation is aligned relative to the z-axis. For continuous wave heteronuclear decoupling $\theta = 0$, therefore the splitting terms above are zero. For perfect homonuclear decoupling $\theta = 54.7\,^\circ$, as described in section 3.2.2. ω_{eff} is the effective *rf* nutation frequency of homonuclear decoupling, which is equal to $\omega_{rf}/\sin\theta$. As described in section 2.4.4, the heteronuclear dipolar coupling and CSA are averaged under a complete MAS rotation, the above terms detail cross-terms between the heteronuclear dipolar coupling and applied *rf* frequency irradiated on the I spin. Equation 4.4 describes the splitting term to the first-order, and acts to scale the heteronuclear J coupling under decoupling conditions. This is seen in both experiment and simulation via changes in the zero crossing point in spin-echo curves in Fig. 4.4 (experiment) and Fig. 4.9 (simulation).

Inspection of the second-order contribution towards the splitting, described in equation 4.5, reveals that the second-order contribution is inversely proportional to the effective nutation frequency of homonuclear decoupling. The terms described by ${\omega_D}^{(2)}$ are odd-order with respect to the effective nutation frequency, and are consequently removed by frequency switching. In the context of heteronuclear decoupling, these odd-order terms have been shown to correspond to CSA terms. [142] Confirmation that the second-order cross-term, described by the CSA interaction, does not significantly contribute towards dephasing of the signal is seen in Fig. 4.9, where in addition to the curves presented in Fig. 4.8a and b, a spin-echo curve recorded with a ^{1}H CSA interaction of magnitude 2 kHz was included for both eDUMBO-1_{22} and FSLG decou-

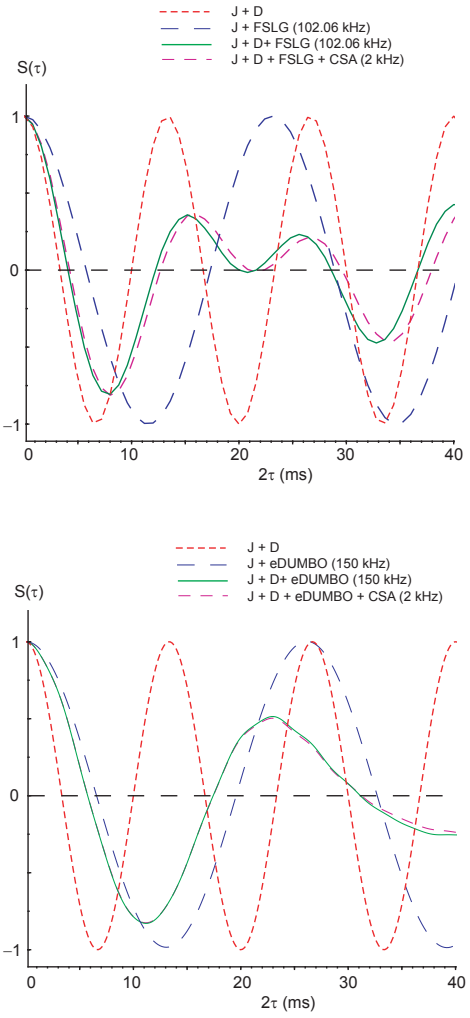

Figure 4.9: ^{13}C-^{1}H simulated spin-echo curves obtained at a ^{1}H Larmor frequency of 600 MHz. The curves are the same as those presented in Fig. 4.8, with the addition of an additional curve recorded with a ^{1}H CSA interaction of magnitude 2 kHz. The effect of the addition of the CSA is minimal. The τ_r/τ_c ratio was equal to 3/2.

pling during τ. Evolution only differs slightly when the ^{1}H CSA interaction is included relative to its absence, therefore the contribution from CSA terms can be considered negligible. The final component in equation 4.5 is dependent upon the offset of the decoupling sequence. For a sequence such as FSLG, each decoupling block is applied with opposite frequency and therefore the second-order term cancels over an even number of cycle periods. Decoupling schemes such as eDUMBO-1_{22} are not applied off-resonance, consequently this term does not significantly effect the magnitude of the splitting term.

The third-order cross-term does not cancel under FSLG as it is even-order relative to ω_{eff}, therefore a sizeable third-order contribution remains (for a C-H through bond interaction, it is approximately 100 Hz). As the effect is purely heteronuclear, it is

not removed by a heteronuclear spin-echo sequence. It is noteworthy that the splitting term is inversely proportional to the square of the effective homonuclear decoupling nutation frequency. The third-order contribution in equation 4.6 has an orientational dependency of:

$$\Delta^3 \propto d^{(2)}_{2,0}(\beta_{PL})[d^{(2)}_{2,0}(\beta)_{PL}]^2 \propto \sin^2\beta_{PL}\ \sin^2 2\beta_{PL} \tag{4.7}$$

where β_{PR} is the angle between the principal-axis of the heteronuclear dipolar coupling and laboratory frame, as was introduced in section 2.4. The implication of equation 4.7 is that the third-order contribution will be at a minimum magnitude when aligned at the magic angle relative to the external field, whereas splitting is at a maximum for β_{PR} values of 0° and 90°.

In Fig. 4.10, modulation curves simulated using FSLG decoupling during τ periods for a range of single crystallite orientations are shown, where the angle β_{PR} is relative to B_0. It is evident that the scaling factor due to homonuclear decoupling is orientationally dependent. Therefore, when recorded over all orientations, as is the case for a powder sample, destructive interference will occur between all possible crystallite orientations, the consequence of which is fast dephasing in the NMR signal. Inspection of different orientations reveals that the fastest oscillation rate occurs at the magic angle, and slowest dephasing at $\beta_{PR} = 90°$, as predicted in equation 4.7.

The data in Fig. 4.10a and b was simulated using different FSLG nutation frequencies of 102.06 kHz and 220.45 kHz, respectively. Separating the modulation into individual crystallite components shows that the range of oscillation rates dramatically decreases at higher *rf* nutation frequencies, thus destructive interference is not as significant when a spin-echo curve is recorded over all orientations. From equation 4.6, it is known that the third-order contribution is inversely proportional to ω^2_{eff}, hence the damping observed decreases as the effective nutation frequency is increased. This is in agreement with experimental observations, where provided suitable cycle times were chosen, an increase in nutation frequency resulted in an increase in dephasing times, i.e., slower dephasing (see Table 4.2).

Figure 4.11 show simulated modulation curves, accompanied by the respective Fourier transformed spectra, simulated with and without homonuclear dipolar cou-

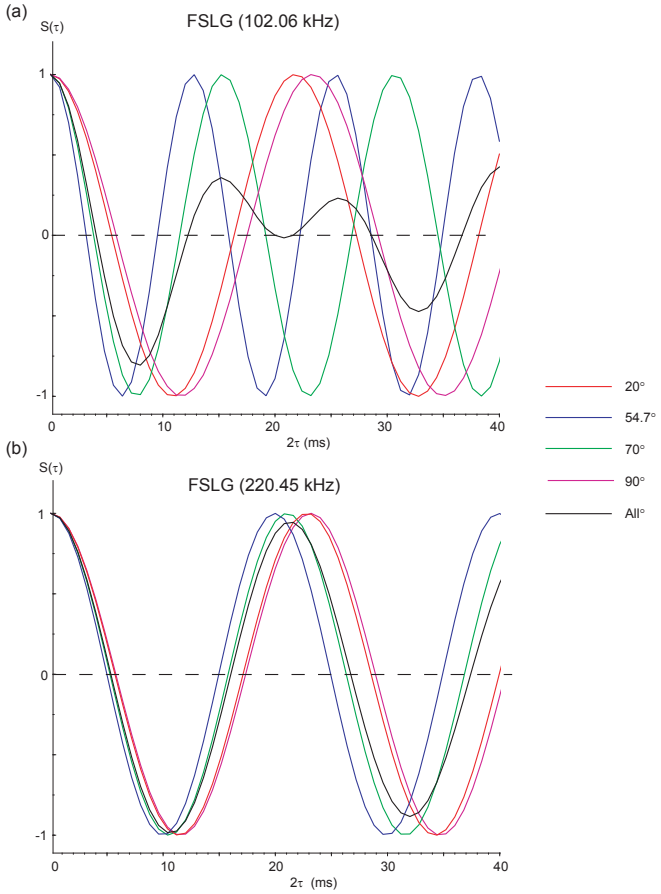

Figure 4.10: ^{13}C-^{1}H (600 MHz) simulated spin-echo curves recorded for a range of single crystallite orientations. FSLG decoupling was applied during τ periods at *rf* nutation frequencies of (a) 102.06 kHz ($\tau_r/\tau_c = 25/4$) and (b) 220.45 kHz ($\tau_r/\tau_c = 27/2$).

plings, applying (a, b) FSLG and (c, d) eDUMBO-1_{22} homonuclear decoupling during τ periods. This is achieved by construction of two separate spin systems, a CH spin pair used in previous simulations, and a CH_7 system based around L-alanine, described in the simulation details above, which includes homonuclear dipolar couplings between proton nuclei. Decoupling cycle times were chosen to maximise performance at higher ω_{eff} values. It is not beneficial to increase the *rf* nutation frequency without changing the time period for a complete decoupling cycle period. This is applicable to both FSLG and eDUMBO-1_{22} examples presented. FSLG cycle times were altered according to theoretical cycle times shown in section 3.2.3, whereas eDUMBO-1_{22} cycle times were chosen and an appropriate *rf* nutation frequency selected by optimising in simulation for a maximum dephasing time.

It is clear that the oscillation rate does not change as additional through-space protons are introduced, only a small increase in modulation damping is seen between

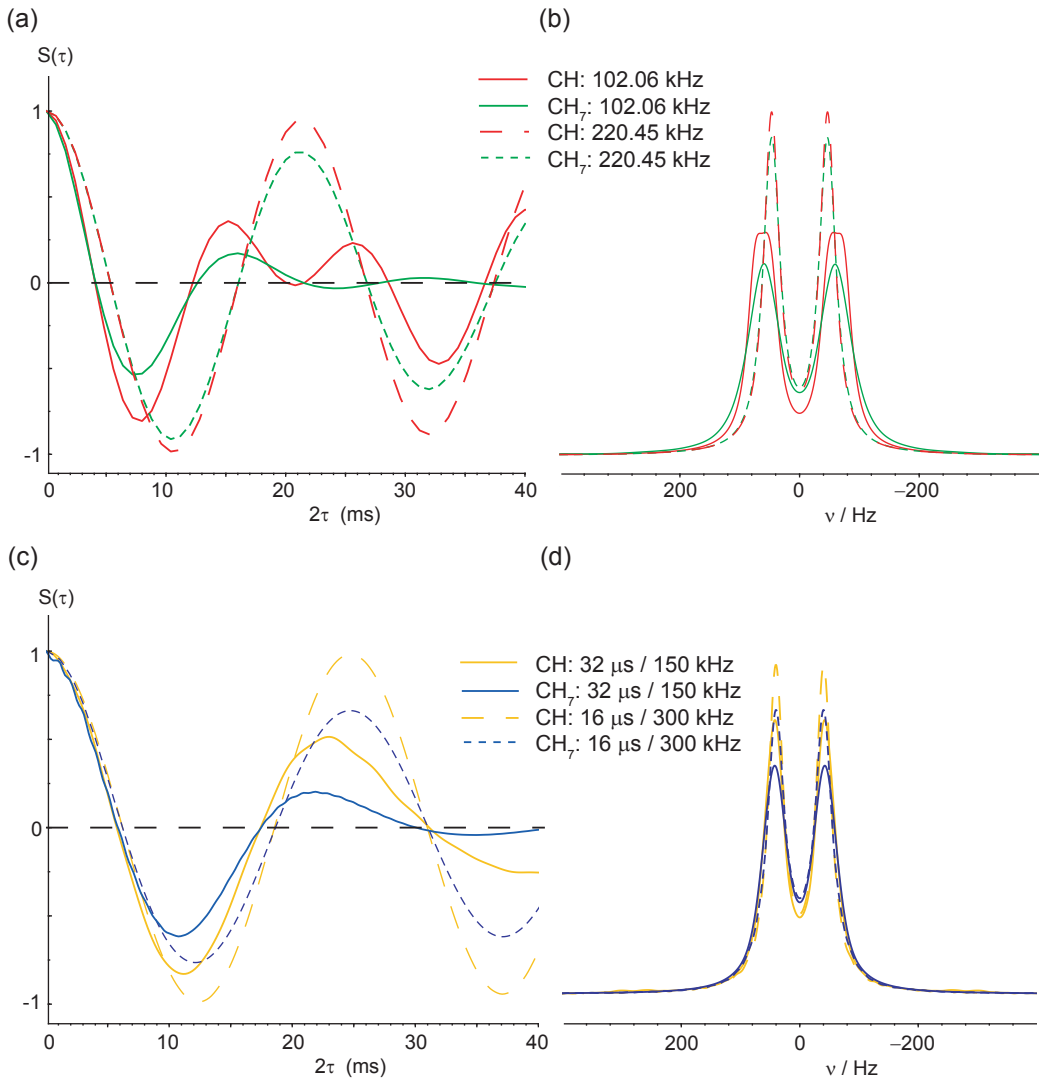

Figure 4.11: ^{13}C-^{1}H (600 MHz, ν_r(FSLG) = 10 kHz, ν_r(eDUMBO-1$_{22}$) = 20.833 kHz) simulated spin-echo curve and corresponding spectra obtained for a CH group with no additional protons, and a CH group with 6 additional protons, where positions are extracted from a geometry optimised structure of L-alanine. (a, b) were obtained using FSLG at *rf* nutation frequencies of 102.06 kHz (τ_r/τ_c = 25/4) and 220.45 kHz (τ_r/τ_c = 27/2). (c, d) were obtained using eDUMBO-1$_{22}$ at *rf* nutation frequencies of 150 kHz (32 μs cycle time, τ_r/τ_c = 3/2) and 300 kHz (16 μs cycle time, τ_r/τ_c = 3)

the 2-spin and 8-spin cases. Reassuringly, this demonstrates that the homonuclear decoupling does average out strong homonuclear proton dipolar couplings, and that a significant proportion of dephasing is attributed to the effects of heteronuclear dipolar couplings when homonuclear *rf* decoupling is applied. Comparison between 2-spin and 8-spin models demonstrate the validity of using 2-spin systems in earlier simulations, as the scaling of the isotropic couplings is not effected; only a small additional damping factor is seen as additional protons are introduced to the spin system.

Further insight into the relationship between eDUMBO-1_{22} cycle time and nutation frequency is revealed by Fig. 4.12. For a CH spin pair, the relationship between the eDUMBO-1_{22} decoupling cycle time and ω_{eff} was investigated. A decrease in scaling of the through-bond coupling as the nutation frequency is increased is noted for all cycle times, which is in general agreement with experimental observations. Furthermore, dephasing times do not increase indefinitely with an increase in *rf* nutation frequency. In Fig. 4.12a, where a 32 μs eDUMBO-1_{22} cycle time is employed, best performance is found at 150 kHz, seen by the maximum negative inversion of the spin-echo curve, corresponding to a longer T_2' dephasing time. Higher *rf* nutation frequencies then lead to a decrease in T_2' dephasing times until the modulation curve no longer inverts, thus restricting identification of a J-splitting. However, it is noteworthy that higher nutation frequencies do result in an improvement in performance provided a suitable decoupling cycle time is chosen, as seen when cycle times are decreased to 24 μs and 16 μs and the *rf* nutation frequency correspondingly increased, as demonstrated in parts (b) and (c). Inspection of Fig. 4.12 also reveals that the range of oscillation rates also decreases for the shorter cycle times. When spin-echo curves are obtained using a 32 μs eDUMBO-1_{22} cycle time, the range of effective couplings over a ω_{eff} range of 50 kHz is greater than the range of effective couplings observed when using a 16 μs eDUMBO-1_{22} cycle time obtained over a ω_{eff} range of 100 kHz. This concurs with the experimental observations in Fig. 4.4, where using a 24 μs cycle time relative to a 32 μs cycle time expanded the range of *rf* nutation frequencies where dephasing times remained favourable.

As has been noted above, increasing *rf* nutation frequencies combined with the correct choice of the decoupling cycle time decreases the magnitude of third-order cross-terms which contribute towards dephasing. Further evidence of the effect of strong

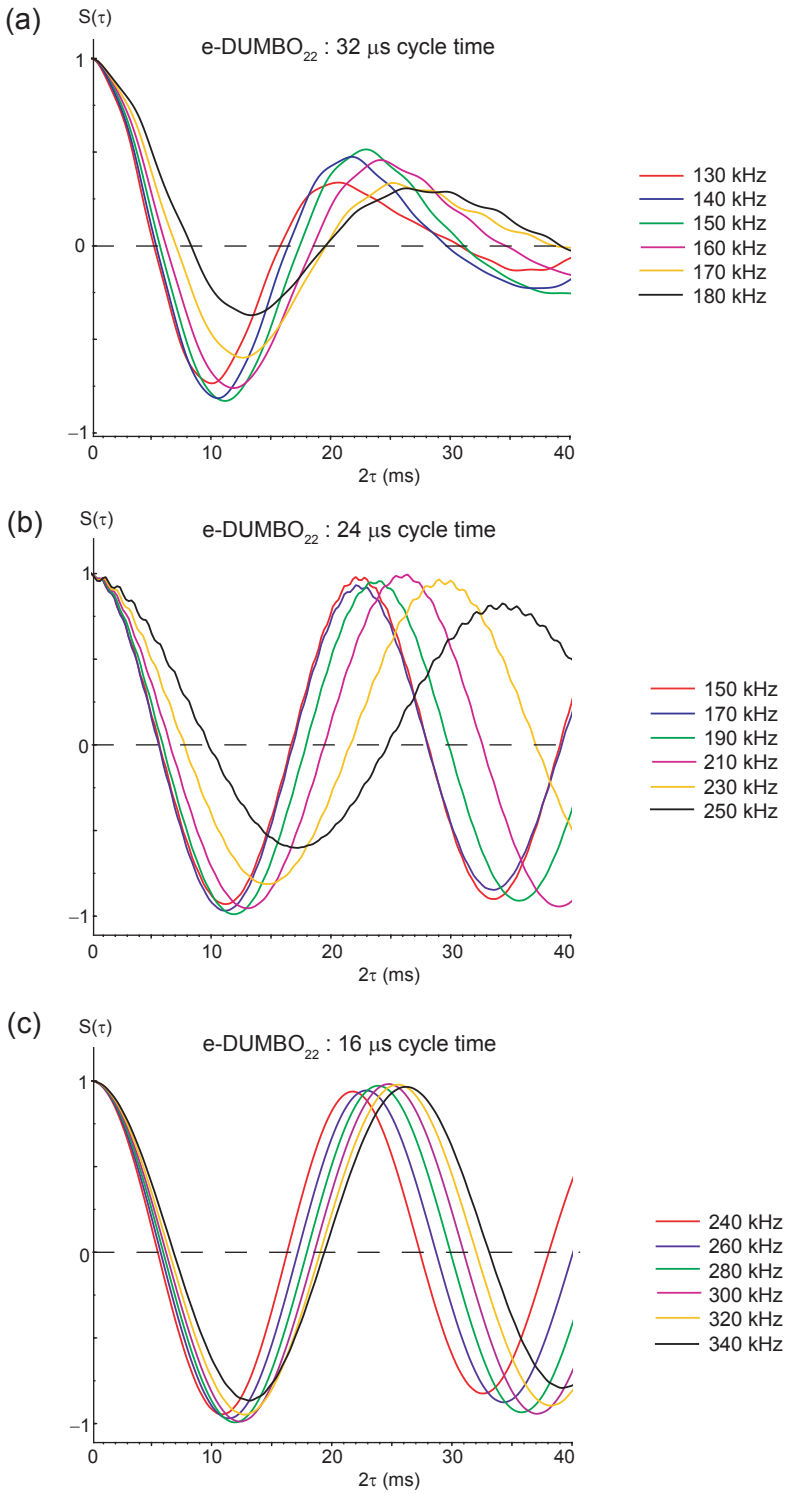

Figure 4.12: Simulated ^{13}C-^{1}H spin-echo curves obtained for a CH group employing eDUMBO-1_{22} decoupling during τ periods, at a ^{1}H Larmor frequency of 600 MHz. (a) Obtained using a 32 μs eDUMBO-1_{22} cycle time at an MAS frequency of 20.833 kHz ($\tau_r/\tau_c = 3/2$), (b) a 24 μs eDUMBO-1_{22} cycle time obtained at an MAS frequency of 25 kHz ($\tau_r/\tau_c = 5/3$), (c) 16 μs eDUMBO-1_{22} cycle time obtained at an MAS frequency of 20.833 kHz ($\tau_r/\tau_c = 3$).

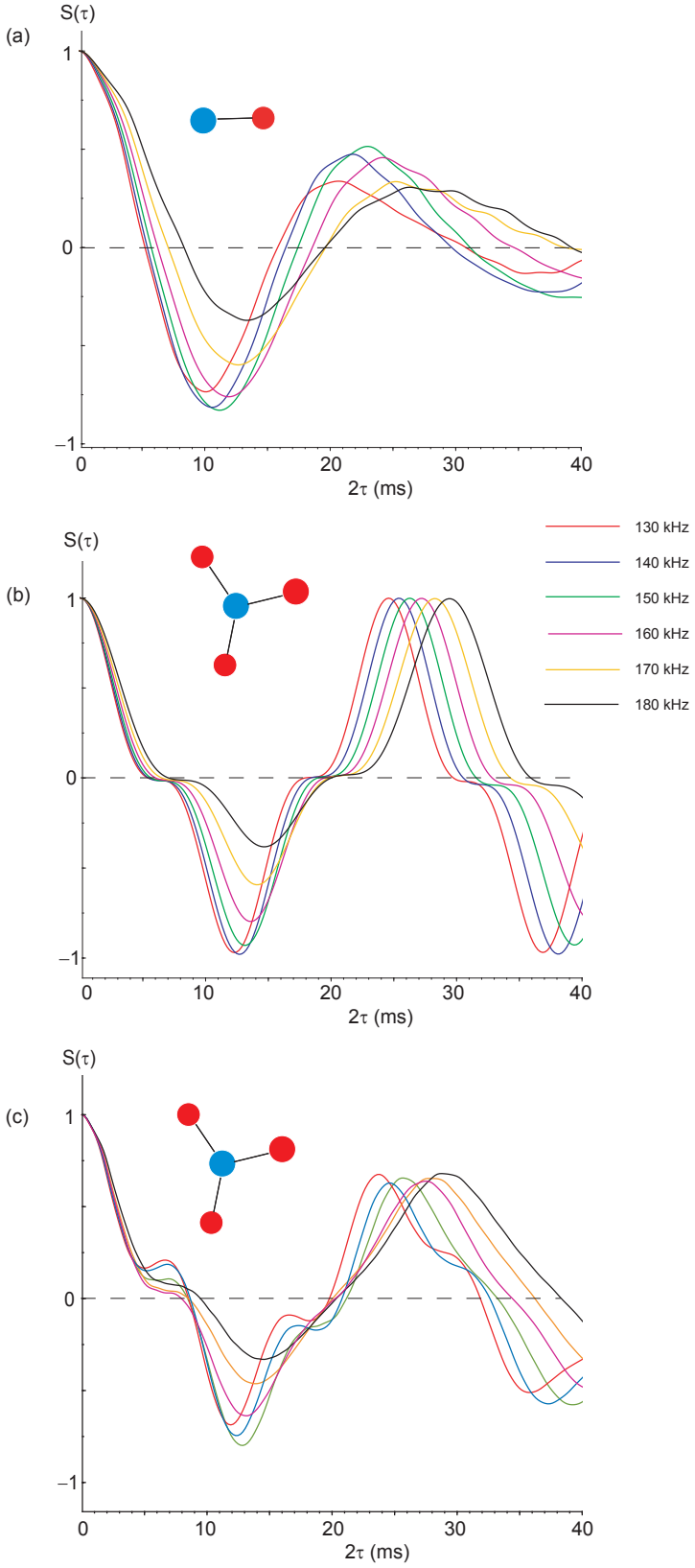

Figure 4.13: Simulated ^{13}C-^{1}H spin-echo curves obtained for (a) a CH group and (b-c) a CH_3 group obtained using a 32 μs eDUMBO-1_{22} cycle time during τ periods, at a ^{1}H Larmor frequency of 600 MHz. The τ_r/τ_c ratio for all modulation curves was 3/2. (b) Heteronuclear dipolar couplings only were included, whereas (c) was obtained with all dipolar couplings present. All J coupling values were 150 Hz.

heteronuclear dipolar couplings is observed through comparison between CH and CH_3 modulation. As protons in a CH_3 group are subject to motional averaging at room temperature, [143, 144] the magnitude of heteronuclear dipolar couplings is reduced in a methyl group relative to a CH spin pair, and therefore the dephasing effect is expected to be less pronounced.

Figure 4.13b, c presents simulated heteronuclear spin-echo modulation curves obtained using coordinates taken from a CH_3 group in L-alanine, with proton exchange included. Spin-echo curves were obtained for a range of *rf* nutation frequencies using eDUMBO-1_{22} decoupling during τ periods, with a cycle time of duration 32 μs. Additionally, CH spin-echo curves obtained at identical eDUMBO-1_{22} *rf* nutation frequencies are included for reference in part a. Fig. 4.13b includes heteronuclear dipolar couplings and a heteronuclear J coupling, whereas Fig. 4.13c includes both heteronuclear and homonuclear couplings. Interestingly, scaling factors were not as varied over the same range of nutation frequencies for a CH_3 group relative to a CH group. This provides further evidence that the dephasing effect described herein is dependent upon strong heteronuclear dipolar coupling, therefore motional averaging, which partially averages heteronuclear dipolar couplings, reduces the dephasing effect and range of scaling factors. Additionally, although the introduction of homonuclear dipolar couplings increases spectral deterioration, the zero crossing points are not adversely effected by the presence of homonuclear dipolar couplings.

4.4 Conclusions

Experimental and simulation results clearly demonstrate that the heteronuclear dipolar coupling is not inactive when subject to homonuclear *rf* decoupling; the interaction results in additional signal dephasing in heteronuclear spin-echo experiments. This was particularly evident experimentally in Fig. 4.6 and from simulation in Fig. 4.8. Homonuclear decoupling is an experimentally demanding technique to set up, therefore previous observations may have been assumed to be a result of poor adjustment of decoupling parameters. In addition to analogous effects demonstrated elsewhere, [1, 145] dephasing effects were particularly evident when comparing extracted dephasing times in heteronuclear and homonuclear spin-echo experiments. When homonuclear

decoupling is applied, dephasing times were observed to shorten by approximately a factor of 3 relative to solely applying heteronuclear decoupling, as observed in Fig. 4.6.

The interaction between heteronuclear dipolar coupling and homonuclear decoupling contributes a sizeable, orientationally dependent third-order cross-term. Therefore, in a powder sample destructive interference occurs when a FID is recorded, as all possible crystallite orientations are present.

The third-order splitting term is inversely proportional to the decoupling *rf* nutation frequency, as was evident in simulations. Experimental evidence of this was limited as higher ^{1}H *rf* nutation frequencies ($\nu_{rf} > 150$ kHz) are not routinely available. However, when a 24 μs eDUMBO-1_{22} cycle time was applied experimental dephasing times slightly increased relative to a 32 μs eDUMBO-1_{22} cycle time, which performed best at lower *rf* nutation frequencies (see Tables 4.1 and 4.2). As advances in hardware technology are introduced, specifically access to higher *rf* nutation frequencies, then third-order effects are expected to diminish accordingly, provided that decoupling sequences that work well at higher *rf* and under MAS are available. Additionally, during investigation of eDUMBO-1_{22} and FSLG decoupling sequences, it was found that for higher *rf* nutation frequencies, provided cycle times were adjusted accordingly, that the range of nutation frequencies that yield acceptable dephasing times is expanded. Consequently, in addition to higher *rf* nutation frequencies diminishing third-order effects, it is also expected that sensitivity to the choice of decoupling nutation frequency will be reduced.

For lower γ nuclei, such as ^{15}N, third-order cross terms are expected to decrease in magnitude, as heteronuclear dipolar couplings are reduced. The consequence of smaller heteronuclear dipolar couplings was observed in spin-echo curves of methyl groups, where motional averaging reduces the effective heteronuclear dipolar couplings, consequently extending dephasing times and increasing the range of *rf* nutation frequencies where improved performance was available (see Tables 4.1 and 4.2). It was evident from simulation that the presence of homonuclear decoupling remains an important consideration for heteronuclear correlation experiments, as seen for comparisons between CH and CH_7 systems. The introduction of homonuclear dipolar couplings does not influence the zero crossing point, therefore validating the use of two-spin CH simulations to establish the effect of homonuclear decoupling upon heteronuclear

interactions.

The future development of new homonuclear decoupling sequences capable of cancelling the newly identified third-order cross terms whilst maintaining efficient averaging of homonuclear dipolar couplings is expected to be heavily dependent upon optimisation via simulation. Due to the complexity of many homonuclear decoupling sequences, and the apparent requirement for higher *rf* nutation frequencies, simulations are useful as interactions that are inactive can be ignored. Furthermore, access to higher *rf* nutation frequencies and spinning frequencies not readily obtainable in experiment allows the user to develop sequences with future developments in mind.

CHAPTER

FIVE

^{15}N SPECTRAL EDITING TECHNIQUES

5.1 Introduction

Nitrogen functional groups are often utilised in the pharmaceutical industry due to their pharmalogical properties. [81] Therefore, correct identification of different functional groups is crucial in understanding pharmalogical properties, both chemical and physical, throughout the drug design process.

As discussed in the introduction, improvements in physical properties, such as solubility, stability and bio-availability, of an API can be achieved through formation of a multi-component delivery form, the most common of which are crystalline salts. Protonation of an amine group by an acid typically improves stability and in some cases can offer access to a crystalline form where the free base is known to be in an amorphous form, which can be undesirable as the amorphous state is typically thermodynamically unstable. Alternatively, cocrystal formations, where molecular components remain in their non-ionised form, have been shown to improve physical properties such as solubility and stability. [84] For weaker ionising acid-base reactions it may not be clear if proton transfer has occurred, or if the constituents remain neutral and a cocrystal has formed. For ambiguous cases such as these, definitive identification of proton transfer is an important patent and regulatory concern. Tracking of proton transfer in solution is typically measured through pK_a values: an empirical rule states that the pK_a of an acid should be at least 2 pH units lower than the pK_a of the base compound in its free base form. [146] However, accurate determination of pK_a is not straightforward, nor

does protonation in the solution state always coincide with salt formation at the same nitrogen position in the solid state. [147]

A simple method of assigning ^{15}N resonances is comparison to known shifts in the solution state. However, this does not account for differences between solution and solid phases, which often are the most interesting features. It has been shown that the ^{15}N chemical shift of a protonated nitrogen site will often shift upfield when protonated relative to the free base. [148, 149] However, this does not account for shifts owing to a different polymorphism state. Furthermore, the size of the up-field shift can be small, or even in some cases the shift could be downfield. Additionally, a more comprehensive method able to identify the number of attached protons in any material, not limited to pharmaceutical salts, is desirable.

Current solid-state NMR methodologies applied to probe the protonation of nitrogen functional groups include dipolar dephasing, [150] and spectral editing methods applying different CP contact times to establish the immediate proton environment. [149] Initial dipolar dephasing techniques were demonstrated for the identification of protonated and non-protonated CH_n groups, [151–155] however as both ^{13}C and ^{15}N nuclei are spin-$\frac{1}{2}$ spectral editing techniques are largely interchangeable between ^{13}C-^{1}H and ^{15}N-^{1}H cases, as demonstrated by application of ^{15}N dipolar dephasing experiments to pharmaceutical compounds. [156, 157] Dipolar dephasing techniques are limited by motional effects which disrupt polarisation transfer (e.g., methyl groups, NH_3^+ groups), therefore complicating the identification of different moieties. Furthermore, dipolar dephasing experiments are often unable to discriminate between a protonated nitrogen and a non-protonated nitrogen which resides in a proton rich environment, due to both types of nitrogens being similarly dephased by the immediate proton environment, in addition to being unable to discriminate between NH and NH_2 groups.

Through-bond NH couplings are not susceptible to motional effects nor are they influenced by close-proximity through-space couplings. An adaption of the $^{1}J_{13C\text{-}1H}$ spin-echo experiment modulated by scalar couplings, which was presented in chapter 4, has been modified for ^{15}N spectral editing. $^{1}J_{15N\text{-}1H}$ spectral editing is able to distinguish between different numbers of directly attached protons to a nitrogen site, and therefore readily differentiate an ionised from a non-ionised nitrogen species for all amine moieties. As was discussed in section 3.3.2, ^{15}N species with two directly

attached protons will always have a positive spin-echo modulation, whereas an inversion in signal will be observed for ^{15}N species with one or three directly attached protons after a suitable τ increment.

The suitability of $^{1}J_{15N\text{-}1H}$ spectral editing in pharmaceutical development is demonstrated here by the characterisation of a range of pharmaceutical compounds with interesting chemical properties and a range of different ^{15}N functional groups. Accurate measurement of unscaled ^{15}N-^{1}H J coupling values falls outside the scope of this thesis. As through-bond couplings are isotropic, they are subject to a scaling factor when homonuclear dipolar decoupling is applied, as detailed in section 3.2.5, and observed experimentally in chapter 4, therefore complicating the calculation of the magnitude of NH through bond couplings. Selection of a suitable τ increment to observe any inversion was aided from knowledge of the spin-echo curve for ^{15}N labelled L-histidine HCl.H_2O in Fig. 5.1. If no inversion was observed then further spectra were recorded at different τ increments to confirm the signal is not at, or close to, zero intensity in a J modulated spin-echo curve. If an inversion is noted, then this indicates that the ^{15}N site cannot have an even number of attached protons.

5.2 Experimental and Computational Details

5.2.1 Sample preparation

Labelled L-histidine HCl.H_2O was purchased from Cambridge Isotopes Laboratories and used without further purification. The protonation state in L-histidine HCl.H_2O is known from the single-crystal structure diffraction structure (CSD refcode:HISTCM01), [158] and from the ^{1}H chemical shift values in the solid state. The dipeptide β-AspAla was purchased from Bachem (Bubendorf, Switzerland) and used without further purification. The protonation state of the dipeptide β-AspAla is identified from the single-crystal diffraction structure (CSD refcode:FUMTEM), [159] and from the ^{1}H chemical shift values in the solid-state. Cimetidine Form A, tenoxicam form III and pazopanib were provided by GlaxoSmithKline.

5.2.2 Solid-State NMR

^{15}N spectral editing experiments were recorded using a Bruker Avance-III spectrometer operating at ^{1}H and ^{15}N Larmor frequencies of 500.1 and 50.7 MHz, respectively (B_0 = 11.7 T). A narrow-bore 4 mm HX double-resonance probe was used with an MAS frequency of 5 kHz, except spectra for the dipeptide β-AspAla, which were obtained using a spinning frequency of 10 kHz. All experiments were performed at room temperature, unless otherwise stated. ^{1}H 90° and 180° pulses were applied for durations of 2.5 μs and 5 μs, respectively, and a ^{15}N 180° pulse of duration 14 μs was used. ^{15}N magnetisation was achieved using a cross-polarisation ramp of magnitude 50% to 100%, with a contact time of 1 ms for L-histidine HCl.H_2O and the dipeptide β-AspAla, and 5 ms for all remaining compounds. The contact time was optimised in order to maximise the magnetisation transfer to quaternary nitrogen sites. ^{1}H -^{1}H homonuclear and ^{1}H -^{15}N heteronuclear decoupling schemes were both applied with a ^{1}H nutation frequency equal to 100 kHz. Homonuclear decoupling during spin-echo periods utilised eDUMBO-1_{22} consisting of 320 pulses of duration 100 ns. As ^{15}N-^{1}H dipolar couplings, relative to CH dipolar couplings, are of a smaller magnitude if considered over the same distance, then effects introduced in chapter 4 are not as pertinent. However, the highest achievable ^{1}H *rf* was chosen, with the corresponding cycle time selected accordingly, in order to combat the effects described in chapter 4. Pre-pulses of length 1.5 μs were applied before and after each homonuclear decoupling period. Heteronuclear decoupling during t_2 was achieved using SPINAL-64, [112] with each pulse of duration 5.1 μs. A nested 8-step phase cycle was used to achieve changes in coherence of $\Delta p = \pm 1$ on the initial ^{1}H pulse (2 steps) and $\Delta p = \pm 2$ (4 steps) for the ^{15}N 180° pulse. A proton offset of 20 ppm was applied throughout. The number of co-added transients and recycle delay used for each spectrum can be found in their respective figure captions. ^{15}N spectral editing experiments were referenced to uniformly ^{15}N and ^{13}C labelled L-histidine.HCl.H_2O, which has an NH_3^+ resonance at -333.1 ppm, corresponding to a primary reference of CH_3NO_2 at 0 ppm.

5.2.3 Computational

First-principles calculations were performed using the academic release of CASTEP version 4.3, which implements density-functional theory using a planewave basis set.

All calculations presented used a PBE exchange-correlation functional [160] and on-the-fly pseudopotentials. Initial geometry optimisation of all atoms was performed by starting with the X-ray single-crystal structure (obtained from the CSD database, ref-code CIMETD, Z = 4, i.e., 132 atoms in the unit cell) [161]. The geometry optimisation and NMR calculations used a cut-off energy equal to 800 eV and a k-point spacing of $0.1 \times 2\pi$ Å^{-1} with a Monkhurst-Pack grid.

5.3 Experimental Results

5.3.1 L-histidine HCl.H_2O

Calibration of the $^1J_{15N\text{-}1H}$ spectral editing sequence was performed on ^{15}N singly labelled, at the ϵ^2 site (highlighted in Fig. 5.1), L-histidine HCl.H_2O. An important consideration during calibration was the manner in which eDUMBO-1_{22} decoupling during τ periods was implemented. Suitable synchronisation between the homonuclear decoupling cycle time (τ_c), the time for a complete rotation of the rotor (τ_r), and the total τ increment applied in the spin-echo is required. If the spin-echo τ period is not rotor-synchronised then inhomogeneous field effects are not refocused. Furthermore, as demonstrated in chapter 4, if τ_r/τ_c is a small integer ratio then destructive signal interference occurs. The consequence of not meeting the latter requirement is not demonstrated within this chapter (cycle times and spinning frequencies were chosen to avoid this condition). If synchronisation between the τ increment and rotor period is not met, then the effects are clearly seen in Fig. 5.1. For the red line, integer ratios between the 2τ increment and rotor period were used and a smooth oscillation is obtained. It is evident from the black line, where many of the 2τ increments were not rotor synchronised, that a rapid oscillation of the modulation is observed. Corresponding 2τ increments between the two modulation curves do agree with each other. The oscillation can severely inhibit correct assignment of a modulation curve, and if severe enough could lead to incorrect identification of an NH_n moiety.

The interaction between the heteronuclear dipolar coupling and homonuclear decoupling discussed in the previous chapter is less pronounced when studying ^{15}N compared to ^{13}C, owing to the smaller gyromagnetic ratio of ^{15}N relative to ^{13}C (approximately 2.5 times smaller). However, as demonstrated in chapter 4, choice of

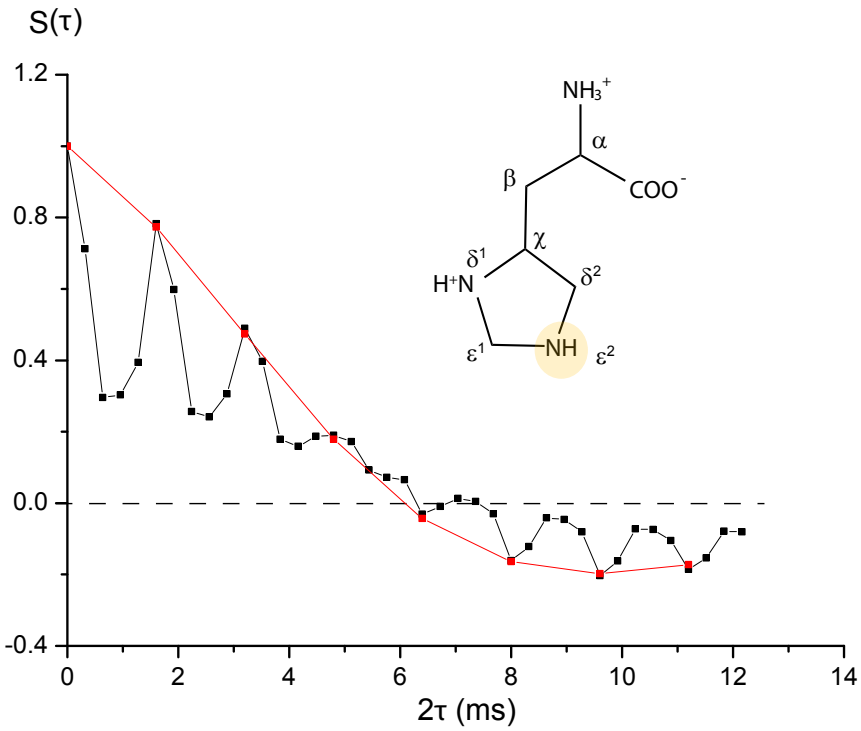

Figure 5.1: ^{15}N spin-echo curves for the down-field NH group in L-histidine.HCl.H_2O (highlighted in the skeletal structure) showing the effect of different 2τ increments, all points were recorded at a ^{1}H Larmor frequency of 500 MHz. The black line consists of the peak heights of spectra recorded at 2τ intervals of 160 μs, where each point was recorded using 16 co-added transients. The red line was recorded at intervals of 2τ intervals of 800 μs, and each point was recorded using 32 co-added transients. The MAS frequency was 5 kHz, corresponding to a duration of 200 μs for one rotor rotation period. One complete eDUMBO-1_{22} cycle was of duration 32 μs.

suitable non-integer τ_r/τ_c ratios is an important experimental set-up consideration. The modulation in the red curve in Fig. 5.1 clearly follows the expected modulation of an NH group, i.e., the signal is negative after a suitable τ increment.

5.3.2 Dipeptide β-AspAla

In order to assess the viability of the editing technique at natural abundance, $^1J_{15N\text{-}1H}$ spectral editing experiments were performed for the dipeptide β-AspAla. This dipeptide contains two chemically distinct nitrogen sites, an NH and NH_3^+, as seen in the structure in Fig. 5.2d. Efficient proton homonuclear decoupling was found to be particularly important in obtaining high quality spectra, as this increases T_2' dephasing times, if dephasing is too rapid then no modulation signal can be observed.

A ^{15}N CPMAS spectrum presented in Fig. 5.2a shows that for a relatively short contact time of 1 ms both resonances are clearly present, suggesting both sites have

proton(s) in close-range proximity. Although for this particular sample the different nitrogen functional groups are known, for an unknown sample the number of attached protons would not be identifiable from a CPMAS spectrum alone. It is feasible that the nitrogen species could be in close proximity to proton(s) without being directly bonded to a proton.

Figure 5.2b and c show $^{1}J_{15N\text{-}1H}$ spectral editing spectra obtained at 2τ increments of 12 ms and 18 ms. After a suitable 2τ increment of 12 ms the NH signal, seen at an approximately -250 ppm, is clearly inverted, indicating the presence of a single through-bond coupling. The lower ppm ^{15}N site remains positive at the shorter 2τ period. After a longer 2τ increment of 18 ms, the NH_3^+ signal inverts as the number of attached protons is an odd number. The NH signal remains negative, however the magnitude of the inversion is now less than that of the NH_3^+ signal.

5.3.3 Cimetidine

The calculated and experimental ^{15}N chemical shifts are listed in Table 5.1 and are observed to be in good agreement. The root mean squared difference between experimental and calculated shifts is 1.1 ppm. If peaks are assigned from comparison to calculated shifts only it would be difficult to assign peaks that have similar isotropic chemical shift values, such as between N12 and N15. Therefore, additional discrimination can be achieved using spectral editing techniques. Fig. 5.3 presents $^{1}J_{15N\text{-}1H}$ spectral editing spectra of cimetidine recorded for a range of 2τ values at an MAS frequency of 5 kHz. Spinning sidebands were assigned by recording spectra at different MAS frequencies, and are marked with an asterix. Only spectral regions of interest are shown. The initial ^{15}N CPMAS experiment shown in Fig. 5.3a confirms the presence of six nitrogen sites, as expected from an inspection of the skeletal structure. Peak assignments were aided by a combination of GIPAW calculated ^{15}N chemical shifts and $^{1}J_{15N\text{-}1H}$ edited spectra.

The three nitrogens N1, N12 and N14 are not protonated and therefore their ^{15}N CPMAS signal intensity is less than that of the other three resonances, N3, N10 and N15, which have a directly-bonded proton in close proximity to enhance ^{15}N polarisation. N1, N12 and N14 are still observed as the contact time was sufficiently long to allow for sufficient spin diffusion between longer-range NH proximities. However, this

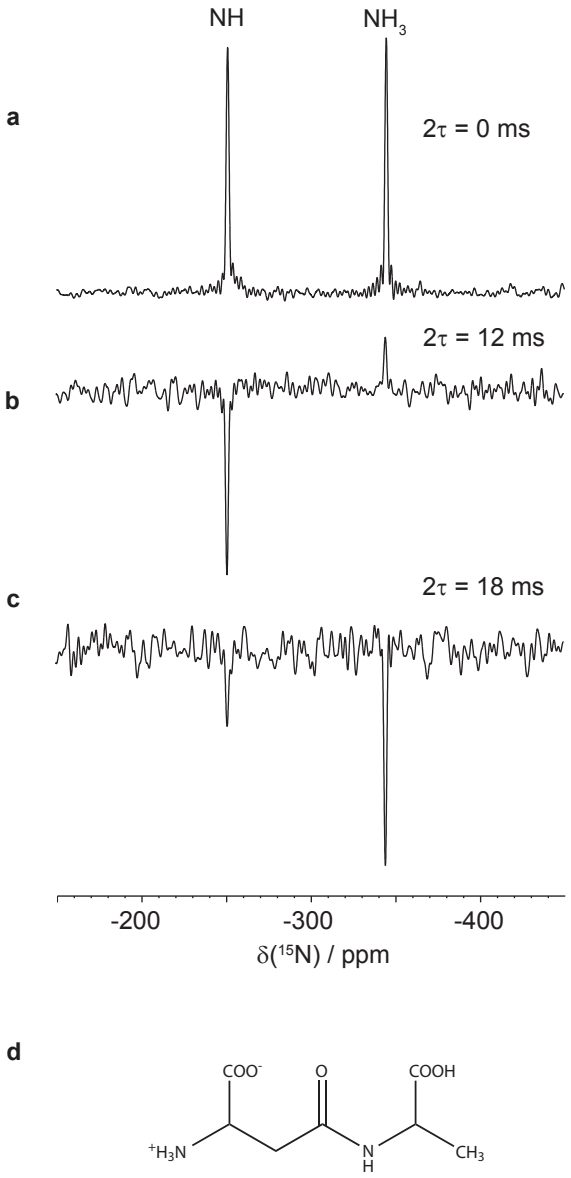

Figure 5.2: (a) ^{15}N CPMAS and (b-c) $^{1}J_{15N\text{-}1H}$ edited spectra obtained for the dipeptide β-AspAla recorded at 2τ spin-echo increments of 12 and 18 ms, respectively. Spectra were obtained at 11.7 T and a MAS frequency of 10 kHz. Experimental times were approximately (a) 11 hours (8192 transients were co-added with a recycle delay of 5 s) and (b) 28 and (c) 78 hours (20564 and 56320 transients were co-added, respectively, each with a recycle delay of 5 s) (d) Structure of the dipeptide β-AspAla.

Table 5.1: ^{15}N GIPAW calculated and experimental isotropic chemical shift values for cimetidine.

Site	$\delta(^{15}\mathrm{N})_{expt}$/ppm	$\delta(^{15}\mathrm{N})_{calc}{}^{a}$ / ppm
N1	−128.1	−132.5
N3	−210.7	−206.6
N10	−284.6	−286.7
N12	−295.4	−296.5
N14	−191.3	−190.0
N15	−297.7	−295.3

[a] $\delta_{iso} = -(\sigma_{iso} - \sigma_{ref})$, where $\sigma_{ref} = -165.2$ ppm. σ_{ref} was calculated from averaging over the sum of $\delta(^{15}\mathrm{N})_{expt}$ and σ_{iso} values, and is in acceptable agreement with a previous value found in first-principles ^{15}N studies. [3]

is not a definitive method to discriminate between different NH_n groups, or to identify a non-protonated nitrogen site which resides in a proton rich environment.

For the initial 2τ interval of 3.2 ms (see Fig. 5.3b), all signals remain positive; an absence of fast dephasing typical of a nitrogen species with two directly attached protons indicates that none of the signals are from a primary amine functional group, consistent with the structure shown. However, dephasing at a significantly faster rate is observed for the N3, N10 and N15 resonances when the τ periods are incremented. Longer 2τ values show clear inversion of the N3 (2τ = 6.4 ms), N10 (2τ = 9.6 ms) and N15 (2τ = 9.6 ms) resonances, confirming that these nitrogen species have an odd number of direct one-bond J coupling(s) to a proton. For the remaining three resonances (N1, N12 and N14), the signal stays positive at all investigated 2τ values, i.e., evolution under only T_2' dephasing is observed.

Using a combination of GIPAW calculation and $^{1}J_{15N\text{-}1H}$ spectral editing methods a full assignment of nitrogen sites in cimetidine has been achieved. For this material, discrimination between N12 and N15 is challenging by assignment from known chemical shift values, or using GIPAW calculated chemical shifts only. Only through utilising a spectral editing technique was it possible to definitively differentiate between N12 (non-protonated ^{15}N species) and N15 (protonated ^{15}N site).

5.3.4 Tenoxicam

As an illustration of the application of the $^{1}J_{15N\text{-}1H}$ spectral editing technique to the confirmation of the protonation state of a nitrogen functional group, a $^{1}J_{15N\text{-}1H}$ spec-

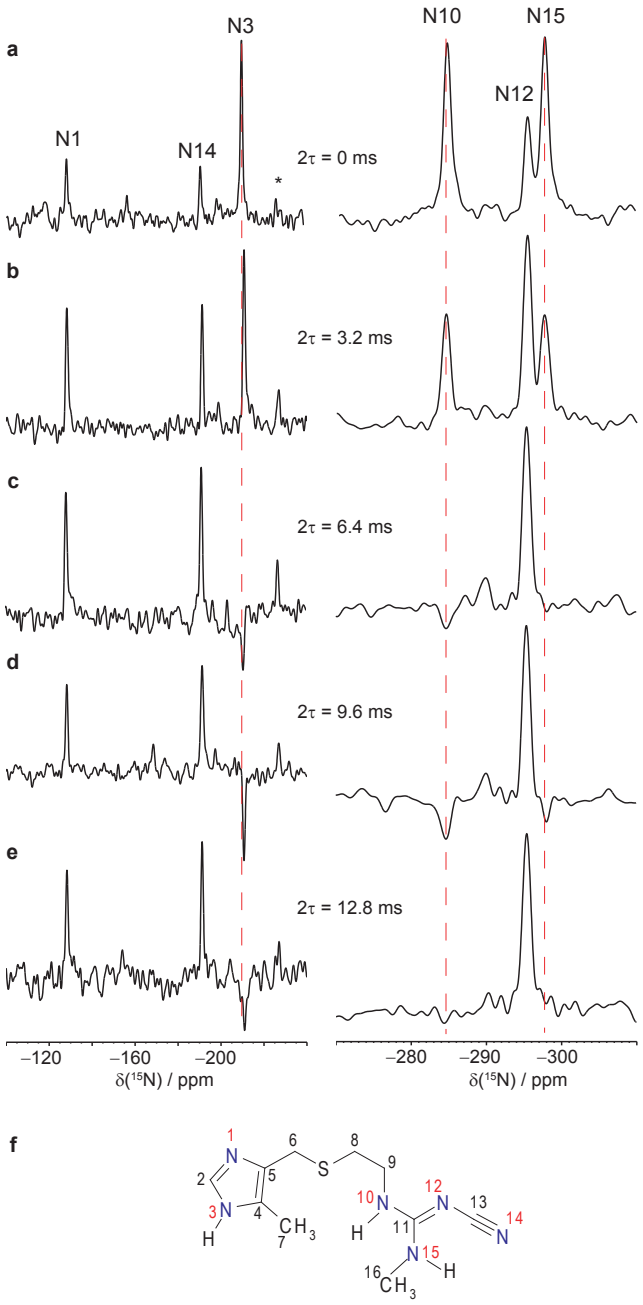

Figure 5.3: (a) ^{15}N CPMAS and (b-e) $^{1}J_{15N\text{-}1H}$ edited spectra of cimetidine recorded for a range of rotor-synchronised spin-echo durations. Only spectral regions of interest are shown. Spinning sidebands are indicated by asterisks (*) and were identified by recording ^{15}N CPMAS spectra at different MAS frequencies. The dashed vertical lines assist in the observation of a zero crossing for a peak due to modulation by a $^{1}J_{15N\text{-}1H}$ coupling. Spectra were obtained at 11.7 T and a MAS frequency of 5 kHz. Experimental times were approximately 3 hours (2048 transients were co-added with a recycle delay of 5 s) and 28 hours (20480 transients were co-added with a recycle delay of 5 s) for (a) and (b-e), respectively. (f) Labelled structure of cimetidine.

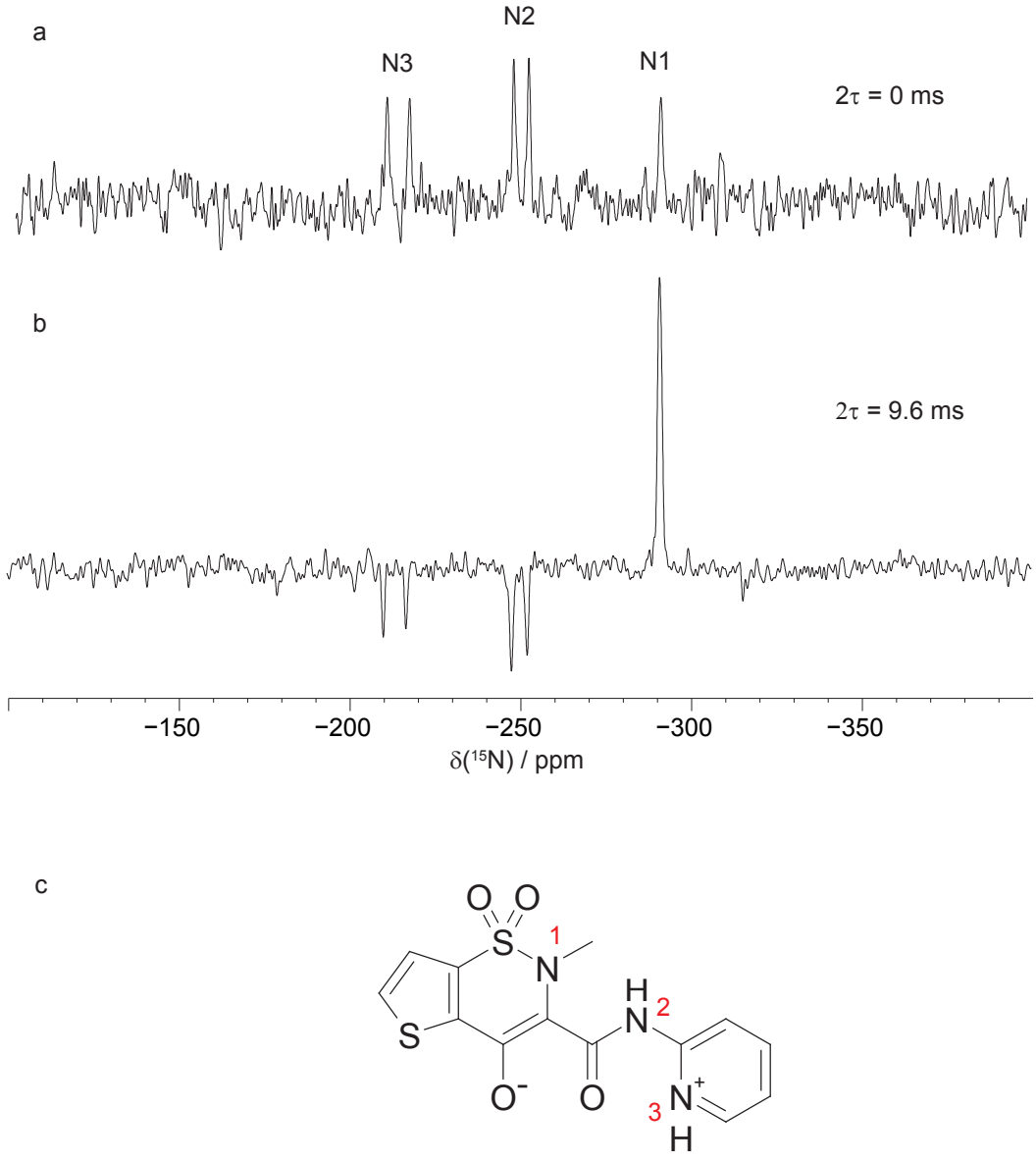

Figure 5.4: (a) ^{15}N CPMAS and (b) $^{1}J_{15N\text{-}1H}$ edited spectrum ($2\tau = 9.6$ ms). Spectra were obtained at 11.7 T and a MAS frequency of 5 kHz. Experimental times were (a) 9 hours (6144 transients were co-added with a recycle delay of 5 s) and (b) 115 hours (8288 transients were co-added with a recycle delay of 50 s). (d) Structure of tenoxicam form III.

tral editing spectrum was recored for tenoxicam form III, [162] a non-steroidal anti-flammatory drug, whose pyridine nitrogen is protonated in the solid state, according to a single-crystal X-ray diffraction (SCXRD) structure, by proton transfer from the acidic phenol group.

A ^{15}N CPMAS spectrum and $^{1}J_{15N\text{-}1H}$ spectral editing spectrum of tenoxicam are shown in Fig. 5.4; the peak assignments have been taken from a previous ^{15}N solid-state NMR study. [163] The observation of two peaks per distinct nitrogen atom (for N2 and N3) is due to the presence of two distinct molecules in the asymmetric unit cell. The inversion of the ^{15}N resonance for the pyridine nitrogen N3 (Fig. 5.4b) unambiguously shows that it is a protonated N^+ species with one covalently bonded proton. Furthermore, it is clear that the amide NH site, labelled N2, has also inverted for the same 2τ increment, confirming a one-bond coupling. Inversion was observed for all four N2 and N3 resonances, demonstrating that the editing technique is applicable to materials with more than one distinct molecule per asymmetric unit cell. Finally, the thiazine nitrogen (N1) does not invert or dephase rapidly, confirming no one-bond coupling is present and evolution is under T_2' relaxation effects only.

5.3.5 Pazopanib

The API pazopanib is a cancer treatment drug, [164] which is expected to have a protonated pyrazine nitrogen site relative to its free base after an acid-base reaction with hydrochloric acid. In addition to a pyrazine ring, a range of interesting nitrogen functional groups are present, including a tertiary amine with methyl protons in close proximity, a primary amine and an imidazole ring.

Figure 5.5 shows a ^{15}N CPMAS spectrum and subsequent spectral editing spectra (b-g) recorded using different 2τ times. XRD data indicates that N12a is not protonated, however because of the close proximity to a methyl group the CPMAS signal of N12a is enhanced relative to other non-protonated nitrogen sites. This demonstrates the potential limitations associated with characterisation using different dephasing times or CPMAS contact times to establish the presence of through-bond proton coupling(s). The nitrogen sites in the down-field region (N1, N2 and N16a) are not protonated, and have a weaker signal relative to up-field nitrogen sites.

$^{1}J_{15N\text{-}1H}$ spectral editing was applied to pazopanib to identify different nitrogen

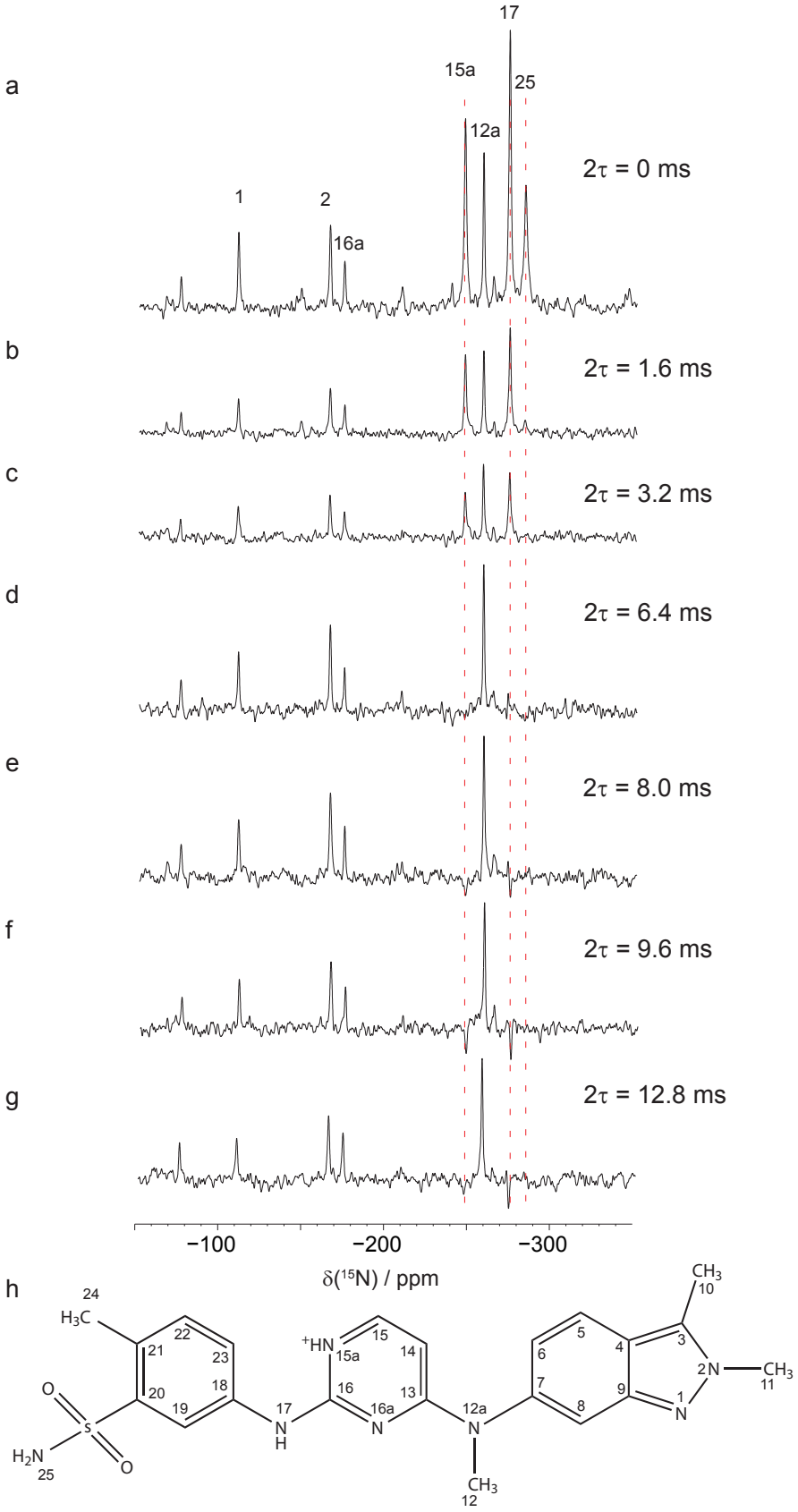

Figure 5.5: (a) ^{15}N CPMAS and (b-g) $^{1}J_{15N\text{-}1H}$ edited spectra ranging from 2τ = 1.6 ms to 2τ = 12.8 ms obtained for pazopanib. Spectra were obtained at 11.7 T and a MAS frequency of 5 kHz. Experimental times were (a) 8.5 hours (6144 co-added transients), (b-c) 28.5 hours (20480 co-added transients) and (d-g) 57 hours (40960 co-added transients). All spectra shown were recorded with a recycle delay of 5 seconds. (h) Structure of pazopanib.

functional groups. For a short 2τ increment (3.2 ms), the signal of N25, a primary amine, rapidly dephases as expected. For the primary amine, N25, the modulation rapidly dephases, however an inversion is not observed at any 2τ increment afterwards, inferring that N25 has two directly-bonded protons.

Longer 2τ periods reveal inversion of the secondary amine (N17) modulation, and importantly signal inversion of a pyrazine nitrogen site, namely N15a. The inversion of the N15a signal proves that proton transfer has occurred in an acid-base reaction. However, the N16a signal does not invert for any 2τ value recorded, indicating proton transfer to only one of the pyrazine nitrogens. As modulation is determined by through-bond proton couplings, then the close proximity of methyl protons (labelled H12) to N12a does not effect the modulation during 2τ. Faster dephasing of N12a may be expected relative to other non-protonated sites owing to the dipolar couplings to these close proximity protons. Fast dephasing due to third-order cross terms discussed in chapter 4 are likely to be relatively small however, as the closest proton proximity is a methyl group, therefore fast exchange between protons will occur, reducing the dipolar couplings. Furthermore, ^{15}N-^{1}H dipolar couplings are smaller in magnitude than ^{13}C-^{1}H dipolar couplings over the same distance. Over all 2τ periods presented, no inversion was observed for N1, N2, N12a and N16a, indicating T_2' dephasing only.

5.4 Summary and Conclusions

The spectra shown demonstrate the successful identification of different nitrogen functional groups via through-bond proton couplings. $^{1}J_{15N\text{-}1H}$ based editing methods are not susceptible to motional effects as the J coupling is an isotropic interaction. Discrimination between NH_n groups, including between NH and NH_2 sites, is achievable using $^{1}J_{15N\text{-}1H}$ techniques, as opposed to the distinction between protonated or non-protonated sites achievable using dipolar dephasing techniques. However, owing to the smaller magnitude of J coupling values relative to dipolar couplings, it is imperative that efficient homonuclear dipolar decoupling is applied during τ periods with the correct rotor-synchronisation and non-integer τ_r/τ_c conditions.

Proton transfer to a primary amine often occurs after an acid-base reaction, therefore tracking of proton transfer in pharmaceutical salts is crucial for both regu-

latory and patent reasons. As proton transfer to nitrogen in solution state does not always coincide with the same position in the solid state it is important that reliable solid state methodologies are available. It is anticipated that $^{1}J_{15N\text{-}1H}$ based editing techniques will be beneficial for cases where weakly ionising acids or bases are used and it is ambiguous whether a salt or cocrystal has formed.

Demonstration of an acid-base proton transfer was evident for tenoxicam and pazopanib using $^{1}J_{15N\text{-}1H}$ spectral editing. For tenoxicam, inversion of the pyridine nitrogen signal unambiguously shows that proton transfer has occurred, and therefore salt formation can be inferred. In pazopanib, an inversion of a pyrazine nitrogen signal was seen, proving salt formation, as in its free base form, this nitrogen has no directly attached proton. Identifying proton transfer is an important characterisation step, as the chemical and physical properties can be significantly different for the free base form relative to a corresponding salt formation.

Furthermore, distinction between different NH_n groups is achievable by the $^{1}J_{15N\text{-}1H}$ spectral editing method. A primary amine signal should not invert for any 2τ increment, as the cosine term which describes the modulation is to the squared power, and the modulation dephases rapidly. Both of these observations were made for the primary amine in pazopanib, allowing for clear distinction between NH and NH_2 groups not easily attainable using dipolar dephasing methods. All functional groups studied behaved according to crystal structure predictions. Slow dephasing of a resonance was indicative of T_2' dephasing only, whereas a signal inversion indicated an odd number of attached protons. Non-protonated nitrogen sites which reside in a proton rich local environment did not zero-cross, and evolved under T_2' dephasing effects only.

CHAPTER

SIX

^{14}N-^{1}H EXPERIMENTS AT 850 MHZ

6.1 Introduction

Nitrogen is an important element in nearly all branches of chemistry. Both naturally occurring nitrogen isotopes are NMR active, however, to date application in solid-state NMR at natural abundance has been limited, compared to studies of other frequently appearing nuclei, such as ^{13}C and ^{1}H. ^{15}N solid-state NMR is more commonly implemented, owing to its favourable spin-$\frac{1}{2}$ properties and higher gyromagnetic ratio. However, ^{15}N is only 0.37% naturally abundant, therefore unless samples are isotopically enriched, experimental times can be a limiting factor. Quadrupolar effects present for a ^{14}N isotope hinder resolution in an NMR spectrum, however they also contain information regarding the electric field gradient traversing a nucleus, which is inaccessible from ^{15}N NMR. Furthermore, there is no requirement for isotopic labelling, as ^{14}N has 99.6% natural abundance levels. ^{14}N is a spin-1 nucleus, therefore high-resolution NMR experiments applicable to a half-integer quadrupolar nucleus with a central transition, such as Multiple-Quantum MAS (MQMAS) [165, 166] and Satellite-Transition MAS (STMAS) [167, 168] cannot be used. Numerous direct detection methods for ^{14}N have been demonstrated, [169] including overtone spectroscopy, [170, 171] single crystal detection, [172–174] ^{14}N excitation using frequency-swept pulses, [175, 176] and nuclear quadrupolar resonance (NQR). [177, 178] Recently, 2D HMQC ^{14}N-^{1}H/^{13}C experiments, where ^{14}N lineshapes are indirectly detected via a spin-$\frac{1}{2}$ spy nucleus have been demonstrated. [51] The development and application of these experiments are the

subjects of this chapter.

To date, the spy nucleus used to detect ^{14}N has been either ^{13}C or ^{1}H. Detection via ^{13}C [179–181] can be advantageous as ^{13}C lineshapes are typically narrower relative to ^{1}H lineshapes, therefore increasing resolution in F_2. The coherence transfer mechanism exploited for ^{13}C detection is a combination of residual dipolar splittings (RDS), [182–184] and ^{14}N-^{13}C through-bond couplings. Large gains in sensitivity can be achieved through ^{1}H acquisition, owing to a significantly higher gyromagnetic ratio and 99.99% natural abundance levels, compared to 1.03% natural abundance levels of ^{13}C.

Coherence transfer between ^{14}N and ^{1}H has been demonstrated using either through-space couplings, [50, 185] or a combination of ^{14}N-^{1}H through-bond couplings and residual dipolar splittings. [186–188] In both cases, the presence of strong homonuclear ^{1}H-^{1}H dipolar couplings leads to broad proton resonances, which hinders assignment. Deuteration of proton sites that do not participate in NH correlations can potentially reduce ^{1}H linewidths, however this is not always practical. A directly bonded ^{14}N-^{1}H dipolar coupling is more than an order of magnitude larger than a ^{14}N-^{1}H through-bond coupling and RDS combined. Therefore, the efficiency of coherence transfer is much improved if correlation is achieved using through-space couplings. However, as discussed in section 2.4.4, heteronuclear dipolar couplings are averaged to zero under MAS, therefore, in order to achieve correlation via through-space couplings, the ^{14}N-^{1}H dipolar couplings are reintroduced using heteronuclear dipolar recoupling schemes. Herein, rotary resonance recoupling (R^3), [34] using the $n = 2$ resonance condition, was implemented in all spectra shown, which recouples heteronuclear ^{14}N-^{1}H dipolar couplings, whilst not interfering with the fast MAS applied to average strong homonuclear ^{1}H-^{1}H couplings. 2D ^{14}N-^{1}H HMQC spectra obtained using symmetry based RN recoupling schemes, [38, 189] have been presented elsewhere. [185, 190]

In this chapter, 2D ^{14}N-^{1}H HMQC experiments are presented for the dipeptide β-Asp.Ala. The effect of different recoupling durations upon the observed ^{14}N-^{1}H correlations is presented in conjunction with density matrix simulations. An application beyond a dipeptide is then presented, specifically, hydrogen bonding interactions are probed in a guanosine derivative using 2D ^{14}N-^{1}H HMQC experiments.

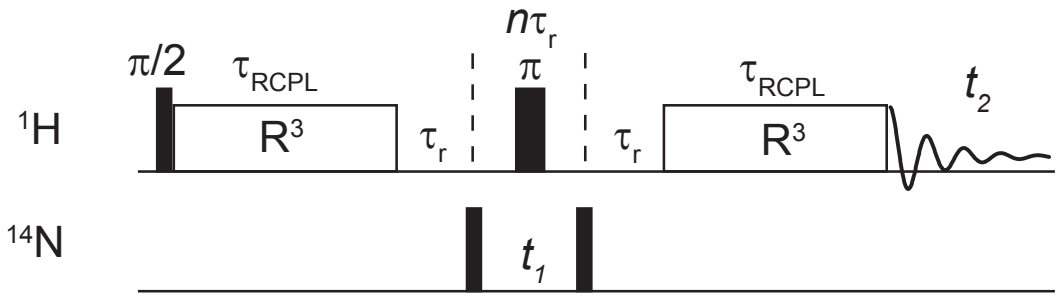

Figure 6.1: Pulse sequence applied for ^{14}N-^{1}H HMQC experiments, using rotary resonance to achieve ^{14}N-^{1}H correlation transfer. In order to remove large first-order quadrupolar interactions, it is imperative that the magic-angle is accurately calibrated, and that the experiment is rotor-synchronised, therefore stable spinning is required.

6.2 Experimental and computational details

6.2.1 Sample preparation

The dipeptide β-AspAla was purchased from Bachem (Bubendorf, Switzerland) and used without further purification. The protonation state of the dipeptide β-AspAla is identified from the single-crystal diffraction structure (CSD refcode:FUMTEM), [159] and from the ^{1}H chemical shift values in the solid-state. A guanosine derivative was supplied by the group of Professor Gian Piero Spada at Bologna University. Further details regarding synthesis can be found in refs. [3, 191].

6.2.2 Solid-state NMR

2D ^{14}N-^{1}H HMQC experiments were performed on a Bruker Avance III spectrometer operating at a ^{1}H Larmor frequency of 850.2 MHz ($B_0 = 20.0$ T) using a Bruker 1.3 mm triple resonance probe, operating in double resonance mode, at an MAS frequency of 60 kHz unless otherwise stated. All experiments were performed at room temperature unless otherwise stated. Rotary resonance recoupling (R^3) was applied at the $n = 2$ condition, with an x−x phase inversion [192] on each rotor-synchronised pulse, i.e., corresponding to a duration of 16.7 μs when using an MAS frequency of 60 kHz. The States method was used to achieve sign discrimination in F_1. [108] A 4-step nested phase cycle was used to select changes in coherence order $\Delta p = \pm 1$ (on the first ^{1}H pulse, 2 steps) and $\Delta p = \pm 1$ (on the last ^{14}N pulse, 2 steps). Magic angle setup was achieved by calibration of a ^{23}Na STMAS [167, 168] experiment for Na_2HPO_4, where

accurate magic angle setting (within $\pm 0.003°$) is also required to remove any large first order quadrupolar interactions. ^{14}N shifts were referenced to a saturated NH_4Cl aqueous solution at -352.9 ppm, corresponding to a primary reference of CH_3NO_2 at 0 ppm. [193] ^{1}H shifts were referenced to adamantane at 1.63 ppm, corresponding to a primary reference of TMS at 0 ppm. ^{1}H 90° pulses of duration 1.3 μs were used, whereas ^{14}N pulses of duration of 4 μs (β-AspAla) and 6 μs (guanosine derivative) at a nutation frequency of 120 kHz were used. For 2D ^{14}N-^{1}H HMQC spectra of $dG(C_3)_2$, for the experiment with the shorter recoupling period 80 transients were co-added for each of 36 t_1 FIDs. For the longer recoupling period experiment, 240 transients were co-added for each of 80 t_1 FIDs. A recycle delay of duration 2 seconds was implemented for all $dG(C_3)_2$ ^{14}N-^{1}H experiments. Further experimental details specific to each spectrum presented can be found in the respective figure captions.

A 2D ^{1}H-^{15}N REPT HSQC experiment was performed by Dr. Tran Pham at Warwick University on a Chemagnetics Infinity spectrometer operating at a ^{1}H Larmor frequency of 600.1 MHz, using a 3.2 mm triple resonance probe, operating in double-resonance mode, at a MAS frequency of 22 kHz. The pulse sequence employed is shown in Fig. 3 of ref [194]. The application of the sequence was preceded by a pulse comb on the ^{15}N channel. XiX ^{1}H decoupling [195, 196] with a pulse duration of 9 μs was applied during the acquisition of the ^{15}N FID. A 16-step nested phase cycle was used to select changes in coherence order $\Delta p = \pm 1$ (on the first ^{1}H pulse, 2 steps), $\Delta p = \pm 1$ (on the first ^{15}N pulse, 2 steps) and $\Delta p = \pm 2$ (on the first ^{15}N 180° pulse, 4 steps). For each of 128 t_1 FIDs (using the Time Proportional Phase Incremented (TPPI) method [197] to achieve sign discrimination in F_1 with a rotor-synchronised increment of 45.5 μs), 80 transients were co-added with a recycle delay of 5 s corresponding to a total experimental time of 14 h.

6.2.3 Computational

First-principles calculations were performed using the academic release of CASTEP version 4.3, which implements density-functional theory using a planewave basis set. All calculations presented used a PBE exchange-correlation functional [160] and on-the-fly pseudopotentials. [55]

GIPAW calculations for the dipeptide β-AspAla were performed by Dr. Jonathan

Bradley whilst at Warwick University. For the dipeptide β-AspAla, initial geometry optimisation of all atoms was performed by starting with the X-ray single-crystal structure (obtained from the CSD database, refcode FUMTEM, [159] Z = 4, i.e., 104 atoms in the unit cell). The geometry optimisation used a cut-off energy equal to 1100 eV and a k-point spacing of $0.1 \times 2\pi$ Å^{-1} with a Monkhurst-Pack grid, whereas NMR calculations used a cut-off energy equal to 1200 eV and a k-point spacing of $0.3 \times 2\pi$ Å^{-1} with a Monkhurst-Pack grid.

For $dG(C_3)_2$, initial geometry optimisation of all atoms was performed by starting with the X-ray single-crystal structure (obtained from the CSD database, refcode MOFBUE, [198] Z = 2, i.e., 96 atoms in the unit cell). For both the geometry optimisation and NMR calculations, a cut-off energy equal to 800 eV and a k-point spacing of $0.08 \times 2\pi$ Å^{-1} with a Monkhurst-Pack grid was used. Geometry optimisation of the guanosine crystal structure was performed by Dr. Amy Webber using the CASTEP code, whilst at Warwick University.

All density matrix simulations were performed using SPINEVOLUTION. [53] Each simulation was performed as a 1D ^{1}H row of a 2D ^{14}N-^{1}H HMQC experiment, at a t_1 value of 0 ms. A total of 1024 points were recorded during t_2. Each point in the simulated NH dipolar build-up curve was extracted as the intensity of the ^{1}H resonance of interest. All simulations used an MAS frequency of 60 kHz and ^{1}H Larmor frequency of 850 MHz, in order to match experiment. Rotary resonance recoupling was simulated at an $n = 2$ condition, with an x−x phase inversion, as per experiment. All further pulses were applied as ideal pulses, which are of zero duration whilst achieving the desired flip-angle. Use of ideal pulses simplifies the rotor-synchronisation conditions required for density-matrix simulations in order to reduce computational times. Coordinate systems were constructed from the geometry optimised atomic positions of β-AspAla. Individual NH_3^+ and NH simulation systems were constructed using the nitrogen site of interest, and the seven nearest protons to the stated nitrogen site. Motional exchange of CH_3 and NH_3^+ protons was included. The corresponding ^{1}H and ^{14}N isotropic chemical shifts were taken from experimental results, whereas anisotropic chemical shift and quadrupolar parameters were extracted from GIPAW calculations. All dipolar couplings were present. Powder averaging was performed using 100 α and β powder angle pairs using the REPULSION averaging scheme, [139] and a total of 16

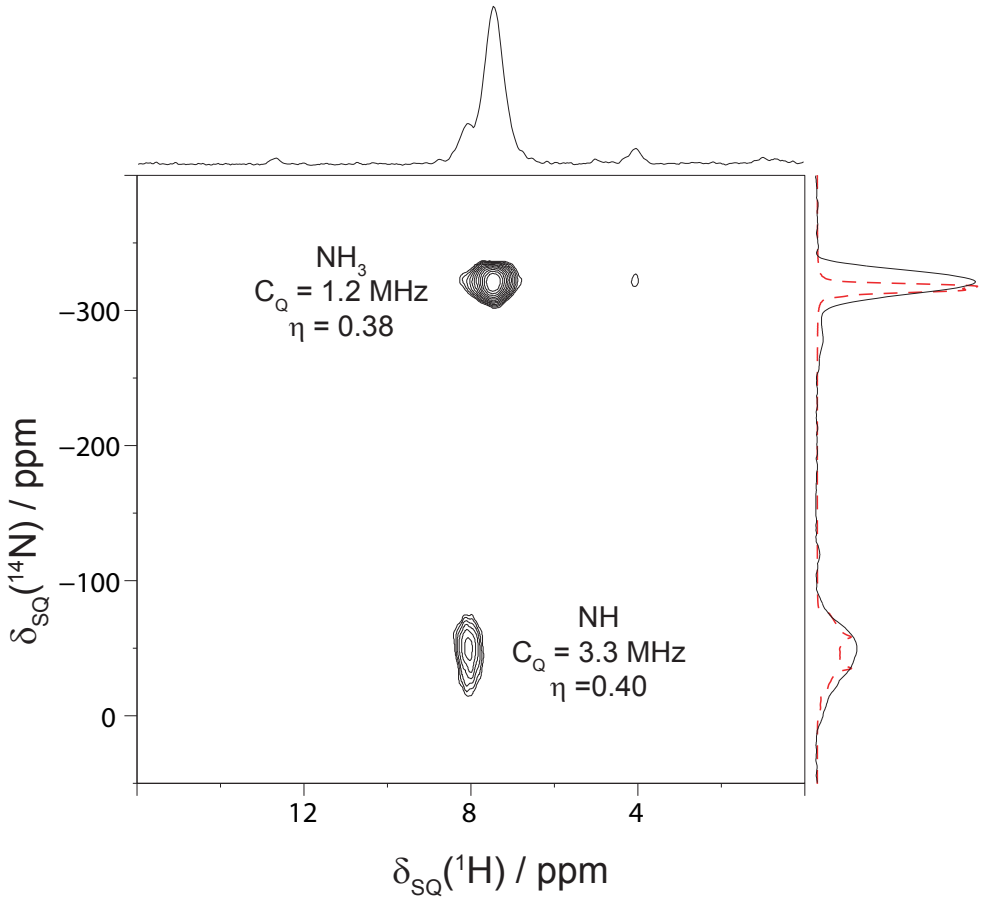

Figure 6.2: ^{14}N-^{1}H HMQC spectrum obtained for the dipeptide β-AspAla at an MAS frequency of 60 kHz, recorded at B_0 = 20.0 T. The recoupling duration, τ_{RCPL}, was equal to 166.7 μs. GIPAW calculated C_Q and η_Q values are stated for each ^{14}N site. The red dashed line represents simulated ^{14}N lineshapes, according to GIPAW calculations performed using SPINEVOLUTION. A consistent scaling factor of 0.95 was applied to calculated C_Q values. For each of 96 t_1 FIDs, 16 transients were co-added, with a recycle delay of 2 s, corresponding to a total experimental time of 50 min. The base contour levels are at 10% relative to the maximum peak height.

γ-angles. Analysis was performed using the GSim platform. A typical SPINEVOLUTION input file is presented in the Appendix.

6.3 Results and Discussion

6.3.1 Dipeptide β-AspAla: spinning frequency dependence

Figure 6.2 shows a 2D ^{14}N-^{1}H HMQC spectrum obtained for the dipeptide β-AspAla using a τ_{RCPL} duration equal to 66.7 μs, and a spinning frequency of 60 kHz. In chapter 5, a ^{15}N CPMAS spectrum of the dipeptide β-AspAla was presented in Fig. 5.2. As discussed, the dipeptide β-AspAla has two nitrogen sites, which in the ^{15}N CP-

MAS spectrum have an isotropic chemical shift separation of approximately 100 ppm. In Fig. 6.2, it is evident that the ^{14}N shift between the two sites is approximately 300 ppm. The additional contribution to the ^{14}N shift, relative to the ^{15}N shift, is attributed to the isotropic quadrupolar induced shift, which was introduced in section 2.4.5. Comparing isotropic nitrogen shifts in Fig. 5.2 and Fig. 6.2, it is clear that the C_Q is significantly larger for the NH site, relative to the NH_3^+ site, as $\delta_{\mathrm{QIS}}(\mathrm{NH})$ is approximately 200 ppm larger than $\delta_{\mathrm{QIS}}(NH_3^+)$. This was confirmed from GIPAW calculation performed using the CASTEP platform. Calculated C_Q and η_Q values are annotated on Fig. 6.2. Also included in Fig. 6.2 are simulated ^{14}N projections along F_1, performed using SPINEVOLUTION. Simulated projections are calculated using experimentally recorded ^{15}N isotropic chemical shifts, and GIPAW calculated quadrupolar parameters. It is evident that there is good agreement between experiment and GIPAW calculations performed for the dipeptide β-AspAla.

2D ^{14}N-^{1}H HMQC spectra recorded at MAS frequencies of (a) 30 kHz, (b) 45 kHz and (c) 60 kHz are presented in Fig. 6.3. The length of one recoupling block was equal to the inverse of the spinning frequency in order to maintain rotor-synchronisation, however the recoupling time, τ_{RCPL}, was equal to 133.3 μs for all spectra presented in Fig. 6.3. The rotary resonance recoupling condition is defined by n, where $n = \nu_1/\nu_r$. An $n = 2$ condition was applied for all 2D ^{14}N-^{1}H HMQC experiments presented. This resonance condition recouples both the heteronuclear dipolar couplings and the ^{1}H CSA interaction, however the CSA is refocused during a 2D ^{14}N-^{1}H HMQC experiment, analogous to a rotary resonance echo sequence. [199] An $n = 1/2$ resonance condition recouples homonuclear dipolar couplings, whereas an $n = 1$ resonance condition recouples CSA interactions, heteronuclear dipolar couplings and homonuclear dipolar couplings.

A τ_{RCPL} time of 133.3 μs is relatively short, therefore only correlation peaks corresponding to one-bond couplings are observed for all spectra in Fig. 6.3. The NH_3^+ (N1) site ($C_Q = 1.2$ MHz, $\eta_Q = 0.38$) is reasonably well resolved at all spinning frequencies presented, indicating that a relatively high quality 2D ^{14}N-^{1}H HMQC spectrum is achievable for lower C_Q sites when using a lower spinning frequency, i.e., $\nu_r = 30$ kHz. However, it is noteworthy that the higher C_Q NH site ($C_Q = 3.3$ MHz, $\eta_Q = 0.40$) is barely evident using a spinning frequency of 30 kHz. Increasing the MAS frequency

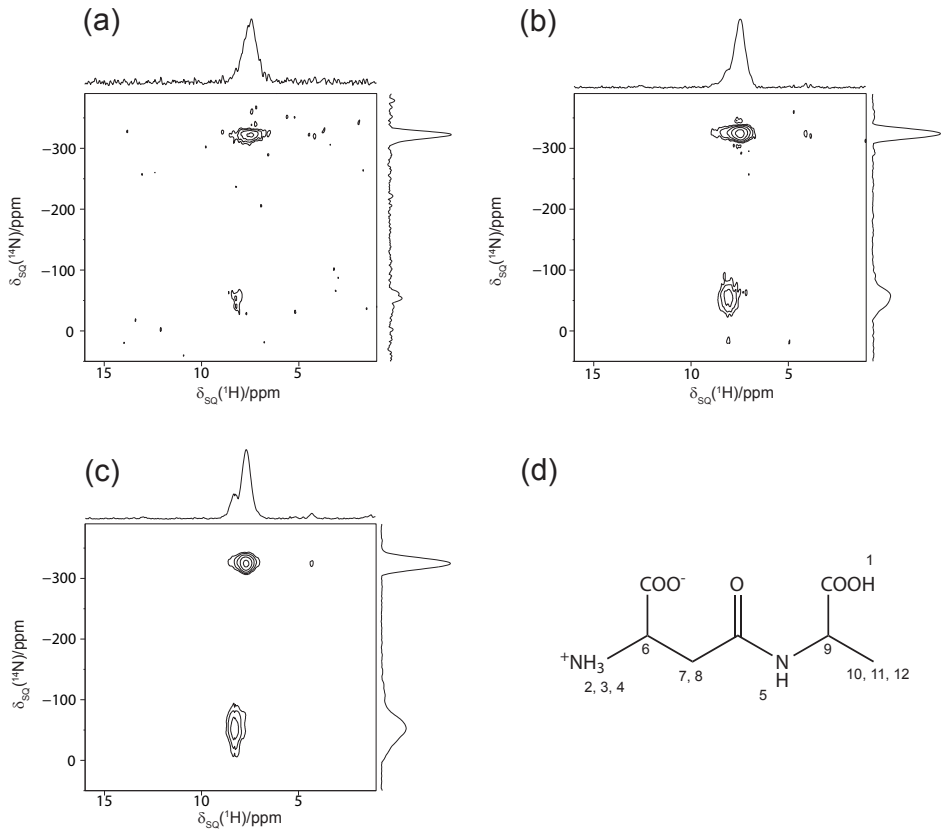

Figure 6.3: (a)-(c) ^{14}N-^{1}H HMQC spectrum obtained for the dipeptide β-AspAla at MAS frequencies of 30 kHz, 45 kHz, and 60 kHz. All spectra were recorded at B_0 = 20.0 T, using a Bruker 1.3 mm probe, and a τ_{RCPL} duration of 133.3 μs. For each of 60 t_1 FIDs, 16 transients were co-added, with a recycle delay of 2 s, corresponding to a total experimental time of approximately 30 min. The base contour levels are at (a) 16%, (b) 6% and (c) 8% with respect to the maximum peak height. (d) Structure of the dipeptide β-AspAla.

to 45 kHz improves the intensity and resolution in F_2 of the NH site. However, it is still not possible to assign each ^{14}N site to their respective close proximity proton(s). Increasing the MAS frequency to 60 kHz improves the intensity of both ^{14}N sites, as is clearly evident from a reduction in the noise levels in the projections along both F_1 and F_2. Furthermore, the resolution in the proton projection is further improved, and it is possible to resolve between ^{1}H chemical shifts of the NH_3^+ site (δ_{iso} = 8.0 ppm) and the NH site (δ_{iso} = 7.5 ppm). The advantages of very fast spinning frequencies in 2D ^{14}N-^{1}H HMQC experiments has also been demonstrated by Nishiyama *et. al.*. [9] They obtained a 2D ^{14}N-^{1}H HMQC spectrum of glycine and glycyl-l-alanine, at a MAS frequency of 70 kHz in 5 minutes. Access to very fast spinning frequencies assists in averaging of ^{1}H-^{1}H homonuclear dipolar couplings, and lengthens ^{1}H transverse relaxation times.

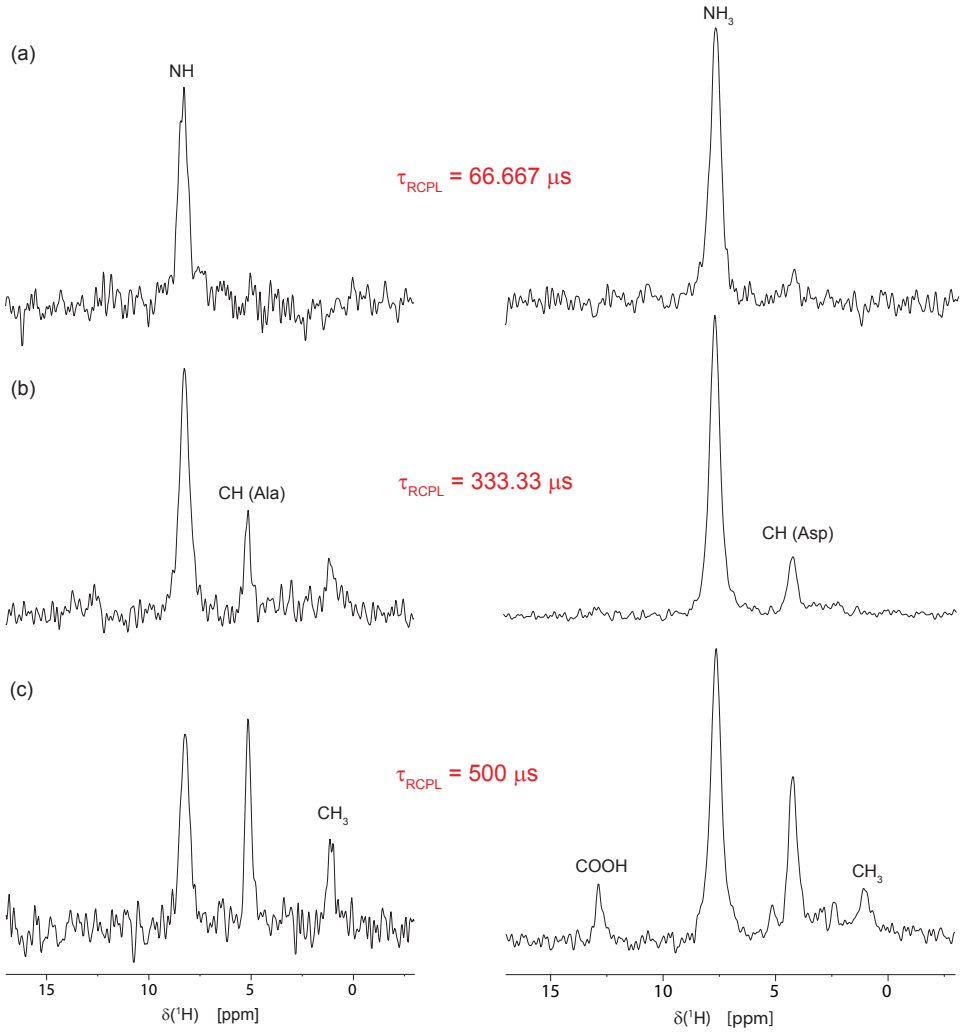

Figure 6.4: ^{1}H rows taken through the centre of gravity of the NH ^{14}N (left) and NH_3^+ ^{14}N (right) site in 2D ^{14}N-^{1}H HMQC spectra recorded for the dipeptide β-AspAla, using τ_{RCPL} durations of (a) 66.7 μs, (b) 333.3 μs and (c) 500 μs. All spectra were recorded using an MAS frequency of 60 kHz and B_0 = 20.0 T. Each 2D ^{14}N-^{1}H spectrum was recorded using a total of 96 rotor-synchronised t_1 increments of 16.7 μs; for each t_1 slice a total of 16 co-added transients were recorded, using a recycle delay of 2 s.

6.3.2 Dipeptide β-AspAla: effect of recoupling duration

Using heteronuclear dipolar couplings to achieve NH coherence transfer, as opposed to scalar couplings and RDS, is advantageous as coherence transfer is more efficient as through-space couplings are generally an order of magnitude larger, therefore reducing the excitation and reconversion times that are required. Heteronuclear recoupling schemes can also suppress homonuclear dipolar coupling during the excitation and conversion periods. Increasing the recoupling duration period reveals longer range proximity NH correlations. As protons are often located at the extremities of a molecule, e.g., methyl groups, probing N...H distances can reveal intermolecular packing configu-

rations, and therefore reveal interactions that describe molecular association. A series of 2D ^{14}N-^{1}H HMQC experiments were carried out for the dipeptide β-AspAla for a range of recoupling durations. In Fig. 6.4, a ^{1}H row taken through the maximum point of the nitrogen site of interest are presented for τ_{RCPL} times of 66.7 μs, 333.3 μs, and 500 μs.

Firstly, consider the ^{1}H row taken through the NH site, shown in the left hand column of Fig. 6.4. Unsurprisingly, a short recoupling time reveals only one-bond NH correlations. For a recoupling period of 333.33 μs, a longer-range intramolecular correlation between the NH nitrogen and the CH alanine proton is observed. At a recoupling period of 500 μs, a correlation between the NH nitrogen and the CH_3 protons is seen. Interestingly, the relative intensity of the one-bond NH correlation noticeably decreases relative to the longer range NH-CH(Ala) correlation as the recoupling period is increased. The NH site resides at a relatively central position in the molecule, therefore intermolecular proximities are not evident for the recoupling times applied.

In the right hand column of Fig. 6.4, ^{1}H rows taken through the NH_3^+ nitrogen site at different τ_{RCPL} times are presented. For a short recoupling time, only through-bond correlations are evident. A longer recoupling time of 333.33 μs reveals a further intramolecular correlation peak between the NH_3^+ nitrogen and the aspartic acid proton, H6. Increasing τ_{RCPL} to 500 μs reveals two intermolecular correlations, a correlation between the NH_3^+ nitrogen and a carboxyl acid proton, H1, and a further NH correlation to the methyl protons, H10, H11 and H12. Intermolecular proximities are evident when observing a proton projection through NH_3^+, as the NH_3^+ site resides at the periphery of the dipeptide β-AspAla molecule.

The rows presented in Fig. 6.4 were selected from a wider range of recoupling times implemented. Extraction of proton rows through the highest point in the relevant ^{14}N peak, in the same manner as presented in Fig. 6.4, allows for construction of NH dipolar build-up curves for specific ^{1}H resonances as a function of the recoupling duration. In order to assist in the interpretation of NH dipolar build-up curves, simulated NH dipolar build-up curves were performed for comparison to experiment. The simulation systems were constructed using coordinates from a geometry optimised crystal structure of β-AspAla. In simulations, intensity values presented were extracted from the integration of proton lineshapes, as opposed to ^{14}N lineshapes, which are compli-

cated by the presence of the quadrupolar interaction. The integration ranges for the separate proton resonances were: NH(9 - 6 ppm), CH(Ala)(5.5 - 4.1), NH_3^+(9 - 6 ppm) and CH(Asp)(4.5 - 3.2 ppm).

Comparison between experimental and simulated build-up curves observed for one-bond NH and sites are presented in Fig. 6.5. Experimental and simulated intensities are normalised relative to the maximum intensity in the respective proton projection. If the NH dipolar build-up curves in Fig. 6.5a are considered, then as indicated from the NH proton rows in the left hand column of Fig. 6.4, the through-bond NH dipolar build-up curve reaches a maximum intensity at a faster rate than is the case for the longer-range N...H proximities. This is not surprising, as correlation is achieved via dipolar couplings, which are inversely proportional to the cubic power of the internuclear distance. Furthermore, one-bond NH dipolar build-up curves have a higher maximum value relative to longer range correlation cases. For a longer range NH...CH(Ala) proximity, the maximum intensity occurs at a longer recoupling duration. Agreement between the NH through-bond experimental and simulated NH dipolar build-up curves is also relatively good, although it is evident that dephasing rates are faster in experiment.

The computational time required for a simulation is dependent upon 2^N, therefore an 8-spin system was selected as the most suitable size spin system to closely match experiment, whilst maintaining acceptable calculation times. As a consequence of the limited simulated spin size system, experimental dephasing effects cannot be completely replicated, hence explaining why dephasing occurs at a faster rate experimentally. This is in agreement with investigations into the effect that the size of a spin system has upon ^{1}H-^{1}H double quantum build-up curves presented by Bradley *et. al.*, [200] where simulated ^{1}H DQ build-up curves always dephased at a slower rate than experimental ^{1}H DQ build-up curves.

Inspection of the NH dipolar build-up curves in Fig. 6.5b reveals that once again the maximum intensity is found at a shorter recoupling time for the through-bond NH_3^+ build-up curve, compared to a longer range correlation between the NH_3^+ nitrogen site and the CH(Asp) proton. Furthermore, the intensity of the through-bond curve, relative to a longer range through-space proximity, is much higher. Dynamics in the NH_3^+ group complicate the analysis of the build-up curves in Fig. 6.5b, as motional

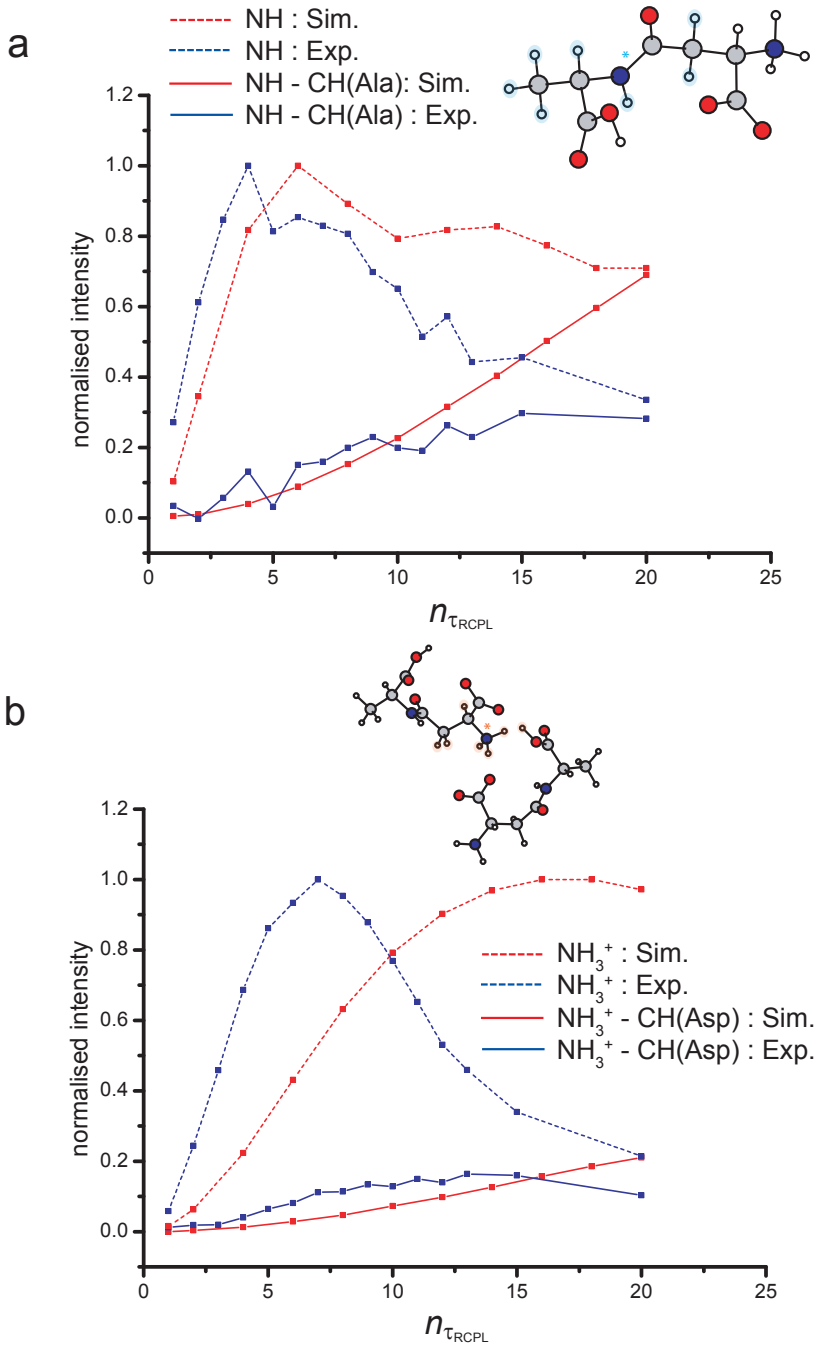

Figure 6.5: (a) NH and (b) NH_3^+ experimental (blue lines) and simulated (red lines) dipeptide β-AspAla NH build-up curves recorded as a function of the recoupling time. One-bond NH curves are denoted with a dashed lines, whereas longer range proximities are denoted as solid lines. The experimental points were extracted from 2D ^{14}N-^{1}H HMQC spectra (see Fig. 6.4). Each τ_{RCPL} integer is equal to 33.33 μs, i.e., rotor-synchronised with a spinning frequency of 60 kHz, where two x−x pulses are included. Simulated build-up curves were constructed using 1D ^{1}H slices recorded at $t_1 = 0$ ms. Experimental and simulated build-up curves were separately normalised to their respective maximum. For the dipeptide β-AspAla structures included in each annotation, protons used in simulations are highlighted, whereas the ^{14}N site of interest is annotated with a *. Error bars for the experimental intensities are (a) 0.06 (NH) and (b) 0.01 (NH_3^+)

effects average dipolar couplings, therefore the effect of strong ^{1}H-^{1}H dipolar couplings is reduced, consequently decreasing dephasing times. Correlation between experiment and simulation is not in as strong agreement as that found for the NH group in part (a). Motional effects are included in simulation, however this assumes precession at an effectively infinite exchange rate.

6.3.3 Dipeptide β-AspAla: through-bond correlation

In Fig. 6.6, correlation was achieved through a combination of ^{14}N-^{1}H heteronuclear through-bond couplings and RDS. The experiment is referred to herein as a 2D ^{14}N-^{1}H J-HMQC experiment, where for completeness J encompasses both scalar couplings and residual dipolar splittings. In all other spectra presented, rotary resonance was applied during the excitation and reconversion periods as the coherence transfer mechanism was ^{14}N-^{1}H dipolar couplings.

As discussed, the strength of a through-bond ^{14}N-^{1}H coupling and RDS combined, relative to a one-bond ^{14}N-^{1}H through-space coupling, is typically over an order of magnitude smaller. Therefore, excitation and reconversion times required are significantly longer, increasing the potential loss of transverse magnetisation during excitation and reconversion periods. In Fig. 6.6, the intensity decreases by approximately a factor of two relative to a comparable spectrum in Fig. 6.2. This is primarily owed to the much longer excitation and reconversion times ($\tau_{RCPL} = 900$ μs) implemented in Fig. 6.6, compared to a τ_{RCPL} duration of 133.3 μs in Fig. 6.2. Both spectra were acquired with an identical number of co-added transients in each t_1 increment, and the same number of t_1 increments. The advantage of using correlation via through-bond couplings is that the spectrum is more selective, as only directly bonded NH connectivities are observable.

6.4 Deoxy-guanosine derivative, dG$(C_3)_2$

Guanine can operate as either a proton acceptor or donor, therefore numerous self assembly modes are possible, including ribbon or quartet formations. This versatility means that they have found much usage in supramolecular chemistry, for instance in the construction of nanowires and biosensors, [201] and as a bridge in nanocontacts

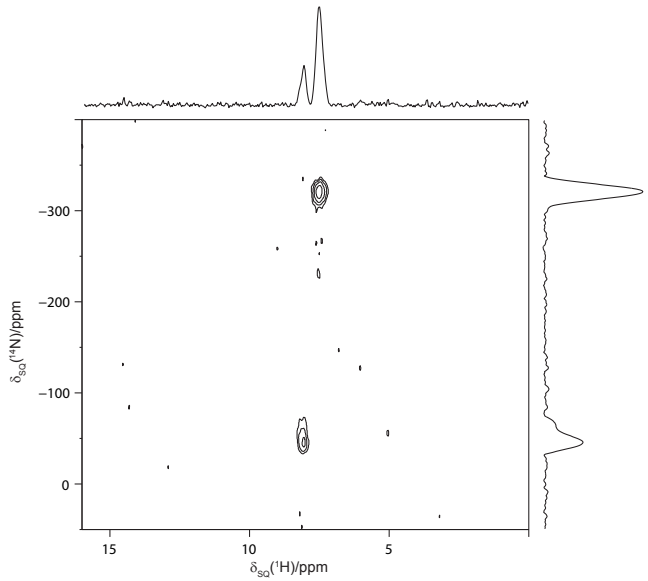

Figure 6.6: ^{14}N-^{1}H (850 MHz, 60 kHz MAS) J-HMQC spectrum recorded for the dipeptide β-AspAla. Coherence is transferred via a combination of through-bond couplings and residual dipolar splittings. For each of 96 t_1 FIDs, 16 transients were co-added, with a recycle delay of 2 s, corresponding to a total experimental time of approximately 50 min. A τ_{RCPL} of duration 900 μs was applied. The base contour levels are at 11% with respect to the maximum peak height.

constructed from electron beam lithography, which depending upon the size of the gap, produce devices that can act as a photoconductor [202] or a rectifier. [203] Solid-state NMR has been demonstrated as a suitable probe of guanosine derivatives, namely using ^{15}N NMR experiments, [204, 205] and more recently a range of ^{13}C and ^{1}H solid-state NMR methods. [3] Additionally, 2D ^{14}N-^{1}H HMQC experiments have been shown to be well suited to the identification of hydrogen bonding motifs present in guanosine self assembly formations. Herein, 2D ^{14}N-^{1}H HMQC experiments are presented for a shorter chain deoxyguanosine derivative, (see Fig. 6.7) which using single crystal X-ray diffraction has been demonstrated to self-assemble in a ribbon formation, [198] in the form shown in Fig. 6.8f.

2D ^{14}N-^{1}H HMQC spectra of a deoxyguanosine derivative, dG(C3)$_2$, recorded for τ_{RCPL} periods of 67.7 μs and 666.7 μs are presented in Fig. 6.8a and b. In Fig. 6.8a, a shorter recoupling time is used, consequently only one-bond NH peaks are observed. It is evident that there are two independent molecules per asymmetric unit cell, demonstrated by the presence of two crystallographically distinct H1 resonances, labelled A and B, as is recorded by the X-ray single crystal diffraction structure. Note that four distinct NH_2 proton resonances are not observed, rather only two NH_2 proton

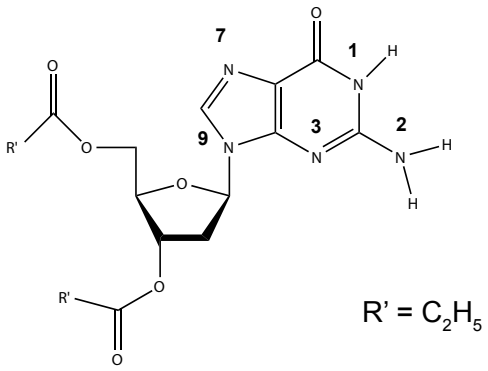

Figure 6.7: Structure of a deoxyguanosine derivative.

resonances are resolved. NH_2 moieties, labelled H2a (5.6 ppm (A) and 6.1 ppm (B)) and H2b (7.5 ppm (A) and 8.0 ppm (B)), are not resolved, rather a superposition of H2a and H2b peaks is observed.

Application of a longer duration τ_{RCPL} time reveals longer range NH correlations. As longer range proximities are visible, it is possible to determine intermolecular packing configurations detailed by hydrogen bonding interactions. NH proximities, extracted from a geometry optimised crystal structure, are presented in Table 6.2, inspection of which indicates that the N7...H1-N1 hydrogen bond is expected to be the strongest hydrogen bonding interaction, however the intensity of this cross-peak is relatively weak, owing to fast dephasing of the H1 signal. Fast dephasing of the H1 signal for a longer recoupling time is evident when comparing the relative intensities of the one-bond correlations recorded at a shorter recoupling time. The N1-H1 peak has rapidly dephased relative to N2-H2a,b cross peaks in Fig. 6.8b. An intermolecular correlation across the hydrogen bonding interface, between N7...H2b, is observed at a ^{14}N shift of approximately 60 ppm. No peak is observed between N7 and H2a, owing to this proton pointing in the opposite direction to N7. Furthermore, at a longer recoupling duration, an intramolecular NH correlation is observed between the CH8 proton and N7. Experimental CH8 proton chemical shifts of 7.5 ppm and 7.7 ppm are reported for each distinct molecule per unit cell, [3] therefore it is not possible to resolve between N7-H8 and N7-H2b cross-peaks. A long-range intramolecular correlation between N3 and H2a, as a tail of the much stronger one-bond NH-H2a cross-peak, is evident at a ^{14}N shift of 0 ppm for a longer recoupling duration. The tail is not observed for a shorter

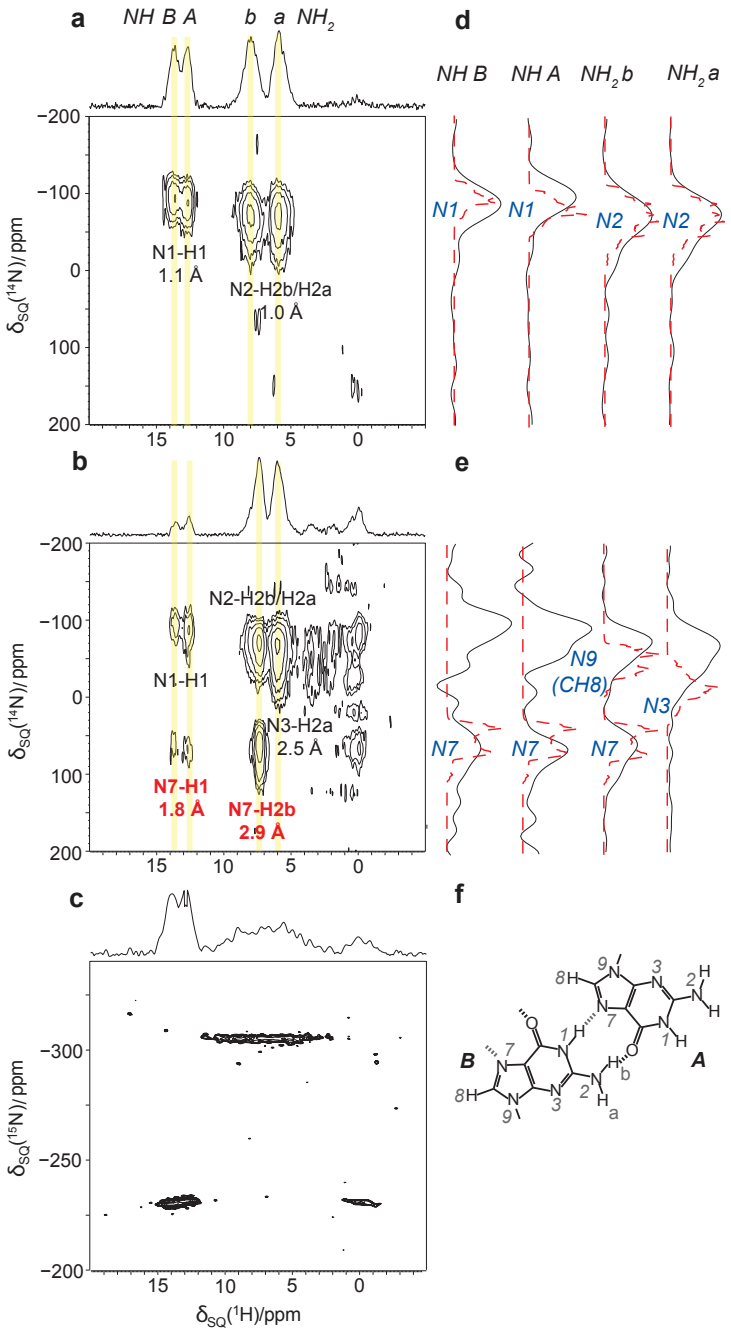

Figure 6.8: (a, b) ^{14}N-^{1}H (850 MHz, 60 kHz MAS) HMQC spectra of dG(C$_3$)$_2$ recorded using $n = 2$ rotary resonance recoupling (R^3) of the ^{14}N-^{1}H heteronuclear dipolar couplings with duration (a) 167 μs and (b) 667 μs. (c) ^{1}H-^{15}N (600 MHz, 22 kHz MAS) REPT-HSQC spectrum of ^{15}N-labelled dG(C$_3$)$_2$ recorded using one rotor period of REDOR recoupling of the ^{1}H-^{15}N heteronuclear dipolar couplings. Skyline projections are shown for the ^{1}H dimension. The base contour level is at (a) 14%, (b) 8% and (c) 15%. (d, e) Comparison of experimental ^{14}N spectra (solid lines) corresponding to columns through the NH or NH$_2$ ^{1}H resonances, with spectra simulated (red lines) using SPINEVOLUTION for the previously determined experimental isotropic ^{15}N (same as ^{14}N) chemical shifts and quadrupolar parameters as calculated using the GIPAW method, with a consistent scaling of the calculated C$_Q$ values by a factor of 0.96. (f) Schematic representation of intermolecular hydrogen-bonding in dG(C$_3$)$_2$.

Table 6.1: A comparison of ^{15}N and ^{14}N experimental and GIPAW calculated shifts for $dG(C_3)_2$.

Sites	$\delta(^{15}N)_{expt}$ / ppm	$\delta(^{15}N)_{calc}{}^{a}$ / ppm	$\delta(^{14}N)_{expt}{}^{b}$ / ppm	$\delta(^{14}N)_{calc}{}^{c}$ / ppm
N1A	−230.4	−233.8	−90	−94.9
N1B	−231.9	−231.1	−95	−110.0
N2A	−305.5	−305.9	−70	−71.6
N2B	−305.5	−305.1	−70	−93.4
N3A	−215.8	−215.8	N/A	−62.7
N3B	−217.7	−212.4	N/A	−56.0
N7A	−139.0	−145.2	70	57.1
N7B	−143.1	−140.1	60	60.3
N9A	−210.2	−210.4	−50	−50.7
N9B	−210.2	−209.2	−50	−50.7

[a] $\delta_{iso} = -(\sigma_{iso} - \sigma_{ref})$, where σ_{ref} for ^{15}N was −160.4 ppm. This was calculated from addition of the mean average of the experimental isotropic chemical shifts and the mean average of σ_{iso} values. [b] Centre of gravity of the second-order quadrupolar broadened lineshape, with an associated error of ±5 ppm.
[c] $\delta(^{14}N)_{calc} = \delta(^{15}N)_{expt} + \delta_{QIS}(^{14}N)_{calc}$, where $\delta_{QIS}(^{14}N)_{calc}$ has been calculated using a consistent scaling of the GIPAW calculated C_Q values by a factor of 0.96.

recoupling time, demonstrating that this peak is separate to the N2-H2a cross-peak. Inspection of extracted NH distances suggests that a N9 correlation to CH8 proton should be observed. Furthermore, GIPAW calculations and experimental ^{15}N isotropic shift report that the N9 ^{14}N shift should be found at approximately −50 ppm. Therefore, any experimentally observed cross-peak is likely to be dominated by the presence of the significantly stronger one-bond N2-H2b cross-peak.

The dashed lines are simulated ^{14}N projections, performed using the SPINEVOLUTION package. The inputted isotropic chemical shift values were extracted from the ^{15}N CPMAS spin-echo spectrum reported by Pham *et. al.*. [205] Simulated projections include both ^{14}N sites from each molecule per distinct unit cell. Quadrupolar parameters were extracted from a GIPAW calculation using the CASTEP platform. In order to better align experimental ^{14}N projections to simulated projections, a consistent scaling factor of 0.96 was applied to all calculated ^{14}N C_Q values. The simulated projections provide additional evidence that the cross-peak at approximately 0 ppm does agree with the expected shift of N3, which as discussed is seen as a tail adjacent to N2-H2a cross-peak. The predicted N9 resonance is included in the projection taken through H2b; as discussed, the proton chemical shifts are indistinguishable from CH8.

A 2D ^{1}H-^{15}N REPT-HSQC (recoupled polarisation transfer heteronuclear single-

Table 6.2: NH distances up to 3 Å in $dG(C_3)_2$, extracted from the geometry optimised (CASTEP) crystal structure. One-bond correlations are denoted in bold and intermolecular correlations shown in italic.

Site	Distance / Å	Sites	Distance / Å
N1 A - H1 A	**1.05**	**N1 B - H1 B**	**1.06**
N1 A - H2b A	2.61	N1 B - H2b B	2.60
N2 A - H2a A	**1.02**	**N2 B - H2a B**	**1.02**
N2 A - H2b A	**1.03**	**N2 B - H2b B**	**1.03**
N2 A - H1 A	2.51	N2 B - H1 B	2.51
N3 A - H2a A	2.49	N3 B - H2a B	2.51
N3 A - CH1' A	2.72	N3 B - CH1' B	2.57
N7 A - H1 B	*1.77*	*N7 B - H1 A*	*1.84*
N7 A - CH8 A	2.14	N7 B - CH8 B	2.13
N7 A - H2b B	*2.90*	*N7 B - H2b A*	*2.96*
N9 A - CH1' A	2.06	N9 B - CH1' B	2.05
N9 A - CH8 A	2.16	N9 B - CH8 B	2.17

quantum correlation) [194] spectrum is presented in Fig 6.8c, note that the spectrum has been rotated by 90° in order to aid comparison between ^{1}H and nitrogen projections, relative to Fig. 6.8a and b. In the actual dataset, F_1 corresponds to ^{1}H, and F_2 corresponds to ^{15}N. A short recoupling time was applied, therefore only one-bond NH correlations are observed. From a comparison between the 2D ^{1}H-^{15}N and ^{14}N-^{1}H correlation spectra, it is evident that the ^{1}H lineshapes are significantly broader in Fig. 6.8c. This is owed to the relative spinning frequencies between the two cases, (22 kHz versus 60 kHz respectively). Unsurprisingly, ^{15}N lineshapes are significantly narrower relative to ^{14}N lineshapes. As ^{15}N lineshapes have no contribution from the quadrupolar interaction, quadrupolar broadening effects are not present, unlike ^{14}N lineshapes, where the quadrupolar interaction contributes a significant broadening effect. Furthermore, there is a noticeable difference between the ^{15}N shifts relative to ^{14}N. As discussed above, the second-order quadrupolar interaction contains an isotropic term, which for a spin-1 nucleus is described by equation 2.112, explaining the significant difference between ^{15}N and ^{14}N isotropic shifts.

6.5 Conclusions

The 2D ^{14}N-^{1}H HMQC experiment indirectly observes ^{14}N via a spy nucleus, in this case ^{1}H, in relatively short experimental times, without any requirement for isotopic labelling. Where correlation is achieved through NH heteronuclear dipolar couplings, a qualitative description of relative distances between proton and nitrogen atoms can be established through variation of the heteronuclear dipolar recoupling time. Furthermore, information concerning electric field gradients, which may yield further insight into the structure and dynamics, and which is inaccessible from ^{15}N NMR, can also be extracted from a 2D ^{14}N-^{1}H HMQC spectrum.

Investigation into the effect of spinning frequencies showed that successful observation of higher ^{14}N C_Q sites in ^{14}N-^{1}H spectrum is dependent upon using faster spinning frequencies, i.e., $\nu_r = 60$ kHz. Faster spinning frequencies are necessary to average strong ^{1}H-^{1}H dipolar couplings, and also lengthen ^{1}H dephasing times. The majority of spectra presented achieved NH correlation by exploiting heteronuclear dipolar couplings. The advantage of this approach is that by recording spectra using different duration recoupling periods, it is possible to establish different range proximities within a molecule. This was evident for the dipeptide β-AspAla, where short recoupling periods revealed one-bond couplings only, however an increase in the recoupling duration revealed longer range correlations. Acquisition of 2D ^{14}N-^{1}H HMQC spectra at a series of recoupling durations allow for the construction of NH dipolar build-up curves. Build-up curves were presented for the dipeptide β-AspAla; short range couplings were observed to dephase rapidly at longer recoupling times, whereas in general, longer range proximities continued to increase in intensity at longer recoupling times. Using SPINEVOLUTION, simulations for 8-spin systems constructed around the NH and NH_3^+ β-AspAla groups were presented; for the NH group in β-AspAla this was observed to be in relatively good agreement with experiment. Complete agreement was not possible, as including all relaxation mechanisms in a simulation is challenging owing to the limited spin-size in simulations.

As opposed to magnetisation transfer exploiting heteronuclear dipolar couplings, transfer mechanisms via through-bond couplings and residual dipolar splitting is also possible. Correlation in this manner is more definitive for identifying directly bonded

NH groups. The disadvantage of this method is that it does not reveal longer-range NH proximities, and therefore does not yield information concerning intermolecular packing configurations. Furthermore, owing to the relative small magnitude of scalar couplings and RDS, then transfer efficiency is diminished, observed herein as a decrease in intensity by a factor of two for comparable ^{14}N-^{1}H correlation spectra of β-AspAla.

Probing hydrogen bonding motifs is of importance as they reveal intermolecular packing configurations which influence the physical properties of a material. Hydrogen bonding motifs in a guanosine derivative were identified using 2D ^{14}N-^{1}H HMQC experiments. For a short recoupling time, only one-bond correlations are observed, however at a longer recoupling time, longer-range correlations were observed. For the guanosine derivative, different duration recoupling periods revealed various NH correlations: short recoupling periods revealed one-bond NH correlations only, however increasing the recoupling duration revealed intermolecular correlations, including hydrogen bonding interactions.

CHAPTER

SEVEN

^{14}N-^{1}H SPECTRA OF PHARMACEUTICALS

7.1 Introduction

In the design process of an active pharmaceutical ingredient (API), preferred chemical properties do not always coincide with favourable physical properties, such as solubility, bio-availability and chemical stability. Currently, a number of methodologies are available to improve physical properties, the most common of these being delivery as a pharmaceutical salt. However, this requires the API to contain an ionisable functional group, consequently limiting accessible design space. A less established drug delivery form are cocrystals, [80, 82–85] which have been demonstrated to enhance numerous physical properties in a range of APIs. [149, 206–208] As discussed in chapter 1, a pharmaceutical cocrystal is typically considered to consist of two or more neutral molecular constituents, that are solid when separate, where one of the constituents is the API, non-covalently bound in a crystal lattice, and most commonly interacting via hydrogen bonding. [88] A wide range of molecules can be potentially used to form cocrystals with an API as there is no requirement for a sufficiently ionising functional group, therefore increasing the accessible design space attainable compared to salts. Widespread acceptance is partially limited by a lack of suitable characterisation techniques for confirming cocrystal formation. As discussed in chapter 1, the solvent drop grinding (SDG) method is the most common methodology used for cocrystal discovery, however SDG does not easily allow for growing of a single crystal required for Single Crystal X-ray Diffraction (SCXRD). [209] Additionally, powder X-ray diffraction methods are limited

by an inability to identify different potential polymorphs that may be formed during synthesis. Locating the positions of light elements (e.g., ^{1}H), which is an important consideration when determining the presence of a hydrogen bonding interaction, can also be challenging when using diffraction methods.

Amorphous solid dispersions also offer relative improvements of physical properties such as solubility, which can impact upon bio-availability. [86,87,210–212] Amorphous dispersions in the solid state typically consist of a poorly water soluble drug in a solid dispersion with a polymeric hydrophilic carrier. Amorphous phases often have improved solubility relative to the crystalline state. However, owing to the deviation away from the equilibrium state, amorphous forms are considered thermodynamically unstable and readily convert back to the crystalline state, often under typical pharmaceutical storage conditions. [213] Solid dispersions of an amorphous solid with a highly water-soluble polymer can improve stability, whilst maintaining improved physical properties associated with the amorphous form. [214,215] In solid dispersions, the API can exist as a separate amorphous or crystalline phase, or as a glass solution where the degree of contact varies from a full intimate mixture, towards a state consisting of regions of distinct amorphous or crystalline character. [87] A glass solution is typically favourable, as it is generally most soluble and the risk of separation into less desirable crystalline phases is diminished. [216–218] Differential scanning calorimetry (DSC) and other thermal methods are widely utilised for the characterisation of solid amorphous dispersions. [219,220] However the potential complexity of dispersions can impair the suitability of thermal methods if applied as a stand-alone method. [93] Furthermore, whilst providing access to the bulk properties of the material, detailed structural information is limited from thermal methods. Traditional X-ray diffraction techniques are hindered by a lack of long-range order, and are generally only used to ascertain an absence of crystalline material. [93]

2D ^{14}N-^{1}H HMQC experiments introduced in chapter 6 are demonstrated as a potential screening method for pharmaceutical solids. Firstly, application of the 2D ^{14}N-^{1}H pulse sequence to a pharmaceutical compound, namely cimetidine, which was studied using ^{15}N NMR methods in chapter 5, is presented. 2D ^{14}N-^{1}H HMQC experiments for a cocrystal and an amorphous dispersion were performed, with the principal aim of identifying hydrogen bonding interactions between individual molecular compo-

nents, and therefore proving molecular association. Experimental results were complemented by using the GIPAW methodology to calculate ^{1}H and ^{14}N isotropic chemical shifts and ^{14}N EFG (electric field gradient) parameters, where crystal structure are available.

7.2 Experimental and computational details

7.2.1 Sample preparation

A cocrystal of nicotinamide and palmitic acid was prepared as described in previous studies. [89] A solid amorphous dispersion containing 50% w/w acetaminophen (Sigma-Aldrich, St. Louis, MO) and PVP was prepared as described by de Villers *et. al.*. [221] All samples were provided by GlaxoSmithKline, and prepared at their facilties. PVP and a 50% w/w PVP-acetaminophen amorphous dispersion were heated at 110 °C for 24 hours prior to acquisition, and samples packed in a glove box in order to limit water absorption.

7.2.2 Solid-state NMR

^{14}N-^{1}H experiments were performed using a Bruker Avance III spectrometer operating at a ^{1}H Larmor frequency of 850.1 MHz using a Bruker 1.3 mm triple resonance probe, operating in double resonance mode at an MAS frequency of 60 kHz unless otherwise stated. A recycle delay of 30 seconds was used for all samples unless otherwise stated. Rotary resonance recoupling (R^3) with an $n = 2$ resonance condition with an x−x phase inversion of individual block lengths of duration 16.7 μs was implemented. The States method was applied to restore sign-discrimination in F_1 for all 2D ^{14}N-^{1}H spectra presented. A 4-step nested phase cycle was used to select changes in coherence order $\Delta p = \pm 1$ (on the first ^{1}H pulse, 2 steps) and $\Delta p = \pm 1$ (on the final ^{14}N pulse, 2 steps). Magic angle calibration was achieved by optimising a ^{23}Na Satellite Transition MAS (STMAS) experiment for Na_2HPO_4, where accurate magic angle setting is also required to remove any large first order quadrupolar interactions. For cimetidine, 2D ^{14}N-^{1}H HMQC experiments were performed with a rotor-synchronised t_1 increment, and for each t_1 FID, 80 transients were co-added. A recycle delay of 5 s was used for all cimetidine experiments. Nitrogen chemical shifts were secondary referenced to a

saturated NH_4Cl aqueous solution at -352.9 ppm, which was primary referenced to CH_3NO_2 at 0 ppm. ^{1}H chemical shifts were secondary referenced to adamantane at 1.63 ppm, primary referenced to TMS at 0 ppm.

^{15}N CPMAS experiments were performed using a Bruker Avance III spectrometer operating at a ^{1}H Larmor frequency of 500.1 MHz, using a 4 mm Bruker triple resonance probe operating in double resonance mode at a spinning frequency of 10 kHz. SPINAL-64 ^{1}H decoupling was applied during t_2 at a nutation frequency of 100 kHz, using acquisition times of 20 ms (nicotinamide), 30 ms (nicotinamide palmitic-acid), and 20 ms (PVP, acetaminophen, 50% w/w PVP-acetaminophen). A CP contact time of 6 ms was used in all ^{15}N CPMAS spectra. A 90-100 % ramp was used for nicotinamide palmitic-acid, acetaminophen and PVP-acetaminophen, whereas a constant amplitude cross-polarisation step was used for nicotinamide and PVP. ^{15}N chemical shifts are referenced to NH_3^+ in L-histidine.HCl.H_2O at -333.4 ppm, corresponding to CH_3NO_2 at 0 ppm. Further experimental details can be found in the respective figure captions.

2D ^{1}H-^{15}N CP HETCOR experiments were recorded by Dr. Frederick Vogt at GlaxoSmithKline, USA, using a Bruker Avance II+ spectrometer operating at a ^{1}H Larmor frequency of 500.1 MHz and a 4 mm probe at a spinning frequency of 14 kHz. The ^{1}H 90° pulse was of duration 2.5 μs. ^{15}N magnetisation was created using a CP ramp of magnitude 50% to 100%. 1024 transients were co-added using a recycle delay of 5 seconds. A total of 32 t_1 FIDs were recorded at increments of 56.6 μs using the States-TPPI method to achieve sign discrimination in F_1. Homonuclear decoupling at a ^{1}H nutation frequency of 100 kHz was achieved using FSLG decoupling. ^{15}N chemical shifts were directly referenced to CH_3NO_2. Further experimental details can be found in the respective figure captions.

7.2.3 Computational

First-principles calculations were performed using the academic release of CASTEP version 4.3, which implements density-functional theory using a planewave basis set. All calculations presented used a PBE exchange-correlation functional and on-the-fly pseudopotentials.

The calculation parameters used for cimetidine were presented in chapter 5.2.3. Isolated molecule calculations were performed by extraction of a single molecule from

the geometry optimised crystal structure. The extracted molecule was then used to construct a periodically repeating unit cell containing one molecule with a unit cell with dimensions 20 x 20 x 20 Å, therefore effectively removing any intermolecular interactions.

Initial geometry optimisation of protons was performed by starting with the X-ray single-crystal structure obtained from the CSD database. For nicotinamide the CSD refcode is NICOAM01, [222] and Z = 4, i.e., 60 atoms in the unit cell. The CSD refcode of nicotinamide palmitic-acid is JEMDIP, [223] and Z = 2, i.e., 130 atoms in the unit cell. The geometry optimisation and NMR calculations used a cut-off energy equal to 1100 eV and a k-point spacing of 0.1 $\times$ 2π Å^{-1} with a Monkhurst-Pack grid.

7.3 Cimetidine

Cimetidine, an anti-ulcer drug, was introduced in section 5.3.3. It was demonstrated, using ^{15}N CPMAS and $^{1}J_{15N\text{-}1H}$ spectral editing methods, that cimetidine has six nitrogen sites, three of which have couplings to directly bonded protons. However, details regarding intermolecular packing configurations are not easily obtained from the ^{15}N spectra presented in chapter 5. 2D ^{14}N-^{1}H HMQC experiments were applied to cimetidine Form A to demonstrate their suitability for probing intra- and intermolecular nitrogen-proton proximities. In order to aid assignment, a one-pulse ^{1}H NMR spectrum, obtained using an MAS frequency of 60 kHz, is presented in Fig. 7.1; note that the NH and aromatic CH proton resonances are well resolved. GIPAW calculations were also employed to aid assignment (see Table 7.1). In Fig. 7.2, a comparison between the molecular positions before and after geometry optimisation, performed using the CASTEP code, is presented.

Figure 7.3a shows ^{14}N-^{1}H correlation spectra of cimetidine recored with two different recoupling times, τ_{RCPL} = (a) 200 μs and (b) 600 μs, which allow the observation of one-bond and longer-range correlations, respectively. One-bond ^{14}N-^{1}H correlation peaks are observed in Fig. 7.3a, as annotated on the 2D contour plot. An additional weaker, longer-range, correlation is also seen for N3 to H2, corresponding to an intramolecular proximity to an aromatic proton within the same 5-membered ring.

For the ^{14}N-^{1}H spectrum in Fig. 7.3b, recorded with the longer recoupling time

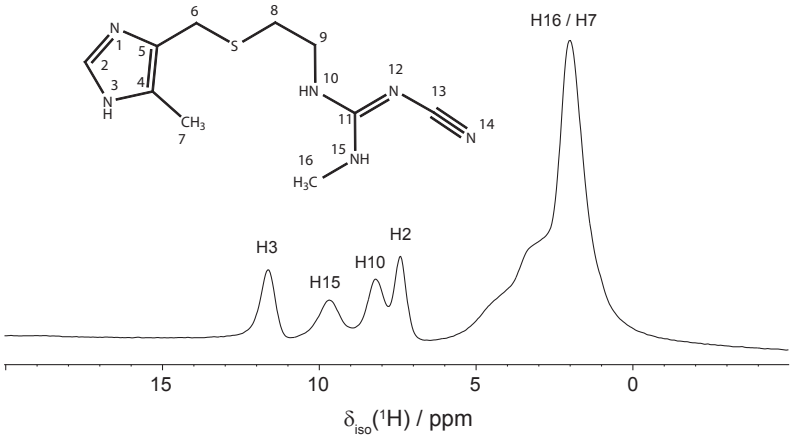

Figure 7.1: ^{1}H (850 MHz, 60 kHz MAS) one-pulse spectrum of cimetidine form A. Proton resonances of particular interest are labelled. Transverse magnetisation was created using a 1.2 μs 90° pulse, and the t_2 acquisition time was equal to 16 ms. A total of 16 transients were co-added using a recycle delay of 5 s.

Table 7.1: A comparison of ^{15}N and ^{14}N experimental and GIPAW calculated shifts for cimetidine

Sites	$\delta(^{15}\mathrm{N})_{expt}$ / ppm	$\delta(^{15}\mathrm{N})_{calc}{}^{a}$ / ppm	$\delta(^{14}\mathrm{N})_{expt}{}^{b}$ / ppm	$\delta(^{14}\mathrm{N})_{calc}{}^{c}$ / ppm
N1	−128.1	−132.5	75	67.2
N3	−210.7	−206.6	−155	−134.8
N10	−284.6	−286.7	−20	1.3
N12	−295.4	−296.5	−65	−68.5
N14	−191.3	−190.0	−95	−106.4
N15	−297.7	−295.3	−70	−41.1

[a] $\delta_{iso} = -(\sigma_{iso} - \sigma_{ref})$, where σ_{ref} for ^{15}N was −165.2 ppm. This was calculated from addition of the mean average of the experimental isotropic chemical shifts and the mean average of σ_{iso} values. [b] Centre of gravity of the second-order quadrupolar broadened lineshape, with an associated error of ±5 ppm.
[c] $\delta(^{14}\mathrm{N})_{calc} = \delta(^{15}\mathrm{N})_{expt} + \delta_{QIS}(^{14}\mathrm{N})_{calc}$, where $\delta_{QIS}(^{14}\mathrm{N})_{calc}$ has been calculated using a consistent scaling of the calculated C_Q values by a factor of 0.95.

of $\tau_{\mathrm{RCPL}} = 600$ μs, longer-range N...H correlations were observed in addition to the one-bond N-H correlations. Of particular interest are the two longer-range intermolecular N...H correlations. These arise from intermolecular N...H-N hydrogen-bonding motifs, as visualised in Fig. 7.3f, namely N14...H10-N10 and N12...H3-N3. Additionally, longer-range intramolecular through-space correlations are seen for N15 to the H16 methyl protons, N3 to the H7 methyl protons and N1 to the aromatic H2 proton. Note that a correlation peak between N1 and H15 corresponding to the N1...H15-N15 intramolecular hydrogen bond is not evident above the noise level. This is a consequence of faster dephasing for the H15 resonance, which is evident from the larger reduction

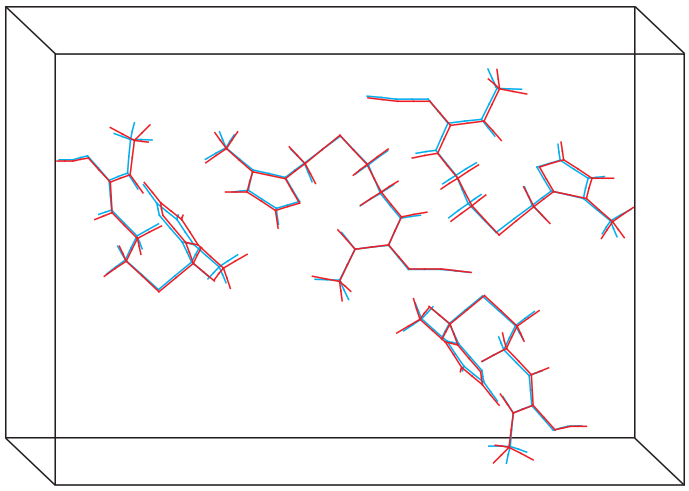

Figure 7.2: Cimetidine crystal structure (CIMETD) [161] showing: before (blue) and after (red) geometry optimisation. The single molecule used for calculations presented in Table 7.3 was extracted from the geometry optimised full crystal structure without further optimisation.

in signal of the one-bond N15-H15 correlation peak relative to that of the other one-bond correlations at the longer recoupling time (Fig. 7.3b). To aid assignment, all NH distances less than 3 Å are presented in Table 7.2. One-bond correlations are in bold typeface, and intermolecular correlations in italic typeface. Distances were extracted from the geometry optimised full crystal structure of cimetidine.

For comparison, a ^{1}H-^{15}N CP-HETCOR spectrum of cimetidine Form A is presented in Fig. 7.3c, rotated through 90° in order to aid comparison to the ^{14}N-^{1}H spectra presented in Fig. 7.3a and b. The striking difference (50-260 ppm) between the ^{14}N shifts (Fig. 7.3a and b) and the ^{15}N isotropic chemical shifts (Fig. 7.3c) is due to the contribution from the isotropic second-order quadrupolar shift. In this respect, comparison between ^{15}N isotropic chemical shifts and the centre of gravity of the ^{14}N lineshapes that are broadened due to second-order quadrupolar broadening allows the experimental determination of P_Q, which is inaccessible from ^{15}N NMR.

GIPAW calculated isotropic ^{1}H chemical shifts and the corresponding experimental values for cimetidine are listed in Table 7.3. Quantitative insight into intermolecular hydrogen-bonding strengths can be extracted by comparing chemical shifts calculated for the full crystal structure with those calculated for an isolated molecule.

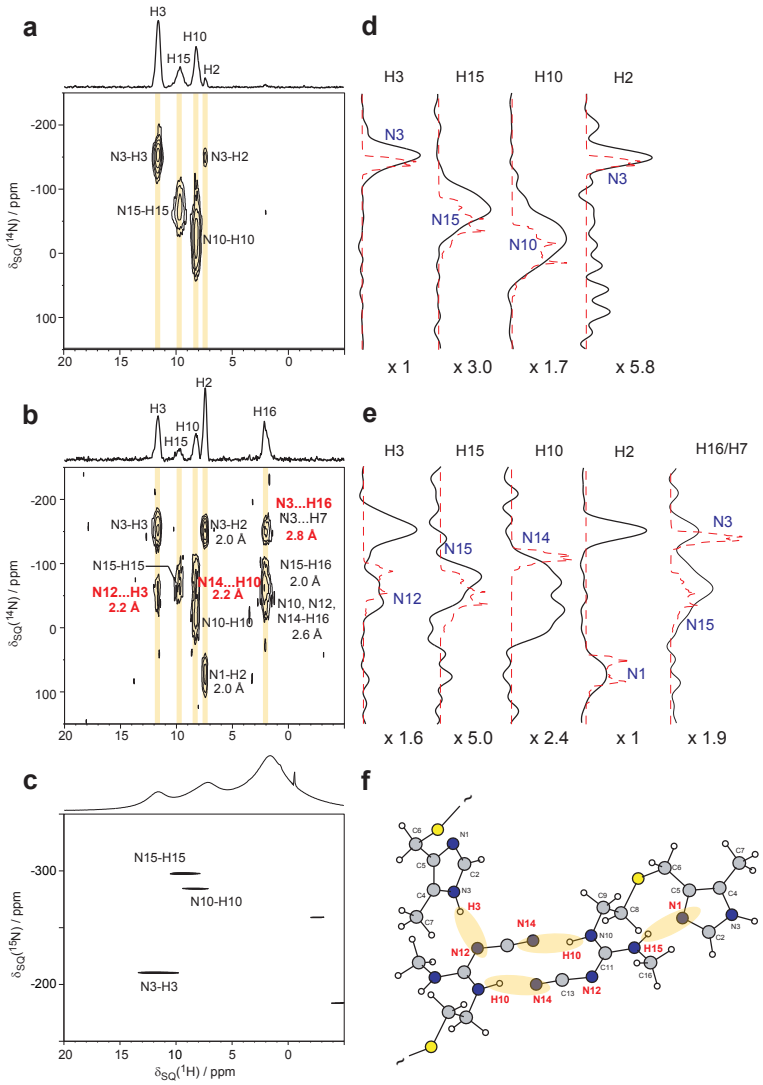

Figure 7.3: (a, b) 2D ^{14}N-^{1}H HMQC spectra with ^{1}H skyline projections of cimetidine ($\nu_r = 60$ kHz) recorded at 850 MHz using $n = 2$ rotary resonance recoupling (R^3) of ^{14}N-^{1}H heteronuclear dipolar couplings for (a) $\tau_{RCPL} = 200$ μs and (b) $\tau_{RCPL} = 600$ μs. For peaks corresponding to longer-range N...H proximities, the nearest distance as extracted from the geometry-optimised (CASTEP) crystal structure is stated. Intermolecular hydrogen-bonding correlations are shown in red. (c) 2D ^{1}H-^{15}N CP-HETCOR spectrum ($\nu_r = 14$ kHz, 500 MHz) acquired with a contact time of 100 μs and applying ^{1}H FSLG homonuclear decoupling in t_1. The single-pulse ^{1}H MAS spectrum is plotted along the rotated F_1 (horizontal) axis. The experimental times were 6 hours for the ^{14}N-^{1}H experiments and 46 hours for the ^{1}H-^{15}N experiment. The base contour levels are at (a) 8%, (b) 10% and (c) 62% with respect to the maximum peak height. (d, e) Individual ^{14}N subspectra taken through each ^{1}H resonance (black trace) overlaid with spectra simulated for each ^{14}N site using SPINEVOLUTION (red trace). ^{14}N isotropic chemical shift parameters used in simulation were found experimentally using ^{15}N CPMAS (Fig. 5.3), while the corresponding ^{14}N quadrupolar parameters were calculated using the GIPAW method within CASTEP - a consistent scaling by a factor of 0.95 was applied to the calculated C_Q values to give best agreement between the centres of gravity of the experimental and simulated lineshapes. (f) Visualisation of the geometry-optimised (CASTEP) crystal structure, showing N...H-N hydrogen bonding (red numbering).

Table 7.2: NH distances up to 3 Å in cimetidine form A, extracted from the geometry optimised (CASTEP) crystal structure. One-bond correlations are denoted in bold and intermolecular correlations shown in italic.

Sites	Distance / Å	Sites	Distance / Å
N1-H15	1.84	**N3-H3**	**1.04**
N1-H2	2.16	N3-H2	2.15
N1-H8a	2.42	N3-H7b	2.81
N1-H6a	2.78	*N3-H16a*	*2.88*
N1-H16a	*2.99*	N3-H7c	2.93
N10-H10	**1.04**	**N15-H15**	**1.05**
N10-H9a	2.07	N15-H16a	2.06
N10-H9b	2.08	N15-H16c	2.12
N10-H16a	2.61	N15-H16b	2.12
N10-H8a	2.72	N15-H9b	2.62
N10-H8b	2.80	N15-H8a	2.95
N12-H3	*1.88*	*N14-H10*	*1.88*
N12-H10	2.61	N14-H16c	2.59
N12-H16b	2.63	*N14-H6a*	*2.93*
N12-H7a	*2.92*	*N14-H9b*	*2.97*

Table 7.3: A comparison for cimetidine between experimental ^{1}H isotropic chemical shifts and isotropic chemical shifts calculated using the GIPAW method for the full crystal structure and an isolated molecule.

Site	δ_{iso}(exp) / ppm	δ_{iso}(crystal)^a / ppm	δ_{iso}(molecule)^a / ppm
H7a	2.0	2.0	0.9
H7b	2.0	0.4	0.9
H7c	2.0	1.6	1.1
H16a	2.0	0.4	1.2
H16b	2.0	1.5	2.0
H16c	2.0	2.6	1.3
H8a	2.0 - 4.0	1.3	2.0
H8b	2.0 - 4.0	0.2	0.4
H9a	2.5 - 3.4	2.4	2.4
H9b	2.5 - 3.4	2.7	1.7
H6a	4.0 - 4.5	3.4	2.7
H6b	4.0 - 4.5	3.0	1.8
H2	7.4	7.1	6.5
H10	8.2	8.2	5.2
H15	9.7	9.6	8.6
H3	11.6	11.9	8.1

[a] $\delta_{iso} = -(\sigma_{ref} - \sigma_{iso})$, where σ_{ref} for ^{1}H was 29.6 ppm. The σ_{ref} value was calculated from addition of the mean average of the experimental isotropic chemical shifts and the mean average of the calculated σ_{iso} values. Due to limited resolution of the methyl and aliphatic protons, only CH and NH experimental values were included for ^{1}H σ_{ref} calculations.

Compared to a full molecule, protons involved in intermolecular hydrogen bonding are not deshielded for an isolated molecule. Therefore, when comparing calculations between isolated and full crystal structure calculated proton chemical shifts, protons with large differences in $\delta_{iso}(^1\mathrm{H})$ are assumed to be strongly hydrogen bonded in the full crystal structure. Inspection of Table 7.3 reveals significant deshielding of H3 and H10 in the full crystal structure calculation as compared to the single molecule calculation, that is due to strong intermolecular hydrogen bonding between N3-H3...N12 and N10-H10...N14. A much smaller crystal to molecule change is observed for H15, which participates in an intramolecular N15-H15...N1 hydrogen bond.

Using a combination of ^{14}N-^{1}H correlation experiments and GIPAW calculations a detailed picture of NH proximities in cimetidine has been established. Identification of hydrogen bonding interactions which involve NH correlations were determined from ^{14}N-^{1}H correlation experiments, which were complemented by comparison between GIPAW calculated ^{1}H chemical shifts for the full crystal structure and an isolated single molecule. Identifying intermolecular hydrogen bonding interactions, where nitrogen often acts as either a proton acceptor or donor, is of particular interest for proving molecular association in various solid delivery forms described within this chapter. Further work is required to understand the fast dephasing of nitrogen correlations to specific protons, namely H15 in cimetidine, which may be problematic when observing longer range NH correlations (e.g., > 2Å).

7.4 Cocrystals

The example cocrystal chosen was nicotinamide palmitic-acid (CSD refcode: JEMDIP [223]), shown in Fig. 7.4, which consists of two molecular components, nicotinamide (CSD refcode: NICOAM01 [222]) and palmitic-acid (CSD refcode: YEFWEM [224]). Previous work has demonstrated the capability of solid-state NMR for the characterisation of cocrystal formations using a series of ^{13}C and ^{1}H solid-state NMR techniques, [89–91] however ^{14}N-^{1}H HMQC experiments offer a direct probe of hydrogen bonding motifs involving an N...H hydrogen bond.

Figure 7.5 presents a 2D ^{14}N-^{1}H HMQC spectrum of nicotinamide and the nicotinamide palmitic-acid cocrystal, both recorded with a τ_{RCPL} duration of 666.7 μs.

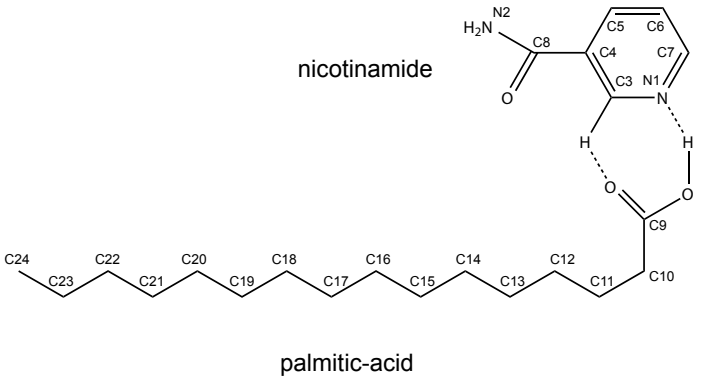

Figure 7.4: Skeletal structure of the nicotinamide palmitic-acid cocrystal

Table 7.4: NH distances within 3 Å proximity taken from the geometry optimised (CASTEP) crystal structures of nicotinamide (top) and nicotinamide palmitic-acid (bottom). One-bond correlations are denoted in bold, and intermolecular correlations are denoted in italic.

Sites	Distance / Å	Sites	Distance / Å
N1-H2b	*2.06*	**N2-H2a**	**1.03**
N1-H3	2.06	**N2-H2b**	**1.03**
N1-H7	2.07	N2-H5	2.70
N1-H1	*1.67*	**N2-H2a**	**1.03**
N1-H3	2.06	**N2-H2b**	**1.04**
N1-H7	2.07	N2-H5	2.66

In Fig. 7.5a, the spectrum shows distinct cross-peaks for both nitrogen sites in nicotinamide. The strongest correlations are one-bond correlations between N2 and the NH_2 protons (H2a and H2b). A weaker NH correlation for pyridine N1 was also observed. The proximity of H2b, H3 and H7 to N1 are comparable (see Table 7.4), which combined with a narrow proton chemical shift range and poor proton resolution suggests that the cross-peak is a combination of different proton correlations to N1. Cross-peaks between N1...H3 and N1...H7 correlations arise from intramolecular correlations, whereas N1...H2b is an intermolecular dipolar correlation across the hydrogen bond.

In Fig. 7.5b, the 2D spectrum of nicotinamide palmitic-acid is presented. A clear correlation between a nitrogen of nicotinamide (N1) and a hydrogen in palmitic-acid (H1) is observed, and is labelled N1...H1. The stark difference in the isotropic chemical shift of H1 in palmitic acid relative to any nicotinamide proton and the absence of nitrogen nuclei in palmitic-acid unambiguously show that the NH cross-peak is indicative of a hydrogen bonding interaction between N1...H1-O2, illustrating molec-

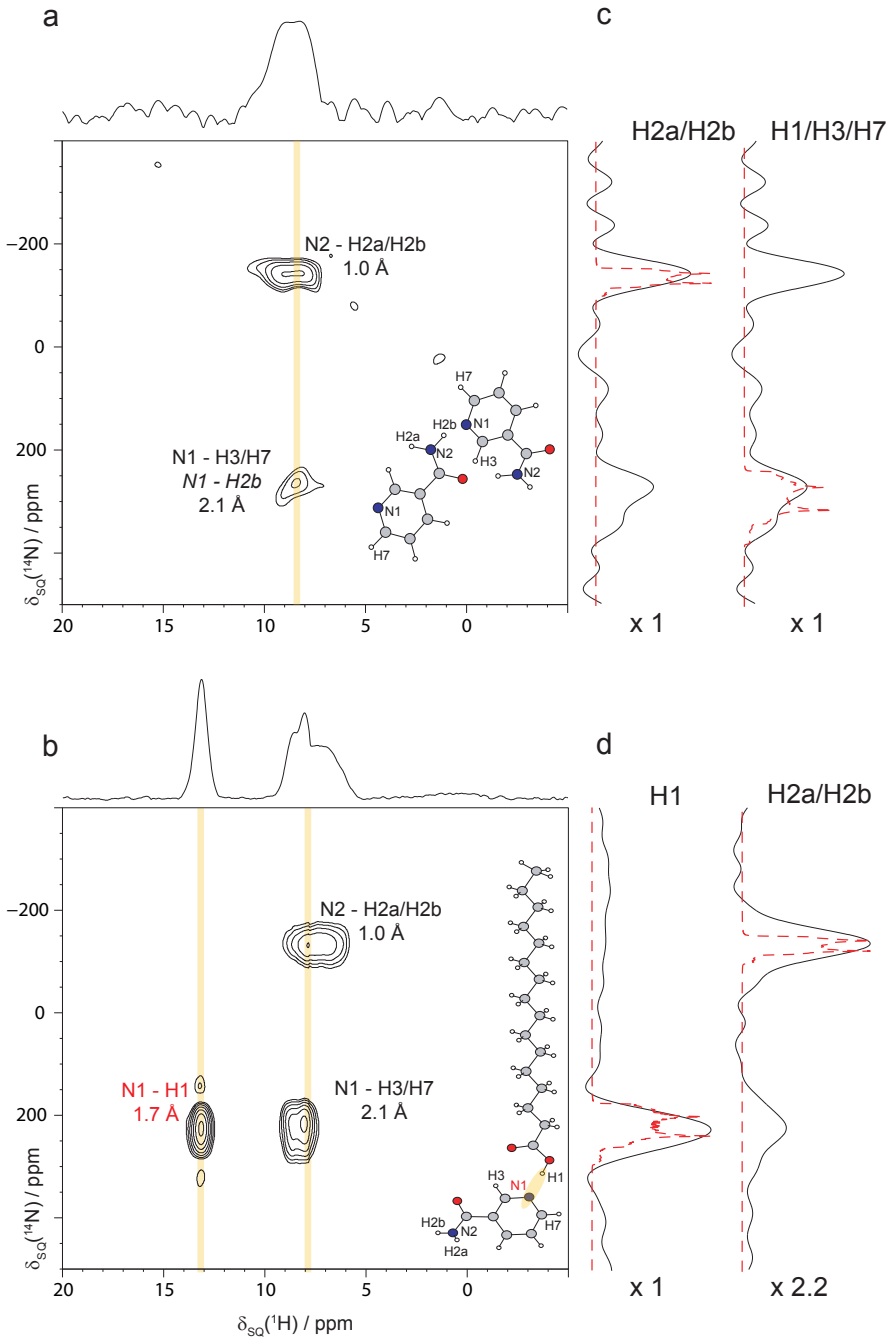

Figure 7.5: 2D ^{14}N-^{1}H HMQC spectra recorded at $\nu_0(^1\mathrm{H}) = 850.1$ MHz and for an MAS frequency of 60 kHz (a) nicotinamide and (b) the nicotinamide palmitic-acid cocrystal using recoupling at the $n = 2$ rotary resonance condition for a τ_{RCPL} duration of 666.7 μs for both cases. For nicotinamide, each of the 26 t_1 FIDs were recorded with a total of 184 co-added transients, whereas 30 t_1 FIDs increments were acquired using 100 co-added transients for nicotinamide palmitic-acid. The base contour levels are at (a) 35% and (b) 12% to the maximum peak height. (c, d) ^{14}N lineshape extractions taken through the highlighted area of the spectrum, overlaid with simulated lineshapes calculated using SPINEVOLUTION. Inputted isotropic chemical shift parameters were taken from ^{15}N CPMAS spectra (see Fig. 7.6) and quadrupolar parameters from GIPAW calculations discussed above. In order to aid comparison between experimental and simulated ^{14}N lineshapes, projections along F_1 were simulated with C_Q values scaled by (c) 96% and (d) 97% of calculated GIPAW values.

Table 7.5: A comparison of ^{15}N and ^{14}N experimental and GIPAW calculated shifts for nicotinamide (top) and nicotinamide palmitic-acid (bottom).

Site	$\delta(^{15}\mathrm{N})_{expt}$ / ppm	$\delta(^{15}\mathrm{N})_{calc}{}^{a}$ / ppm	$\delta(^{14}\mathrm{N})_{expt}{}^{b}$ / ppm	$\delta(^{14}\mathrm{N})_{calc}{}^{c}$ / ppm
N1	−77.6	−78.3	270	293.6
N2	−276.6	−274.3	−140	−131.5
N1	−86.9	−84.1	225	225.9
N2	−272.4	−276.7	−130	−134.8

[a] $\delta_{iso} = -(\sigma_{iso} - \sigma_{ref})$, where σ_{ref} for ^{15}N was −160.4 ppm. This was calculated from addition of the mean average of the experimental isotropic chemical shifts and the mean average of σ_{iso} values.
[b] Centre of gravity of the second-order quadrupolar broadened lineshape, with an associated error of ±5 ppm. [c] $\delta(^{14}\mathrm{N})_{calc} = \delta(^{15}\mathrm{N})_{expt} + \delta_{QIS}(^{14}\mathrm{N})_{calc}$, where $\delta_{QIS}(^{14}\mathrm{N})_{calc}$ has been calculated using a consistent scaling of the calculated C_Q values by a factor of 0.96 (nicotinamide) and 0.97 (nicotinamide palmitic-acid).

ular association. The N1...H1 distance measured from the geometry optimised crystal structure is 1.7 Å (see Table 7.4); therefore owing to the close range proximity, a strong N1-H1 correlation peak is observed at a suitable recoupling duration. Furthermore, intramolecular pyridine nitrogen correlations are observed between N1 and the H3/H7 protons. As in the nicotinamide spectrum, an N2 correlation to the NH_2 protons is observed. Additionally, a small decrease in the relative shielding of the NH_2 proton chemical shifts in the cocrystal relative to nicotinamide is observed, again providing evidence of a change in the intermolecular packing configuration.

Inspection of Table 7.5 reveals significant differences between the isotropic ^{15}N chemical shift values and the ^{14}N isotropic shift projections. As discussed above, this is due to ^{14}N being a $I = 1$ nucleus, therefore the quadrupolar interaction must be taken into consideration, unlike for spin-$\frac{1}{2}$ nuclei such as ^{1}H or ^{15}N. GIPAW calculations and ^{15}N CPMAS spectra (see Fig. 7.6) both show that there are only small differences in the ^{15}N isotropic chemical shifts between the cocrystal and nicotinamide for both N1 and N2. Note, that in Fig. 7.6a, the resonance N1 is assigned from a GIPAW calculation, as the experimental signal to noise is not sufficiently high enough to reliably assign from the ^{15}N CPMAS spectrum alone. Therefore, the additional isotropic shift in the ^{14}N dimension for N1 in nicotinamide relative to the cocrystal is attributed to a larger second order quadrupolar induced shift for N1 (nicotinamide). Previous studies have found that the C_Q of a nucleus, and consequently δ_{QIS}, is sensitive to changes in hydrogen-bonding geometry. [98] The observed change in δ_{QIS} is further evidence of a change in

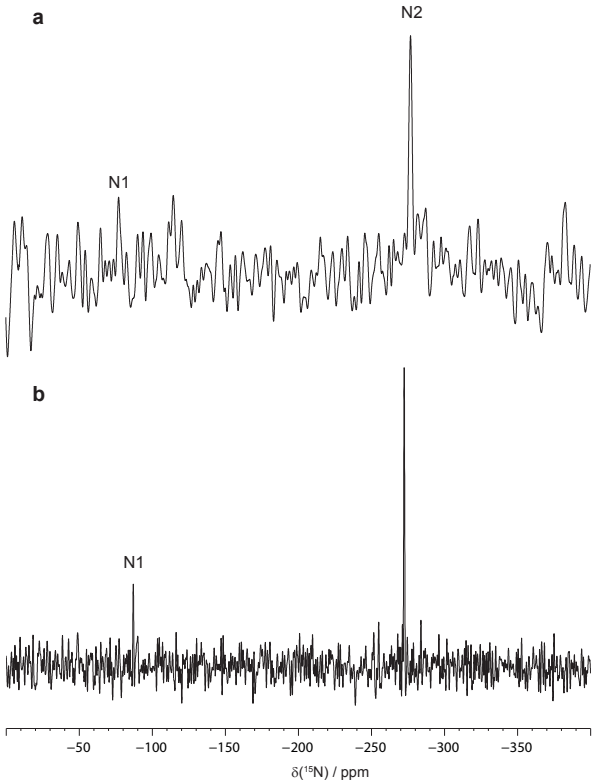

Figure 7.6: ^{15}N CPMAS (500 MHz, 10 kHz MAS) spectra of (a) nicotinamide and (b) nicotinamide palmitic-acid. (a) A total of 1890 co-added transients were recorded using a recycle delay of 120 seconds. (b) A total of 2060 co-added transients were recorded using a recycle delay of 30 seconds.

the hydrogen bonding configuration between nicotinamide and nicotinamide palmitic-acid obtainable using 2D ^{14}N-^{1}H HMQC experiments. Finally, as for the guanosine and cimetidine spectra, simulated ^{14}N projections calculated using SPINEVOLUTION are included. Inputted isotropic chemical shift values were extracted from ^{15}N CPMAS spectra, and quadrupolar parameters were obtained by GIPAW calculations.

It is evident from Fig. 7.5 that the presence of an additional NH dipolar correlation peak at a longer recoupling time is clear proof of molecular association between the individual constituents. Furthermore, the changes in the P_Q values are more pronounced in N1 (which participates in hydrogen bonding between the two separate constituents) relative to N2, due to a significant change in the surrounding local environment.

Table 7.6: A comparison of ^{15}N and ^{14}N experimental isotropic shifts for PVP, acetaminophen and 50% w/w PVP-acetaminophen amorphous dispersion.

Material	Site	$\delta(^{15}\mathrm{N})$ / ppm	$\delta(^{14}\mathrm{N})^{b}$ / ppm	$\delta_{QIS}(^{14}\mathrm{N})^{b,c}$ / ppm
PVP	Ne	-252 [a]	-5	247
Acetaminophen	N1	-244	-125	119
50% w/w	Ne	-250	0	250
50% w/w	N1	-244	-60	184

[a] ^{15}N spectral resolution of Ne (see Fig. 7.9) was calculated as an average of peaks in the amorphous CPMAS spectrum.
[b] The associated error with $\delta(^{14}\mathrm{N})_{exp}$ and consequently $\delta_{QIS}(^{14}\mathrm{N})_{exp}$ is $\pm$ 5 ppm.
[c] $\delta_{QIS}(^{14}\mathrm{N})_{exp}$ is calculated from the difference between the ^{15}N isotropic chemical shift and the experimental ^{14}N isotropic shift, and is quoted to $\pm$5 ppm

7.5 Amorphous solid-dispersions

A solid amorphous dispersion containing 50% w/w of acetaminophen and PVP was chosen to demonstrate the suitability of the ^{14}N-^{1}H HMQC experiment for amorphous dispersion characterisation. Solid-state NMR has been demonstrated in previous work as a suitable probe of amorphous dispersions, including an acetaminophen-PVP amorphous dispersion. [92]

Figure 7.7 shows 2D ^{14}N-^{1}H HMQC spectra recorded for PVP, acetaminophen and a 50% w/w PVP-acetaminophen amorphous dispersion. Recoupling times were chosen to reflect the relative NH proximities. In Fig. 7.7a, the PVP spectrum presented reveals a strong Ne-water cross peak owing to the high water content of PVP. The more interesting signal is the correlation between Ne and the aliphatic protons (Hb, Hc, Hd, Hg), seen here in the proton projection as a shoulder of the water peak at approximately 2 ppm. Confirmation that the shoulder peak does correspond to aliphatic proton chemical shifts can be seen in the 1D proton spectra in Fig. 7.8a and Fig. 7.8b, where comparison between a dried (as detailed in section 7.2.1) and a non-dried sample demonstrates that the ^{1}H resonance at approximately 2 ppm does not change when subject to high temperature, and is therefore attributed to aliphatic protons. The ^{14}N-^{1}H HMQC spectrum of acetaminophen observed in Fig. 7.7b reveals a close-range correlation labelled N1-H1, at a proton chemical shift of approximately 8 ppm.

Fig. 7.7c shows the ^{14}N-^{1}H HMQC spectrum for the amorphous dispersion using a longer τ_{RCPL} time of 666.7 μs. Interestingly, the N1 resonance has shifted from ap-

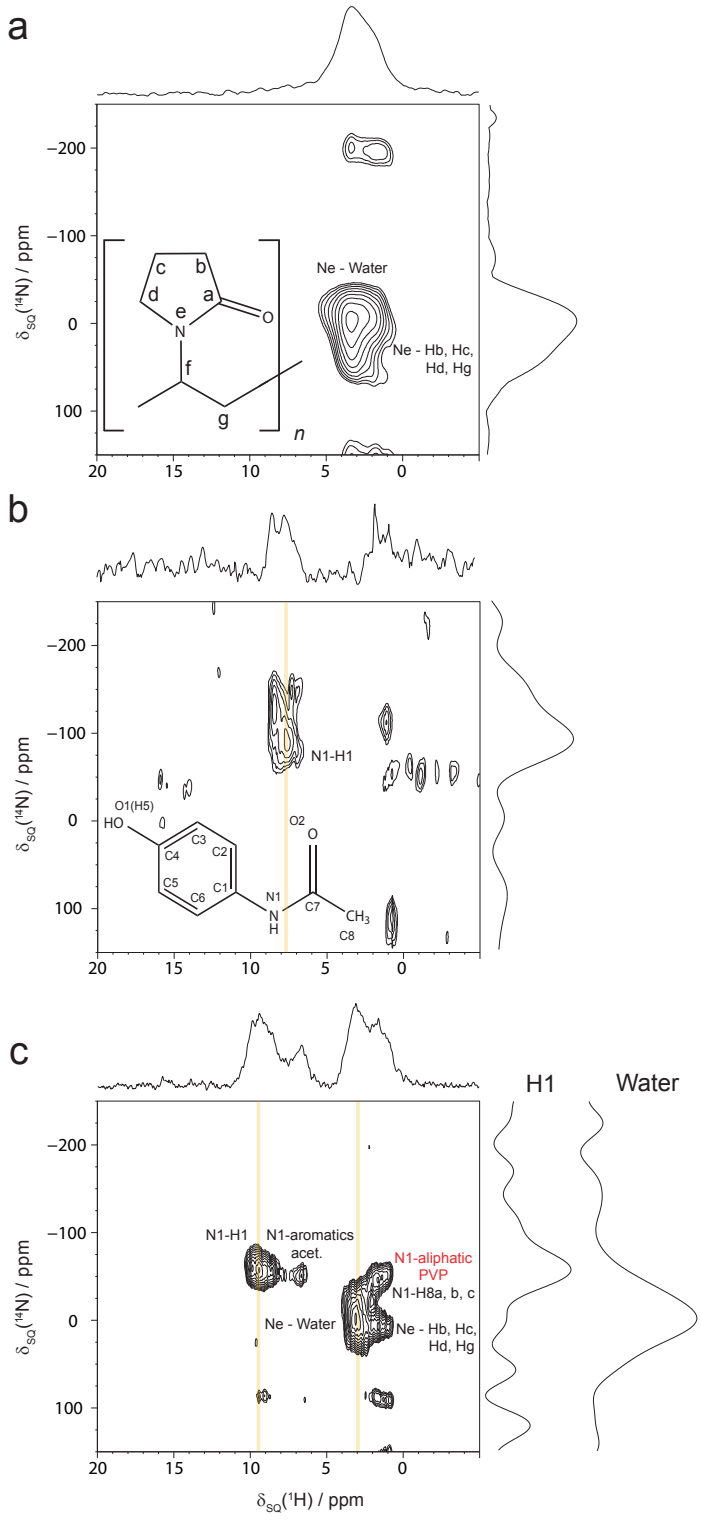

Figure 7.7: 2D ^{14}N-^{1}H HMQC spectra recorded at $\nu_0(^1\mathrm{H}) = 850$ MHz and an MAS frequency of 60 kHz for (a) PVP, (b) acetaminophen and (c) a 50% w/w PVP-acetaminophen dispersion, using the $n = 2$ rotary resonance condition for a τ_{RCPL} duration of 533.3 μs, 400 μs and 666.7 μs, respectively. The total number of co-added transients in (a-c) were 72, 64, and 100, respectively, recorded at t_1 increments of 16.7 μs for a total of 32, 30 and 40 t_1 FIDs, respectively. The base contour levels are at (a) 22%, (b) 45% and (c) 33% of the maximum peak height. Intermolecular correlations are labelled in red.

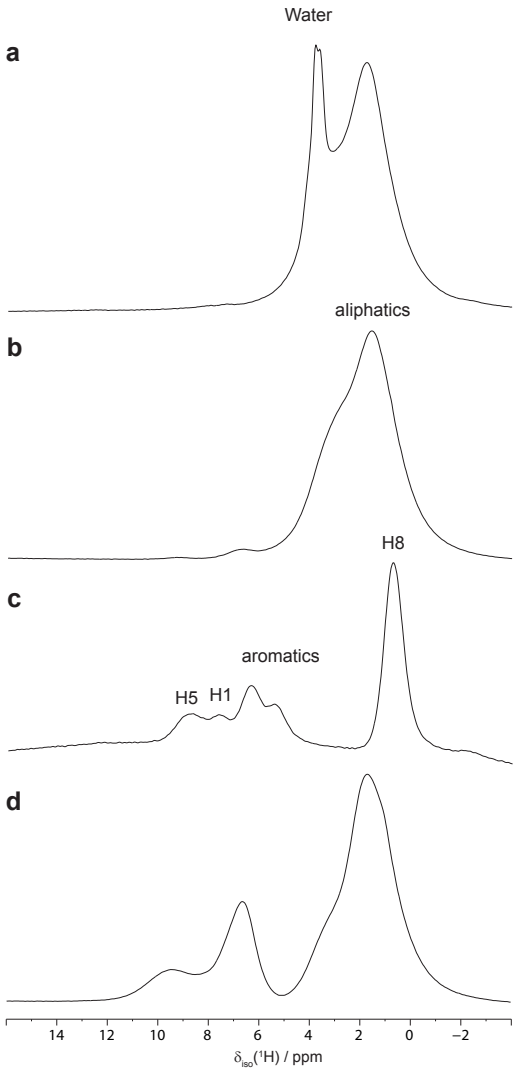

Figure 7.8: ^{1}H (850 MHz, 60 kHz MAS) one-pulse spectra of (a) PVP (non-dried), (b) PVP (dried), (c) acetaminophen and (d) a 50% w/w PVP-acetaminophen dispersion. Recycle delays of (a) 2 seconds, (b) 60 seconds, (c) and (d) 30 seconds were used, for (a, c) 32 and (b, d) 16 co-added transients.

proximately −125 ppm in the acetaminophen spectrum to approximately −60 ppm in the solid amorphous dispersion spectrum. Extraction of ^{15}N isotropic chemical shift values from ^{15}N CPMAS experiments (see Fig. 7.9) show that there is no significant change between the N1 ^{15}N chemical shift in acetaminophen and the PVP-acetaminophen dispersion; therefore, the change must be attributed to different contributions from the isotropic second-order quadrupolar induced shift, as shown in Table 7.6. The increase in ^{14}N shift indicates a change in δ_{QIS} for N1 in the amorphous dispersion relative to acetaminophen, providing evidence of a change in the hydrogen bonding geometry. If molecular association had not occurred it would be expected that both components

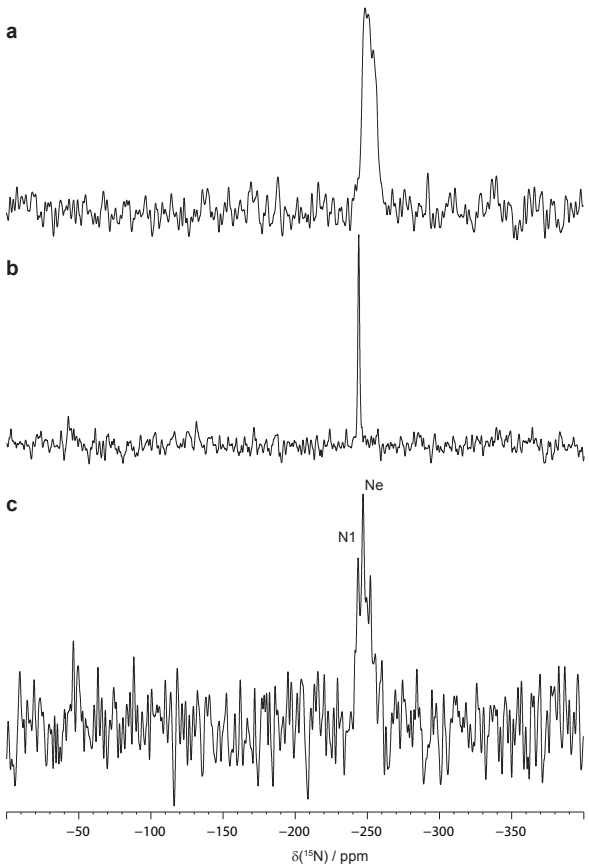

Figure 7.9: ^{15}N (500 MHz, 10 kHz MAS) CPMAS spectra of (a) PVP, (b) acetaminophen and (c) a 50 % w/w PVP-acetaminophen amorphous dispersion. A total of (a) 8440, (b) 352, (c) 6000 co-added transients were recorded using a recycle delay of (a) 10 s, (b) 90 s and (c) 10 s.

would closely match the ^{14}N shift values observed for separate molecular components, as presented in Fig. 7.7a and 7.7b.

A previously reported ^{13}C-^{1}H HETCOR spectrum of the amorphous dispersion has shown that it is not possible to discriminate between the similar ^{1}H chemical shifts of H8 in acetaminophen and most of the aliphatic protons in PVP. [92] This is also evident in the ^{1}H spectra presented in Fig. 7.8d. When acquired for the individual components, the proton chemical shifts of most aliphatic PVP protons and H8 protons in acetaminophen are distinguishable, as is observed in the individual ^{1}H spectra in Fig. 7.8. In the amorphous dispersion spectrum, it is not possible to definitively assign the N1 correlation to the proton resonance at approximately 2 ppm. However, if the cross-peak contains a contribution from dipolar coupling between N1 and H8 then this must mean that the ^{1}H chemical shift of H8 is deshielded relative to acetaminophen, as seen when compared to observation in Fig. 7.7. This would indicate a change

in the local chemical environment surrounding H8, suggesting a different molecular configuration. Alternatively, if H8 is not participating in this NH correlation transfer, then the peak at proton shift of 2 ppm must then be assigned to aliphatic protons in PVP, demonstrating molecular association between the acetaminophen and PVP constituents. An intramolecular through bond N1-H1 correlation is clearly resolved at a ^{1}H chemical shift of approximately 10 ppm. The ^{1}H chemical shift of H1 is deshielded in the amorphous dispersion relative to acetaminophen freebase, again indicating a change in the molecular packing configuration between acetaminophen and the PVP-acetaminophen dispersion. A weaker longer range intramolecular correlation between N1 and aromatic protons is also observed.

Unlike for the example cocrystal system presented in section 7.4, molecular association between API and hydrophilic carrier is not clearly evidenced from an NH dipolar cross-peak. However, by comparing isotropic ^{1}H chemical shifts and ^{14}N quadrupolar parameters extracted from the ^{14}N-^{1}H spectrum of the dispersion, relative to values extracted from the individual constituents, it is possible to identify changes in the hydrogen bonding configuration, and therefore to determine molecular association between the separate components.

7.6 Conclusions

In cimetidine, with the aid of GIPAW calculations, two intermolecular N-H...N hydrogen bonding motifs were successfully resolved. Additional insight into hydrogen bonding motifs is obtained from a comparison between calculated ^{1}H isotropic shifts for the full crystal structure compared to a single molecule calculation, where intermolecular forces are effectively zero. As the ^{1}H chemical shift is sensitive to changes in hydrogen bonding configurations, any larger differences in ^{1}H chemical shift between the two cases can be attributed to a change in the hydrogen bonding motif. This was demonstrated for cimetidine, where protons involved in intermolecular hydrogen bonding showed large deshielding of $\delta_{iso}(^{1}\mathrm{H})$ between the two calculations. In contrast, protons participating in intramolecular hydrogen bonding interactions exhibited only small deviations in $\delta_{iso}(^{1}\mathrm{H})$.

It is shown that 2D ^{14}N-^{1}H HMQC experiments have much potential for the

characterisation of cocrystal formations and amorphous solid dispersions. Clear evidence of hydrogen bonding was observed in nicotinamide palmitic-acid via a strong NH dipolar cross-peak, which was absent in nicotinamide. Furthermore, as ^{14}N isotropic shifts have a contribution from the quadrupolar interaction, which is sensitive to changes in hydrogen bonding configurations, comparison between nicotinamide and nicotinamide palmitic-acid ^{14}N shifts provide further evidence of changes in hydrogen bonding configurations.

Additionally, ^{14}N-^{1}H HMQC experiments were shown to be applicable to an amorphous system. Identification of hydrogen bonding interactions via ^{14}N-^{1}H spectra provides evidence of molecular association in amorphous solid dispersions. For a 50% w/w acetaminophen-PVP dispersion, definitive evidence of hydrogen bonding through identification of cross peaks was limited by overlapping proton resonances. However, a comparison of the relevant proton chemical shifts and ^{14}N δ_{QIS} values obtained from individual constituents to those found for an acetaminophen-PVP dispersion allowed for the identification of different hydrogen bonding configurations and therefore establishment of molecular association between the individual molecular components.

CHAPTER

EIGHT

SUMMARY AND CONCLUSIONS

Within this thesis, solid-state NMR pulse sequences have been demonstrated with the aim of assisting in the characterisation of pharmaceutically interesting compounds. In particular, heteronuclear $^{14}N/^{15}N$-^{1}H experiments were utilised as screening methodologies of different pharmaceutical solid delivery forms. Furthermore, the effect of homonuclear decoupling sequences upon heteronuclear couplings was investigated using a combination of experimental and density-matrix simulation results.

In organic materials, such as pharmaceuticals, strong homonuclear dipolar couplings exist, which are not completely averaged by MAS. Increasingly complex homonuclear dipolar coupling techniques have been introduced as *rf* console technologies have advanced. During heteronuclear ^{13}C-^{1}H spin-echo experiments it was noted that the application of homonuclear decoupling results in rapid dephasing of signal, relative to that observed in a ^{13}C homonuclear spin-echo experiment. Using density-matrix simulations, it was realised that the evolution due to heteronuclear dipolar coupling under the application of homonuclear dipolar decoupling causes marked dephasing of the NMR signal. Utilising density-matrix simulations, the effect of parameters inaccessible from experiment, notably very high *rf* nutation frequencies, could be established. In agreement with mathematical descriptions of the effect of homonuclear dipolar decoupling upon heteronuclear couplings, higher *rf* nutation frequencies were shown to diminish the effect of third-order cross terms, which are responsible for dephasing of the NMR signal. It is envisaged that the size of third-order cross terms will diminish as the trend towards higher *rf* nutation frequencies continues. Alternatively, develop-

ment of homonuclear sequences where the anisotropic components are removed, whilst maintaining the heteronuclear J coupling, would enhance the efficiency of transfer under heteronuclear J couplings. The effect of changing the eDUMBO-1_{22} decoupling *rf* nutation frequency upon the scaling factor of the J coupling was also examined. It was evident that an increase in the *rf* nutation frequency for a fixed cycle time resulted in a decrease in the scaling factor.

$^{1}J_{15N\text{-}1H}$ spectral editing experiments were implemented to determine the number of directly attached protons to a nitrogen atom. As nitrogen moieties often participate in acid-base reactions, identifying the number of attached protons is an important development issue in pharmaceutical salts. In two pharmaceutical salts, namely tenoxicam and pazopanib, proton transfer relative to the freebase was proved using $^{1}J_{15N\text{-}1H}$ spectral editing methods. Furthermore, NH_2 and NH_3^+ resonances were correctly identified, as the NMR signal observed for an even number of attached protons will never invert, whereas an odd-number of attached proton(s) will invert after a suitable τ increment. As scalar couplings are invariant to motional effects, limitations associated with dipolar based techniques are not a concern. It is envisaged that the $^{1}J_{15N\text{-}1H}$ spectral editing method will be a useful tool for characterising ambiguous cases where salt formation is not clear.

^{14}N-^{1}H correlations were investigated using 2D ^{14}N-^{1}H HMQC experiments applied to the dipeptide β-AspAla. It was evident from investigations into the dependence upon the MAS frequency that higher spinning frequencies, i.e., $\nu_r = 60$ kHz, were important for obtaining a high quality spectrum, particularly for sites with a large C_Q value. Faster spinning frequencies lengthen ^{1}H coherence lifetimes and reduce residual broadening due to strong ^{1}H-^{1}H dipolar couplings. Since correlation is achieved through heteronuclear dipolar couplings, the use of a longer recoupling duration allows for the observation of longer range NH correlations. In conjunction with density-matrix simulations, correlation transfer for short range NH proximities was found to reach a maximum at a much faster rate than longer range NH proximities. Furthermore, shorter range NH proximities had a higher maximum intensity, which is unsurprising as the exchange mechanism was via NH dipolar couplings.

2D ^{14}N-^{1}H HMQC experiments were shown to be adept at identifying hydrogen bonding motifs in pharmaceutically interesting samples. A full ^{14}N assignment

was performed using 2D ^{14}N-^{1}H HMQC experiments for the pharmaceutical molecule, cimetidine. With the assistance of single molecule GIPAW calculations, intra and intermolecular hydrogen bonding interactions were identified. Cocrystals and amorphous solid dispersions are a promising alternative to more traditional solid delivery formations. Herein, ^{14}N-^{1}H correlation experiments offered multiple indicators of intermolecular hydrogen bonding motifs. Firstly, observation of an NH dipolar correlation between nuclei participating in a hydrogen bonding interaction provides definitive evidence of a hydrogen bond. Such a correlation was evident for a cocrystal of nicotinamide palmitic-acid. Furthermore, comparison between a molecular component and cocrystal can be used to indicate changes in hydrogen bonding interactions between components. Inspection of ^{1}H chemical shifts, which are are known to be sensitive to changes in the hydrogen bonding configuration, also reveal molecular association. Furthermore, ^{14}N C_Q values were demonstrated to be sensitive to different hydrogen bonding motifs. Both of these indicators were noted when comparing acetaminophen relative to an amorphous 50% w/w PVP-acetaminophen dispersion.

APPENDIX

A

REPRESENTATIVE SPINEVOLUTION INPUT FILES

A.1 Chapter 4 Input Files

The SPINEVOLUTION file presented below is representative of an input file used in chapter 4, for the example shown FSLG at an effective nutation frequency of 102.06 kHz is simulated during τ periods. This example is for an 8-spin system constructed using the atomic coordinates of L-alanine.

A.1.1 Main Input File

```
****** The System ************************************
spectrometer(MHz) 600
spinning_freq(kHz)10
channels          C13 H1
nuclei            C13 H1 H1 H1 H1 H1 H1 H1
atomic_coords     ch7.cor
cs_isotropic      50 3.5 8.5 8.5 8.5 1.1 1.1 1.1 ppm
csa_parameters    *
j_coupling        ch7.j
quadrupole        *
dip_switchboard   on_8.dsw on_8.dsw on_8.dsw
csa_switchboard   *
exchange_nuclei   (6 7 8) (3 4 5)
bond_len_nuclei   *
bond_ang_nuclei   *
tors_ang_nuclei   *
groups_nuclei     *
******* Pulse Sequence **********************************
CHN 1
timing(usec)      (400)256 (0.5) (400)256
```

```
power(kHz)        0        1000  0
phase(deg)        0        90    0
freq_offs(kHz)    0        0     0
CHN 2
timing(usec)      (FSLG_102060Hz.seq) (0.5) (FSLG_102060Hz.seq)
power(kHz)        *                   1000  *
phase(deg)        *                   90    *
freq_offs(kHz)    *                   0     *
**************************VARIABLES**********************
******* Options etc ************************************
rho0              -I1x
observables       I1p
EulerAngles       rep100
n_gamma           10
line_broaden(Hz)  *
zerofill          *
FFT_dimensions    *
```

A.1.2 Supplementary Input Files

```
ch_7.cor
−3.16816  1.97648  −3.74922  C1
−3.41550  3.04150  −3.84357  H1
−1.31096  2.35538  −4.59138  H2
−2.47401  1.82760  −5.72239  H3
−1.74874  0.70698  −4.66338  H4
−4.79536  1.35750  −5.04425  H5
−5.17374  1.28018  −3.29491  H6
−4.13246  0.04787  −4.03459  H7
```

```
ch_7.j
1  2  150
1  3  0
1  4  0
1  5  0
1  6  0
1  7  0
1  8  0
```

```
on_8.dsw                  off_8.dsw
*                         *
1 *                       0 *
1 1 *                     0 0 *
1 1 1 *                   0 0 0 *
1 1 1 1 *                 0 0 0 0 *
1 1 1 1 1 *               0 0 0 0 0 *
1 1 1 1 1 1 *             0 0 0 0 0 0 *
1 1 1 1 1 1 1 *           0 0 0 0 0 0 0 *
```

```
FSLG_102060Hz.seq
8   102.06   0   72.1673
8   102.06   180 −72.1673


FSLG_220450Hz.seq
3.70370370   220.45   0   155.88
3.70370370   220.45   180 −155.88
```

A.2 Chapter 6 Input Files

The SPINEVOLUTION file presented below is representative of an example input file used in chapter 6, using a τ_{RCPL} time of 33.33 μs and a coordinate system constructed around the NH group in the dipeptide β-AspAla.

A.2.1 Main Input File

```
****** The System ************************************
spectrometer(MHz) 850
spinning_freq(kHz) 60
channels          H1 N14
nuclei            H1 H1 H1 H1 H1 H1 H1 N14
atomic_coords     nh_aspala+4h.cor
cs_isotropic      8.0 5.0 2.7 2.2 0.9 0.9 0.9 -251.1 ppm
csa_parameters    nh_aspala+4h.csa ppm
j_coupling        *
quadrupole        8 3300 0.40 0 0 0
dip_switchboard   *
csa_switchboard   *
exchange_nuclei   (5 6 7)
bond_len_nuclei   *
bond_ang_nuclei   *
tors_ang_nuclei   *
groups_nuclei     *
******* Pulse Sequence ***********************************
CHN 1
timing(usec)      (0.25) (r3x2_1.seq) (16.667) (0) (16.667) (0.5) (16.667)
                  (0)    (16.667)     (r3x2_1.seq)  (10)1024
power(kHz)        1000   *            0        0   0        1000  0
                  0      0            *        0
phase(deg)        90     *            0        0   0        0     0
                  0      0            *        0
freq_offs(kHz)    0      *            0        0   0        0     0
                  0      0            *        0
phase_cycling     2424   *            *        *   *        *     *
                  *      *            *        *   1331(RCV)
```

```
CHN 2
timing(usec)      (0) (33.3334) (16.667) (0.4) (16.667) (0) (16.667)
                  (0.4)         (16.667) (33.3334)  (10)
power(kHz)        0             0        0     1000     0   0     0
                  1000          0        0     0
phase(deg)        0             0        0     0        0   0     0
                  0             0        0     0
freq_offs(kHz)    0             0        0     0        0   0     0
                  0             0        0     0
phase_cycling     *             *        *     *        *   *     *
                  1133          *        *     *
*****************************VARIABLES**********************
******* Options etc ************************************
rho0              I1z+I2z+I3z+I4z+I5z+I6z+I7z+I8z
observables       I1p+I2p+I3p+I4p+I5p+I6p+I7p
EulerAngles       rep100
n_gamma           10
line_broaden(Hz)  *
zerofill          *
FFT_dimensions    *
```

A.2.2 Supplementary Input Files

```
nh_aspala+4h.cor
2.45  3.56  11.28  H5
4.84  4.99  10.17  H9
2.74  2.00  12.75  H7
4.33  1.24  12.71  H8
3.40  5.33  8.11   H10
2.12  4.34  8.84   H11
3.69  3.60  8.42   H12
3.45  3.75  11.12  N2
```

```
nh_aspala+4h.csa
1  8.2   0.78  156  220  300  H5
2  4.2   0.53  10   50   110  H9
3  3.7   0.82  47   85   245  H7
4  −5.9  0.71  60   145  220  H8
5  6.9   0.33  200  15   300  H10
6  3.4   0.83  89   340  150  H11
7  6.6   0.18  25   125  225  H12
8  113.7 0.26  100  150  190  N2
```

```
r3x2_1.seq
16.6667   120   0   0
16.6667   120   180 0
```

REFERENCES

[1] A. S. Tatton, I. Frantsuzov, S. P. Brown, and P. Hodgkinson. Unexpected effects of third-order cross-terms in heteronuclear spin systems under simultaneous radio-frequency irradiation and magic-angle spinning NMR. *J. Chem. Phys.*, 136:084503 (1 – 12), 2012.

[2] A. S. Tatton, T. N. Pham, F. G. Vogt, D. Iuga, A. J. Edwards, and S. P. Brown. Probing intermolecular interactions and nitrogen protonation in pharmaceuticals by novel ^{15}Nedited and 2D ^{14}N^{1}H solid-state NMR. *CrystEngComm*, 14:2654 – 2659, 2012.

[3] A. L. Webber, S. Masiero, S. Pieraccini, J. C. Burley, A. S. Tatton, D. Iuga, T. N. Pham, G. P. Spada, and S. P. Brown. Identifying Guanosine Self Assembly at Natural Isotopic Abundance by High-Resolution ^{1}H and ^{13}C Solid-State NMR Spectroscopy. *J. Am. Chem. Soc.*, 133:19777–19795, 2011.

[4] E. M. Purcell, H. C. Torrey, and R.V. Pound. Resonance absorption by nuclear magnetic moments in a solid. *Phys. Rev.*, 69:37–38, 1946.

[5] F. Bloch, W. W. Hansen, and M. Packard. The nuclear induction experiment. *Phys. Rev.*, 70:474–485, 1946.

[6] E. R. Andrew, A. Bradbury, and R. G. Eades. Nuclear magnetic resonance spectra from a crystal rotated at high speed. *Nature*, 182:1659–1659, 1958.

[7] E. R. Andrew, A. Bradbury, and R. G. Eades. Removal of dipolar broadening of nuclear magnetic resonance spectra of solids by specimen rotation. *Nature*, 183:1802–1803, 1959.

[8] I. J. Lowe. Free Induction Decays of Rotating Solids. *Phys. Rev. Lett.*, 2:285–287, 1959.

[9] Y. Nishiyama, Y. Endo, T. Nemoto, H. Utsumi, K. Yamauchi, K. Hioka, and T. Asakura. Very fast magic angle spinning ^{1}H-^{14}N 2D solid-state NMR: Sub-micro-liter sample data collection in a few minutes. *J. Magn. Reson.*, 208:44–48, 2011.

[10] M. Lee and W. I. Goldburg. Nuclear-magnetic-resonance line narrowing by a rotating rf field. *Phys. Rev. A*, 140:1261–1271, 1965.

[11] J. S. Waugh, L. M. Huber, and U. Haeberlen. Approach to High-Resolution NMR in solids. *Phys. Rev. Lett.*, 20:180–182, 1968.

[12] U. Haeberlen and J. S. Waugh. Coherent averaging effects in magnetic resonance. *Phys. Rev.*, 175:453–467, 1968.

[13] B. C. Gerstein, R. G. Pembleton, R. C. Wilson, and L. M. Ryan. High-resolution NMR in randomly oriented solids with homonuclear dipolar broadening - combined multiple pulse NMR and magic angle spinning. *J. Chem. Phys.*, 66:361–362, 1977.

[14] G. Scheler, U. Haubenreisser, and H. Rosenberger. High-resolution ^{1}H NMR in solids with multiple-pulse sequences and magic-angle sample spinning at 270-MHz. *J. Magn. Reson.*, 44:134–144, 1981.

[15] R. K. Harris, P. Jackson, L. H. Merwin, and B. J. Say. Perspectives in high-resolution solid-state nuclear magnetic resonance, with emphasis on combined rotation and multiple-pulse spectroscopy. *J. Chem. Soc., Faraday Trans. 1*, 84:3649–3672, 1988.

[16] A. Bielecki, A. C. Kolbert, and M. H. Levitt. Frequency-switched pulse sequences - homonuclear decoupling and dilute spin NMR in solids. *Chem. Phys. Lett.*, 155:341–346, 1989.

[17] M. H. Levitt, A. C. Kolbert, A. Bielecki, and D. J. Ruben. High-resolution ^{1}H NMR in solids with frequency-switched multiple-pulse sequences. *Solid State Nucl. Magn. Reson.*, 2:151–163, 1993.

[18] E. Vinogradov, P. K. Madhu, and S. Vega. High-resolution proton solid-state NMR spectroscopy by phase-modulated Lee-Goldburg experiment. *Chem. Phys. Lett.*, 314:443–450, 1999.

[19] D. Sakellariou, A. Lesage, P. Hodgkinson, and L. Emsley. Homonuclear dipolar decoupling in solid-state NMR using continuous phase modulation. *Chem. Phys. Lett.*, 319:253 – 260, 2000.

[20] A. Lesage, D. Sakellariou, S. Hediger, B. Elena, P. Charmont, S. Steuernagel, and L. Emsley. Experimental aspects of proton NMR spectroscopy in solids using phase-modulated homonuclear dipolar decoupling. *J. Magn. Reson.*, 163:105–113, 2003.

[21] B. Elena, G. de Paepe, and L. Emsley. Direct spectral optimisation of proton-proton homonuclear dipolar decoupling in solid-state NMR. *Chem. Phys. Lett.*, 398:532–538, 2004.

[22] A. Lesage, S. Steuernagel, and L. Emsley. Carbon-13 spectral editing in solid-state NMR using heteronuclear scalar couplings. *J. Am. Chem. Soc.*, 120:7095–7100, 1998.

[23] D. Sakellariou, A. Lesage, and L. Emsley. Spectral editing in solid-state NMR using scalar multiple quantum filters. *J. Magn. Reson.*, 151:40–47, 2001.

[24] E. L. Hahn. Spin echoes. *Phys. Rev.*, 80:580–594, 1950.

[25] H. Y. Carr and E. M. Purcell. Effects of Diffusion on Free Precession in Nuclear Magnetic Resonance Experiments. *Phys. Rev.*, 94:630–638, 1954.

[26] L. Duma, W. C. Lai, M. Carravetta, L. Emsley, S. P. Brown, and M. H. Levitt. Principles of spin-echo modulation by J-couplings in Magic-Angle-Spinning Solid-State NMR. *ChemPhysChem*, 5:815–833, 2004.

[27] A. Lesage, D. Sakellariou, S. Steuernagel, and L. Emsley. Carbon-proton chemical shift correlation in solid-state NMR by through-bond multiple-quantum spectroscopy. *J. Am. Chem. Soc.*, 120:13194–13201, 1998.

[28] A. Lesage and L. Emsley. Through-Bond Heteronuclear Single-Quantum Correlation Spectroscopy in Solid-State NMR, and Comparison to Other Through-Bond and Through-Space Experiments. *J. Magn. Reson.*, 148:449 – 454, 2001.

[29] A. Lesage, M. Bardet, and L. Emsley. Through-bond carbon-carbon connectivities in disordered solids by NMR. *J. Am. Chem. Soc.*, 121:10987–10993, 1999.

[30] F. Fayon, D. Massiot, M. H. Levitt, J. J. Titman, D. H. Gregory, L. Duma, L. Emsley, and S. P. Brown. Through-space contributions to two-dimensional double-quantum J correlation NMR spectra of magic-angle-spinning solids. *J. Chem. Phys.*, 122:19413 (1 – 14), 2005.

[31] S. Cadars, J. Sein, L. Duma, A. Lesage, T. N. Pham, J. H. Baltisberger, S. P. Brown, and L. Emsley. The refocused INADEQUATE MAS NMR experiment in multiple spin-systems: Interpreting observed correlation peaks and optimising lineshapes. *J. Magn. Reson.*, 188:24–34, 2007.

[32] B. Elena, A. Lesage, S. Steuernagel, A. Bockmann, and L. Emsley. Proton to carbon-13 INEPT in solid-state NMR spectroscopy. *J. Am. Chem. Soc.*, 127:17296–17302, 2005.

[33] A. L. Webber, B. Elena, J. M. Griffin, J. R. Yates, T. N. Pham, F. Mauri, C. J. Pickard, A. M. Gil, R. Stein, A. Lesage, L. Emsley, and S. P. Brown. Complete ^{1}H resonance assignment of beta-maltose from ^{1}H-^{1}H DQ-SQ CRAMPS and ^{1}H (DQ-DUMBO)-^{13}C SQ refocused INEPT 2D solid-state NMR spectra and first principles GIPAW calculations. *Phys. Chem. Chem. Phys.*, 12:6970–6983, 2010.

[34] M. H. Levitt, T. G. Oas, and R. G. Griffin. Rotary Resonance Recoupling in Heteronuclear Spin Pair Systems. *Isr. J. Chem.*, 28:271–282, 1988.

[35] T. Gullion and J. Schaefer. Rotational-echo double-resonance NMR. *J. Magn. Reson.*, 81:196–200, 1989.

[36] R. Tycko and G. Dabbagh. Measurement of nuclear magnetic dipole-dipole couplings in magic angle spinning NMR. *Chem. Phys. Lett.*, 173:461–465, 1990.

[37] M. Hohwy, H. J. Jakobsen, M. Eden, M. H. Levitt, and N. C. Nielsen. Broadband dipolar recoupling in the nuclear magnetic resonance of rotating solids: A compensated C7 pulse sequence. *J. Chem. Phys.*, 108:2686–2694, 1998.

[38] M. Carravetta, M. Eden, X. Zhao, A. Brinkmann, and M. H. Levitt. Symmetry principles for the design of radiofrequency pulse sequences in the nuclear magnetic resonance of rotating solids. *Chem. Phys. Lett.*, 321:205–215, 2000.

[39] S. R. Hartmann and E. L. Hahn. Nuclear Double Resonance in the Rotating Frame. *Phys. Rev.*, 128:2042–2053, 1962.

[40] A. Pines, M. G. Gibby, and J.S. Waugh. Proton-enhanced nuclear induction spectroscopy. a method for high resolution NMR of dilute spins in solids. *J. Chem. Phys.*, 56:1776–1777, 1972.

[41] A. Pines, M. G. Gibby, and J. S. Waugh. Proton-enhanced NMR of dilute spins in solids. *J. Chem. Phys.*, 59:569–590, 1973.

[42] J. Schaefer and E. O. Stejskal. ^{13}C nuclear magnetic-resonance of polymers spinning at magic angle. *J. Am. Chem. Soc.*, 98:1031–1032, 1976.

[43] R. K. Harris. NMR studies of organic polymorphs & solvates. *Analyst*, 131:351–373, 2006.

[44] K. Schmidt-Rohr, J. Clauss, and H. W. Spiess. Correlation of structure, mobility, and morphological information in heterogeneous polymer materials by two-dimensional wideline-separation NMR spectroscopy. *Macromolecules*, 25:3273–3277, 1992.

[45] H. J. M. de Groot, B. J. van Rossum, C. P. de Groot, V. Ladizhansky, and S. Vega. A method for measuring heteronuclear (^{1}H-^{13}C) distances in high speed MAS NMR. *J. Am. Chem. Soc.*, 122:3465–3472, 2000.

[46] S. P. Brown and H. W. Spiess. Advanced solid-state NMR methods for the elucidation of structure and dynamics of molecular, macromolecular, and supramolecular systems. *Chem. Rev.*, 101:4125–4155, 2001.

[47] S. P. Brown. Probing proton-proton proximities in the solid state. *Prog. Nucl. Magn. Reson. Spectrosc.*, 50:199–251, 2007.

[48] D. Massiot, F. Fayon, B. Alonso, J. Trebosc, and J. P. Amoureux. Chemical bonding differences evidenced from J-coupling in solid state NMR experiments involving quadrupolar nuclei. *J. Magn. Reson.*, 164:160–164, 2003.

[49] D. Iuga, C. Morais, Z. H. Gan, D. R. Neuville, L. Cormier, and D. Massiot. NMR heteronuclear correlation between quadrupolar nuclei in solids. *J. Am. Chem. Soc.*, 127:11540–11541, 2005.

[50] Z. H. Gan, J. P. Amoureux, and J. Trebosc. Proton-detected ^{14}N MAS NMR using homonuclear decoupled rotary resonance. *Chem. Phys. Lett.*, 435:163–169, 2007.

[51] S. Cavadini. Indirect detection of nitrogen-14 in solid-state NMR spectroscopy. *Prog. Nucl. Magn. Reson. Spectrosc.*, 56:46–77, 2010.

[52] M. Bak, J. T. Rasmussen, and N. C. Nielsen. Simpson: A general simulation program for solid-state NMR spectroscopy. *J. Magn. Reson.*, 147:296–330, 2000.

[53] M. Veshtort and R. G. Griffin. SPINEVOLUTION: A powerful tool for the simulation of solid and liquid state NMR experiments. *J. Magn. Reson.*, 178:248–282, 2006.

[54] S. J. Clark, M. D. Segall, C. J. Pickard, P. J. Hasnip, M. J. Probert, K. Refson, and M. C. Payne. First principles methods using CASTEP. *Z. Kristallogr.*, 220:567–570, 2005.

[55] D. Vanderbilt. Soft Self-Consistent Pseudopotentials in a Generalized Eigenvalue Formalism. *Phys. Rev. B*, 41:7892–7895, 1990.

[56] C. J. Pickard and F. Mauri. All-electron magnetic response with pseudopotentials: NMR chemical shifts. *Phys. Rev. B*, 63:245101 (1 – 13), 2001.

[57] J. R. Yates, C. J. Pickard, and F. Mauri. Calculation of NMR chemical shifts for extended systems using ultrasoft pseudopotentials. *Phys. Rev. B*, 76:024401 (1 – 11), 2007.

[58] R. K. Harris, P. Hodgkinson, C. J. Pickard, J. R. Yates, and V. Zorin. Chemical shift computations on a crystallographic basis: some reflections and comments. *Magn. Reson. Chem.*, 45:S174–S186, 2007.

[59] T. Charpentier. The PAW/GIPAW approach for computing NMR parameters: A new dimension added to NMR study of solids. *Solid State Nucl. Mag.*, 40:1–20, 2011.

[60] C. Gervais, R. Dupree, K. J. Pike, C. Bonhomme, M. Profeta, C. J. Pickard, and F. Mauri. Combined first-principles computational and experimental multinuclear solid-state NMR investigation of amino acids. *J. Phys. Chem. A*, 109:6960–6969, 2005.

[61] S. E. Ashbrook, L. Le Polles, C. J. Pickard, A. J. Berry, S. Wimperis, and I. Farnan. First-principles calculations of solid-state ^{17}O and ^{29}Si NMR spectra of Mg_2SiO_4 polymorphs. *Phys. Chem. Chem. Phys.*, 9:1587–1598, 2007.

[62] F. Pourpoint, C. Gervais, L. Bonhomme-Coury, F. Mauri, B. Alonso, and C. Bonhomme. Calcium phosphates: First-principles calculations vs. solid-state NMR experiments. *C. R. Chim.*, 11:398–406, 2008.

[63] S. A. Joyce, J. R. Yates, C. J. Pickard, and S. P. Brown. Density Functional Theory Calculations of Hydrogen-Bond-Mediated NMR J Coupling in the Solid State. *J. Am. Chem. Soc.*, 130:12663–12670, 2008.

[64] J. R. Yates, S. E. Dobbins, C. J. Pickard, F. Mauri, P. Y. Ghi, and R. K. Harris. A combined first principles computational and solid-state NMR study of a molecular crystal: flurbiprofen. *Phys. Chem. Chem. Phys.*, 7:1402–1407, 2005.

[65] N. Mifsud, B. Elena, C. J. Pickard, A. Lesage, and L. Emsley. Assigning powders to crystal structures by high-resolution H-1-H-1 double quantum and H-1-C-13 J-INEPT solid-state NMR spectroscopy and first principles computation. a case study of penicillin G. *Phys. Chem. Chem. Phys.*, 8:3418–3422, 2006.

[66] E. Salager, R. S. Stein, C. J. Pickard, B. Elena, and L. Emsley. Powder NMR crystallography of thymol. *Phys. Chem. Chem. Phys.*, 11:2610–2621, 2009.

[67] J. P. Bradley, S. P. Velaga, O. N. Antzutkin, and S. P. Brown. Probing intermolecular crystal packing in gamma-indomethacin by high-resolution ^{1}H solid-state NMR spectroscopy. *Cryst. Growth Des.*, 11:3463–3471, 2011.

[68] R. T. Berendt, D. M. Sperger, P. K. Isbester, and E. J. Munson. Solid-state NMR spectroscopy in pharmaceutical research and analysis. *Trac-Trend Anal. Chem.*, 25:977–984, 2006.

[69] M. Geppi, G. Mollica, S. Borsacchi, and C. A. Veracini. Solid-state NMR studies of pharmaceutical systems. *Appl. Spectrosc. Rev.*, 43:202–302, 2008.

[70] F. G. Vogt. Evolution of solid-state NMR in pharmaceutical analysis. *Future Med. Chem.*, 2:915–921, 2010.

[71] R. K. Harris. Applications of solid-state NMR to pharmaceutical polymorphism and related matters. *J. Pharm. Pharmacol.*, 59:225–239, 2007.

[72] F. G. Vogt, L. M. Katrincic, S. T. Long, R. L. Mueller, R. A. Carlton, Y. T. Sun, M. N. Johnson, R. C. B. Copley, and M. E. Light. Enantiotropically-related polymorphs of 4-(4-Chloro-3-Fluorophenyl)-2-[4-(Methyloxy)Phenyl]-1, 3-Thiazol-5-yl acetic acid: Crystal structures and multinuclear solid-state NMR. *J. Pharm. Sci.*, 97:4756–4782, 2008.

[73] F. G. Vogt, J. Brum, L. M. Katrincic, A. Flach, J. M. Socha, R. M. Goodman, and R. C. Haltiwanger. Physical, crystallographic, and spectroscopic characterization of a crystalline pharmaceutical hydrate: Understanding the role of water. *Cryst. Growth Des.*, 6:2333–2354, 2006.

[74] J. M. Griffin, D. R. Martin, and S. P. Brown. Distinguishing anhydrous and hydrous forms of an active pharmaceutical ingredient in a tablet formulation using solid-state NMR spectroscopy. *Angew. Chem. Int. Edit.*, 46:8036–8038, 2007.

[75] T. J. Offerdahl, J. S. Salsbury, Z. Dong, D. J. W. Grant, S. A. Schroeder, I. Prakash, E. M. Gorman, D. H. Barich, and E. J. Munson. Quantitation of crystalline and amorphous forms of anhydrous neotame using 13C CPMAS NMR spectroscopy. *J. Pharm. Sci.*, 94:2591–2605, 2005.

[76] J. W. Lubach, D. Xu, B. E. Segmuller, and E. J. Munson. Investigation of the effects of pharmaceutical processing upon solid-state NMR relaxation times and implications to solid-state formulation stability. *J. Pharm. Sci.*, 96:777–787, 2007.

[77] E. Carignani, S. Borsacchi, and M. Geppi. Detailed Characterization of the Dynamics of Ibuprofen in the Solid State by a Multi-Technique NMR Approach. *ChemPhysChem*, 12:974–981, 2011.

[78] R. K. Harris, P. Hodgkinson, T. Larsson, and A. Muruganantham. Quantification of bambuterol hydrochloride in a formulated product using solid-state NMR. *J. Pharm. Biomed. Anal.*, 38:858 – 864, 2005.

[79] G. Mollica, M. Geppi, R. Pignatello, and C. Veracini. Molecular Properties of Flurbiprofen and its Solid Dispersions with Eudragit RL100 Studied by High- and Low-Resolution Solid-State Nuclear Magnetic Resonance. *Pharm. Res.*, 23:2129–2140, 2006.

[80] S. Aitipamula, R. Banerjee, A. K. Bansal, K. Biradha, M. L. Cheney, A. Roy Choudhury, G. R. Desiraju, A. G. Dikundwar, R. Dubey, N. Duggirala, P. P. Ghogale, S. Ghosh, P. K. Goswami, N. R. Goud, R. R. K. R. Jetti, P. Karpinski, P. Kaushik, D. Kumar, V. Kumar, B. Moulton, A. Mukherjee, G. Mukherjee, A. S. Myerson, V. Puri, A. Ramanan, T. Rajamannar, C. M. Reddy, N. Rodriguez-Hornedo, R. D. Rogers, T. N. G. Row, P. Sanphui, N. S., G. Shete, A. Singh, C. C. Sun, J. A. Swift, R. Thaimattam, T. S. Thakur, R. Kumar Thaper, S. P. Thomas, S. Tothadi, V. R. Vangala, N. Variankaval, P. Vishweshwar, D. R. Weyna, and M. J. Zaworotko. Polymorphs, salts, and cocrystals: What's in a name? *Cryst. Growth Des.*, 12:2147–2152, 2012.

[81] P. Heinrich Stahl and Camille G. Wermuth. *Monographs on Acids and Bases.* VHCA ; Wiley-VCH, Weinheim ; New York, 2002, 311-312.

[82] O. Almarsson and M. J. Zaworotko. Crystal engineering of the composition of pharmaceutical phases. Do pharmaceutical co-crystals represent a new path to improved medicines? *Chem. Commun.*, pages 1889–1896, 2004.

[83] P. Vishweshwar, J. A. McMahon, J. A. Bis, and M. J. Zaworotko. Pharmaceutical co-crystals. *J. Pharm. Sci.*, 95:499–516, 2006.

[84] N. Schultheiss and A. Newman. Pharmaceutical cocrystals and their physicochemical properties. *Cryst. Growth Des.*, 9:2950–2967, 2009.

[85] H. G. Brittain. Cocrystal Systems of Pharmaceutical Interest: 2010. *Cryst. Growth Des.*, 12:1046–1054, 2012.

[86] A. T. M. Serajuddin. Solid dispersion of poorly water-soluble drugs: Early promises, subsequent problems, and recent breakthroughs. *J. Pharm. Sci.*, 88:1058–1066, 1999.

[87] S. Janssens and G. Van den Mooter. Review: physical chemistry of solid dispersions. *J. Pharm. Pharmacol.*, 61:1571–1586, 2009.

[88] J. Bernstein, M. C. Etter, and L. Leiserowitz. *The Role of Hydrogen Bonding in Molecular Assemblies*, pages 431–507. Wiley-VCH Verlag GmbH, 2008.

[89] F. G. Vogt, J. S. Clawson, M. Strohmeier, A. J. Edwards, T. N. Pham, and S. A. Watson. Solid-state NMR analysis of organic cocrystals and complexes. *Cryst. Growth Des.*, 9:921–937, 2009.

[90] M. Khan, V. Enkelmann, and G. Brunklaus. Crystal Engineering of Pharmaceutical Co-crystals: Application of Methyl Paraben as Molecular Hook. *J. Am. Chem. Soc.*, 132:5254–5263, 2010.

[91] M. Khan, V. Enkelmann, and G. Brunklaus. Heterosynthon mediated tailored synthesis of pharmaceutical complexes: a solid-state NMR approach. *CrystEngComm*, 13:3213–3223, 2011.

[92] T. N. Pham, S. A. Watson, A. J. Edwards, M. Chavda, J. S. Clawson, M. Strohmeier, and F. G. Vogt. Analysis of amorphous solid dispersions using 2D solid-state NMR and ^{1}H T_1 relaxation measurements. *Mol. Pharm.*, 7:1667–1691, 2010.

[93] A. Newman, D. Engers, S. Bates, I. Ivanisevic, R. C. Kelly, and G. Zografi. Characterization of amorphous API:Polymer mixtures using X-ray powder diffraction. *J. Pharm. Sci.*, 97:4840–4856, 2008.

[94] G. R. Desiraju. A Bond by Any Other Name. *Angew. Chem. Int. Ed.*, 50:52–59, 2011.

[95] S. P. Brown. Applications of high-resolution ^{1}H solid-state NMR. *Solid State Nucl. Mag.*, 41:1–27, 2012.

[96] R. K. Harris, P. Y. Ghi, R. B. Hammond, C. Y. Ma, and K. J. Roberts. Refinement of hydrogen atomic position in a hydrogen bond using a combination of solid-state NMR and computation. *Chem. Commun.*, pages 2834–2835, 2003.

[97] S. Sharif, D. Schagen, M. D. Toney, and H. H. Limbach. Coupling of functional hydrogen bonds in pyridoxal-5 '-phosphate-enzyme model systems observed by solid-state NMR spectroscopy. *J. Am. Chem. Soc.*, 129:4440–4455, 2007.

[98] L. A. O'Dell and R. W. Schurko. Static solid-state 14N NMR and computational studies of nitrogen EFG tensors in some crystalline amino acids. *Phys. Chem. Chem. Phys.*, 11:7069–7077, 2009.

[99] I. C. M. Kwan, X. Mo, and G. Wu. Probing hydrogen bonding and ion-carbonyl interactions by solid-state ^{17}O NMR spectroscopy: G-ribbon and G-quartet. *J. Am. Chem. Soc.*, 129:2398–2407, 2007.

[100] J. R. Yates, T. N. Pham, C. J. Pickard, F. Mauri, A. M. Amado, A. M. Gil, and S. P. Brown. An investigation of weak CH...O hydrogen bonds in maltose anomers by a combination of calculation and experimental solid-state NMR spectroscopy. *J. Am. Chem. Soc.*, 127:10216–10220, 2005.

[101] A. C. Uldry, J. M. Griffin, J. R. Yates, M. Perez-Torralba, M. D. S. Maria, A. L. Webber, M. L. L. Beaumont, A. Samoson, R. M. Claramunt, C. J. Pickard, and S. P. Brown. Quantifying weak hydrogen bonding in uracil and 4-cyano-4 '-ethynylbiphenyl: A combined computational and experimental investigation of NMR chemical shifts in the solid state. *J. Am. Chem. Soc.*, 130:945–954, 2008.

[102] A. L. Webber, L. Emsley, R. M. Claramunt, and S. P. Brown. NMR crystallography of Campho[2,3-c]pyrazole (Z '=6): Combining High-Resolution ^{1}H-^{13}C Solid-State MAS NMR Spectroscopy and GIPAW Chemical-Shift Calculations. *J. Phys. Chem. A*, 114:10435–10442, 2010.

[103] P. J. Hore, J. A. Jones, and S. Wimperis. *NMR: The Toolkit*. Oxford University Press, Oxford, 2000.

[104] M. H. Levitt. *Spin Dynamics*. Wiley, Chichester, 2001.

[105] M. J. Duer. *Introduction to Solid-State NMR Spectroscopy*. Blackwell, Oxford, Oxford, 2004.

[106] U. Haeberlen. *Advances in Magnetic Resonance*. Academic Press, New York, 1976.

[107] A. Samoson. Satellite transition high-resolution NMR of quadrupolar nuclei in powders. *Chem. Phys. Lett.*, 119:29 – 32, 1985.

[108] D. J. States, R. A. Haberkorn, and D. J. Ruben. A Two-Dimensional Nuclear Overhauser Experiment with Pure Absorption Phase in 4 Quadrants. *J. Magn. Reson.*, 48:286–292, 1982.

[109] W. Sommer, J. Gottwald, D. E. Demco, and H. W. Spiess. Dipolar heteronuclear multiple-quantum NMR spectroscopy in rotating solids. *J. Magn. Reson., Ser. A*, 113:131–134, 1995.

[110] P. Hodgkinson. Heteronuclear decoupling in the NMR of solids. *Prog. Nucl. Magn. Reson. Spectrosc.*, 46:197–222, 2005.

[111] A. E. Bennett, C. M. Rienstra, M. Auger, K. V. Lakshmi, and R. G. Griffin. Heteronuclear decoupling in rotating solids. *J. Chem. Phys.*, 103:6951–6958, 1995.

[112] A. Khitrin and B. M. Fung. Design of heteronuclear decoupling sequences for solids. *J. Chem. Phys.*, 112:2392–2398, 2000.

[113] B. M. Fung, A. K. Khitrin, and K. Ermolaev. An improved broadband decoupling sequence for liquid crystals and solids. *J. Magn. Reson.*, 142:97–101, 2000.

[114] D. P. Burum, M. Linder, and R. R. Ernst. Low-power multipulse line narrowing in solid-state NMR. *J. Magn. Reson.*, 44:173–188, 1981.

[115] E. Vinogradov, P. K. Madhu, and S. Vega. Proton spectroscopy in solid state nuclear magnetic resonance with windowed phase modulated Lee-Goldburg decoupling sequences. *Chem. Phys. Lett.*, 354:193 – 202, 2002.

[116] G. Metz, L. Wu, and S. O. Smith. Ramped-amplitude cross-polarization in magic-angle-spinning NMR. *J. Magn. Reson.*, 110:219–227, 1994.

[117] S. Hediger, B. H. Meier, N. D. Kurur, G. Bodenhausen, and R.R. Ernst. NMR cross-polarization by adiabatic passage through the Hartmann-Hahn condition (APHH). *Chem. Phys. Lett.*, 223:283–288, 1994.

[118] P. Palmas, S. Ilas, and E. Girard. Sensitivity improvement of ^{1}H-^{15}N cross-polarization at high MAS frequency applied to NMR structural characterization of organic solids. *Magn. Reson. Chem.*, 49:788–794, 2011.

[119] J. R. Yates and C. J. Pickard. Computation of magnetic resonance parameters for crystalline systems: Principles. Encyclopedia of Magnetic Resonance, Wiley, pages 29 - 40, 2007.

[120] F. Allen. The Cambridge Structural Database: a quarter of a million crystal structures and rising. *Acta Crystallogr. B*, 58:380–388, 2002.

[121] M. D. Segall, P. J. D. Lindan, M. J. Probert, C. J. Pickard, P. J. Hasnip, S. J. Clark, and M. C. Payne. First-principles simulation: ideas, illustrations and the CASTEP code. *J. Phys.-Condens. Matter*, 14:2717–2744, 2002.

[122] P. Hodgkinson. pNMRsim: a general simulation program for large problems in solid-state NMR. URL: `http://www.dur.ac.uk/solids.nmr/software/pnmrsim/`.

[123] J. M. Griffin, C. Tripon, A. Samoson, C. Filip, and S. P. Brown. Low-load rotor-synchronised hahn-echo pulse train (RS-HEPT) ^{1}H decoupling in solid-state NMR: factors affecting MAS spin-echo dephasing times. *Magn. Reson. Chem.*, 45:S198–S208, 2007.

[124] M. Aluas, C. Tripon, J. M. Griffin, X. Filip, V. Ladizhansky, R. G. Griffin, S. P. Brown, and C. Filip. CHHC and ^{1}H–^{1}H magnetization exchange: Analysis by experimental solid-state NMR and 11-spin density-matrix simulations. *J. Magn. Reson.*, 199:173–187, 2009.

[125] J.-N. Dumez and L. Emsley. A master-equation approach to the description of proton-driven spin diffusion from crystal geometry using simulated zero-quantum lineshapes. *Phys. Chem. Chem. Phys.*, 13:7363–7370, 2011.

[126] S. Hafner and H. W. Spiess. Multiple-Pulse Line Narrowing under Fast Magic-Angle Spinning. *J. Magn. Reson., Ser. A*, 121:160 – 166, 1996.

[127] M. Leskes, P. K. Madhu, and S. Vega. Supercycled homonuclear dipolar decoupling in solid-state NMR: Toward cleaner ^{1}H spectrum and higher spinning rates. *J. Chem. Phys.*, 128:052309, 2008.

[128] P. K. Madhu. High-resolution solid-state NMR spectroscopy of protons with homonuclear dipolar decoupling schemes under magic-angle spinning. *Solid State Nucl. Mag. Reson.*, 35:2 – 11, 2009.

[129] E. Salager, R. S. Stein, S. Steuernagel, A. Lesage, B. Elena, and L. Emsley. Enhanced sensitivity in high-resolution 1H solid-state NMR spectroscopy with DUMBO dipolar decoupling under ultra-fast MAS. *Chem. Phys. Lett.*, 469:336 – 341, 2009.

[130] L. Mafra, J. R. B. Gomes, J. Trebosc, J. Rocha, and J. P. Amoureux. ^{1}H-^{1}H double-quantum CRAMPS NMR at very-fast MAS ν_R=35 kHz: A resolution enhancement method to probe ^{1}H-^{1}H proximities in solids. *J. Magn. Reson.*, 196:88–91, 2009.

[131] L. Mafra, R. Siegel, C. Fernandez, D. Schneider, F. Aussenac, and J. Rocha. High-resolution ^{1}H homonuclear dipolar recoupling NMR spectra of biological solids at MAS rates up to 67 kHz. *J. Magn. Reson.*, 199:111–114, 2009.

[132] E. Salager, J-N. Dumez, R. S. Stein, S. Steuernagel, A. Lesage, B. Elena-Herrmann, and L. Emsley. Homonuclear dipolar decoupling with very large scaling factors for high-resolution ultrafast magic angle spinning 1H solid-state NMR spectroscopy. *Chem. Phys. Lett.*, 498:214–220, 2010.

[133] Y. Nishiyama, X. Lu, J. Trebosc, O. Lafon, Z. Gan, P. K. Madhu, and J.-P. Amoureux. Practical choice of ^{1}H-^{1}H decoupling schemes in through-bond ^{1}H-X HMQC experiments at ultra-fast MAS. *J. Magn. Reson.*, 214:151–158, 2012.

[134] J. Brus and A. Jegorov. Through-bonds and through-space solid-state NMR correlations at natural isotopic abundance: signal assignment and structural study of simvastatin. *J. Phys. Chem. A*, 108:3955–3964, 2004.

[135] C. C. Wilson, D. Myles, M. Ghosh, L. N. Johnson, and W. Wang. Neutron diffraction investigations of l- and d-alanine at different temperatures: the search for structural evidence for parity violation. *New J. Chem.*, 29:1318–1322, 2005.

[136] E. Vinogradov, P. K. Madhu, and S. Vega. A bimodal floquet analysis of phase modulated Lee-Goldburg high resolution proton magic angle spinning NMR experiments. *Chem. Phys. Lett.*, 329:207 – 214, 2000.

[137] C. Filip and S. Hafner. Analysis of Multiple-Pulse Techniques under Fast MAS Conditions. *J. Magn. Reson.*, 147:250 – 260, 2000.

[138] V. E. Zorin, M. Ernst, S. P. Brown, and P. Hodgkinson. Insights into homonuclear decoupling from efficient numerical simulation: Techniques and examples. *J. Magn. Reson.*, 192:183–196, 2008.

[139] M. Bak and N. C. Nielsen. REPULSION, a novel approach to efficient powder averaging in solid-state NMR. *J. Magn. Reson.*, 125:132 – 139, 1997.

[140] V. E. Zorin. Gsim - visualisation and processing tool for NMR experiments and simulations. URL: `http://sourceforge.net/projects/gsim`.

[141] M. Ernst. Heteronuclear spin decoupling in solid-state NMR under magic-angle sample spinning. *J. Magn. Reson.*, 162:1 – 34, 2003.

[142] M. Ernst, S. Bush, A. C. Kolbert, and A. Pines. Second-order recoupling of chemical-shielding and dipolar-coupling tensors under spin decoupling in solid-state NMR. *J. Chem. Phys.*, 105:3387–3397, 1996.

[143] A. Schleicher, K. Muller, and G. Kothe. Two dimensional nuclear magnetic resonance relaxation spectroscopy of molecular solids. *J. Chem. Phys.*, 92:6432–6440, 1990.

[144] J. Brus, H. Petrickova, and J. Dybal. Influence of local molecular motions on the determination of ^{1}H-^{1}H internuclear distances measured by 2D ^{1}H spin-exchange experiments. *Solid State Nucl. Magn. Reson.*, 23:183–197, 2003.

[145] R. K. Harris, P. Hodgkinson, V. Zorin, J.-N. Dumez, B. Elena-Herrmann, L. Emsley, E. Salager, and R. S. Stein. Computation and NMR crystallography of terbutaline sulfate. *Magn. Reson. Chem.*, 48:S103–S112, 2010.

[146] W. Q. Tong and G. Whitesell. In situ salt screening–a useful technique for discovery support and preformulation studies. *Pharm. Dev. Technol.*, 3:215–23, 1998.

[147] D. Giron and D. J. W. Grant. *Handbook of pharmaceutical salts : properties, selection, and use.* VHCA ; Wiley-VCH, 2002, pp. 41-81.

[148] S. Berger, S. Braun, and H. O. Kalinowski. *NMR spectroscopy of the non-metallic elements.* John Wiley & Sons, New York, 1997.

[149] Z. J. Li, Y. Abramov, J. Bordner, J. Leonard, A. Medek, and A. V. Trask. Solid-state acid-base interactions in complexes of heterocyclic bases with dicarboxylic acids: Crystallography, hydrogen bond analysis, and N-15 NMR spectroscopy. *J. Am. Chem. Soc.*, 128:8199–8210, 2006.

[150] S. J. Opella and M. H. Frey. Selection of nonprotonated carbon resonances in solid-state nuclear magnetic resonance. *J. Am. Chem. Soc.*, 101:5854–5856, 1979.

[151] M. Alla and E. Lippmaa. High-Resolution Broad Line ^{13}C NMR and Relaxation in Solid Norbornadiene. *Chem. Phys. Lett.*, 37:260–264, 1976.

[152] X. L. Wu and K. W. Zilm. Complete Spectral Editing in CPMAS NMR. *J. Magn. Reson., Ser. A*, 102:205–213, 1993.

[153] X. L. Wu and K. W. Zilm. Methylene-Only Subspectrum in CPMAS NMR. *J. Magn. Reson., Ser. A*, 104:119–122, 1993.

[154] R. Sangill, N. Rastrupandersen, H. Bildsoe, H. J. Jakobsen, and N. C. Nielsen. Optimized Spectral Editing of C-13 MAS NMR-Spectra of Rigid Solids Using Cross-Polarization Methods. *J. Magn. Reson. Ser. A*, 107:67–78, 1994.

[155] X. L. Wu, S. T. Burns, and K. W. Zilm. Spectral Editing in CPMAS NMR - Generating Subspectra Based on Proton Multiplicities. *J. Magn. Reson., Ser. A*, 111:29–36, 1994.

[156] M. Bauer, R. K. Harris, R. C. Rao, D. C. Apperley, and C. A. Rodger. NMR study of desmotropy in irbesartan, a tetrazole-containing pharmaceutical compound. *J. Chem. Soc., Perkin Trans. 2*, 3:475–482, 1998.

[157] E. D. L. Smith, R. B. Hammond, M. J. Jones, K. J. Roberts, J. B. O. Mitchell, S. L. Price, R. K. Harris, D. C. Apperley, J. C. Cherryman, and R. Docherty. The Determination of the Crystal Structure of Anhydrous Theophylline by X-ray Powder Diffraction with a Systematic Search Algorithm, Lattice Energy Calculations, and C-13 and N-15 Solid-State NMR: A Question of Polymorphism in a Given Unit Cell. *J. Phys. Chem. B*, 105:5818–5826, 2001.

[158] K. Oda and H. Koyama. A refinement of the crystal structure of histidine hydrochloride monohydrate. *Acta Crystallogr. Sec. B*, 28:639–642, 1972.

[159] C. H. Gorbitz. Crystal and molecular-structures of the isomeric dipeptides alpha-l-aspartyl-l-alanine and beta-l-aspartyl-l-alanine. *Acta Chem. Scand. Ser. B*, 41:679–685, 1987.

[160] J. P. Perdew, K. Burke, and M. Ernzerhof. Generalized gradient approximation made simple. *Phys. Rev. Lett.*, 77:3865–3868, 1996.

[161] E. Hadicke, F. Frickel, and A. Franke. Structure of Cimetidine (N"-Cyano-N-Methyl-N'-[2-[(5-Methyl-1h-Imidazol-4-yl)-Methylthio]Ethyl]Guanidine), a Histamine H2-Receptor Antagonist. *Chem. Ber. -Recl.*, 111:3222–3232, 1978.

[162] M. R. Caira, L. R. Nassimbeni, and M. Timme. Zwitterionic nature of tenoxicam - crystal-structures and thermal analyses of a polymorph of tenoxicam and a 1/1 tenoxicam/acetonitrile solvate. *J. Pharm. Sci.*, 84:884–888, 1995.

[163] J. R. Patel, R. A. Carlton, F. Yuniatine, T. E. Needham, L. Wu, and F. G. Vogt. Preparation and structural characterization of amorphous spray-dried dispersions of tenoxicam with enhanced dissolution. *J. Pharm. Sci.*, 101:641–663, 2012.

[164] P. A. Harris, A. Boloor, M. Cheung, R. Kumar, R. M. Crosby, R. G. Davis-Ward, A. H. Epperly, K. W. Hinkle, R. N. Hunter, J. H. Johnson, V. B. Knick, C. P. Laudeman, D. K. Luttrell, R. A. Mook, R. T. Nolte, S. K. Rudolph, J. R. Szewczyk, A. T. Truesdale, J. M. Veal, L. Wang, and J. A. Stafford. Discovery of 5-[[4-[(2,3-dimethyl-2H-indazol-6-yl)methylamino]-2-pyrimidinyl]amino]-2-methylbenzenesulfonamide (pazopanib), a novel and potent vascular endothelial growth factor receptor inhibitor. *J. Med. Chem.*, 51:4632–4640, 2008.

[165] L. Frydman and J. S. Harwood. Isotropic Spectra of Half-Integer Quadrupolar Spins from Bidimensional Magic-Angle Spinning NMR. *J. Am. Chem. Soc.*, 117:5367–5368, 1995.

[166] A. Medek, J. S. Harwood, and L. Frydman. Multiple-quantum magic-angle spinning NMR: A new method for the study of quadrupolar nuclei in solids. *J. Am. Chem. Soc.*, 117:12779–12787, 1995.

[167] Z. H. Gan. Isotropic NMR spectra of half-integer quadrupolar nuclei using satellite transitions and magic-angle spinning. *J. Am. Chem. Soc.*, 122:3242–3243, 2000.

[168] S. E. Ashbrook and S. Wimperis. High-resolution NMR of quadrupolar nuclei in solids: the satellite-transition magic angle spinning (STMAS) experiment. *Prog. Nucl. Magn. Reson. Spectrosc.*, 45:53 – 108, 2004.

[169] L. A. O'Dell. Direct detection of nitrogen-14 in solid-state NMR spectroscopy. *Prog. Nucl. Magn. Reson. Spectrosc.*, 59:295 – 318, 2011.

[170] R. Tycko and S.J. Opella. High-resolution ^{14}N overtone spectroscopy: An approach to natural abundance nitrogen NMR of oriented and polycrystalline systems. *J. Am. Chem. Soc.*, 108:3531–3532, 1986.

[171] D.-K. Lee and A. Ramamoorthy. Off-resonance proton-decoupling in overtone NMR spectroscopy of solids. *Chem. Phys. Lett.*, 286:403–407, 1998.

[172] R. E. Stark, R. A. Haberkorn, and R. G. Griffin. ^{14}N NMR determination of NH bond lengths in solids. *J. Chem. Phys.*, 68:1996–1997, 1978.

[173] G. Bodenhausen, R. E. Stark, D. J. Ruben, and R. G. Griffin. Separation of dipolar and quadrupolar splittings in single crystal nitrogen-14 NMR. *Chem. Phys. Lett.*, 67:424 – 427, 1979.

[174] C. Qian, R. Fu, P. Gor'kov, W. W. Brey, T. A. Cross, and Z. Gan. ^{14}N Polarization Inversion Spin Exchange at Magic Angle (PISEMA). *J. Magn. Reson.*, 196:96–99, 2009.

[175] L. A. O'Dell and R. W. Schurko. Fast and simple acquisition of solid-state ^{14}N NMR spectra with signal enhancement via population transfer. *J. Am. Chem. Soc.*, 131:6658–6659, 2009.

[176] L. A. O'Dell and C. I. Ratcliffe. Ultra-wideline ^{14}N NMR spectroscopy as a probe of molecular dynamics. *Chem. Commun.*, 46:6774–6776, 2010.

[177] R. Blinc, M. Mali, R. R. Osredkar, A. Prelesnik, J. Seliger, Z. Zupanĉiĉ, and L. Ehrenberg. ^{14}N NQR Spectroscopy of Some Amino Acids and Nucleic Bases via Double Resonance in the Laboratory Frame. *J. Chem. Phys.*, 57:5087–5093, 1972.

[178] D. T. Edmonds and C. P. Summers. ^{14}N pure quadrupole resonance in solid amino acids. *J. Magn. Reson.*, 12:134 – 142, 1973.

[179] Z. H. Gan. Measuring amide nitrogen quadrupolar coupling by high-resolution ^{14}N/^{13}C NMR correlation under magic-angle spinning. *J. Am. Chem. Soc.*, 128:6040–6041, 2006.

[180] S. Cavadini, A. Lupulescu, S. Antonijevic, and G. Bodenhausen. ^{14}N NMR spectroscopy using residual dipolar splittings in solids. *J. Am. Chem. Soc.*, 128:7706–7707, 2006.

[181] Z. Gan. ^{13}C/^{14}N heteronuclear multiple-quantum correlation with rotary resonance and REDOR dipolar recoupling. *J. Magn. Reson.*, 184:39 – 43, 2007.

[182] J. G. Hexem, M. H. Frey, and S. J. Opella. Influence of nitrogen-14 on carbon-13 NMR spectra of solids. *J. Am. Chem. Soc.*, 103:224–226, 1981.

[183] R. K. Harris and A. C. Olivieri. Quadrupolar effects transferred to spin-$\frac{1}{2}$ magic-angle spinning spectra of solids. *Prog. NMR Spectrosc.*, 24:435 – 456, 1992.

[184] S. Antonijevic and G. Bodenhausen. High-Resolution NMR Spectroscopy in Solids by Truly Magic-Angle Spinning. *Angew. Chem. Int. Edit.*, 44:2935–2938, 2005.

[185] S. Cavadini, A. Abraham, and G. Bodenhausen. Proton-detected nitrogen-14 NMR by recoupling of heteronuclear dipolar interactions using symmetry-based sequences. *Chem. Phys. Lett.*, 445:1–5, 2007.

[186] S. Cavadini, S. Antonijevic, A. Lupulescu, and G. Bodenhausen. Indirect detection of ^{14}N in solids via protons by nuclear magnetic resonance spectroscopy. *J. Magn. Reson.*, 182:168–172, 2006.

[187] S. Cavadini, S. Antonijevic, A. Lupulescu, and G. Bodenhausen. Indirect detection of nitrogen-14 in solid-state NMR spectroscopy. *ChemPhysChem*, 8:1363–1374, 2007.

[188] S. Cavadini, A. Abraham, and G. Bodenhausen. Coherence transfer between spy nuclei and nitrogen-14 in solids. *J. Magn. Reson.*, 190:160–164, 2008.

[189] A. Brinkmann and M. H. Levitt. Symmetry principles in the nuclear magnetic resonance of spinning solids: Heteronuclear recoupling by generalized Hartmann-Hahn sequences. *J. Chem. Phys.*, 115:357–384, 2001.

[190] S. Cavadini, A. Abraham, S. Ulzega, and G. Bodenhausen. Evidence for dynamics on a 100 ns time scale from single- and double-quantum ^{14}N NMR in solid peptides. *J. Am. Chem. Soc.*, 130:10850–10851, 2008.

[191] I. Manet, L. Francini, S. Masiero, S. Pieraccini, G. P. Spada, and G. Gottarelli. An ESI-MS and NMR Study of the Self-Assembly of Guanosine Derivatives. *Helv. Chim. Acta*, 84:2096–2107, 2001.

[192] P. R. Costa, J. D. Gross, M. Hong, and R. G. Griffin. Solid-state NMR measurement of ψ in peptides: a NCCN 2Q-heteronuclear local field experiment. *Chem. Phys. Lett.*, 280:95 – 103, 1997.

[193] J. Mason. *Nitrogen NMR: Encyclopedia of Magnetic Resonance*. John Wiley & Sons, Ltd, 1996.

[194] K. Saalwächter, R. Graf, and H. W. Spiess. Recoupled Polarization-Transfer Methods for Solid-State ^{1}H-^{13}C Heteronuclear Correlation in the Limit of Fast MAS. *J. Magn. Reson.*, 148:398 – 418, 2001.

[195] P. Tekely, P. Palmas, and D. Canet. Effect of Proton Spin Exchange on the Residual ^{13}C MAS NMR Linewidths. Phase-Modulated Irradiation for Efficient Heteronuclear Decoupling in Rapidly Rotating Solids. *J. Magn. Reson., Ser. A*, 107:129 – 133, 1994.

[196] A. Detken, E. H. Hardy, M. Ernst, and B. H. Meier. Simple and efficient decoupling in magic-angle spinning solid-state NMR: the XiX scheme. *Chem. Phys. Lett.*, 356:298 – 304, 2002.

[197] D. Marion and K. Wüthrich. Application of phase sensitive two-dimensional correlated spectroscopy (COSY) for measurements of ^{1}H-^{1}H spin-spin coupling constants in proteins. *Biochem. Biophys. Res. Commun.*, 113:967 – 974, 1983.

[198] T. Giorgi, F. Grepioni, I. Manet, P. Mariani, S. Masiero, E. Mezzina, S. Pieraccini, L. Saturni, G. P. Spada, and G. Gottarelli. Gel-Like Lyomesophases Formed in Organic Solvents by Self-Assembled Guanine Ribbons. *Chem.Eur. J.*, 8:2143–2152, 2002.

[199] Z. Gan, D. M. Grant, and R. R. Ernst. NMR chemical shift anisotropy measurements by RF driven rotary resonance. *Chem. Phys. Lett.*, 254:349 – 357, 1996.

[200] J. P. Bradley, C. Tripon, C. Filip, and S. P. Brown. Determining relative proton-proton proximities from the build-up of two-dimensional correlation peaks in ^{1}H double-quantum MAS NMR: insight from multi-spin density-matrix simulations. *Phys. Chem. Chem. Phys.*, 11:6941–6952, 2009.

[201] J. T. Davis. G-quartets 40 Years Later: From 5'-GMP to Molecular Biology and Supramolecular Chemistry. *Angew. Chem. Int. Edit.*, 43:668–698, 2004.

[202] R. Rinaldi, E. Branca, R. Cingolani, S. Masiero, G. P. Spada, and G. Gottarelli. Photodetectors fabricated from a self-assembly of a deoxyguanosine derivative. *Appl. Phys. Lett.*, 78:3541–3543, 2001.

[203] G. Maruccio, P. Visconti, V. Arima, S. D'Amico, A. Biasco, E. D'Amone, R. Cingolani, R. Rinaldi, S. Masiero, T. Giorgi, and G. Gottarelli. Field Effect Transistor Based on a Modified DNA Base. *Nano Lett.*, 3:479–483, 2003.

[204] T. N. Pham, S. Masiero, G. Gottarelli, and S. P. Brown. Identification by ^{15}N Refocused INADEQUATE MAS NMR of Intermolecular Hydrogen Bonding that Directs the Self-Assembly of Modified DNA Bases. *J. Am. Chem. Soc.*, 127:16018–16019, 2005.

[205] T. N. Pham, J. M. Griffin, S. Masiero, S. Lena, G. Gottarelli, P. Hodgkinson, C. Filip, and S. P. Brown. Quantifying hydrogen-bonding strength: the measurement of $^{2h}J_{NN}$ couplings in self-assembled guanosines by solid-state ^{15}N spin-echo MAS NMR. *Phys. Chem. Chem. Phys.*, 9:3416–3423, 2007.

[206] J. F. Remenar, S. L. Morissette, M. L. Peterson, B. Moulton, J. M. MacPhee, H. R. Guzman, and O. Almarsson. Crystal engineering of novel cocrystals of a triazole drug with 1,4-dicarboxylic acids. *J. Am. Chem. Soc.*, 125:8456–8457, 2003.

[207] D. P. McNamara, S. L. Childs, J. Giordano, A. Iarriccio, J. Cassidy, M. S. Shet, R. Mannion, E. O'Donnell, and A. Park. Use of a glutaric acid cocrystal to improve oral bioavailability of a low solubility API. *Pharmaceut. Res.*, 23:1888–1897, 2006.

[208] A. V. Trask, W. D. S. Motherwell, and W. Jones. Physical stability enhancement of theophylline via cocrystallization. *Int. J. Pharm.*, 320:114–123, 2006.

[209] T. Friscic, A. V. Trask, W. Jones, and W. D. S. Motherwell. Screening for inclusion compounds and systematic construction of three-component solids by liquid-assisted grinding. *Angew. Chem. Int. Edit.*, 45:7546–7550, 2006.

[210] S. Torrado, S. Torrado, J. J. Torrado, and R. Cadorniga. Preparation, dissolution and characterization of albendazole solid dispersions. *Int. J. Pharm.*, 140:247–250, 1996.

[211] J. Desai, K. Alexander, and A. Riga. Characterization of polymeric dispersions of dimenhydrinate in ethyl cellulose for controlled release. *Int. J. Pharm.*, 308:115–123, 2006.

[212] J. Brouwers, M. E. Brewster, and P. Augustijns. Supersaturating drug delivery systems: The answer to solubility-limited oral bioavailability? *J. Pharm. Sci.*, 98:2549–2572, 2009.

[213] C. Bhugra and M. J. Pikal. Role of thermodynamic, molecular, and kinetic factors in crystallization from the amorphous state. *J. Pharm. Sci.*, 97:1329–1349, 2008.

[214] H. Konno and L. S. Taylor. Influence of different polymers on the crystallization tendency of molecularly dispersed amorphous felodipine. *J. Pharm. Sci.*, 95:2692–2705, 2006.

[215] A. Newman, G. Knipp, and G. Zografi. Assessing the performance of amorphous solid dispersions. *J. Pharm. Sci.*, 101:1355–1377, 2012.

[216] W. L. Chiou and S. Riegelma. Pharmaceutical applications of solid dispersion systems. *J. Pharm. Sci.*, 60:1281–1302, 1971.

[217] A. C. F. Rumondor, P. J. Marsac, L. A. Stanford, and L. S. Taylor. Phase Behavior of Poly(vinylpyrrolidone) Containing Amorphous Solid Dispersions in the Presence of Moisture. *Mol. Pharm.*, 6:1492–1505, 2009.

[218] A. C. F. Rumondor and L. S. Taylor. Effect of Polymer Hygroscopicity on the Phase Behavior of Amorphous Solid Dispersions in the Presence of Moisture. *Mol. Pharm.*, 7:477–490, 2010.

[219] K. H. Kim, M. J. Frank, and N. L. Henderson. Application of differential scanning calorimetry to the study of solid drug dispersions. *J. Pharm. Sci.*, 74:283–289, 1985.

[220] J. A. Baird and L. S. Taylor. Evaluation of amorphous solid dispersion properties using thermal analysis techniques. *Adv. Drug Deliver. Rev.*, 64:396 – 421, 2012.

[221] M. M. de Villiers, D. E. Wurster, J. G. Van der Watt, and A. Ketkar. X-ray powder diffraction determination of the relative amount of crystalline acetaminophen in solid dispersions with polyvinylpyrrolidone. *Int. J. Pharmaceut.*, 163:219–224, 1998.

[222] Y. Miwa, T. Mizuno, K. Tsuchida, T. Taga, and Y. Iwata. Experimental charge density and electrostatic potential in nicotinamide. *Acta Crystallogr. S. B*, 55:78–84, 1999.

[223] M. Amai, M. Kamijo, H. Nagase, N. Ogawa, T. Endo, and H. Ueda. Crystal Structure of a 1:1 Complex of Palmitic acid and Nicotinamide. *Anal. Sci.*, 22:x121–x122, 2006.

[224] E. Moreno, R. Cordobilla, T. Calvet, F. J. Lahoz, and A. I. Balana. The C form of n-hexadecanoic acid. *Acta Crystallogr. Sec. C*, 62:129–131, 2006.